The Dynamics of the Cold Conveyor Belt and Sting Jet in an Extratropical Cyclone and the Influence of Diabatic Processes

Timothy Peter Baker

Submitted in accordance with the requirements for the degree of
Doctor of Philosophy

The University of Leeds
School of Earth and Environment
December 2014

Declaration of Authorship

The candidate confirms that the work submitted is his own, except where the work which has formed part of jointly authored publications has been included. The contribution of the candidate and the other authors has been explicitly indicated below. The candidate confirms that appropriate credit has been given within the thesis where reference has been made to the work of others.

The candidates jointly authored publications that share content with this thesis are:

G. Vaughan, J. Methven, D. Anderson, B. Antonescu, L. Baker, T. P. Baker, S. P. Ballard, K. N. Bower, P. R. A. Brown, J. Chagnon, T. W. Choularton, J. Chylik, P. J. Connolly, P. A. Cook, R. J. Cotton, J. Crosier, C. Dearden, J. R. Dorsey, T. H. A. Frame, M. W. Gallagher, M. Goodliff, S. L. Gray, B. J. Harvey, P. Knippertz, H. W. Lean, D. Li, G. Lloyd, O. MartínezâĂŞAlvarado, J. Nicol, J. Norris, E. Öström, J. Owen, D. J. Parker, R. S. Plant, I. A. Renfrew, N. M. Roberts, P. Rosenberg, A. C. Rudd, D. M. Schultz, J. P. Taylor, T. Trzeciak, R. Tubbs, A. K. Vance, P. J. van Leeuwen, A. Wellpott, A. Woolley, (2014). Cloud Banding and Winds in Intense European Cyclones: Results from the DIAMET Project, Bulletin of the American Meteorological Society, In Press.

This paper was written to highlight the DIAMET project and present a first look at some of the data. It presents an overview of the DIAMET project and the observations collected during it. The science is focused on cyclone Friedhelm which is also the subject of this thesis. The majority of the work for this paper was carried out by G. Vaughan and J. Methven. The candidate was involved in the project during the collection of the data and in commenting on drafts of the paper. Figure 1 of the paper is reproduced in Chapter 4.

Acknowledgements

I would like to thank my initial supervisors Peter Knippertz and Alan Blyth for their interest and commitment over the course of the PhD. Also to Doug Parker for stepping in and providing invaluable advice and direction following Peter's repatriation to Germany. The assistance of Doug, Peter and Alan have been pivotal in my progression as a scientist. I would also like to thank my RSG members for their knowledgeable advice.

I would like to thank the DIAMET team for providing encouragement and support, as well as some of the most exciting experiences possible on the '-146'. In particular Chris Dearden for help with the modelling aspects of this study, and Phil Rosenberg for his help and advice on aircraft data. Many enlightening scientific conversations have occurred over the last four years, those with Tim Slater, Tim Hewson, David Schultz, David Smart, Laura, Jenny and Oscar, have been particularly enjoyable. Richard Rigby has provided exceptional computing support.

ICAS has provided the most fantastic support network and I am grateful to all those, past and present, who have talked, discussed, sympathised, encouraged, played football and, most importantly, laughed with me. Particular thanks go to Alex, Ross, Cat, Tom, Ed, Lindsay, Dom, Joey, Jenny and Fuzz. A special thanks must go to Erin for her immeasurable support and good humour. My thanks also go to all those friends, housemates and random acquaintances who I have had the pleasure to know.

Lastly, I would like to give thanks for the support of my family. Their unwavering support will always be appreciated.

Abstract

This thesis examines the influences on the development of high winds in a case of a damaging extratropical cyclone. Extratropical cyclones are a regular occurrence over the United Kingdom (UK) and much of western Europe: strong cyclones can cause major damage and disruption through high winds, flooding and wave damage. Cyclone Friedhelm occurred on the 7^{th}-8^{th} December 2011, and was observed as part of the "DIAbatic Influence on Mesoscale features in ExTratropical Storms" (DIAMET) field campaign. A case of explosive cyclogenesis, Cyclone Friedhelm exhibited a deepening of 44 hPa in 24 hours, almost double that necessary to be considered a meteorological "bomb". As the storm passed over the UK, strong winds caused widespread damage and disruption, particularly across Scotland. These high winds and their influences are the focus of this thesis, in particular the high-wind region to the south-west of the cyclone centre, in which two high wind phenomena can occur, the cold-conveyor belt (CCB) and sting jets (SJ). The Weather Research and Forecasting (WRF) model is used with a high-resolution setup to investigate the mesoscale wind features, while a lower-resolution configuration is employed to examine the large-scale storm development. The high-resolution simulation is compared to routine observations, and those made specifically as part of the DIAMET project. The WRF model is shown to recreate the storm with a good degree of accuracy. The dynamics of the high wind regions are investigated in order to identify the features and the processes that contribute to their evolution. Trajectories are used to identify parcel ensembles resembling both the SJ and CCB. The effects of forces and balanced flows are discussed and a novel way to calculate the gradient flow is presented. The results of this analysis show a systematic region of super-gradient flow to the south and south-west of the cyclone centre and a region of sub-gradient flow to the north. The SJ parcels are analysed in relation to the past literature including a number of different theories on the cause of the SJ's descent. Unlike some theories on SJs, latent cooling is shown to have little effect on the wind field, although it does change trajectory evolution. The lower-resolution setup shows

that latent heating is key to the deepening of the cyclone, but little change in the track is observed when it is removed. The low-level PV anomaly is shown to be key in driving the deepening of the storm. Varying the time during the simulation at which latent heating is switched off shows the importance of the cyclone's deepening rate on the wind speed development. Other novel analyses are conducted in order to examine the relationships between circulation and the high winds, showing a strong relationship between the circulation energy and cyclone pressure.

Contents

Declaration of Authorship **iii**

Acknowledgements **v**

Abstract **vii**

List of Figures **xiii**

List of Tables **xxi**

Abbreviations **xxiii**

1 Introduction **1**
1.1 Motivation 1
1.2 Aims and Objectives 7

2 Background **9**
2.1 Extratropical Cyclone Development 9
2.1.1 Norwegian Model 10
2.1.2 Shapiro-Keyser Model 11
2.1.3 Explosive Development 11
2.2 Dynamical Aspects and Processes of Intense Cyclones 13
2.2.1 Background State 13
2.2.1.1 Baroclinicity 13
2.2.1.2 Large Scale Flow 13
2.2.2 Balances and Idealised Flows 14
2.2.2.1 Geostrophic Balance 14
2.2.2.2 Cyclostrophic Balance 15
2.2.2.3 Inertial Flow 15
2.2.2.4 Gradient Flow 16
2.2.3 Potential Vorticity 17
2.2.4 Atmospheric Instability 18
2.2.4.1 Inertial Instability 18
2.2.4.2 Conditional Instability 19
2.2.4.3 Conditional symmetric instability 19

2.2.5 Kinetic Energy in Cyclones . . . 19
2.3 Diabatic Processes . . . 20
2.3.1 Latent Heat Release . . . 20
2.3.2 Surface Fluxes . . . 21
2.4 Cyclone Features . . . 21
2.4.1 Warm Conveyor Belt . . . 22
2.4.2 Cold Conveyor Belt . . . 23
2.4.3 Sting Jets . . . 24
2.4.3.1 Description of SJs . . . 25
2.4.3.2 Idealised Sting Jets . . . 27
2.4.3.3 Sting Jet Climatologies . . . 28
2.4.3.4 Influence of Conditional Symmetric Instability . . . 28
2.4.3.5 Role of Evaporational Cooling . . . 30
2.4.3.6 Frontolysis Induced Descent . . . 31
2.5 Summary of Literature . . . 31

3 Modelling and Tools 33
3.1 WRF Modelling . . . 33
3.1.1 Model Dynamics . . . 34
3.1.2 Initial and Boundary Conditions . . . 35
3.1.3 Resolution and Nesting . . . 36
3.1.4 Parameterisations . . . 37
3.1.4.1 Cumulus Parameterisation . . . 38
3.1.4.2 Microphysics . . . 39
3.1.4.3 Boundary Layer Scheme . . . 40
3.1.4.4 Land-Surface Model . . . 40
3.1.4.5 Surface Layer Scheme . . . 41
3.1.4.6 Radiation Schemes . . . 41
3.1.5 Model Setup and Computing Summary . . . 42
3.2 Data . . . 43
3.2.1 Dropsondes . . . 43
3.2.2 Lidar . . . 44
3.3 Analysis Methods . . . 44
3.3.1 RIP Trajectories . . . 44

4 Storm Evolution and Model Evaluation 45
4.1 Background Conditions . . . 45
4.2 Observed and Modelled Storm Evolution . . . 46
4.2.1 Sea Level Pressure Evolution . . . 46
4.2.2 Frontal Structure . . . 51
4.2.3 Winds . . . 53
4.2.3.1 ASCAT Comparison . . . 53
4.2.3.2 WRF Winds . . . 55
4.2.4 Satellite . . . 59
4.2.5 Radar . . . 63
4.2.6 Dropsonde Sections . . . 67

4.2.6.1 Dropsonde Leg 1 . . . 70
4.2.6.2 Dropsonde Leg 2 . . . 75
4.3 Summary . . . 77

5 Modelled Storm Dynamics and Processes 83
5.1 Identification of Regions of Interest . . . 83
5.2 Wind Speed Trajectories, Diagnostics and Analysis . . . 87
5.2.1 1000 UTC Trajectories . . . 92
5.2.2 1100 UTC Trajectories . . . 99
5.2.3 1200 UTC Trajectories . . . 104
5.3 Dynamical Flows and Force Balance . . . 108
5.3.1 Geostrophic Wind and Pressure Gradient Force . . . 108
5.3.2 Gradient Wind . . . 112
5.3.2.1 Gradient Wind Methodology . . . 112
5.3.2.2 Gradient Wind Results . . . 116
5.3.3 Bernoulli Function . . . 121
5.4 Latent Heating and Cooling Processes . . . 122
5.5 Frontogenesis . . . 125
5.6 Potential Vorticity . . . 130
5.6.1 Relationship of Potential Vorticity to Absolute Vorticity . . . 132
5.7 Summary . . . 135

6 Sensitivities to Latent Heating and Microphysics 139
6.1 Inclusion of Graupel or Hail in the Microphysics Scheme . . . 139
6.1.1 Effect on Wind Speeds . . . 140
6.2 Effect of Latent Cooling on Winds . . . 144
6.2.1 Trajectories . . . 144
6.3 Large-scale sensitivity to Latent Heating . . . 147
6.3.1 Control Development and Evaluation . . . 148
6.3.1.1 Cumulus Parameterisation Sensitivity . . . 151
6.3.2 Latent Heating Sensitivity . . . 154
6.3.2.1 Track and Deepening . . . 154
6.3.2.2 Wind Speed Differences . . . 156
6.3.2.3 Influence of PV . . . 157
6.3.2.4 Circulation and Kinetic Energy . . . 165
6.3.2.5 Varying the Latent Heating Switch Off Time . . . 171
6.4 Summary . . . 178

7 Conclusions and Further Work 181
7.1 Conclusions . . . 181
7.1.1 Evaluation of WRF Modelling . . . 181
7.1.2 Dynamics of Cyclone Friedhelm . . . 182
7.1.2.1 Identification of a Sting Jet . . . 182
7.1.2.2 Influences on Sting Jet Trajectories . . . 182
7.1.2.3 CCB Trajectories . . . 184
7.1.2.4 Unbalanced Nature of the High Winds . . . 184
7.1.3 Role of Latent Heating . . . 185

7.1.3.1 Kinetic Energy 187
7.1.4 Summary of Key Conclusions 187
7.2 Future Work 188
7.3 Concluding Remarks 189

References **191**

List of Figures

1.1 MODIS satellite image of Cyclone Friedhelm at 1226 UTC. Red line indicates the FAAM-146 flight track. 5

2.1 Conceptual models of the evolution of extratropical cyclones. (a) Norwegian model. (b) Shapiro-Keyser frontal fracture model showing the four stages of development: (I) incipient frontal cyclone (II) frontal fracture (III) bent back warm front (IV) warm seclusion. From Schultz et al. (1998) 10

2.2 Climatology of the 24 hour deepening of one year of extratropical storms. Two separate normal distributions are combined to form the solid line, continuation of each separate distribution indicated by dashed lines. From Roebber (1984) 12

2.3 Schematic structure of a mature (stage III) Shapiro-Keyser cyclone. SCF - surface cold front; SWF - surface warm front; BBF - bent-back front; CCB - cold conveyor belt; SJ - sting jet airstream; DI - dry intrusion; WCB - warm conveyor belt; WCB1 - WCB anticyclonic branch; WCB2 - WCB cyclonic branch; X represents the cyclone center at the surface; white shading indicates cloud top. From Martínez-Alvarado et al. (2014) 22

2.4 Plan (top) and cross sectional (bottom) schematic of SJ evolution and location taken from Clark et al. (2005) 26

2.5 Schematic from Browning (2004) showing how slantwise motions within the cloud head may be responsible for the descending SJ. 29

2.6 Schematic vertical cross-section of the idealised vertical motions associated with (a) frontogenetic regions and (b) frontolytic regions. The warm and cold air masses are represented by the red and blue shading with the front indicated by the purple line. Idealised vertical motions are shown by the black arrows. 32

3.1 Vertical η coordinates in the WRF ARW system. This idealised example shows six levels from the surface p_{hs} to the model top p_{ht}. The relaxation of the terrain-following disturbance with height is visible as the levels increase. From Skamarock et al. (2008) 35

3.2 Schematic of the Arakawa-C grid used in the WRF-ARW model. Horizontal discretisation is shown in (a) and vertical in (b). From Skamarock et al. (2008) . . . 36

3.3 Plots showing the domain size and location for: (a) the high resolution simulations where domain 1 is the total map size and the two nests are indicated by the two marked boxes; and, (b) the NA simulation domain where no nests are included. . 38

4.1 Time series of the 300 hPa zonal wind through November, December and January 2011/2012 for the North Atlantic (between 40-60°N and 10-60°W). Blue line indicates the 2011/2012 values with the ERA-INTERIM (1979-2010) mean and standard deviation are indicated by the black solid and dashed lines respectively. The strong extratropical cyclones over the UK during the period are marked by the letters, with cyclone Friedhelm highlighted by the red circle. From Vaughan et al. (2014) 46
4.2 NWS/NCEP 500 hPa analysis charts for 0000 7th (top) and 8th (bottom) December 2011. Thickness shown in solid black lines and wind barbs. 47
4.3 MO synoptic analysis chart at 0000 07^{th} December 2011. © Crown Publishing . 48
4.4 MO synoptic analysis charts at (a) 0000, (b) 0600, (c) 1200 and (d) 1800 on the 8^{th} December 2011. © Crown Publishing 49
4.5 WRF modelled sea level pressure from Domain 1 at (a) 0000, (b) 0600, (c) 1200 and (d) 1800 UTC 8^{th} December 2011. 50
4.6 Tracks of MO analysis and WRF minimum SLP locations. Red crosses indicate WRF minimum SLP locations every six hours from 0000 UTC 8^{th} Dec. to 1200 UTC 9^{th}. Green crosses indicate approximate MO analysis minimum SLP location. 52
4.7 Domain 1 plots of wind speed (ms^{-1}) - filled colours, and θ_e (K) - white contours every 2 K, on the 850 hPa pressure level at (a) 0000, (b) 0600, (c) 1200 and (d) 1800 UTC 8^{th} December 2011. 53
4.8 Comparison of ASCAT derived winds and WRF modelled winds. (a) ASCAT satellite scatterometer measured wind speeds from the 1134 UTC 8^{th} December 2011 overpass (plot from: $http://manati.star.nesdis.noaa.gov/datasets/ASCATData.php$). (b) WRF modelled 10 m winds at 1130 UTC. 54
4.9 Domain 3 plots of 780 hPa level wind speed (ms^{-1}, shading) and SLP (black contours, every 4 hPa). Plots are shown from 0600, 0800, 1000 and 1200 UTC, (a)-(d) respectively. 57
4.10 As Figure 4.9 but for the 850 hPa level. 59
4.11 As Figure 4.9 but for the 925 hPa level. The white regions indicate where the 925 hPa isobar has intercepted the ground in mountainous regions. 60
4.12 Time series of the maximum mean winds in domain 3 on the 8^{th} December. 780, 850 and 925 hPa pressure levels are indicated by the red, orange and yellow markers and lines, respectively. 61
4.13 IR MSG satellite images at (a) 0800, (c) 1000 and (e) 1200 UTC and WRF outgoing longwave radiation (OLR) images at the same times. (Satellite images courtesy and copyright EUMETSAT/UKMO) 62
4.14 UKMO 1 km composite radar images at (a) 0500, (c) 0800, (e) 1000 and (g) 1200 UTC on the 08^{th} December 2011. Plots (b), (d), (f) and (h) show the corresponding times from the WRF model with rain rate calculated from the simulated reflectivity (dBz) using Equation 4.1 64
4.15 Map of the dropsonde drift throughout their descent. The dropsondes drift west-to-east during descent following the general wind. 68
4.16 780 hPa wind speed (shading and SLP (black lines) at (a) 1200 UTC and (b) 1300 UTC. Black (1-10) and white (11-17) crosses show dropsonde release locations for legs 1 and 2 respectively. Solid black (white) lines show the WRF section locations for leg 1 (2). Dashed black line shows the location of the model section used by Martínez-Alvarado et al. (2014) 71

4.17 Top: Dropsonde section interpolated from dropsonde Leg 1 (Sondes 1-10, Figure 4.16 (a)) showing windspeed (shading) and lidar cloud tops (black peaks). Bottom: WRF simulated wind speed (shading) section for Leg 1 (black solid line Figure 4.16 (a)) at 1200 UTC with cloud mixing ratio (white lines at $1x10^{-7}$ & $2x10^{-7}$ gkg^{-1}) to indicate cloud extent. 72
4.18 As Figure 4.17 but with shading showing θ_e (K). 74
4.19 Figures 4 (b) and (d) (noted here as (a) and (b), respectively) from Martínez-Alvarado et al. (2014). UM Model sections for dropsonde legs 1 (a) and 2 (b). Color shades represent horizontal wind speed (ms^{-1}); thin lines show equivalent potential temperature, with a separation of 1 K; and solid (dashed) bold contours show 80% (90%) relative humidity with respect to ice. 75
4.20 As Figure 4.17 but for dropsonde Leg 2 at 1300 UTC. 78
4.21 As Figure 4.20 but at 1230 UTC. 79
4.22 As Figure 4.18 but for dropsonde Leg 2 80

5.1 Wind speed (shaded) at 780 hPa and SLP (black contours) at (a) 1000 UTC, (b) 1100 UTC and (c) 1200 UTC 8^{th} December. White lines labelled A-A' to H-H' indicate locations of cross-sections. All cross-sections consist of 80 horizontal grid points (240 km) in length. 84
5.2 Cross-sections (a) C-C', (b) B-B' and (c) A-A' at 1000 UTC as marked on Figure 5.1 (a). Wind speed (shaded, ms^{-1}), θ_e (every 2 K, solid blue lines), w (every 0.1 ms^{-1}, negative dashed and zero suppressed, black lines), RH (90-100% every 5%, solid white lines) and cloud (0.005 g kg^{-1}, solid grey lines). Note that (a) is plotted against longitude, while (b) and (c) are plotted against latitude to account for the relative orientation of each cross-section as shown in Figure 5.1 86
5.3 Cross-sections (a) C-C', (b) B-B' and (c) A-A' at 1100 UTC as marked on Figure 5.1 (a). Contours and axes as Figure 5.2. 88
5.4 Cross Sections (a) D-D', (b) B-B' and (c) A-A' at 1200 UTC as marked on Figure 5.1 (a). Contours and axes as Figure 5.2. 89
5.5 850 hPa wind speed (shaded), SLP (black contours) and trajectory location shown every 3 hours from 0300 UTC to 1500 UTC ((a)-(e) respectively). White, gray and black markers indicate trajectory initialisation times of 1000, 1100 and 1200 UTC, respectively, while maker shapes indicate initialisation level: circles - 780 hPa, triangles - 850 hPa, diamonds - 925 hPa. 91
5.6 Storm relative trajectory paths for (a) t1000-780, (b) -850 and (c) -925 trajectories. Trajectory swarms are plotted over the horizontal wind speed on the level of trajectory initiation at 1000 UTC (filled contours, ms^{-1}) and SLP (black contours, every 4 hPa) 92
5.7 Diagnostics from the 64, t1000-780 trajectories: (a) Pressure (hPa), (b) horizontal wind speed (red) and geostrophic wind speed (black) (ms^{-1}), (c) RH with respect to ice (%), (d) Geopotential height (m), (e) θ_w, (f) vertical wind speed (cm s^{-1}). Coloured vertical lines represent times of interest for each trajectory: green - start of acceleration, light blue - start of ascent, navy - start of descent, orange - V_g maximum, red - wind speed maximum, grey, dashed - trajectory initiation time. . 93

5.8 Diagnostics from the 64, t1000-850 trajectories: (a) Pressure (hPa), (b) horizontal wind speed (red) and geostrophic wind speed (black) (ms^{-1}), (c) RH with respect to ice (%), (d) Geopotential height (m), (e) θ_w, (f) vertical wind speed (cm s^{-1}). Coloured vertical lines represent times of interest for each trajectory: green - start of acceleration, light blue - start of ascent, navy - start of descent, orange - V_g maximum, red - wind speed maximum, grey, dashed - trajectory initiation time. . 94

5.9 Diagnostics from the 64, t1000-925 trajectories: (a) Pressure (hPa), (b) horizontal wind speed (red) and geostrophic wind speed (black) (ms^{-1}), (c) RH with respect to ice (%), (d) Geopotential height (m), (e) θ_w, (f) vertical wind speed (cm s^{-1}). Coloured vertical lines represent times of interest for each trajectory: green - start of acceleration, light blue - start of ascent, navy - start of descent, orange - V_g maximum, red - wind speed maximum, grey, dashed - trajectory initiation time. . 95

5.10 Time series of t1000-780 trajectory MPV. 98

5.11 Static stability ($\theta_{850} - \theta_{900}$) at 0600 and 0700 UTC. Locations of the t1000-780 and t1000-850 trajectories are marked by the grey circles and triangles, respectively. 99

5.12 Storm relative trajectory paths for (a) t1100-780, (b) -850 and (c) -925 trajectories. Trajectory swarms are plotted over the horizontal wind speed on the level on trajectory initiation at 1000 UTC (filled contours, ms^{-1}) and SLP (black contours, every 4 hPa) 100

5.13 Diagnostics from the 64, t1100-780 trajectories: (a) Pressure (hpa), (b) horizontal wind speed (red) and geostrophic wind speed (black) (ms^{-1}), (c) RH with respect to ice (%), (d) Geopotential height (m), (e) θ_w, (f) vertical wind speed (cm s^{-1}). Coloured vertical lines represent times of interest for each trajectory: Green - start of acceleration, light blue - start of ascent, navy - start of descent, orange - V_g maximum, red - wind speed maximum, grey, dashed - trajectory initiation time. . 101

5.14 Diagnostics from the 64, t1100-850 trajectories: (a) Pressure (hpa), (b) horizontal wind speed (red) and geostrophic wind speed (black) (ms^{-1}), (c) RH with respect to ice (%), (d) Geopotential height (m), (e) θ_w, (f) vertical wind speed (cm s^{-1}). Coloured vertical lines represent times of interest for each trajectory: Green - start of acceleration, light blue - start of ascent, navy - start of descent, orange - V_g maximum, red - wind speed maximum, grey, dashed - trajectory initiation time. . 102

5.15 Diagnostics from the 64, t1100-925 trajectories: (a) Pressure (hpa), (b) horizontal wind speed (red) and geostrophic wind speed (black) (ms^{-1}), (c) RH with respect to ice (%), (d) Geopotential height (m), (e) θ_w, (f) vertical wind speed (cm s^{-1}). Coloured vertical lines represent times of interest for each trajectory: Green - start of acceleration, light blue - start of ascent, navy - start of descent, orange - V_g maximum, red - wind speed maximum, grey, dashed - trajectory initiation time. . 103

5.16 Storm relative trajectory paths for (a) t1200-780, (b) -850 and (c) -925 trajectories. Trajectory swarms are plotted over the horizontal wind speed on the level on trajectory initiation at 1000 UTC (filled contours, ms^{-1}) and SLP (black contours, every 4 hPa) 104

5.17 Diagnostics from the 64, t1200-780 trajectories: (a) Pressure (hpa), (b) horizontal wind speed (red) and geostrophic wind speed (black) (ms^{-1}), (c) RH with respect to ice (%), (d) Geopotential height (m), (e) θ_w, (f) vertical wind speed (cm s^{-1}). Coloured vertical lines represent times of interest for each trajectory: Green - start of acceleration, light blue - start of ascent, navy - start of descent, orange - V_g maximum, red - wind speed maximum, grey, dashed - trajectory initiation time. . 105

5.18 Diagnostics from the 64, t1200-850 trajectories: (a) Pressure (hpa), (b) horizontal wind speed (red) and geostrophic wind speed (black) (ms^{-1}), (c) RH with respect to ice (%), (d) Geopotential height (m), (e) θ_w, (f) vertical wind speed (cm s^{-1}). Coloured vertical lines represent times of interest for each trajectory: Green - start of acceleration, light blue - start of ascent, navy - start of descent, orange - V_g maximum, red - wind speed maximum, grey, dashed - trajectory initiation time. . 106

5.19 Diagnostics from the 64, t1200-925 trajectories: (a) Pressure (hpa), (b) horizontal wind speed (red) and geostrophic wind speed (black) (ms^{-1}), (c) RH with respect to ice (%), (d) Geopotential height (m), (e) θ_w, (f) vertical wind speed (cm s^{-1}). Coloured vertical lines represent times of interest for each trajectory: Green - start of acceleration, light blue - start of ascent, navy - start of descent, orange - V_g maximum, red - wind speed maximum, grey, dashed - trajectory initiation time. . 107

5.20 Geostrophic wind speed on (a) 780 hPa, (c) 850 and (e) 925 hPa levels and difference to actual wind speed $V_g - V$ on corresponding levels (b, d, f, respectively). Black lines are SLP and white z on the levels of the winds. White, gray and black markers indicate trajectory from initialisation times of 1000, 1100 and 1200 UTC, respectively, while maker shapes indicate initialisation level: circles - 780 hPa, triangles - 850 hPa, diamonds - 925 hPa. 109

5.21 Along-flow PGF component on t1000 (a) -780, (b) -850 and (c) -925 trajectories. Coloured lines as Figures 5.7, 5.8 and 5.9, respectively 111

5.22 Along-flow PGF component on t1100 (a) -780, (b) -850 and (c) -925 trajectories. Coloured lines as Figures 5.13, 5.14 and 5.15, respectively 111

5.23 Along-flow PGF component on t1200 (a) -780, (b) -850 and (c) -925 trajectories. Coloured lines as Figures 5.17, 5.18 and 5.19, respectively 111

5.24 Gradient wind calculation boxes and CCPs: (a) plotted over wind speed on 780 hPa (shaded) with SLP and 780 hPa level z shown by the black and white contours, respectively. Solid grey lines indicate the boxes for which Gradient wind will be calculated, while dashed grey lines show the regions selected as possible centre points. Grey crosses mark the calculated centre points for the respective boxes as denoted by the colours. Panels (b) and (c) show the best correlating R vs. z scatter plots for the A and A' boxes in (a) respectively. 115

5.25 V_{gr} at 780 hPa calculated from the CCP of (a) boxes A/B (dark gray boxes in Figure 5.24 (a)), (b) boxes A'/B' (light gray boxes in Figure 5.24 (a)). Plot (c) is the difference (a)-(b) 116

5.26 Gradient wind at 1000 UTC on (a) 780 hPa, (c) 850 hPa and (e) 925 hPa. Panels (b), (d) and (f) show the difference (V-V_{gr}) on the respective levels. SLP and geopotential height are shown by the black and white contours respectively. Light grey, grey and black markers indicate trajectory from initialisation times of 1000, 1100 and 1200 UTC, respectively, while marker shapes indicate initialisation level: circles - 780 hPa, triangles - 850 hPa, diamonds - 925 hPa. White/black cross indicates the computed centre of curvature. 117

5.27 Gradient wind at 1100 UTC on (a) 780 hPa, (c) 850 hPa and (e) 925 hPa. Panels (b), (d) and (f) show the difference (V-V_{gr}) on the respective levels. SLP and geopotential height are shown by the black and white contours respectively. Light grey, grey and black markers indicate trajectory from initialisation times of 1000, 1100 and 1200 UTC, respectively, while marker shapes indicate initialisation level: circles - 780 hPa, triangles - 850 hPa, diamonds - 925 hPa. White/black cross indicates the computed centre of curvature. 118

5.28 Gradient wind at 1200 UTC on (a) 780 hPa, (c) 850 hPa and (e) 925 hPa. Panels (b), (d) and (f) show the difference (V-V_{gr}) on the respective levels. SLP and geopotential height are shown by the black and white contours respectively. Light grey, grey and black markers indicate trajectory from initialisation times of 1000, 1100 and 1200 UTC, respectively, while marker shapes indicate initialisation level: circles - 780 hPa, triangles - 850 hPa, diamonds - 925 hPa. The white or black cross indicates the computed centre of curvature. 119

5.29 Bernoulli Function and equation terms along the t1000-780 trajectories. (a) Bernoulli number (B); (b) Montgomery Potential M; (c) Φ (zg); (d) c_pT; (e) $\frac{1}{2}\mathbf{U}^2$. Y-axis spacing on (a)-(d) is equal for comparison, spacing on (e) is reduced by a factor of 10. 123

5.30 Time series of latent heating rate (K/hr) for trajectory swarms (a) t1000-780 (b) t1000-850 and (c) t1000-925. Coloured lines are as Figures 5.7, 5.8 and 5.9, respectively. 124

5.31 Time series of latent heating rate (K/hr) for trajectory swarms (a) t1100-780 (b) t1100-850 and (c) t1100-925. Coloured lines are as Figures 5.13, 5.14 and 5.15, respectively. 125

5.32 Time series of latent heating rate (K/hr) for trajectory swarms (a) t1200-780 (b) t1200-850 and (c) t1200-925. Coloured lines are as Figures 5.17, 5.18 and 5.19, respectively. 125

5.33 Frontogenesis at 0700 UTC. (a) and (b) show frontogenesis (shading) on the 700 and 850 hPa levels, respectively, with SLP (black contours). Black circles denote the locations of the t1000-780 trajectories with the black line indicating the location of the cross section shown in (c). Grey triangles and line indicates the t1000-850 trajectory location and the cross section in (d). (c) and (d) show frontogenesis (shading) on the cross-sections indicated by the black and gray lines in (a) and (d), respectively. Red contours indicate horizontal wind speed (every 4 ms^{-1}), black lines show vertical wind speed (every 0.1 ms^{-1}, negative dashed, zero suppressed) and grey contours indicate the cloud mixing ratio (0.005 and 0.001 g kg^{-1}). Green cross indicates mean trajectory pressure, with pluses showing maximum and minimum trajectory pressure. 128

5.34 As Figure 5.33 but for 0800 UTC. 129

5.35 850 hPa PV (shaded), wind speed (green contours, every 5 ms^{-1} from 35 ms^{-1}) SLP (black contours, every 4 hPa) and trajectory location shown every 2 hours from 0600 UTC to 1200 UTC ((a)-(e) respectively). White, gray and black markers indicate trajectory initialisation times of 1000, 1100 and 1200 UTC, respectively, while maker shapes indicate initialisation level: circles - 780 hPa, triangles - 850 hPa, diamonds - 925 hPa. The PV and wind speed have been passed through a smoother 5 and 2 times respectively to reduce the small scale noise. 132

5.36 Figure 7 from Schemm and Wernli (2013): Low-level vertically averaged (1000-850hPa) PV and wind for (a) the moist idealized simulation and (b) a dry simulation. Also shown are the 290-, 295-, and 300-K isentropes at 850 hPa and the region of strong low-level wind 30, 35, and 40 ms^{-1}; green contours) 133

5.37 Evolution of PV hourly from 0600 UTC to 1400 UTC on (a) 700 hPa, (b) 800 hPa and (c) 900 hPa. Coloured contours show PV=5 PVU where colour denotes time as follows: Blue = 0600 UTC, Cyan = 0700 UTC, Dark green = 0800 UTC, Green = 0900 UTC, Yellow = 1000 UTC, Orange = 1100 UTC, Red = 1200 UTC, Pink = 1300 UTC, Magenta = 1400 UTC. 134

5.38 850 hPa η (shaded), wind speed (green contours, every 5 ms^{-1} from 35 ms^{-1}), PV (blue contours, every 2 PVU from 2 PVU) and SLP (black contours, every 4 hPa) and trajectory location shown every 2 hours from 0600 UTC to 1200 UTC ((a)-(d) respectively). light-grey, dark-gray and black markers indicate trajectory initialisation times of 1000, 1100 and 1200 UTC, respectively, while maker shapes indicate initialisation level: circles - 780 hPa, triangles - 850 hPa, diamonds - 925 hPa. The η and wind speed have been passed through a smoother 5 and 2 times respectively to reduce the small-scale noise. 135

6.1 ARCH-CTRL and ARCH-GRAUP wind speed and SLP plots at 1000 UTC. Plots (a), (d)and (g) show ARCH-CTRL on 780, 850 and 925 hPa respectively while (c), (f) and (i) show corresponding levels for the ARCH-GRAUP simulation. Wind speed difference and SLP comparison is shown in the middle column (b), (e) and (h). 141

6.2 ARCH-CTRL and ARCH-HAIL wind speed and SLP plots at 1000 UTC. Plots (a), (d)and (g) show ARCH-CTRL on 780, 850 and 925 hPa respectively while (c), (f) and (i) show corresponding levels for the ARCH-HAIL simulation. Wind speed difference and SLP comparison is shown in the middle column (b), (e) and (h). 142

6.3 Comparison of radar at 1000 UTC to model derived rainrate. Plot (a) shows the UKMO 1 km composite radar image(© Crown Publishing), (b), (c) and (d) show the ARCH-CTRL, graupel and ARCH-HAIL simulations, respectively. 143

6.4 Trajectories initiated from the maximum wind speed location at 1000 UTC on 780 hPa in the no-lc simulation. Coloured vertical lines represent times of interest for each trajectory: green - start of acceleration, light blue - start of ascent, navy - start of descent, orange - V_g maximum, red - wind speed maximum, grey, dashed - trajectory initiation time. 145

6.5 Trajectories initiated in the no-lc simulation from the maximum wind location on 780 hPa from the high-resolution control simulation presented in Chapter 5. Coloured vertical lines represent times of interest for each trajectory: green - start of acceleration, light blue - start of ascent, navy - start of descent, orange - V_g maximum, red - wind speed maximum, grey, dashed - trajectory initiation time. . 146

6.6 Evolution of Cyclone Friedhelm Wind speed (shading) and SLP (black contours) every 12 hours from 1200 UTC 07 December 2011 to 0000 09 December 2011. . 149

6.7 NA domain Wind speed (ms^{-1}) (shading), and θ_e (K) (white contours), on 850 hPa level at (a) 0000, (b) 0600, (c) 1200 and (d) 1800 UTC 8th December 2011. . . . 150

6.8 780 hPa horizontal wind speed (ms^{-1}) at 1200 UTC for (a) CTRL and (b) NO-CU simulations. (c) shows the difference (CTRL-NO-CU) with SLP lines for the ctrl (solid, black) and NO-CU (dashed, grey) runs. 152

6.9 As Figure 6.8 (c) but zoomed in on the centre of the storm. 153

6.10 As Figure 6.9 but showing the difference of the CTRL at 1200 UTC and NO-CU at 1300 UTC. 154

6.11 (a) Tracks of minimum SLP for the CTRL (red), NO-CU (orange) and NO-LH (blue) simulations. Tracks start at 1200 UTC 7th December with crosses marked every 3 hours until 0000 UTC 09th December. Evolution of cyclone minimum SLP (solid lines) shown in (b), (c) and (d) with maximum cyclone wind speeds on 780, 850 and 925 hPa, respectively (dashed lines). Colours are as in (a). Maximum cyclone wind speed in calculated form a 40x40 grid point box centered on the minimum SLP. 155

6.12 Evolution of the 780 hPa wind speed in the CTRL (a, d, g, j), NO-CU (b, e, h, k) and NO-LH (c, f, i, l) simulations. Rows show plots at the same times of 0600, 0900, 1200 and 1500 UTC, top-bottom. 158
6.13 θ contoured onto the 2 PVU surface indicating the dynamic tropopause in the CTRL simulation. Panels (a)-(d) are plotted from 1800 UTC on the 7^{th} every 6 hours. 160
6.14 As 6.13 but for the NO-CU simulation. 161
6.15 As 6.13 but for the NO-LH simulation. 162
6.16 Side-on view of the θ shaded 2 PVU surface. Top row shows CTRL (a), NO-CU (b) and NO-LH (c) at 0600 UTC on 8^{th}. Bottow row (d, e, and f) shows the same runs at 1200 UTC. Surface is shaded from 2 m θ = 284 K to indicate the cyclone position. 163
6.17 PV around the cyclone centre at 1200 UTC. PV (PVU) contoured according to label bar, with values <1 PVU opaque. Surface is shaded from 2 m θ = 284 K to indicate the cyclone position. 164
6.18 Evolution of PV in the CTRL; (a) and (b), NO-CU; (c) and (d) and NO-LH; (e) and (f) on 780 hPa (left column) and 850 hPa (right column). The PV is shown for a 40x40 gridpoint box around the minimum SLP at each time to remove the noise and small scale PV features not associated with the BBF. Contours are marked 1.5 to 3.5 PVU every 1 PVU from 000 UTC 8^{th} Dec. to 0000 UTC 9^{th} Dec every 3 hours as marked in the legend. 166
6.19 As Figure 6.12 but with shading showing PV and green contours indicating wind speed at 35, 40 and 45 ms^{-1}. 167
6.20 Time series of CKE (solid lines) and WKE (dashed lines) on (a) 780, (b) 850 and (c) 925 hPa levels. Coloured lines/markers indicate CTRL (Red), NO-CU (orange) and NO-LH (Blue) simulations. 169
6.21 Scatter plots with lines of best fit of CKE against WKE. Marker and line colours correspond to CTRL - red, NO-CU - orange and NO-LH - Blue. (a), (b) and (c) show CKE from the 780, 850 and 925 hPa levels, respectively. 170
6.22 Scatter plots with lines of best fit of CKE against the minimum cyclone pressure for the CTRL (red), NO-CU (orange) and NO-LH (Blue). (a), (b) and (c) show CKE from the 780, 850 and 925 hPa levels, respectively. Grey lines indicate the line of best fit across the data from all 3 simulations. 172
6.23 As Figure 6.11 but for the NO-CU (orange) and LHo-06 (green) and LHo-00 (dark green) simulations. 174
6.24 NO-CU and LHo-0600 simulation wind speeds and SLP plots at 1200 UTC. Plots (a), (d)and (g) show NO-CU on 780, 850 and 925 hPa respectively while (c), (f) and (i) show corresponding levels for the LHo-0600 simulation. Wind speed difference and SLP comparison is shown in the middle column (b), (e) and (h). . 176
6.25 NO-CU and LHo-0000 simulation wind speeds and SLP plots at 1200 UTC. Plots (a), (d)and (g) show NO-CU on 780, 850 and 925 hPa respectively while (c), (f) and (i) show corresponding levels for the LHo-0000 simulation. Wind speed difference and SLP comparison is shown in the middle column (b), (e) and (h). . 177
6.26 PV differences between the NO-CU simulation and the LHo-0000 (a and c) and the LHo-0600 (b and d) on 780 hPa (top row) and 850 (bottom) hPa level at 1200 UTC 8^{th} Dec. Wind speeds contoured every 5 ms^{-1} from 30 ms^{-1} for NO-CU (green) and the respective LHo (blue). SLP contoured in black for the NO-CU and dashed grey for the LHo simulations. 179

List of Tables

1.1 Details of the most damaging European extratropical storms from 1980 to 2013 (in order of greatest damages). Data from Centre for Research on the Epidemiology of Disasters (www.emdat.be) 2

2.1 Solutions for the Gradient wind equation. From Holton (1992) 17

3.1 Parameterisations used in the control WRF simulations. Note that the Cumulus scheme is switched off at high resolutions (<4 km). 42

4.1 Cyclone Friedhelm minimum SLP and approximate location taken from MO analysis charts, and minimum SLP and location from D01 of the WRF simulation. . . 51
4.2 Dropsonde release times and locations. 68

5.1 Maximum wind speed values and locations for trajectory initiation times and levels. 90
5.2 Possible solutions to the V_{gr} equation 5.7. 113
5.3 Gradient Wind Calculation Values. Lat and Lon indicate the location of the CCP and r^2 shows the correlation of the R against z for this CCP 120

6.1 Maximum wind speed values and locations for trajectory initiation times and levels. 145
6.2 Latent heating sensitivity runs 148
6.3 Line of best fit equations and r^2 values for the CKE and minimum SLP data plotted in Figures 6.22 (a, c, e). "All run" values equate to the grey line calculated from the data from all three of the simulations. 171
6.4 Line of best fit equations and r^2 values for the WKE and minimum SLP data plotted in Figures 6.22 (b, d, f). 173

Abbreviations

Acronym	Description
AMS	American Meteorological Society
ARW	Advanced Research WRF
ASCAT	Advanced Scatterometer
BBF	Bent-back Front
CAPE	Convective Available Potential Energy
CCB	Cold conveyor belt
CCP	Curvature Centre Point
CF	Cold Front
CFL	Courant-Friedrichs-Lewy (errors)
CKE	Circulation Kinetic Energy
CSI	Conditional Symmetric Instability
DI	Dry Intrusion
DIAMET	DIAbatic influences on Mesoscale structures in ExTratropical storms
ECMWF	European Centre for Medium-Range Weather Forecasting
EKE	Eddy Kinetic Energy
EUMETSAT	European Organisation for the Exploitation of Meteorological Satellites
FAAM	Facility for Airborne Atmospheric Measurements
GFS	Global Forecasting System
HPC	High Performance Computing
IPCC	Intergovernmental Panel on Climate Change
LES	Large Eddy Simulation
Lidar	Light Detecting And Ranging Instrument
Metop	Meteorological operational satellite
MetUM	Met Office Unified Model

MO	Met Office
MPV	Moist Potential Vorticity
MST	Mesosphere-Stratosphere-Troposphere radar
NCAR	National Centre for Atmospheric Research
NCEP	National Centers for Environmental Prediction (USA)
NCL	NCAR Command Language
NMM	Nonhydrostatic Mesoscale Model
NWP	Numerical Weather Prediction
NWS	National Weather Service (USA)
OLR	Outgoing Longwave Radiation
PBL	Planetary Boundary Layer
PGF	Pressure Gradient Force
PTE	Pressure Tendency Equation
PV	Potential Vorticity
PVU	Potential Vorticity Unit
RH	Relative Humidity
RIP(4)	Read/Interpolate/Plot program (version 4)
SCAPE	Slantwise Convective Available Potential Energy
SJ	Sting Jet
SLP	Mean Sea Level Pressure
UK	United Kingdom
UTC	Coordinated Universal Time
WCB	Warm Conveyor Belt
WF	Warm Front
WKE	Wind-speed Kinetic Energy
WPS	WRF Preprocessing System
WRF model	Weather Research and Forecasting model

Symbols

Symbol	Description
ζ	Relative vorticity
η	Absolute Vorticity
θ	Potential Temperature
θ_e	Equivalent Potential Temperature
θ_w	Wet-bulb Potential Temperature
ρ	Density of air
Φ	Geopotential
c_p	Specific heat capacity of dry air
f	Coriolis force
g	Acceleration due to gravity
P	Pressure
$\mathbf{U}$	Horizontal Wind speed
V	Speed in natural coordinates
V_{ag}	Ageostrophic wind
V_g	Geostrophic wind
V_{gr}	Gradient wind
z	Geopotential height

Chapter 1

Introduction

This thesis will examine the role of latent heating and cooling in the development of high winds in the cold-conveyor belt (CCB) and sting jet (SJ) region of an extratropical cyclone. High-resolution modelling, combined with in-situ and remote-sensing observations identify the sensitivities of these dynamical phenomena to the microphysical processes involved in the production of latent heating and cooling.

The motivation for this study is outlined in Section 1.1 with the overall aims and specific objectives of this thesis presented in Section 1.2.

1.1 Motivation

Strong winds associated with extratropical cyclones can be a highly damaging and dangerous phenomenon. Extratropical storms occur with high regularity over north-western Europe and often pass with little incident, however, intense storms have the capability to inflict significant damage and disruption. In financial terms, over multiple years, losses from extratropical storms rival those of hurricanes (Malmquist, 1999), with average annual losses from European windstorms between 1979-2008 shown to be approximately US$ 3.6bn (Barredo, 2010).

Table 1.1 shows 12 of the most damaging extratropical storms to affect Europe between 1980-2013. As shown, the financial damage often numbers in the billions of dollars (US). Damaging extratropical storms are not confined to Europe or indeed the recent past, Knox et al. (2011) detail a large number of historically significant worldwide storms and their associated losses from previous

TABLE 1.1: Details of the most damaging European extratropical storms from 1980 to 2013 (in order of greatest damages). Data from Centre for Research on the Epidemiology of Disasters (www.emdat.be)

Date	Name	Damages (US$ Millions)	Deaths
Dec 1999	Lothar	11350	133
Jan 2007	Kyrill	9010	46
Jan 1990	Daria	6860	85
Feb 2010	Xynthia	6074	64
Jan 2005	Erwin (Ulli)	5635	16
Jan 2009	Klaus	5100	28
Dec 1999	Martin	4100	14
Dec 1999	Anatol	3278	27
Oct 1987	"The Great Storm"	3265	24
Feb 1990	Vivian	3230	50
Oct 2002	Jeanett	2532	38
Feb 2008	Emma	1800	13

literature, including 8 of the storms shown in Table 1.1. The North Atlantic storm track can cause several storms to hit European shores in short succession, indeed three of the storms in Table 1.1 (Anatol, Lothar and Martin) all occurred in December 1999, with Lothar and Martin occurring on successive days (Ulbrich et al., 2001). This clustering can cause increased damages through initial wind damage being exacerbated by following storms.

Many financial losses are due to damage to trees in forested areas. Nilsson et al. (2004) show that 110 million m^3 of forests in Sweden were destroyed by 77 recorded storms during the twentieth century. Examples of woodland damages from specific storms include 15 million trees in the UK due to the 1987 "Great Storm" (Quine, 1988) and 5 million m^3 timber damaged by storm "Vivian" (Schüepp et al., 1994)

The threat of these storms is not solely economical, they can be the cause of numerous fatalities as shown in Table 1.1. Ashley and Black (2008) show that in the United States there were 612 deaths from non-convective winds over the period 1980-2005, of these 83% were due to extratropical storms. During the same period over 1000 deaths in Europe have been caused by events listed as storms (CRED, 2013). Alertness to possible danger and correct planning can often help mitigate the human cost of storms like these. Therefore improving understanding, warnings and forecast skill is a continual goal for forecasters and researchers alike.

Although perhaps not as important as sustained and/or heavy rainfall, strong winds can also play

a role in flooding, through storm surges and increased wave height. The deaths of 1,853 Dutch inhabitants in the 1953 North Sea storm surge are a reminder of just how dangerous these phenomena can be (Sterl et al., 2009). The role of extratropical storm high winds on flooding has also been seen recently with storm surges and tidal flooding in the English counties of East Anglia and Somerset during the 2013/2014 winter months (Slingo et al., 2014). This period saw significant damage to coastal locations as a result of wave damage and flooding inland through strong winds coinciding with high tides.

Previous research has identified the south-east quadrant of extratropical storms as a key region for high winds (Grønås, 1995). Two distinct jets have been identified as causes of the high winds in this region, the cold-conveyor belt (CCB) and sting jet (SJ). The CCB is a low level jet which wraps around the low pressure system (Carlson, 1980; Schultz, 2001). This intensifies as it wraps around the low reaching a maximum near the end of the occlusion. SJs are a relatively recent discovery having been first described by Browning (2004). They occur ahead of the occluded front, within the dry slot, having descended from the cloud head. This region and associated phenomena are the focus of this thesis, and a full review of the relevant past literature is presented in Chapter 2.

There have been many studies into the effects of future climate change on extratropical cyclones. Some discrepancies exist over the sign of change in extratropical cyclone intensity with some studies indicating an increase in "intense" extratropical cyclones (Lambert and Fyfe, 2006; Pinto et al., 2007), but others noting a decrease (Pinto et al., 2009). Ulbrich et al. (2009), however, note that this difference is dependant on how "intense" cyclones are classified. They also show that in certain areas, such as the Eastern Atlantic, there is a relatively consistent increase in intense extratropical cyclones in most climate models regardless of the definition of "intense". A number of other possible changes to extratropical cyclones as a result of climate change are also noted. A shortening of the return period for intense extratropical cyclones is seen by Della-Marta et al. (2009). Deser et al. (2010) show that the strongest changes to weather patterns under a climate change scenario will occur in winter, when 95% of European severe storms occur (Alexander et al., 2005). Haarsma et al. (2013) also show an increase in the intensity of autumn extratropical storms through more Atlantic hurricanes undergoing extratropical transition. Autumn storms have the potential to be particularly damaging as trees are still in leaf, giving them a larger surface area and increasing the chances of being felled by strong winds.

Using a number of modelled climate scenarios along with a storm damage model Leckebusch et al. (2007) present a mean potential increase in losses of up to 37% for the UK and Germany, while

Donat et al. (2011) show a mean 25% increase for Germany alone. The threat of coastal flooding may also increase with climate change. Global mean sea levels are expected to rise by up to 1 m by the end of the century (IPCC, 2013). This would increase the risk of tidal and storm surge flooding as a result of windstorms in many areas.

Although CMIP5 simulations do not show significant changes to wind intensities within extratropical cyclones (Zappa et al., 2013), it is important to understand the processes that influence and contribute to damaging storms given the increased numbers expected. It is noted in the IPCC AR5 report (Christensen et al., 2013), that there is low confidence in the long-term projections of the North Atlantic storm track, adding to the uncertainty surrounding our future weather vulnerability. Francis and Vavrus (2012) show that Arctic warming may slow upper-level atmospheric waves causing weather patterns to become more persistent. As stated above, numerous storms in quick succession have been highly damaging in the past, and thus changes to the storm track combined with greater persistence of weather patterns may have significant consequences. A greater fundamental understanding of the drivers and influences on high wind regions can allow us to better predict the potential damages. It is also imperative to understand the limitations and sub-grid scale processes within climate models in order to have confidence in long-term climate predictions.

Currently, the prediction of extratropical storms on a synoptic scale can often be achieved successfully a number of days in advance, however the mesoscale features embedded within these may be poorly forecast spatially, temporally or even missed altogether. It is these features that can cause some of the most damaging weather associated with extratropical storms. Understanding the processes and environments that are important in the formation and evolution of these mesoscale features will help to improve their forecasting. Ashley and Black (2008) show that the majority of deaths due to non-convective winds occur to people in vehicles, boats or outdoors. Increased accuracy in forecasting high winds can allow the public to avoid dangerous situations such as exposed roads or wooded areas, potentially saving lives. With ever increasing computing power and higher resolution operational modelling, the understanding of mesoscale features is essential to ensure models are capable of replicating them in forecasts in order to provide ample warnings and information to public and decision-makers alike.

Much research has been done on extratropical storms since Bjerknes and Soldberg (1922) introduced their seminal paper on the development of North Atlantic cyclones, but numerous uncertainties still remain. These will be examined with a full summary of the relevant literature, presented in

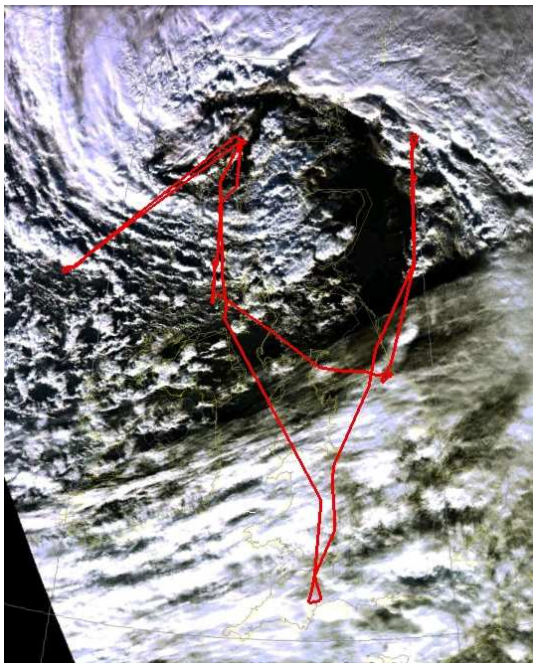

FIGURE 1.1: MODIS satellite image of Cyclone Friedhelm at 1226 UTC. Red line indicates the FAAM-146 flight track.

Chapter 2. A number of recent research programs have sought to better our understanding and predictability of high-impact weather with extratropical windstorms, particularly those over Europe, being key features of interest. This study is part of one such project; the Natural Environment Research Council (NERC) funded "DIAbatic Influence on Mesoscale features in ExTratropical Storms" (DIAMET). DIAMET aims to quantify the diabatic effects and drivers on numerous key mesoscale features within extratropical storms through a combination of observations and high-resolution modelling. DIAMET itself is part of the overarching Storm Risk Mitigation Program which aims to investigate the influences of climate, and the impacts of extratropical storms over the UK as well as the mesoscale focus of DIAMET.

The DIAMET project involved a number of observation periods during which the Facility for Airborne Atmospheric Measurements (FAAM) BAe-146 research aircraft was used to investigate a range of weather systems over the UK. As well as in-situ measurements from the aircraft, other observations such as radiosonde launches and radar scans were also conducted. This thesis will focus on one particular Intense Observation Period (IOP), during which an intense extratropical cyclone passed Northern Europe on the 8^{th} December 2013. DIAMET IOP8 was named Cyclone Friedhelm by the Free University of Berlin adopt-a-vortex naming system. It caused significant damage and disruption to the central belt of Scotland in particular - a full analysis of the storm is

presented in Chapter 4. The FAAM BAe-146 (hereafter FAAM-146) was able to make observations from within the cyclone, which are believed to be the first direct observations from within a SJ cyclone (Vaughan et al., 2014; Martinez-Alvarado et el., 2014). Cyclone Friedhelm is shown in the satellite image in Figure 1.1 with the flight track of the FAAM-146 overlaid. At the time of the image the FAAM-146 was located close to the centre of the storm over the Outer Hebrides.

The FAAM-146 research flight used a number of observational instruments to collect data from within the cyclone, the full suite of on-board instruments is documented in Vaughan et al. (2014). Cloud properties and aerosol numbers are collected using a number of probes designed to cover a wide spread of particle sizes. Winds were measured through a 5-point turbulence probe in the nose of the aircraft. Temperature, trace chemicals (i.e. ozone and carbon monoxide), surface infrared radiation, atmospheric liquid water and water vapour were also measured using a variety of instruments (Vaughan et al., 2014). Dropsondes were releases on three legs of the research sortie, these are explained and examined in more detail in Section 4.2.6.

This thesis investigates the dynamical aspects of Cyclone Friedhelm, particularly the high-wind SJ and CCB regions, and the role of diabatic processes on their development. These areas are often the locations of the highest winds within extratropical storms, but the dynamics and sensitivity of them to diabatic processes are still uncertain. A number of theories have been hypothesised for the formation and development of SJ features (examined in Section 2.4.3) but to date no clear consensus has emerged on their formation. Indeed, all of these hypotheses have not yet been applied to one single case. This thesis will examine all of these theories within the context of a single case, Cyclone Friedhelm, and attempt to identify which theories are most important in SJ development. Identifying the key aspects of the CCB development, including the influence of diabatic processes, will help to address the whole dynamical evolution of the wind fields rather than a blinkered focus on a single feature. Identifying the key processes and conditions that occur in CCBs and SJs can provide benefit not only to the scientific community but also help inform forecasters and provide warnings to the public and commercial sectors.

The Weather Research and Forecasting (WRF) model is used as the main tool for investigating these phenomena. The use of the model allows for the key features within the storm to be analysed in much higher detail than might be otherwise observed. Also, the use of the model allows sensitivity tests can be carried out, in order to identify and investigate the key processes in the cyclone evolution. Although a range of observations were made using the FAAM-146, only some are used in this thesis. This is due to the highly complex nature of the cyclone and the challenges

of comparing in-situ, point data to model data. Other colleagues within the DIAMET project will also focus on detailed model-observation comparisons. However, observations are highly useful for the evaluation of the modelled storm. For these reasons a model evaluation is done using the dropsonde sections, together with the on-board Light Detecting And Ranging instrument (lidar) from the FAAM-146. Chapter 4 examines the WRF model in the context of these observations and others such as satellite imagery and radar data.

1.2 Aims and Objectives

As stated above, extratropical storms can have major social and economic impacts. High winds are the major cause of these impacts, but the mechanisms that influence these high winds are not yet fully understood. This study will address this, with a view to improving forecasting and warnings of these events through our increased knowledge and understanding.

With this in mind the overarching aims of this thesis are to:

- **Understand the dynamical development of the high winds in Cyclone Friedhelm.**
- **Determine the influences of diabatic processes on the high winds, specifically:**
  - **The role of latent cooling on the high winds**
  - **The role of latent heating in the storm development**

These aims will be achieved through completion of the following objectives:

Produce an accurate high-resolution simulation of the storm.

The Weather Research and Forecasting (WRF) model will be used to simulate the case study allowing a four-dimensional picture of the storm to be analysed. Full details of the model and setup are given in Chapter 3

Evaluate the model using observations from the DIAMET campaign and other sources.

The accuracy of the modelled storm evolution will be examined through comparison with a number of observations. The measurements obtained by the FAAM-146 through on-board instruments and dropsonde sections provide a unique dataset with which to do this. The

comparison of the model to these and other observations, such as satellite imagery and wind scatterometer measurements, is discussed in Chapter 4.

Compare storm simulations to previous literature, particularly sting jets.

A full summary of the current scientific literature is given in Chapter 2. The previous work detailed there will supply the context for the dynamical analysis of the simulations presented. The current scientific understanding and knowledge will be scrutinised in light of the results from the model simulations and observations. Chapter 5 will examine the control run within this context, with Chapter 6 focusing on the sensitivity runs.

Document the dynamical evolution of high winds in the SJ & CCB region.

This work will focus on the region of high winds, to the south-west of the cyclone centre, where both SJs and CCBs occur (see Sections 2.4.2 and 2.4.3). The dynamical evolution of the air parcels in these areas will be examined using a number of techniques including trajectory analysis. This will develop an understanding of this particular case and the dynamical processes that are important in the development and evolution of the key features. This dynamical analysis for the control run is presented in Chapter 5.

Compare the dynamical evolution of control simulations to latent heating sensitivity runs.

Chapter 6 will contribute towards the second aim of this work: to investigate the role of diabatic processes on the development of high wind regions. Once the dynamical analysis of the control run is completed, a number of sensitivity runs, where diabatic processes are removed, will be analysed within this context. Comparison of these sensitivity runs to the control will then allow an understanding of the influence of diabatic processes on the high winds in this study in a fully non-linear context.

Synthesise the evidence provided by the simulations presented in Chapters 4-6

The analysis of the literature, storm evolution, dynamical evolution and diabatic sensitivities will allow conclusions to be drawn on the relationship of the high winds to the diabatic processes occurring within the cyclone. These conclusions will be presented in Chapter 7.

Assess the need for future work in this area following the results and conclusions presented.

This thesis will improve our understanding of the dynamics and diabatic processes that are linked with the production of high winds in the CCB and SJ region of an extratropical cyclone. Any outstanding or new questions resulting from this work will be presented in Chapter 7.

Chapter 2

Background

Chapter 1 provided an overview of the aims and objectives for this thesis and the importance of increasing knowledge and understanding within this field. In this Chapter a full literature review is presented to establish the relevant knowledge that will form the base for the results and conclusions hereafter. Initially the development and important processes of extratropical cyclones are discussed. As is evident from the title of this thesis, CCBs and SJs are of particular interest. The theory of these is discussed in Sections 2.4.2 and 2.4.3, respectively.

2.1 Extratropical Cyclone Development

Cyclones develop at widely differing rates. The strongest winds associated with extratropical cyclones often occur in what are know as explosively deepening cyclones or "meteorological bombs". These storms undergo rapid deepening with a central pressure fall of more than 24 hPa in 24 hours (Sanders and Gyakum, 1980).

There are two main theoretical models of cyclonic development; the Norwegian Model and the Shapiro-Keyser model. These both show differences in their evolution and properties during development. Figure 2.1 shows each of their respective developments, which are further described in the following two sub-sections.

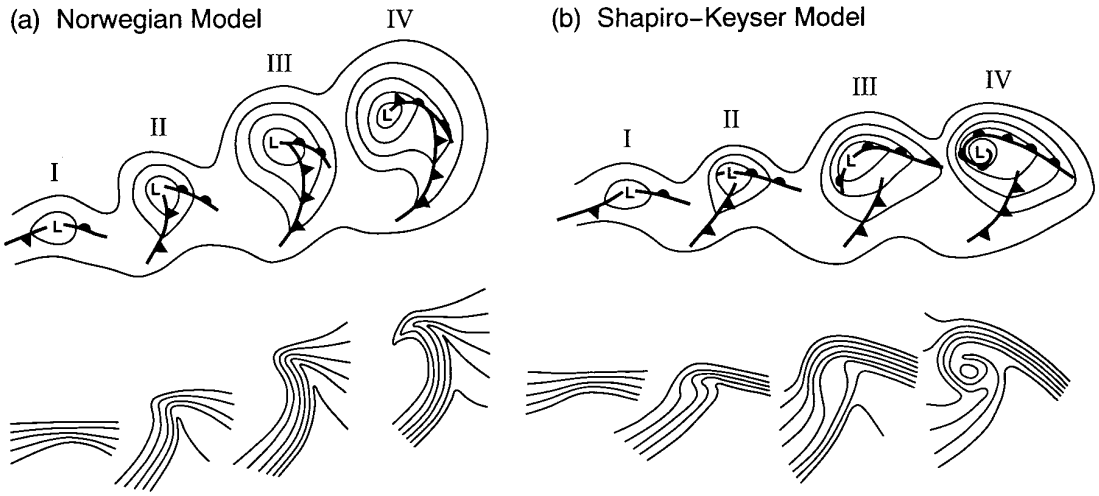

FIGURE 2.1: Conceptual models of the evolution of extratropical cyclones. (a) Norwegian model. (b) Shapiro-Keyser frontal fracture model showing the four stages of development: (I) incipient frontal cyclone (II) frontal fracture (III) bent back warm front (IV) warm seclusion. From Schultz et al. (1998)

2.1.1 Norwegian Model

The Norwegian model was developed in the early 20^{th} century through the work of Bjerknes (1919) and Bjerknes and Soldberg (1922).

The Norwegian model sees an initial cyclonic disturbance on the polar front which causes a warm front (WF) to the east of the cyclone centre to propagate pole-wards. The cold front (CF) to the west travels more rapidly than the preceding warm front. Once the cold front begins to catch up with the warm front it undergoes a process of occlusion (Bjerknes and Soldberg, 1922). This four stage evolution can be seen in Figure 2.1 (a):

- **Stage I** - Incipient cyclone
- **Stage II** - Development of narrow CF and wide WF
- **Stage III** - CF catches WF reducing warm sector, occlusion begins
- **Stage VI** - Occlusion stage as WF is wholly overrun

Schultz et al. (1998) show this evolution occurring when the background flow is diffluent. The Norwegian model persisted as the dominant concept of extratropical cyclone development for

many years. However, it has become apparent that it could not describe the full variety of cyclonic development (Hobbs et al., 1990, 1996; Mass, 1991; Schultz et al., 1998).

2.1.2 Shapiro-Keyser Model

Approximately 70 years on from the presentation of the Norwegian model, Shapiro and Keyser (1990) suggested what is now referred to as the Shapiro-Keyser model (Figure 2.1 (b)). Storms following the Shapiro-Keyser model develop differently from the Norwegian model; here the cold front weakens close to the warm front and splits from it, in a process known as frontal fracture. The CF then continues to propagate away from the cyclone centre, perpendicular to the WF. The WF wraps around the cyclone centre creating a bent-back warm front (or bent-back front, BBF). Often, due to the propagation direction of the system the BBF shows the characteristics of a cold front at the surface. This leads to a seclusion of warm air in the centre of the low. The stages of frontal fracture and the air-flows are shown in the schematic Figure 2.1 (b).

Similar to the Norwegian model, the Shapiro-Keyser model exhibits four stages of development as shown in in Figure 2.1 (b):

- **Stage I** - Incipient cyclone
- **Stage II** - Initial frontal fracture
- **Stage III** - T-bone stage, BBF develops
- **Stage VI** - Warm seclusion forms in storm centre

Shapiro-Keyser cyclones, in contrast to Norwegian type, develop in confluent background flows (Schultz et al., 1998). To date all the identified cases of SJs in the literature are found in Shapiro-Keyser cyclones (Schultz and Sienkiewicz, 2013). As later described in Section 2.4.3, the frontal fracture of the Shapiro-Keyser may be essential for the development of SJs.

2.1.3 Explosive Development

Extratropical cyclones show a broad spectrum of development, in terms of both deepening rate and minimum mean sea-level pressure (SLP). Sanders and Gyakum (1980) describe a storm which

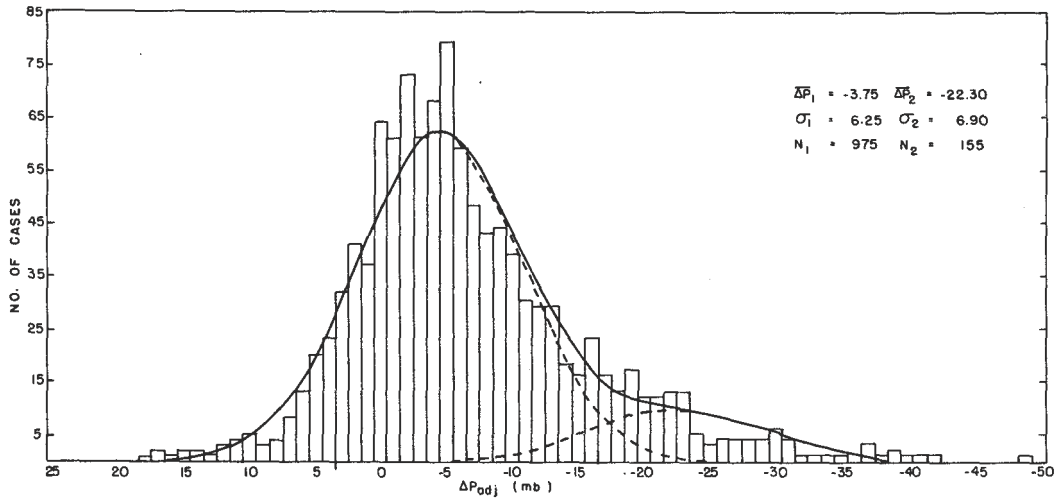

FIGURE 2.2: Climatology of the 24 hour deepening of one year of extratropical storms. Two separate normal distributions are combined to form the solid line, continuation of each separate distribution indicated by dashed lines. From Roebber (1984)

deepens by ~24 hPa in 24 hours as a "bomb" (exact pressure drop is $24 sin\phi / sin60°$ where ϕ is latitude in degrees). These storms have the potential to create large pressure gradient and strong winds.

Explosive deepening is often accompanied by a distinct cloud head structure (Bader, 1995; Böttger et al., 1975). A dry intrusion (DI) of upper-tropospheric or lower stratospheric air will also descend ahead of the hooked cloud head behind the CF (Browning et al., 1997). The DI is often associated with high potential vorticity and can be conducive for cyclogenesis at lower levels (see Section 2.2.3).

Uccellini (1990) show that explosive development of extratropical cyclones is due to a combination of both dynamical and diabatic processes and factors. The literature on these processes is discussed in the following sections.

Roebber (1984) show that the 24 hour deepening of extratropical storms can be described through the sum of two normal distributions (Figure 2.2). The majority of storms show relatively weak deepening, however a sizeable minority undergo strong or very strong deepening, indicated by the right-hand distribution in Figure 2.2. Allen et al. (2010) examine the frequency of explosive cyclonic deepening in both the NH and SH. They show that the frequency of these intense cyclones can be overestimated by some sampling techniques. By using a hybrid technique on Era-Interim NH data, over the period 1989-2008, they identify seasonal averages of 8.2, 20.7 and 7.5 in autumn, winter and spring, respectively.

2.2 Dynamical Aspects and Processes of Intense Cyclones

2.2.1 Background State

The state of the atmosphere in which a cyclone generates is imperative for whether it does indeed generate as well as its evolution after this point.

2.2.1.1 Baroclinicity

Extratropical cyclone development is dependant on a state of background baroclinicity (Charney, 1947; Eady, 1949). Fundamentally, the atmospheric baroclinicity is due to the uneven solar heating of the earth, with large heating at the equator and less towards the poles. This meridional temperature gradient is the cause of the upper-level jets. If perturbations are induced to the basic state they can become amplified and steadily grow. These perturbations can grow to become the cyclones and anticyclones which dominate mid-latitude weather.

2.2.1.2 Large Scale Flow

It has been acknowledged since the 1940s (Rossby and Willett, 1948) that the larger scale flow can have a major influence on the formation of cyclones and, conversely, anticyclones. A number of studies since have shown that different large-scale flows favour different cyclone development patterns (Bader, 1995; Evans et al., 1994; Sawyer, 1950; Schultz et al., 1998; Smigielski and Mogil, 1995).

The jet stream plays an important role in the development of extratropical cyclones. As mentioned in Section 2.2.1.1, a perturbation to the jet stream will grow and amplify due to its inherent instability. For a cyclone to form, there must be divergence aloft to remove the air transported upward through convection and/or large scale ascent. A strong jet can enhance the upper-level divergence strengthening the surface cyclone. Jet streaks are regions of very high momentum air which occur within the larger jet stream. These jet streaks create so-called entrance and exit regions. The right entrance, and left exit regions are particularly conducive for cyclogenesis due to the additional divergence.

Schultz et al. (1998) show that Norwegian-type cyclones are more likely to develop in diffluent background flows. They stretch more meridionally and exhibit stronger CFs accompanied with a weakening and shortening of the WF. Shapiro-Keyser cyclones, however, are more likely to develop in confluent background flows. These exhibit zonal stretching and stronger WFs.

The presence of barotropic shear can play an important role in the evolution of a cyclone. Cyclonic barotropic shear increases the strength of the WF and elongates the cyclone zonally while anticyclonic shear strengthens the CF and elongates meridonally (Davies et al., 1991; Thorncroft et al., 1993). This indicates cyclonic barotropic shear being favourable for Shapiro-Keyser development (Schultz et al., 1998). However, the cyclones which developed in the studies of Davies et al. (1991) and Thorncroft et al. (1993) do not show clear Norwegian or Shapiro-Keyser development, Schultz et al. (1998) suggest that this may be due to a lack of realistic basic state in their model configurations.

2.2.2 Balances and Idealised Flows

There are a number of balances and flows which can be used to describe aspects of atmospheric motion, depending on the circumstances. These are well covered in standard dynamical textbooks such as Holton (1992) and Martin (2006) and are described in the sections below. The balanced flows are idealised and assume steady state without accounting for the effects of vertical velocity or friction (Holton, 1992).

2.2.2.1 Geostrophic Balance

The geostrophic wind is a diagnostic approximation based on the balance of the pressure-gradient force (PGF) and the Coriolis force. Mathematically it is defined in Equation 2.1. It is a good approximation for the wind in large scale synoptic flow in the mid-latitudes being normally within 10-15% of the actual wind (Martin, 2006). The geostrophic wind (V_g), by definition, is always parallel to the isobars. The geostrophic balance is only truly valid where there are no change of motion (i.e. no acceleration) or changes in direction (curvature) and the flow is frictionless.

$$V_g = \frac{-1}{f}\frac{\partial \Phi}{\partial n} \tag{2.1}$$

where V_g is the geostrophic wind, f is the Coriolis parameter, and $\partial\Phi / \partial n$ is the geopotential gradient perpendicular to the flow

Where there is strong curvature or acceleration there can be a large difference between the actual wind and the geostrophic approximation; this difference is known as the ageostrophic wind (Equation 2.2)

$$V_{ag} = V - V_g \tag{2.2}$$

The ageostrophic component of the wind (V_{ag}) will be large where the flow is strongly curved or the acceleration is large. This will be true around systems such as extratropical cyclones meaning the geostrophic approximation is not valid in these regions.

2.2.2.2 Cyclostrophic Balance

The cyclostrophic wind (V_c) is an approximation where the scale is small enough for the Coriolis force to be ignored and the flow is curved, such as for a tornado (Holton, 1992). As shown in Equation 2.3, the change of flow direction is accounted for using the radius of curvature (R).

$$V_c = \left(- R\frac{\partial \Phi}{\partial n} \right)^{\frac{1}{2}} \tag{2.3}$$

As cyclostrophic flow only relates to the PGF and centrifugal flow it may be cyclonic or anticyclonic. At the scale of extratropical cyclones the Coriolis force is large enough to be considered, making cyclostrophic balance unlikely.

2.2.2.3 Inertial Flow

Inertial flow (V_i) is valid where, for a given pressure (geopotential) surface, where the geopotential (pressure) is constant, there is no PGF to contribute to the motion. As a result, the Inertial flow is the balance between the Coriolis and the centrifugal force due to the curvature:

$$V_i = |f|R \tag{2.4}$$

The implication is that there is no acceleration on the flow. Inertial motion is manifested as a circular, anticyclonic flow.

2.2.2.4 Gradient Flow

The gradient flow (V_{gr}) is the combination of the PGF, Coriolis force and the centrifugal force. The flow is parallel to the geostrophic wind, but the addition of curvature makes for a closer estimate of the real wind magnitude in most circumstances (Holton, 1992). As with the geostrophic wind, the gradient wind assumes frictionless flow. The gradient wind can be computed from either the geostrophic streamfunction or from the actual wind (Brill, 2013).

Following Holton (1992) the gradient wind equation is given as,

$$\frac{V^2}{R} + fV = -\frac{\partial \Phi}{\partial n} \tag{2.5}$$

where V is the wind speed and R is the radius of curvature. This can then be solved using the quadratic equation to give,

$$V_{gr} = -\frac{fR}{2} \pm \left(\frac{f^2 R^2}{4} - R\frac{\partial \Phi}{\partial n} \right)^{\frac{1}{2}} \tag{2.6}$$

where, for a given level, $\partial \Phi / \partial n$ can be replaced by $-fV_g$.

This formulation implies that there are multiple results for a given parcel (be it geostrophic or actual). The possible solutions are shown in Table 3.1 in Holton (1992), which is reproduced here in Table 2.1. As shown, a number of the mathematical solutions are impossible due to their non-physical nature. The bold "Positive root" and "Negative root" in Table 2.1 refer to the ± sign in Equation 2.6. The sign of the term R is denoted as to its direction of flow, with R being positive for cyclonic flow and negative for anticyclonic flow.

Brill (2013) shows in his Table 4 the American Meteorological Society (AMS) articles since 2006 which contain "gradient wind" in their abstracts. These show Brill's "steady contour" type to be widely used for tropical cyclone analysis, however it is evident that the gradient wind has been little explored in extratropical cyclones.

Sign $\partial\Phi/\partial n$	R>0	R<0
Positive	Positive root: **Unphysical** Negative root: **Unphysical**	Positive root: **Antibaric flow** (anomalous low) Negative root: **Unphysical**
Negative	Positive root: **Cyclonic flow** (regular low) Negative root: **Unphysical**	Positive root: **Anticyclonic flow** (anomalous flow) Negative root: **Anticyclonic flow** (regular high)

TABLE 2.1: Solutions for the Gradient wind equation. From Holton (1992)

2.2.3 Potential Vorticity

Potential Vorticity (PV) relates the static stability of an air parcel to its vorticity. The basic equation for PV is defined as:

$$PV = \frac{1}{\rho}\eta \cdot \nabla\theta, \tag{2.7}$$

where ρ is the air density, η is the absolute vorticity and $\nabla\theta$ is the gradient of potential temperature. PV is conventionally measured in Potential Vorticity Units (PVU) where 1 PVU = $10^{-6}m^2s^{-1}Kkg^{-1}$. It has two key properties that have made it a highly useful quantity in atmospheric research:

1. Conservation - In adiabatic, frictionless flow PV is, by definition, conserved following isentropic flow. This allows it to be used for assessment of large scale flow and traceability of air masses.

2. Inversion - The properties of PV allow it to be inverted so the full atmospheric flow can be obtained.

A value of 2 PVU is often used in mid- and high-latitudes as a definition of the dynamical tropopause. Due to the high static stability in the stratosphere, PV values there are generally substantially greater than the 0.5 PVU climatological average in the troposphere (Campa and Wernli, 2011).

Since Hoskins et al. (1985), numerous studies have shown PV to play an important role in cyclogenesis and cyclonic deepening (Campa and Wernli, 2011; Schemm and Wernli, 2013; Stoelinga,

1996). Three regions of positive PV anomalies have been identified which contribute to the development of an extratropical cyclone: an upper-level stratospheric intrusion, a low-level anomaly produced through diabatic processes and a surface positive θ anomaly which acts as a positive PV anomaly (Davis and Emanuel, 1991; Kuo et al., 1991; Rossa et al., 2000).

The alignment of the PV anomalies associated with a cyclone is important for the intensification. At the mature stage the three anomalies can become aligned to produce a so-called PV tower. These have been seen in a number of studies of intense cyclones (Bosart et al., 1996; Hoskins and Berrisford, 1988; Uccellini et al., 1987; Wernli et al., 2002; Whitaker et al., 1988), however, they can also occur in less intense cyclones (Rossa et al., 2000). Of these three anomalies, the upper- and low-level have been shown to be more important to the circulation in maritime cyclones while the surface anomaly is more important for continental cyclones (Davis, 1992; Davis et al., 1996). In their climatology of Northern Hemisphere cyclones, Campa and Wernli (2011) show that the upper- and lower-level anomalies determine the cyclone intensity and the lower-level PV is particularly important for producing the most intense cyclones. The low-level anomaly can be responsible for 70% of the strength of a cyclone (Stoelinga, 1996). The upper-level anomaly is usually the precursor for cyclogenesis, with the low-level anomaly being generated as the cyclone deepens (Hoskins and Berrisford, 1988; Rossa et al., 2000; Uccellini, 1990). However, in their study of Cyclone Lothar, Wernli et al. (2002) show a "bottom-up" development where an initial low-level anomaly, caused by strong condensation, induces an upper-level anomaly as the cyclone crosses the jet axis. Wang and Rogers (2001) show the lifetime of the low-level anomalies differs depending on the location of the storm, they also show that storms in the eastern North Atlantic exhibit the low-level PV earlier than those in the western North Atlantic.

2.2.4 Atmospheric Instability

Atmospheric instability is key to the development of both large- and small-scale meteorological features.

2.2.4.1 Inertial Instability

Inertial instability (II) involves the movement of a fluid in the horizontal. It is a product of the centrifugal force due to the rotation of the earth (Emanuel, 1994). In the Northern Hemisphere

absolute vorticity (η) is negative in regions of II. In extratropical systems the flow is inertially stable at synoptic scales (Holton, 1992).

2.2.4.2 Conditional Instability

Conditional Instability (CI) occurs where there is negative moist static stability. In these situations the air is stable if following the dry adiabat but unstable to the moist psuedoadiabat (Holton, 1992). Therefore CI is dependant on the saturation of the air, and will require a forcing such as convergence in order to reach the saturation required for CI to be released.

2.2.4.3 Conditional symmetric instability

Conditional symmetric instability (CSI) has been implicated as a possible driver for SJs. The general theory of CSI is explained here, while its possible contribution to SJ features is examined in detail in Section 2.4.3.

CSI is a moist instability that is released through slantwise motions. It develops where the conditions are stable both inertially and convectively but not in a slantwise sense (Bennetts and Hoskins, 1979; Emanuel, 1983*a*,*b*). In order for CI or CSI to be released, the air must be saturated. Schultz and Schumacher (1999) present a review of CSI, noting that it is often overused or misinterpreted.

SCAPE (Slantwise Convective Available Potential Energy), which is a measure of CSI, has been found to develop more in explosively deepening storms than non-explosive storms (Shutts, 1990*b*). Dixon et al. (2002) show SCAPE to be prevalent in cyclone cloud heads, while there are insignificant values of CAPE, indicating that the majority of circulation within this region will be slantwise. However as shown by Browning et al. (2001), there may be some upright convection in certain areas of the cloud head.

2.2.5 Kinetic Energy in Cyclones

Kinetic energy can be used to investigate and identify numerous aspects of atmospheric motion and cyclones (DiMego and Bosart, 1982; Lackmann et al., 1999; Orlanski and Katzfey, 1991; Orlanski and Sheldon, 1993, 1995; Palmen, 1958).

Papritz and Schemm (2013) show that kinetic energy (KE) is dispersed from the warm sector of their idealised cyclone, some of this is transferred to the region of the BBF. Riviére et al. (2014*b*) examine Cyclones Klaus and Friedhelm from a kinetic energy perspective following Riviére et al. (2014*a*). They show that Eddy Kinetic Energy (EKE) distribution is key to the development and location of the maximum winds around the cyclones. This distribution of the EKE is closely linked to the location of each storm in relation to the upper-level jet. Early in the development both storms are located on the warm side of the jet and the wind maximum is located in the warm sector ahead of the CF. Later the cyclones cross the upper-level jet and the EKE is redistributed to the northern, then south-western sides of the cyclones through the cyclonic motion enhanced by the cyclonic shear of the jet. At this time the wind maxima move to the south-western quadrant of the storm. The wind maxima are sensitive to the addition of the mean flow and therefore the northern side of the cyclone is unfavourable (Riviére et al., 2014*b*).

2.3 Diabatic Processes

Diabatic processes play a major role in the development of extratropical storms, however due to their varied, and often local nature, their effects and relationships with meteorological phenomena are not entirely understood. Providing a better understanding of these processes and the features they influence is one of the key aims of the DIAMET project.

2.3.1 Latent Heat Release

The release of latent heat within the cyclone is a key driver of rapid cyclogenesis and explosive development. A number of studies have described the importance of latent heating in the rapid development of extratropical cyclones (Grønås, 1995; Kuo and Reed, 1988; Shutts, 1990*a*; Wernli et al., 2002). Latent heat release can assist deepening of the storm through enhancement of the low-level PV field and therefore circulation, as well as enhancing the vertical motion increasing the upper divergence and coupling.

Grønås (1995) show the importance of latent heat generated PV anomalies along the BBF in the formation of the warm seclusion. Shutts (1990*a*) showed that in the 1987 Great Storm latent heating was responsible for two thirds of central pressure drop, while Kuo and Reed (1988) found roughly half of the deepening in a Pacific cyclone was a product of the latent heating. Mullen and

Baumhefner (1988) show a similar proportion of deepening from diabatic processes, however, in their case this is equally split between the latent heating and surface fluxes.

As well as the PV generation discussed in section 2.2.3, Stoelinga (1996) showed that latent heat release helped to sustain the coupling of upper- and lower-level anomalies in his case. He also showed that, although being responsible for a significant portion of the deepening, the cyclone was able to form with latent heating removed from the simulation due to the presence of a large upper-level PV anomaly. As stated in Section 2.2.3, the development of storm Lothar was largely attributed to the sustained latent heating at lower-levels, which was then able to interact with the intense upper-level jet (Wernli et al., 2002).

The examples above indicate the varied and interconnected way latent heating can influence cyclone development and the features within them.

2.3.2 Surface Fluxes

Shutts (1990*a*) show that there is negligible effect of surface energy fluxes on the deepening of the 1987 Great Storm in line with a number of previous studies into different cyclones (e.g. Kuo and Reed (1988); Nuss and Anthes (1987)). Other studies have, however, found surface fluxes to play a significant role in the deepening of intense cyclones (Anthes et al., 1983; Mullen and Baumhefner, 1988; Uccellini et al., 1987). Kuo and Reed (1988) concludes that it is therefore evident that although surface fluxes may play a role in the deepening in some cases they are not necessarily an intrinsic part of the process.

2.4 Cyclone Features

Over the years numerous features of Extratropical cyclones have been identified, and their evolutionary theory investigated and honed. Conveyor belts and SJs are key features which produce the high winds in Extratropical cyclones. The literature on these features is examined within this section.

Since the early work of Harrold (1973), Carlson (1980) and Young et al. (1987) the term "conveyor belts" has been widely used to describe specific flows around extratropical cyclones (e.g. Bader (1995); Browning (1990, 1999)). These airstreams are normally simplified into three categories,

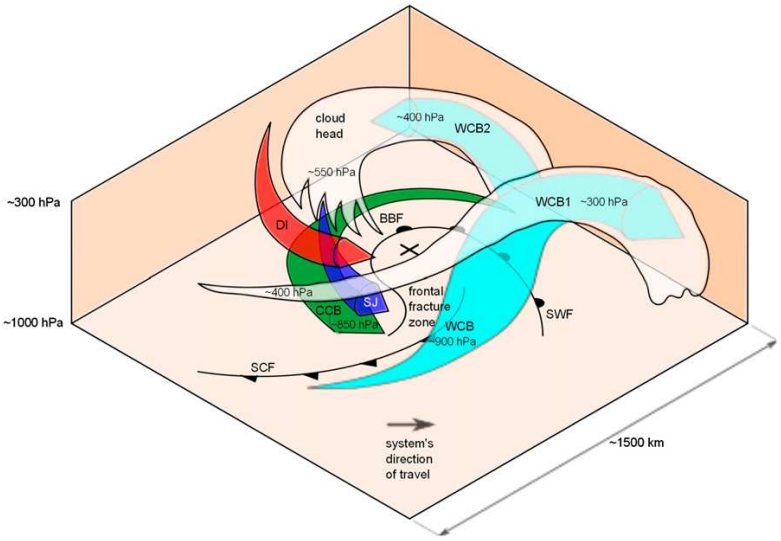

FIGURE 2.3: Schematic structure of a mature (stage III) Shapiro-Keyser cyclone. SCF - surface cold front; SWF - surface warm front; BBF - bent-back front; CCB - cold conveyor belt; SJ - sting jet airstream; DI - dry intrusion; WCB - warm conveyor belt; WCB1 - WCB anticyclonic branch; WCB2 - WCB cyclonic branch; X represents the cyclone center at the surface; white shading indicates cloud top. From Martínez-Alvarado et al. (2014)

the warm conveyor belt (WCB), cold conveyor belt (CCB) and dry intrusion (DI), although in reality this is likely to be an oversimplification of the flows (Bader, 1995; Mass and Schultz, 1993; Reed et al., 1994; Schultz, 2001). Sting jets (SJ) are a more recently identified phenomena, being first described by Browning (2004), and are a potential cause of high winds in strong extratropical storms. The idea of discrete airstreams with distinct boundaries has been questioned in some papers (Kuo et al., 1992; Mass and Schultz, 1993; Reed et al., 1994), however, despite these criticisms the conveyor-belt terminology provides a useful model for investigation of the influences on cyclonic development. Figure 2.3 shows a schematic of these features in a Shapiro-Keyser cyclone at stage III. The literature on cold- and warm-conveyor belts is examined in Sections 2.4.2 and 2.4.1, with SJs in section 2.4.3.

2.4.1 Warm Conveyor Belt

The WCB is a warm, moist jet which flows poleward ahead of the CF in the lower troposphere before rising over the WF (Bader, 1995; Browning, 1990; Carlson, 1980; Harrold, 1973; Young et al., 1987). It can be associated with strong low-level winds along the CF and is the main producer of precipitation within the cyclone (Browning, 1986; Wernli and Davies, 1997). Eckhardt et al. (2004) show that ~60% of extratropical cyclones exhibit a WCB. Upon rising the WCB can turn cyclonically back towards the cyclone or anticyclonically (marked as WCB2 and WCB1 in Figure

2.3, respectively). During the early stages of the storm development, the anticyclonic, WCB1 path, turns downstream of the cyclone while there is an open upper-level wave (Bader, 1995; Browning and Roberts, 1996). The WCB2 parcels tend to originate from the lower reaches of the main WCB (Bader, 1995; Young et al., 1987) and can contribute to the deep cloud of the cloud head (Reed et al., 1994).

The latent heat released during the ascent of the WCB can have large impacts on the flow through the modification of PV. Above the condensational heating within the WCB PV is destroyed, while high PV regions are created below (Wernli and Davies, 1997). However, Joos and Wernli (2012) show a strong region of latent cooling due to the evaporation and sublimation of hydrometeors directly under the WCB. Wernli (1997) uses a Lagrangian framework to show that the WCB itself starts with relatively low PV before increasing to ~1 PVU or more before decreasing again. The latent heat release causes high PV to be generated in the CCB (see section 2.4.2) as it flows under the rising WCB, influencing the high winds and storm development (Schemm and Wernli, 2013). In the WCB outflow low and negative PV values created above the latent heating maximum can influence the large-scale environment and impact the downstream evolution (Pomroy and Thorpe, 2000; Stoelinga, 1996).

2.4.2 Cold Conveyor Belt

The CCB is recognised as a distinct wind maxima which forms on the cold side of the surface WF around the cloud head (Carlson, 1980; Schultz, 2001). The air originates from ahead of the cyclone and is transported under the warm frontal region towards the BBF (green arrow, Figure 2.3). It can be one of the key contributors to high winds within an extratropical storm.

Carlson (1980) described the CCB as a low level jet which flowed westward following the cyclonic flow before flowing back anticyclonically and rising into the cloud head. However, numerous studies have shown a cyclonic continuation of the CCB beyond the point of anticyclonic circulation shown by Carlson (1980). Indeed, in his Table 1, Schultz (2001) shows 19 studies which show this cyclonic path whilst only three show evidence of anticyclonic circulation in debatable CCB airstreams (Kuo et al., 1992; Whitaker et al., 1988). Although some subsequent studies have incorporated both cyclonic and anticyclonic paths of the CCB (Browning, 1990), Schultz (2001) argues that the anticyclonic streams are just a "transition airstream" between the WCB and CCB airstreams. This is emphasised by the lack of clear distinction between the airflows in this region

(Browning and Roberts, 1994; Kuo et al., 1992). Schemm and Wernli (2013) use two criteria to define their CCB trajectories: (a) that the trajectories stay close to the surface (below 800 hPa), and (b) that there is an increase of 2 PVU or more along the trajectories.

Schultz (2001) hypothesises that the large-scale flow relating to open-waves or closed lows at different levels or times may be the difference between the formation of anticyclonic flow or not, with both the Whitaker et al. (1988) and Kuo et al. (1992) storms being associated with open lows and anticyclonic CCB paths.

The CCB can be associated with a strong low-level PV anomaly due to the latent heating in the cloud head (Rossa et al., 2000; Stoelinga, 1996). As mentioned above, following Schultz (2001), Schemm and Wernli (2013) show that, at least some of this PV can be produced by the latent heat release in the rising limb of the WCB as it passes over the WF and CCB. This low-level PV is important in the deepening and strength of the storm as described in Sections 2.2.3 and 2.3.1.

The CCB is one of the major regions of high low-level winds associated with extratropical cyclones. Which of the conveyor belts exhibits the strongest winds is variable. The strength of the conveyor belts is thought to largely depend on the large-scale flow (Bader, 1995; Evans et al., 1994). SJs can also bring the most intense winds (Browning (2004), see section 2.4.3), but in other storms the CCB can be stronger (Smart and Browning, 2014).

One of the defining features of a CCB is its vertical location, consistently within the lower levels of the troposphere during its formation and evolution. This is in contrast to SJs which develop at higher levels as described in Section 2.4.3.

Despite these criticisms the conveyor-belt terminology provides a useful model for investigating the influences on cyclonic development.

2.4.3 Sting Jets

Sting jets (SJs) are mesoscale regions of high winds, located in the region of the end of the BBF as marked by the blue arrow labelled SJ in Figure 2.3 (Browning, 2004; Clark et al., 2005). The term originated from the description of "the dangerous sting in the tail" of the 1992 New Years Day storm (Grønås, 1995).

2.4.3.1 Description of SJs

Analysis of the "Great Storm of 1987" (hereafter the Great Storm) by Browning (2004) identified a mesoscale region of high winds that was not associated with any of the previously documented jets, and has become known as a SJ (Clark et al., 2005). In his analysis of the Great Storm, Browning (2004) noted a number of regions of high winds in the vicinity of the bent-back front. Two of these areas were attributed to a number of factors, including convection along and behind the secondary cold front, while another high wind region was caused by the CCB beneath the cloud head. The final area, the SJ, which caused maximum surface gusts of over 50 ms^{-1}, occurred in the dry slot near the tip of the cloud head. Thus, a SJ was described as a descending jet of high winds that occurs in the dry slot ahead of the cold-conveyor belt, forming as a result of slantwise mesoscale circulations and evaporative cooling (Browning, 2004). These processes were identified somewhat speculatively by Browning (2004). The more recent literature investigating these processes in SJ formation is reviewed in the following sections.

Following Browning (2004), Clark et al. (2005) presented a modelling study of the SJ in the Great Storm. The SJ schematic (Figure 2.4) shows the location of the SJ during stages II and III of the Shapiro-Keyser model (see Figure 2.1 (b)). Since Browning (2004), a number of studies (Baker, 2009; Baker et al., 2013; Gray et al., 2011) have used the following criteria for defining a SJ:

- Descent from ~700 hPa out of the cloud head
- Descends along a constant θ_w surface
- Accelerates during descent whilst reducing relative humidity (RH)
- Causes high wind speeds at the boundary layer top
- Has distinct characteristics from the other recognised jets (i.e CCB, WCB)

Although the initial analysis of Browning (2004) looked at surface winds, more recent studies have used high winds at the top of the boundary layer. Martínez-Alvarado et al. (2010) noted that certain boundary layer conditions may prevent the SJ descending, while parameterisation of boundary layer turbulence can cause surface winds to be poorly represented in models (Schultz and Sienkiewicz, 2013; Smart and Browning, 2014).

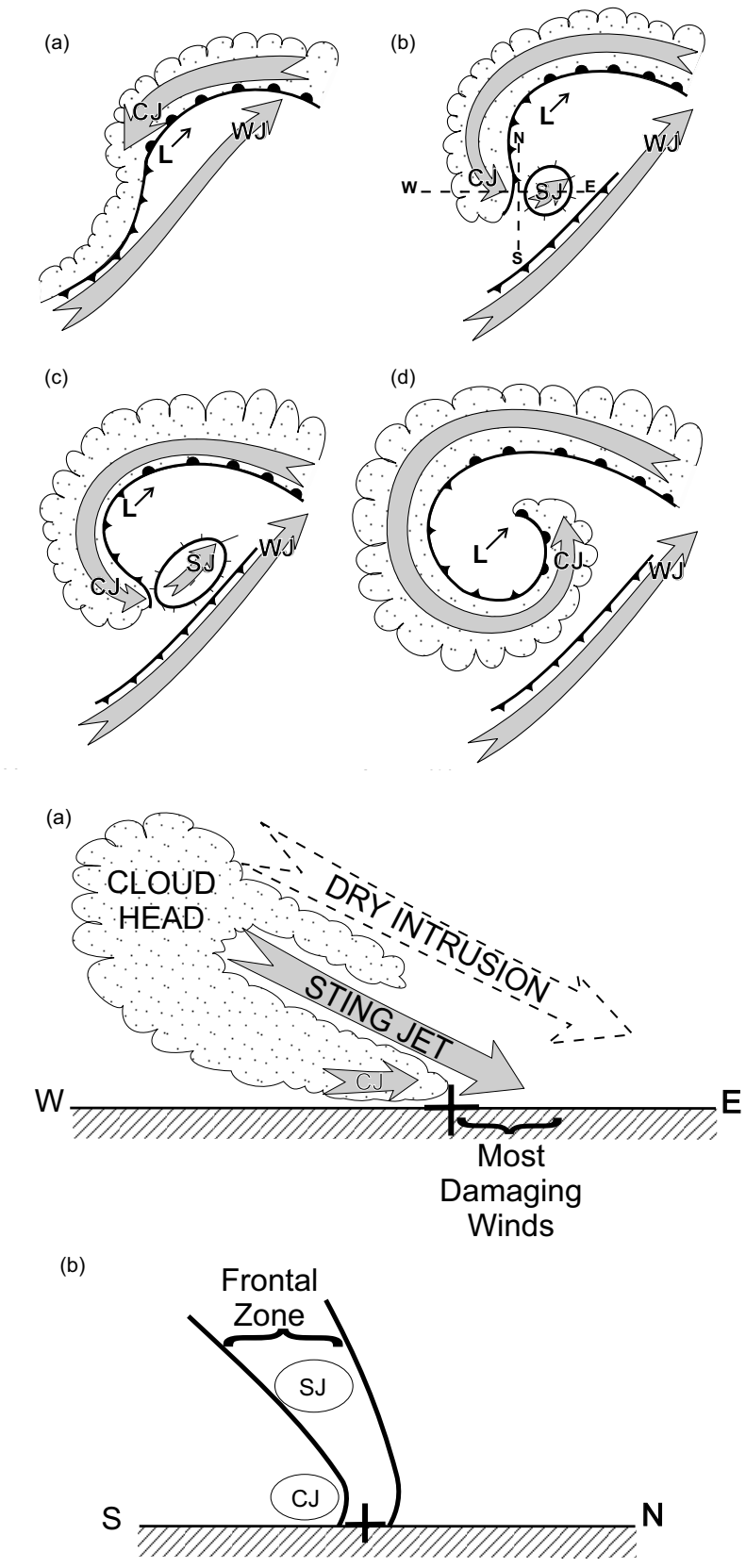

FIGURE 2.4: Plan (top) and cross sectional (bottom) schematic of SJ evolution and location taken from Clark et al. (2005)

2.4.3.2 Idealised Sting Jets

There are, to date, only two papers that examine SJs in a idealised modelling framework; these are examined at length here as they are highly relevant to the current understanding. Baker et al. (2013) presented the first high-resolution idealised simulation of SJ storms using the Met Office Unified Model, while Slater et al. (2014) used a dry idealised baroclinic wave setup of the WRF model to investigate the acceleration of low-level winds. As noted in Baker et al. (2013), Cao (2009) also described a SJ in idealised simulations but the resolution used in that study was too coarse to sufficiently resolve SJ features.

Baker et al. (2013) use the LC1 baroclinic wave simulations of Thorncroft et al. (1993) with moisture and a boundary layer scheme added to produce a more realistic simulation. Although a SJ is positively identified according to the criteria outlined in section 2.4.3.1, in the moist simulations it is weaker than those observed in similar real cases.

In a dry simulation, Baker et al. (2013) find no evidence of a SJ in the wind maxima at the top of the boundary layer. As well as the aforementioned CSI, Baker et al. (2013) also show the possibility that CI and II may contribute to SJ formation. They argue that moist instabilities are essential in forming a SJ and therefore these would not occur in the dry simulation. In contrast, however, Slater et al. (2014), show a number of trajectories which resemble a SJ, despite their simulation being absent of moisture. This would suggest that neither of the previously identified factors of CSI or evaporational cooling are essential in forming a SJ.

The idealised simulation comparison to cyclone Gudrun by Baker et al. (2013) shows that the static stability appears to be important in allowing the SJ to descend to a point where it can increase the surface gusts. The sensitivity experiments also carried out by Baker et al. (2013) show the importance of the initial static stability and large-scale cyclone intensification rate in the strength of the SJ The strength of the SJ was not related to the strength of the CCB identifying these as two distinctly forced phenomena.

Earlier studies indicated that evaporation of hydrometeors as the air leaves the cloud head may force or intensify the descent of the SJ (Browning, 2004; Clark et al., 2005; Martínez-Alvarado et al., 2014, 2011). Simulations testing the sensitivity of the SJ to initial static stability by Baker et al. (2013) appear to show sensitivity to evaporative cooling during the SJ descent. However, runs explicitly examining the sensitivity to evaporation show that in the simulated case it has no

effect on either the descent rate or the strength of the SJ. As the dry simulations of Slater et al. (2014) do not contain moisture they confirm that evaporation is not essential to creating a SJ.

2.4.3.3 Sting Jet Climatologies

Although the majority of SJ literature to date has involved the analysis of case studies, two climatologies have been produced. Parton et al. (2010) produced the first climatology of SJ storms using observational data from the Mesosphere-Stratosphere-Troposphere (MST) radar based at Aberystwyth, Wales. They identified 9 SJs from 117 cyclones over the course of a 7 year period. The identified SJs all occurred in cyclones during stages III and IV of the Shapiro-Keyser model which had undergone rapid development. Slantwise motions are also evident and fit with the 1/50 slope used by Clark et al. (2005). Obviously due to the fixed location of the radar this dataset was somewhat limited, relying on the storm passing within the radar range at the right stages of development.

Martínez-Alvarado et al. (2012) used re-analysis data to identify SJ cyclones through a method of diagnostics of CSI and evaporation. This study of 100 of the most intense North Atlantic cyclones from 1989 to 2009 identified that 25-33% were sting jet cyclones. However, the resolution of the data used means that the SJ itself cannot be directly observed only the supposed precursors of CSI and evaporation. Although Martínez-Alvarado et al. (2012) validate their CSI and evaporation method on a sample of cases, subsequent studies have cast doubt on the influence of these processes (Baker et al., 2013; Slater et al., 2014; Smart and Browning, 2014), and therefore the validity of the method used by Martínez-Alvarado et al. (2012).

2.4.3.4 Influence of Conditional Symmetric Instability

Browning (2004) highlighted a number of bands in the cloud head, and the precipitation, which were attributed to multiple stacked slantwise circulations, which had also been present in other cyclones and shown in previous studies (Browning et al., 1997, 2001, 1995). Figure 2.5 shows the conceptual model developed by Browning (2004) to show the influence of slantwise convection in forming the SJ. This idea has been identified and analysed in a number of subsequent studies (Clark et al., 2005; Gray et al., 2011; Martínez-Alvarado et al., 2010). Martínez-Alvarado et al. (2010) show differences in the timing of CSI release along SJ trajectories between the MetUM and

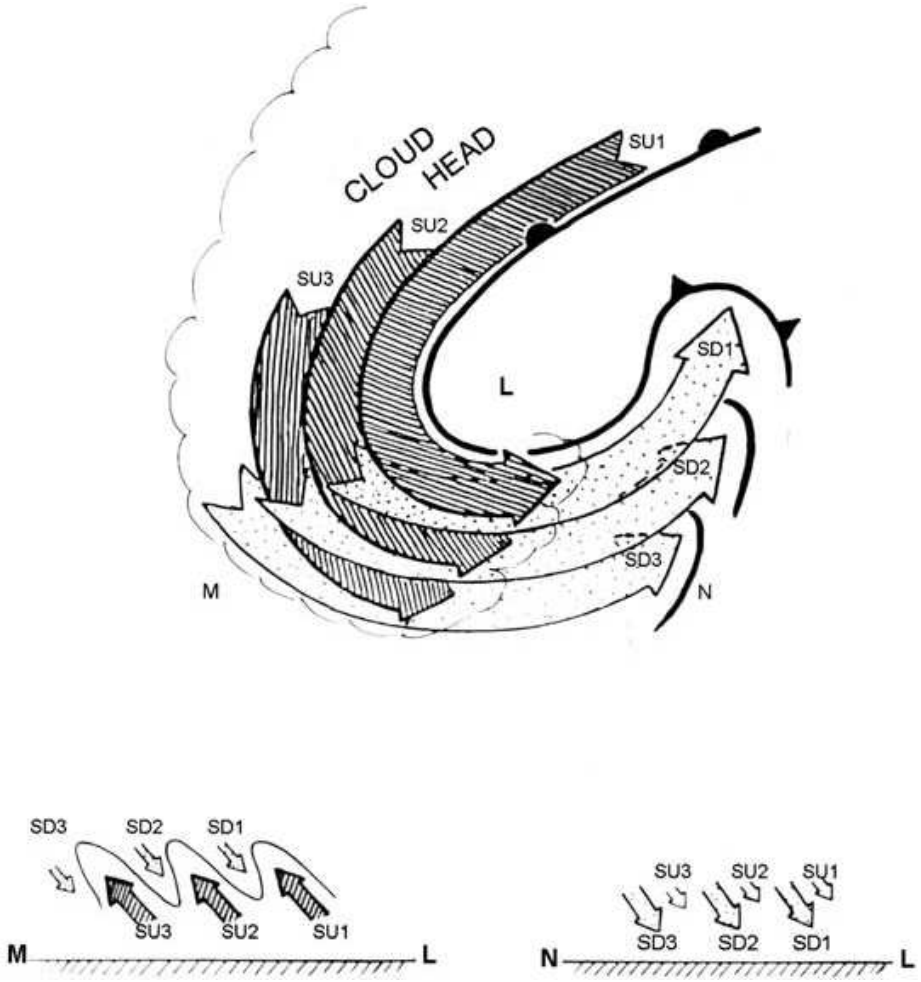

FIGURE 2.5: Schematic from Browning (2004) showing how slantwise motions within the cloud head may be responsible for the descending SJ.

COSMO models but note that 47% and 65% of the respective modelled trajectories descend from areas of CSI.

In their analysis of three SJ storms (and comparison with one non-SJ storm) Gray et al. (2011) investigate the SJs in terms of convective available potential energy (CAPE) and slantwise convective available potential energy (SCAPE), and their downdraught counterparts, downdraught convective available potential energy (DCAPE) and downdraught slantwise convective available potential energy (DSCAPE). In two of the analysed SJ storms (Gudrun and Anna) the presence of SCAPE in the cloud head (which subsequently decays) indicates slantwise circulations. These may be driven by low- or mid-level instability. In the third SJ storm analysed (the Great Storm) the presence of DSCAPE in the cloud head drives slantwise motion from mid-levels (Gray et al., 2011). It is also noted that the non-SJ storm analysed by Gray et al. (2011) does exhibit a weakly

descending jet despite a lack of CSI. This jet descended slower with a descent speed of 0.3 Pa s^{-1} compared to 0.5, 0.8 and 1.5 Pa s^{-1} for those considered to be SJs (Gray et al., 2011).

In their analysis of Cyclone Friedhelm Martínez-Alvarado et al. (2014) found that >50% of the trajectories that classed as a SJ pass through a region of CSI as they begin to descend while the rest of the trajectories are stable. In the preceding hours a number of trajectories have been associated with II as well as the large number with CSI and a smaller group from stable air.

Schultz and Sienkiewicz (2013) state that slantwise motions are not caused by CSI, but vertical motion is needed in order to release it. Therefore, although CSI may indicate a SJ is present, it is not the driving force of its appearance, and instead another mechanism must be present to initiate the vertical motions. This vertical forcing is attributed to frontogenetic/frontolytic flow in the cloud-head region by Schultz and Sienkiewicz (2013). This is discussed further in Section 2.4.3.6.

As noted above, Baker et al. (2013) see less influence of CSI in their trajectories, while Slater et al. (2014) show a SJ where CSI cannot be released due to a lack of moisture in the simulation. These studies, along with that of Schultz and Sienkiewicz (2013) cast some doubt on the importance of CSI and its use as an identifier of SJ trajectories. Given its presence in most of the identified SJ storms, it may be assumed that there is a correlation between CSI presence and SJs. However, there is also a correlation between CSI and deep cyclones (Shutts, 1990*b*), so the relationship between CSI and SJs may be simply coincidental.

2.4.3.5 Role of Evaporational Cooling

Browning (2004) suggested that the evaporative cooling of hydrometeors might be responsible for the intensification of the SJ as it descends from the cloud head, via two methods. The first hypothesis was through the enhancement of the slantwise circulations through intensifying the moist symmetric instability. The second was via the reduction of the static stability within the dry slot allowing increased turbulence to mix the high momentum air towards the surface. Browning (2004) did however note that the evidence for this was, at that time, largely circumstantial. Martínez-Alvarado et al. (2010) also suggested evaporation may be important in driving the descent and the development of the highest winds. More recent studies have cast doubt on this assumption with both idealised modelling and case studies suggesting that evaporational cooling does not affect the presence or strength of the SJ (Baker et al., 2013; Smart and Browning, 2014). Martínez-Alvarado

et al. (2014) claim that latent cooling forces the initial descent of their SJ, however they do not investigate the role of frontolytic secondary circulations as theorised by Schultz and Sienkiewicz (2013). The idealised simulation of Slater et al. (2014) used a dry setup and exhibited SJ trajectories where evaporation cannot be present. Schultz and Sienkiewicz (2013) show that SJ descent can be attributed to frontolytic circulations. This suggests that evaporation is not needed for driving the SJ descent. However, they do suggest that evaporation may have a role in reducing the stability and assisting the mixing of high momentum air to the surface. These recent studies suggest that although evaporational cooling may play a role in assisting the low-level descent of a SJ, it does not appear to be a key driver of the phenomenon.

2.4.3.6 Frontolysis Induced Descent

In their case study, Schultz and Sienkiewicz (2013), show that the transition from frontogenesis to frontolysis at the end of the BBF causes descent on the warm side of the front which brings high momentum air towards the surface in the form of a SJ. The transition is associated with a spreading of the isentropes within the frontal fracture region. The isealised vertical motions are shown in the schematic in Figure 2.6. Once the air is forced to descend by the frontolytic circulations it undergoes evaporation, which supports the findings of Baker et al. (2013) and Smart and Browning (2014) that evaporation is not essential for the formation or intensity of a SJ. Slater et al. (2014) also identify frontolytic regions in areas of initial descent in their idealised study, supporting the usefulness of frontolysis as a forecasting tool for the transfer of high-momentum air towards the surface. As frontolytic regions do not occur in Norwegian cyclones, where there is no spreading of the isentropes, this theory explains why SJs have only been seen to occur in Shapiro-Keyser type cyclones (Parton et al., 2010). Although stating that CSI cannot be the initial cause of the descent, Schultz and Sienkiewicz (2013) acknowledge it may enhance the descent of the SJ and determine whether they are able to penetrate to the surface.

2.5 Summary of Literature

Extratropical cyclones are a highly important weather phenomenon, particularly for Western Europe. The strongest of these cyclones can cause considerable damage. A range of processes influence the initial cyclogenesis, deepening, evolution and lifetime of these storms. High winds

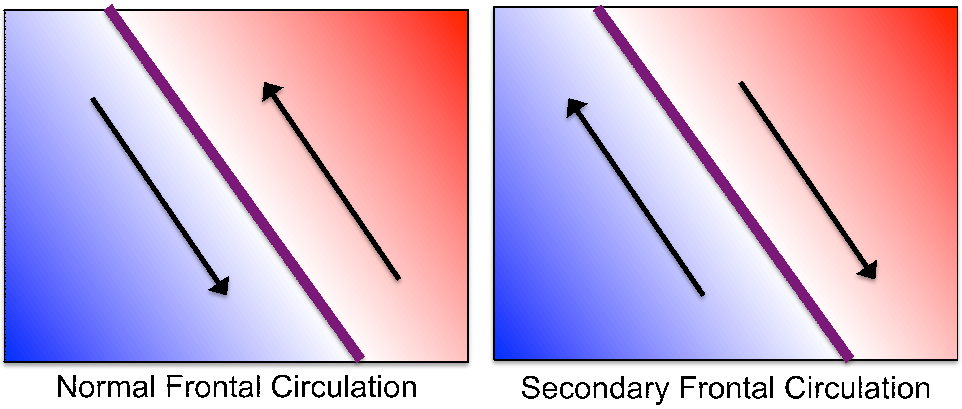

FIGURE 2.6: Schematic vertical cross-section of the idealised vertical motions associated with (a) frontogenetic regions and (b) frontolytic regions. The warm and cold air masses are represented by the red and blue shading with the front indicated by the purple line. Idealised vertical motions are shown by the black arrows.

can develop in a number of regions around cyclones, but the regions to the south and south-west of the storms in which both SJs and CCBs occur is of particular importance. The literature is yet to come to a clear consensus on the influences on the formation and development of SJs. A number of theories including frontolysis, evaporation and CSI have all been identified. The role of balances in the development of high winds such as SJs has not yet been identified. There are also still ambiguities around the development of cyclones in relation to the PV structure and the influences this may have on the high winds.

The following chapters in this thesis will examine some of these gaps in current scientific understanding.

Chapter 3

Modelling and Tools

This thesis is predominantly a modelling study, utilising the Weather Research and Forecasting (WRF) model. The model and the setup used in this thesis are described in Section 3.1. Other data used in the analysis of the storm and evaluation of the model is described in Section 3.2. Further analysis methods used throughout the following Chapters are presented in Section 3.3.

3.1 WRF Modelling

The WRF model is a community-based numerical weather prediction (NWP) model, developed for both research and forecasting purposes (Skamarock et al., 2008). The model development is led by the USA National Center for Atmospheric Research (NCAR). The standard WRF setup includes the option of two dynamical cores. In this study the Advanced Research WRF (ARW) core is used; the other core is the Nonhydrostatic Mesoscale Model (NMM). Multiple other versions of the WRF model exist including ones focused on climate (WRF-Clim), chemistry (WRF-Chem), hurricanes (H-WRF) and even non-earth atmospheres (planetWRF).

The modelling in this study was completed using the WRF model version 3.3.1. The following sections will describe the WRF-ARW (hereafter WRF) model in more detail and the parameterisations used for the simulations in this study. Section 3.1.5 summarises the model setup.

3.1.1 Model Dynamics

The WRF model solves the non-hydrostatic, fully compressible Euler equations based on Ooyama (1990). The full set of model equations can be found in Skamarock et al. (2008). It integrates six prognostic variables; the velocity components (u and v), vertical velocity (w), perturbation potential temperature, perturbation geopotential and perturbation surface pressure of dry air. The model top is set at a constant pressure, in this case 50 hPa.

The vertical coordinates are terrain-following, based on hydrostatic pressure. Following Laprise (1992) the coordinates are set by equation 3.1

$$\eta = \frac{(p_h - p_{ht})}{\mu}, \tag{3.1}$$

where $\mu = (p_{hs} - p_{ht})$, and, p_h is the hydrostatic pressure component, p_{hs} is the surface hydrostatic pressure and p_{ht} is the hydrostatic pressure component at the model top. The number of model levels and the pressure at the model top are set by the user. The exponential change of pressure with height in the atmosphere causes the model levels to be closer together (in terms of altitude) near the surface. This allows for higher vertical resolutions in the boundary layer. Figure 3.1 shows an idealised set of vertical levels and the relaxation of the terrain-following disturbance as a function of altitude (a result of the fixed model top pressure).

The temporal integration in the ARW is a time-split scheme (Skamarock et al., 2008). This means that the meteorologically significant slow- and low-frequency modes use a third-order Runge-Kutta (RK3) scheme (Wicker and Skamarock, 2002). The higher-frequency and acoustic modes are integrated over a smaller time step to increase numerical stability. The model runs through the RK3 loop with the given number of smaller acoustic time step loops within this. The use of the time-split integration increases the efficiency of the model as a result of not needing to integrate the computationally expensive, slow and low-frequency modes at the increased time step of the acoustic variables.

The model time step must be set in order to avoid any Courant-Friedrichs-Lewy (CFL) errors. A rule of thumb for the time step (given in seconds) is suggested as six times the horizontal resolution in kilometres. For nested simulations (see Section 3.1.3) the time step for any nests is set as a ratio of that in the outer domain. The coarse resolution used in this study is 27 km, suggesting a time step of 162 s. In the chosen set-up however, instabilities would often generate when this time step

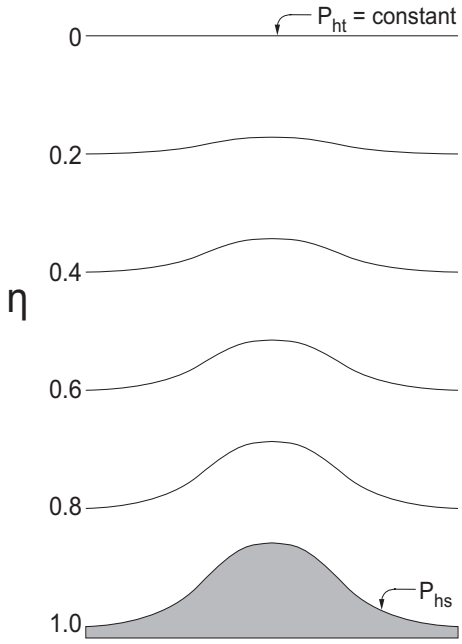

FIGURE 3.1: Vertical η coordinates in the WRF ARW system. This idealised example shows six levels from the surface p_{hs} to the model top p_{ht}. The relaxation of the terrain-following disturbance with height is visible as the levels increase. From Skamarock et al. (2008)

was used; it is believed that these were due to the high vertical resolution and vertical velocities, rather than in the horizontal resolution and motion. Reducing the time step to 54 s removed these numerical instabilities and allowed for smooth running of the model.

WRF runs on an Arakawa-C grid where the horizontal and vertical velocity components (u, v, w) are located on the grid-box edges and other variables (indicated by θ) located in the centre of the grid point. This arrangement of variables is shown in Figures 3.2 (a) and (b) for the horizontal and vertical, respectively.

3.1.2 Initial and Boundary Conditions

The initial conditions and lateral boundary data for WRF real-data cases are interpolated from analysis or forecast data from external models such as ECMWF or GFS. The data are processed into a WRF-readable format in a stand-alone program, the WRF Preprocessor System (WPS), before being computed to the initial and lateral boundary conditions by the WRF "real" processor. The WPS program defines the map-projection, grid and nest locations, and grid points. The input analysis or forecast data are then horizontally interpolated onto the grid. These horizontally interpolated data are passed to the "real" preprocessor. Here it is vertically interpolated from the native vertical spacing onto the specified WRF vertical levels. WPS version 3.3.1 is used for this study.

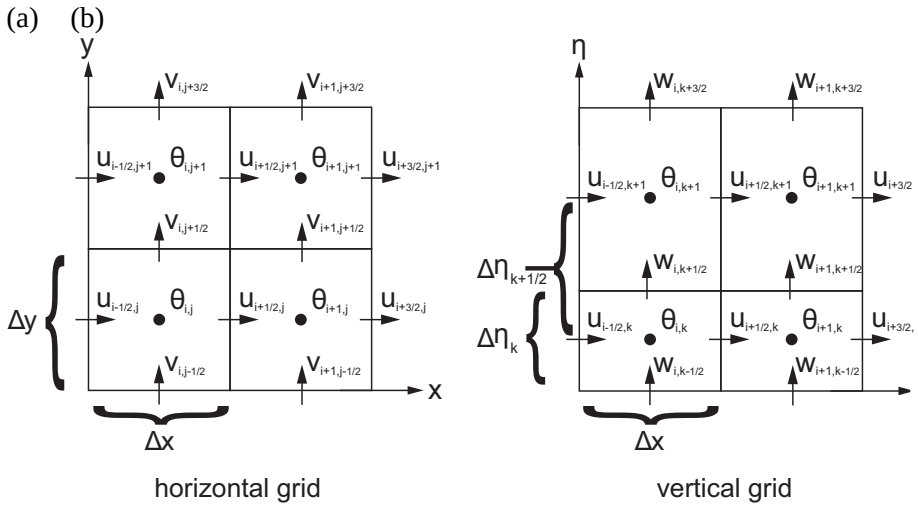

FIGURE 3.2: Schematic of the Arakawa-C grid used in the WRF-ARW model. Horizontal discretisation is shown in (a) and vertical in (b). From Skamarock et al. (2008)

The model simulations presented in Chapters 4, 5 and 6 were initiated from ECMWF operational analysis data with a resolution of 0.5°x0.5° and 37 vertical levels. The analysis data is used to create both the initial conditions, as well as the boundary conditions of the outer domain every six hours. This analysis included assimilated data from the dropsondes released during the DIAMET research flights.

3.1.3 Resolution and Nesting

The WRF model can run at varying resolutions from large-scale global runs to ultra-high resolution large eddy simulations (LES). Nesting can be used in order to step-down smoothly from the input data and resolve areas of interest at higher resolution (Skamarock et al., 2008). Nested domains reside within the coarser "parent" grid and can be placed anywhere as long as the nest is wholly within the boundaries of the parent domain. A parent domain can contain a number of nests; these nests can them themselves contain higher resolution nests. However, a nest can have only one parent domain. It is suggested that the "parent" to "child" resolution ratio is between 2:1 to 6:1 (a 3:1 ratio is widely used). One- and two-way nesting options are available in ARW. One-way nesting means information flows from the coarse grid to the fine grid only. Where two-way nesting is used, the inner-grid replaces the parent grid solution where the grid points overlap. The nested simulations used in this study use one-way nesting only. While nesting can be used to increase horizontal resolution in areas of interest, the vertical resolution must be kept constant between the parent and child domains.

In order to examine the mesoscale details of the storms, the high-resolution simulations were run using a horizontal resolution of 3 km in the inner domain. This was nested within two larger domain of 9 km and 27 km horizontal resolution. The location of these domains is shown in Figure 3.3 (a). These simulations are used for the model evaluation in Chapter 4, the dynamical analysis in Chapter 5 and some of the sensitivity tests in Chapter 6. The storm development sensitivity runs were completed on a lower resolution domain covering the majority of the North Atlantic, shown in Figure 3.3 (b). These simulations were run on a single 27 km resolution domain, and will hereafter be referred to as the NA simulations. The analysis of these runs is presented in Chapter 6.

All the simulations are run with 100 vertical levels which equates to a spacing of roughly 200 m at low levels. A number of papers (e.g. Clark et al. (2005); Martínez-Alvarado et al. (2012)), show the need for high vertical resolution in producing the features of sting jet storms, such as that analysed here. Indeed, the study of Friedhelm by Martínez-Alvarado et al. (2014) uses resolution of 12x12 km in the horizontal and 70 vertical levels to successfully represent the SJ features. To resolve slantwise circulations Clark et al. (2005) use a resolution of 12 km in the horizontal and 90 vertical levels; this allows slopes of roughly 1/50 as recommended by Persson and Warner (1993). Slater et al. (2014) are able to resolve a SJ in an idealised model simulation with a horizontal resolution of 20 km and only 40 vertical levels, with little difference in the wind fields when tested at higher resolutions. The NA simulations here are not designed to identify the mesoscale features such as sting jets, as these may be on the edge of, or outside the effective resolution. The high resolution domains should be sufficient to capture these processes with the model resolution being higher than any previous SJ study.

3.1.4 Parameterisations

The WRF-ARW model uses parameterisation schemes to solve a number of sub-grid processes. These fit into five categories: cumulus, microphysics, planetary boundary layer (PBL), land-surface model and radiation (short- and long-wave). There are a number of possible options for each of these categories. The role of each scheme will be described in the following sections with a brief description of the chosen option. The parameterisations were chosen to be consistent with the simulations of colleagues on the DIAMET project. The model setup has been used previously by Chris Dearden (personal communication) to successfully simulate frontal systems over the UK.

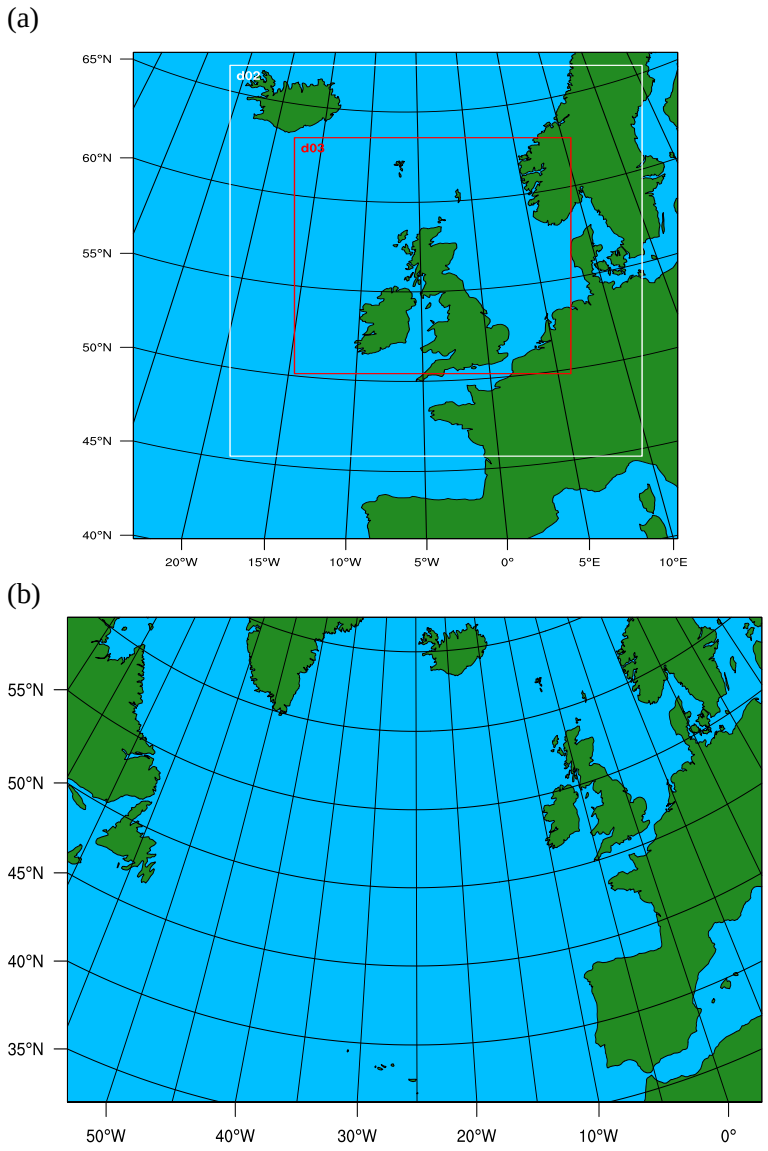

FIGURE 3.3: Plots showing the domain size and location for: (a) the high resolution simulations where domain 1 is the total map size and the two nests are indicated by the two marked boxes; and, (b) the NA simulation domain where no nests are included.

3.1.4.1 Cumulus Parameterisation

The cumulus parameterisation scheme represents the sub-grid convection, and both convective and shallow clouds (Skamarock et al., 2008). The cumulus scheme evaluates the convection and vertical fluxes in a vertical column where the scheme is triggered. The scheme, where triggered, will feedback the vertical heating and moisture profiles for the column as well as the convective component of rainfall. Cumulus schemes are only needed at lower resolutions (>10 km) in order to ensure latent heat is released realistically (Skamarock et al., 2008). At higher resolutions of less than 5 km a cumulus parameterisation should not be used, as the schemes will assume eddies that

are entirely sub-grid, which would therefore not be true at these resolutions. Between 5 and 10 km the schemes may not be needed but can help trigger convection.

Due to the high resolution of the inner-most domain, convective parameterisation is switched off for this domain: it is however switched on in the two coarser parent domains. The Kain-Fritsch convection parameterisation is used in these outer domains for all simulations, as described in Kain (2004) (following Kain (1993); Kain and Fritsch (1990)). This scheme includes detrainment, entrainment, and relatively simple microphysics to model the up- and downdrafts. The Kain-Fritsch scheme was also used by Smart and Browning (2014) in their study of the 3^{rd} January 2012 SJ storm (See section 2.4.3).

The simulations for the NA domain in which LH has been switched off also require convection parameterisation to be removed, as this would provide its own LH feedback. The effect of switching off the convection scheme will also be evaluated to ensure the robustness of this experiment (See Section 6.3.1.1).

3.1.4.2 Microphysics

The microphysics scheme solves for the water, cloud and precipitation processes that are explicitly resolved by the model. WRF contains a number of mircophysics schemes with differing characteristics and complexities, from simple single-moment warm-rain schemes to complex two-moment mixed phase schemes (Skamarock et al., 2008). Single-moment schemes solve only for the mass mixing-ratio based on a set distribution. Two-moment schemes will normally also solve for the number concentration of hydrometeors. Single- and mixed-phase schemes are available; mixed-phase allow the interaction of liquid and ice phase hydrometeors and are therefore recommended for grid sizes less than 10 km (Skamarock et al., 2008).

In this study a modified version of the Morrison et al. (2009) scheme is used. This modification outputs diagnostics of the latent heating processes but does not alter the internal physics. The Morrison scheme is a two-moment scheme which includes ice and mixed-phase processes. The scheme includes 6 hydrometeor species: water vapour, cloud water, cloud ice, rain, snow and hail/graupel. In addition to the solving of the mass mixing-ratio of all 6 water species, the number concentrations of cloud ice, rain, snow and graupel/hail are also calculated. The Morrison scheme uses a gamma function to describe the hydrometeor distribution with the intercept and slope function defined by the number concentration and mass mixing-ratio. The gamma function reduces to

a Marshall-Palmer distribution for precipitating hydrometeors (Morrison et al., 2009). The additional diagnostics mentioned above are used to understand the microphysical drivers in Chapters 5 and 6.

3.1.4.3 Boundary Layer Scheme

The planetary boundary layer (PBL) scheme calculates the sub-grid scale vertical fluxes caused by eddies (Skamarock et al., 2008). Despite its name, the PBL scheme provides for the whole atmospheric column. The PBL scheme, when activated, overrides the explicit vertical diffusion. It is assumed by the PBL scheme that the sub-grid and resolved eddies are separated clearly in scale. This may not be the case at very high resolutions (i.e. less than a few hundred metres), but is valid at the resolutions used in this study.

The Yonsei University (YSU) scheme, described by Hong and Lim (2006), is used here. It was also used in the idealised SJ study of Slater et al. (2014). The scheme represents fluxes from non-local gradients through countergradient terms and explicitly treats the entrainment layer at the PBL top. The top is dependant on the buoyancy profile where entrainment is maximum (Skamarock et al., 2008).

3.1.4.4 Land-Surface Model

The Land-surface model (LSM) acts for land and sea-ice points to give fluxes of moisture and heat (Skamarock et al., 2008). It uses information from other parameterisation schemes as well as built-in information about the land state and surface properties. The information from the parameterisation schemes used is as follows: precipitation - cumulus and microphysics; radiative forcing - radiation scheme; surface information - surface layer scheme. The fluxes are then provided for the vertical transport, either explicitly or through the aforementioned PBL scheme.

In this thesis the Noah LSM is used (Chen and Dudhia, 2001). It contains 4 layers for soil temperature and moisture at 10, 30, 60 and 100 cm below the surface. It also includes canopy moisture and snow cover. From the vegetation categories, monthly vegetation fraction, and soil texture, the root zone, evapotranspiration, soil drainage, and run-off processes provide the fluxes of sensible and latent heat to the PBL. Soil ice, fractional snow cover and surface emissivity are also considered (Skamarock et al., 2008).

3.1.4.5 Surface Layer Scheme

This scheme allows the LSM and PBL schemes to interact with the surface through the calculation of the friction velocities and exchange coefficients. Over water the surface fluxes are controlled by the Surface Layer Scheme, as are the diagnostics of surface properties (Skamarock et al., 2008).

The MM5 Monin-Obukhov surface layer scheme has been used in this study. This scheme must be used when the YSU PBL scheme is used. The MM5 scheme is based on the exchange coefficients for heating, moisture and momentum from Paulson (1970), Dyer and Hicks (1970) and Webb (1970). These are enhanced by a convective velocity addition following Beljaars (1995) over land but only a proportional contribution related to the thermal gradient is used over water. The scheme does not include a thermal roughness length and a Charnock relation is used to equate the roughness length and friction velocity over water.

3.1.4.6 Radiation Schemes

Two radiation schemes are needed for the running of the WRF model. Firstly, the longwave scheme is used, which accounts for the infrared and thermal radiation emitted and absorbed by gases and the surface (Skamarock et al., 2008). Secondly, the shortwave scheme includes the absorption, reflection and scattering of radiation. The surface emissivity and albedo determine the upward longwave and shortwave radiation emitted from the ground surface, respectively. The radiation schemes within the model are single-column for each grid box (Skamarock et al., 2008).

This study uses the Rapid Radiative Transfer Model (RRTM) as the longwave scheme (Mlawer et al., 1997) and the Dudhia scheme for shortwave radiation (Dudhia, 1989). RRMT utilise pre-set "look-up" tables for the longwave calculations based on the quantities of water vapour, ozone, carbon dioxide and trace gases (depending on user choices). The Dudhia scheme uses a downward integration for solar fluxes, clear-air scattering, water vapour absorption and cloud albedo and absorption. It can also alter the solar fluxes based on the terrain slope and shadowing (Skamarock et al., 2008). Both the RRTM and Dudhia schemes were also used by Smart and Browning (2014).

TABLE 3.1: Parameterisations used in the control WRF simulations. Note that the Cumulus scheme is switched off at high resolutions (<4 km).

Parameterisation	Namelist No.	Param. Name	Citation
Cumulus	1	Kain-Fritsch	Kain (2004)
Microphysics	10	Morrison Scheme	Morrison et al. (2009)
PBL	1	YSU scheme	Hong and Lim (2006)
Short-wave	1	Dudhia scheme	Dudhia (1989)
Long-wave	1	RRTM scheme	Mlawer et al. (1997)
Surface Layer	1	MM5 Similarity Monin-Obukhov scheme	Dyer and Hicks (1970); Paulson (1970); Webb (1970)
LSM	2	Noah LSM	Chen and Dudhia (2001)

3.1.5 Model Setup and Computing Summary

The modified Morrison microphysics scheme was provided by Chris Dearden (Uni. of Manchester). Due to technical issues with the scheme, graupel/hail species were switched off for the initial control simulations. These issues were subsequently resolved, however, due to the time constraints it was not plausible to redo the initial simulations. Therefore, simulations including graupel or hail are presented as a sensitivity test in Chapter 6.

The WRF simulations were carried out using the UK's national high-performance computing (HPC) service. Initially this was the HECToR service (http://www.hector.ac.uk/). Towards the end of the PhD period this service was discontinued and the ARCHER HPC service was established (http://www.archer.ac.uk/). Changes in the computing architecture can cause model output to change. As some changes were seen between otherwise identical simulations run on the two machines, only simulations run on the same machine are directly compared in the following chapters.

Table 3.1 summarises the parameterisations used in the model simulations herein. Any changes to these in specific simulations, such as switching off the cumulus parameterisation, will be noted where these results are presented.

The model simulations for the high-resolution setup were all initiated at 1200 UTC 7^{th} December 2011 with the first 6 hours of results discarded to allow for adequate spin-up of the WRF model. The NA simulations are intended to examine the overall development of the cyclone and were therefore initiated at 1200 UTC 6^{th} December, before the storm had formed. Again, the initial 6 hours of results were discarded.

3.2 Data

Chapter 4 will analyse the evolution of Cyclone Friedhelm and compare the WRF simulations to model analyses and observations. One of the key tools for this evaluation are dropsonde sections from the FAAM-146 sortie. A brief description of the dropsonde data is presented in the following section. In conjunction with this lidar data are used to indicate clouds. Information on the lidar is therefore presented in Section 3.2.2.

3.2.1 Dropsondes

The dropsondes used throughout the DIAMET project were Vaisala AVAPS RD94 (Vaughan et al., 2014). During the Cyclone Friedhelm sortie the dropsondes were released from an altitude of approximately 6500-7000 m with a descent time of roughly 10 minutes to the surface. The aircraft is limited to receiving only 2 sets of dropsonde data simultaneously. Given the time to descend and travelling speed of the aircraft ($\sim$100 ms^{-1}) this means launching a dropsonde every 5 minutes with an approximate horizontal resolution of 30 km. For a number of reasons this exact spacing cannot always be achieved, causing the spread to be uneven along the flight legs. The direct meteorological measurements from the dropsondes measured at 2 Hz are temperature, pressure and specific humidity along with time and lat/lon locations. Recorded at 4 Hz is the GPS location which allows horizontal wind speeds to be calculated. The dropsonde sections from cyclone Friedhelm are analysed in Chapter 4.

The data from the dropsondes is sent to the World Meteorological Organisation (WMO) Global Telecommunication System (GTS) in-flight allowing it to be assimilated into operational model analysis. The sonde data from the DIAMET flight into Cyclone Friedhelm was assimilated into the ECMWF data used as the initial and boundary conditions for the WRF model simulations presented in Chapters 4-6 (Tim Hewson, personal communication).

WRF assimilation of the dropsondes was not conducted for this thesis. Data assimilation projects were undertaken by colleagues under the DIAMET project brief. The dropsondes also provide a useful tool for evaluating the WRF model simulations as will be presented in Section 4.2.6.

3.2.2 Lidar

The FAAM-146 was also equipped with a downward-pointing Light Detecting And Ranging instrument (lidar) for many of the flights, including Cyclone Friedhelm. The lidar is a Leosphere ALS450, which uses a wavelength of 355 nm, in the near-UV region of the spectrum. It integrates over a two second time interval giving an approximate horizontal resolution of 200 m, assuming the aircraft "science speed" of 100 ms^{-1}. In the vertical the resolution is ~45 m. Due to the strong attenuation of the signal only a limited depth of cloud can be seen, depending on the optical thickness of the cloud. There is a ~300 m "blind-spot" immediately below the aircraft before the laser and optical reader overlap. This may mean that clouds appear too low, or in highly attenuating areas not at all. The lidar signals are plotted using a threshold for the signal to indicate the cloud tops, this threshold has been tuned for each DIAMET flight due to the varying amounts of noise within the data (Phil Rosenberg, personal communication).

3.3 Analysis Methods

3.3.1 RIP Trajectories

Trajectories are used as an important method of tracking the development of mesoscale features. The trajectories presented in Chapters 5 and 6 were calculated using the "Read/Interpolate/Plot" (RIP) 4 program (Stoelinga, 2009). The trajectories are calculated from the model output with an increased time step of 3 minutes (compared to 30 minute model output) to enhance accuracy (Stoelinga, 2009). The trajectories are interpolated between model output using a bilinear interpolation in the horizontal, and linear interpolation in the vertical and time dimensions.

Diagnostics are output along the trajectories at the model output time step (30 minutes). Due to the limited functions within RIP, some diagnostics were calculated through interpolation from the trajectory lat/lon location onto the closest WRF grid point using the NCAR Command Language (NCL). This may cause some slight changes to the values compared to the RIP derived interpolations but these are not significant when compared using variables available in both programs (not shown).

Chapter 4

Storm Evolution and Model Evaluation

This chapter examines the evolution of Cyclone Friedhelm and the WRF modelled representation of it. Section 4.1 gives an overview of the prevailing conditions at the time of the storm. In section 4.2 the storm is analysed with a number of analysis and observational products to examine the track, deepening and structure as it propagated towards and over the UK. Comparisons and initial analysis of the WRF simulation are presented here. A more detailed analysis of the WRF modelled dynamics is presented in Chapter 5

4.1 Background Conditions

Cyclone Friedhelm developed during a period of frequent intense cyclogenesis in the North Atlantic basin. There was a strong jet stream that assisted a number of intense and damaging storms to develop during November, December and January 2011/2012 (Vaughan et al., 2014). December itself exhibited a North Atlantic Oscillation (NAO) index of 2.52, the highest for any December since 1950 and the third highest for any month over the same period (Vaughan et al., 2014). Figure 4.1, taken from Vaughan et al. (2014), shows the 300 hPa zonal wind for the November, December, January period. The enhanced jet speed compared to the long term average for the period is clear. The decreases in the zonal flow which coincide with the cyclones are a consequence of the intense cyclones disrupting the upper-level flows.

The strong upper-level jet shown in Figure 4.1 was partly responsible for the large number of intense extratropical cyclones experienced in north-western Europe over the 2011/2012 winter,

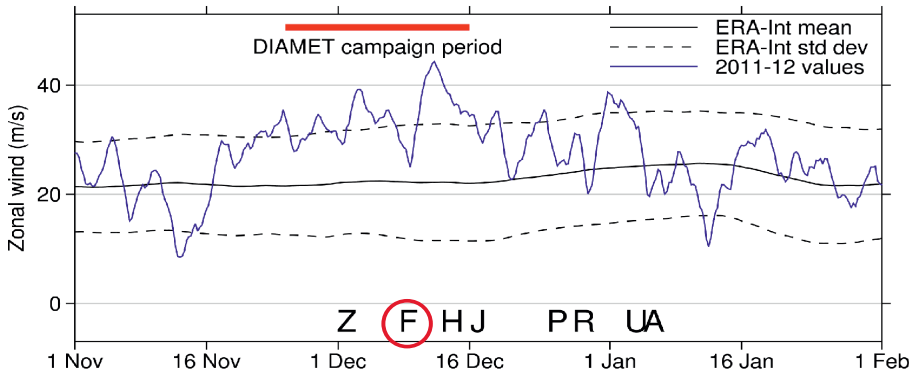

FIGURE 4.1: Time series of the 300 hPa zonal wind through November, December and January 2011/2012 for the North Atlantic (between 40-60°N and 10-60°W). Blue line indicates the 2011/2012 values with the ERA-INTERIM (1979-2010) mean and standard deviation are indicated by the black solid and dashed lines respectively. The strong extratropical cyclones over the UK during the period are marked by the letters, with cyclone Friedhelm highlighted by the red circle. From Vaughan et al. (2014)

including cyclone Friedhelm. Figure 4.2 shows the state of the mid-level jet during the formation and tracking of Friedhelm towards the UK. A particularly strong, zonal jet can be seen right across the Atlantic Ocean with wind speeds near 20°W reaching 110 kts (56.5 ms^{-1}). By 0000 UTC on the 8th (Figure 4.2 (b)) the strength of the jet has weakened slightly although wind speeds in the central and western North Atlantic are still reaching 85 kts (43 ms^{-1}).

4.2 Observed and Modelled Storm Evolution

4.2.1 Sea Level Pressure Evolution

Cyclone Friedhelm itself developed from a secondary wave on a trailing cold front in the Western Atlantic on the 7th December 2011. This can be seen as a marked low (L) with a 1014 hPa central pressure at 50°W in Figure 4.3. The formation of the cyclone was in relatively close proximity to the strong upper-level jet (Riviére et al., 2014*b*).

Figures 4.4 (a)-(d) show the succession of MO synoptic analyses from the 8^{th} December at 0000, 0600, 1200 and 1800 UTC, respectively. The WRF simulated SLP for the same times is shown in Figure 4.5 for comparison. The approximate locations and minimum SLPs in the MO analyses, as well as the modelled values from the WRF simulation are summarised in Table 4.1, with the tracks of the storm compared in Figure 4.6.

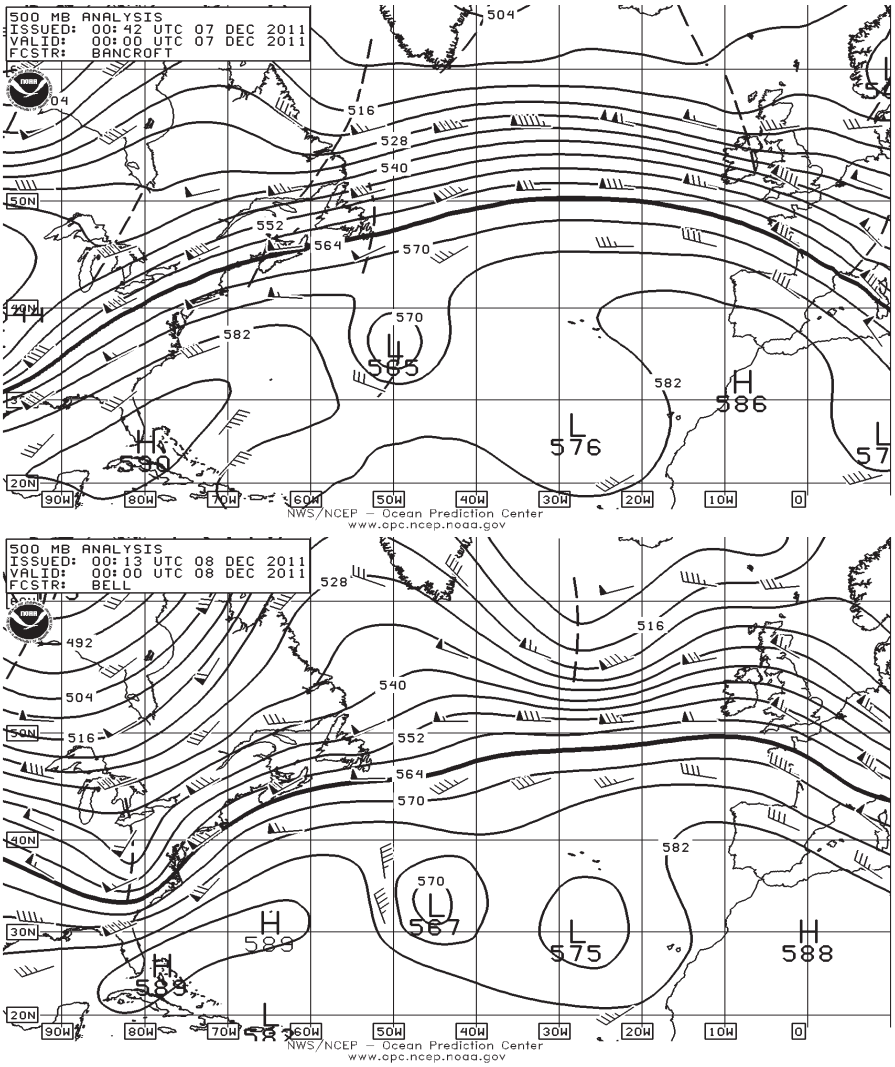

FIGURE 4.2: NWS/NCEP 500 hPa analysis charts for 0000 7th (top) and 8th (bottom) December 2011. Thickness shown in solid black lines and wind barbs.

The MO analysis plots (Figure 4.4) show the general north-eastward path of the storm as it passes the UK. At 0000 UTC, 24 hours after the storm can be seen forming in Figure 4.3, it has deepened to 977 hPa and an occlusion has formed (Figure 4.4 (a)). By 0600 UTC (Figure 4.4 (b)) the occlusion has achieved a characteristic hook shape around much of the low pressure centre, the pressure has dropped to 964 hPa. At this time the surface warm front covers the length of the western mainland UK, while the cold front is approaching landfall to the west of Ireland. The low centre of Friedhelm is situated just to the north-west of Scotland at 1200 UTC (Figure 4.4 (c)) with a central pressure of 957 hPa having deepened by 44 hPa in 24 hours. The surface warm front has passed into the North Sea and the cold front stretches north-east to south-west across northern England and Wales. A trough line is also marked behind the main cold front. The centre of the cyclone then tracks across northern Scotland during the afternoon of the 8^{th} December

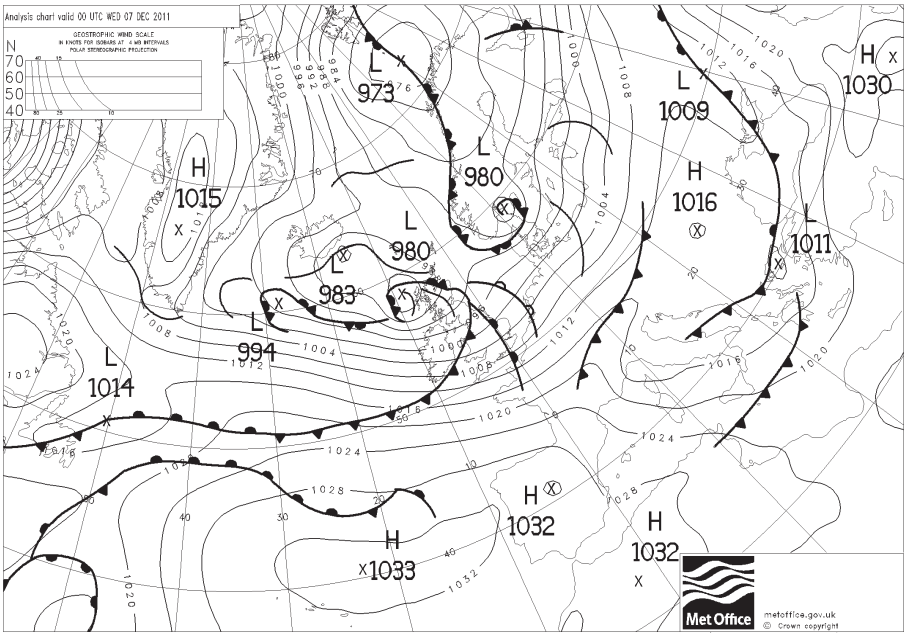

FIGURE 4.3: MO synoptic analysis chart at 0000 07^{th} December 2011. © Crown Publishing

(Figures 4.4 (c) -(d)) before moving north-eastwards towards Norway. By 9^{th} December the storm has begun to fill (not shown). This track means that the south-west quadrant of the storm, where high winds associated with possible CCBs and SJs would be present, passes over central Scotland having undergone it's most rapid deepening. As can be seen from the isobars the gradient in the surface pressure is particularly intense in this region. The minimum pressure reached, according to the MO analysis, was 956 hPa at 1800 8^{th} December, although by this time the cyclone track has swung towards the north-east away from the UK. This is however, only 1 hPa deeper than the minimum central pressure at 1200 UTC when the cyclone is located just to the north of Scotland.

Figure 4.5 shows the WRF modelled SLP from domain 1 at the same times shown in the MO synoptic charts in Figure 4.4. Domain 1 is used here as its larger area gives a better synoptic picture than the smaller, higher-resolution domains 2 or 3. The WRF SLP (Figures 4.5 (a) - (d)) clearly shows the rapidly deepening low moving towards and over Scotland much like the MO charts (Figure 4.4). At 0000 UTC Figure 4.5 (a) shows the low pressure centre is located in the north-western Atlantic at around 20°W. The overall pressure pattern shows a very strong resemblance to the MO synoptic analysis at this time (Figure 4.4 (a)). However, as summarised in Table 4.1, the central pressure is not as deep in the WRF simulation showing only 985 hPa compared to 977

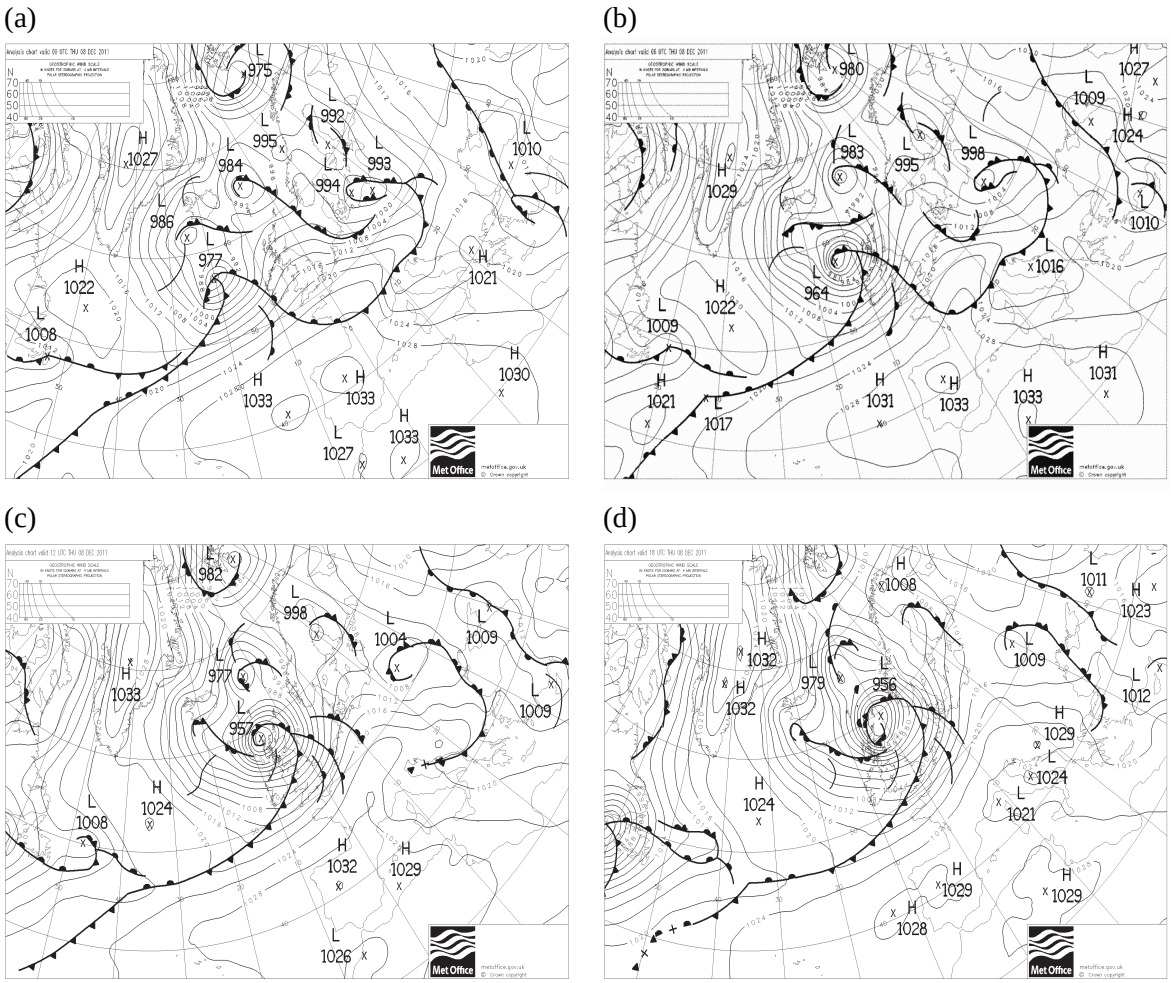

FIGURE 4.4: MO synoptic analysis charts at (a) 0000, (b) 0600, (c) 1200 and (d) 1800 on the 8^{th} December 2011. © Crown Publishing

hPa. This theme continues throughout the simulation with the WRF model simulating minimum central pressures of 973, 965 and 962 hPa at 0600, 1200 and 1800 UTC, respectively (Figures 4.5 (b), (c) & (d)). Comparatively, the MO analysis shows central pressure values of 964, 957 and 956 hPa at these times. Figure 4.5 (c) shows the storm approaches the north of Scotland and appears to slow somewhat between 0600 and 1200 UTC. This is confirmed in the track plot (Figure 4.6) and the locations in Table 4.1. The centre of the low which is slightly stretched longitudinally at 0600 UTC is compacted as it makes land fall at 1200 UTC. This accentuates the strong pressure gradient on the south-western edge of the low. The position contrasts somewhat with the MO analysis which positions the low centre slightly to the north of Scotland. This bunching of the isobars, as the friction causes the storm to slow, increases the pressure gradient to the south and south-west of the low and mitigates the effect of the marginally higher central pressure compared to the MO analyses. This region is the key region for high winds where both SJs and CCBs can occur.

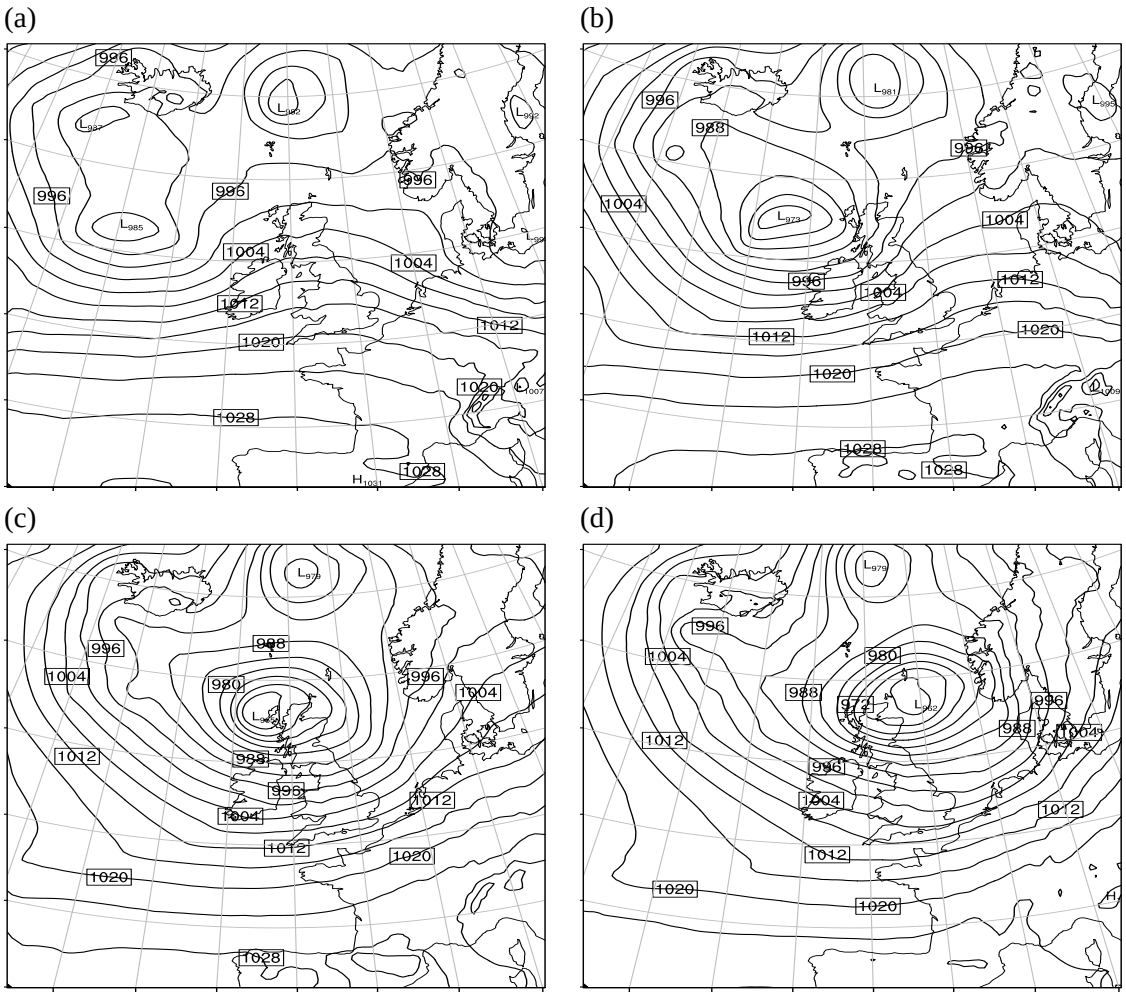

FIGURE 4.5: WRF modelled sea level pressure from Domain 1 at (a) 0000, (b) 0600, (c) 1200 and (d) 1800 UTC 8^{th} December 2011.

Therefore it is important that, although the storm is not quite as deep as the operational analysis suggests, the pressure gradient and curvature on the isobars are well reproduced. The track plot shows the WRF simulation placing the minimum SLP to the south of the MO analyses until around 0000 UTC 9^{th} December. The biggest disparity between the tracks occurs around 1200 UTC 8^{th} December. At this time the MO analysis has the storm centre just to the north-west of Scotland, the WRF model, however, shows it about 100 km to the south-west. These locations mean that the south-west quadrant of the storm will cross land in both the MO analysis and the WRF simulation, and both storms will experience the frictional effects of the land surface. This southward shift may be partially responsible for the different shapes in the SLP pattern as mentioned previously. As can be seen in Table 4.1, Friedhelm developed relatively slowly for most of the 7^{th} December but underwent rapid deepening overnight into the 8^{th} December. The data shows the cyclone deepened by 44 hPa in the 24 hours to both 0600 and 1200 UTC 8th December almost double the deepening

TABLE 4.1: Cyclone Friedhelm minimum SLP and approximate location taken from MO analysis charts, and minimum SLP and location from D01 of the WRF simulation.

		MO Analysis		WRF D01	
Date	**Time**	**Min. Pressure**	**Approx. Location**	**Min. Pressure**	**Approx. Location**
07 Dec	0000	1014	50°W 51°N	-	-
	0600	1008	42°W 52°N	-	-
	1200	1001	35°W 54°N	-	-
	1800	992	26°W 55°N	-	-
08 Dec	0000	977	20°W 57°N	985	19.6°W 56.6°N
	0600	964	15°W 58°N	973	12.6°W 57.6°N
	1200	957	8°W 58°N	965	8.1°W 57.8°N
	1800	956	0°W 60°N	962	0.2°W 58.0°N

(22.7 hPa in 24 hours for a cyclone at 55°N) needed to be considered a meteorological bomb (Sanders and Gyakum, 1980). This is not exactly comparable with the WRF simulation as the storm is not present in the domain until 0000 UTC on the 8^{th}, however, the 0000 UTC to 1200 UTC deepening is equal to that shown by the MO analysis for the same period at 20 hPa. The lowest WRF SLP at 1800 UTC on the 7^{th} December is 995 hPa, however this is on the very edge of the domain within a contour which runs off the edge of the domain (not shown). This would suggest that the WRF model does not capture the deepening rate when the storm first moves into the domain. Given the upper-level PV feature trails the storm at this time, and therefore will still reside outside of the domain, this lack of resolved upper-level forcing may be responsible for the slower deepening.

Other features close to the vicinity of Cyclone Friedhelm such as the small low to the east of Iceland are captured. Again, at 1800 UTC the storm continues to reside slightly further south in the WRF model (Figure 4.5 (d)) compared to the MO analysis (Figure 4.4 (d)). The longitudinal stretch in the pressure field can again be seen in the WRF model, whereas the MO analysis is stretched more latitudinally. These differences are relatively small with the overall shape and strength of the pressure field comparing well with the analysis.

4.2.2 Frontal Structure

The evolution of the equivalent potential temperature (θ_e) field and wind speeds are shown in Figure 4.7. Again, these are shown on domain 1 to give a synoptic picture of the storm development. The wind fields are discussed in Section 4.2.3 along with the high-resolution domain 3 wind.

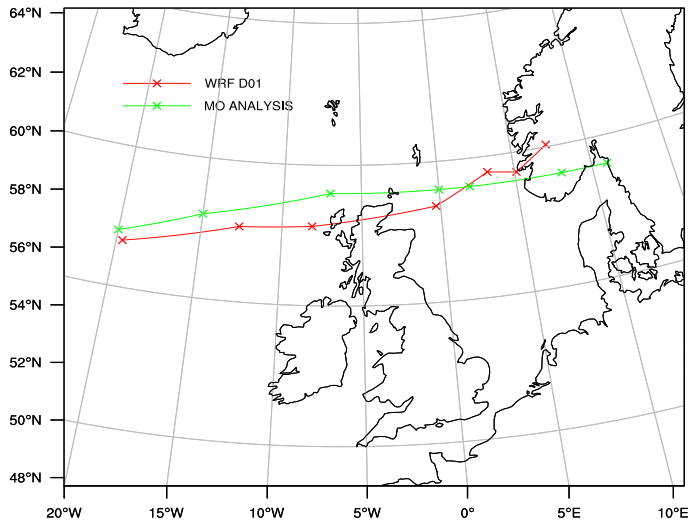

FIGURE 4.6: Tracks of MO analysis and WRF minimum SLP locations. Red crosses indicate WRF minimum SLP locations every six hours from 0000 UTC 8^{th} Dec. to 1200 UTC 9^{th}. Green crosses indicate approximate MO analysis minimum SLP location.

The θ_e evolution shows that the development of the storm follows the Shapiro-Keyser life cycle, as shown in Figure 2.1 (b). At 0000 UTC (Figure 4.7 (a)) the storm resembles a transition between stage I and II of the Shapiro-Keyser evolution with the initial frontal wave developing and evidence of frontal fracture beginning to take place. From 0600 UTC to 1200 UTC (Figures 4.7 (b) & (c) respectively) the development from stage II to stage III can be seen with frontal fracture occurring, followed by the characteristic t-bone frontal structure of stage III clearly shown at 1200 UTC. The development slows and by 1800 UTC (Figure 4.7 (d)) the full warm seclusion of stage IV has not been reached. Development of the storm through the Shapiro-Keyser model has been shown to be essential for the formation of SJs (see Section 2.4.3). Parton et al. (2010) showed that around a third of SJs in their observation-based climatology occurred during phase III with the remainder in phase IV. This shows slightly different development to the MO hindcast of Cyclone Friedhelm presented by Martínez-Alvarado et al. (2014). In their simulation the cyclone has developed signs of a warm seclusion by 1200 UTC despite the cyclone still deepening rapidly until 1800 UTC (see their Figure 2).

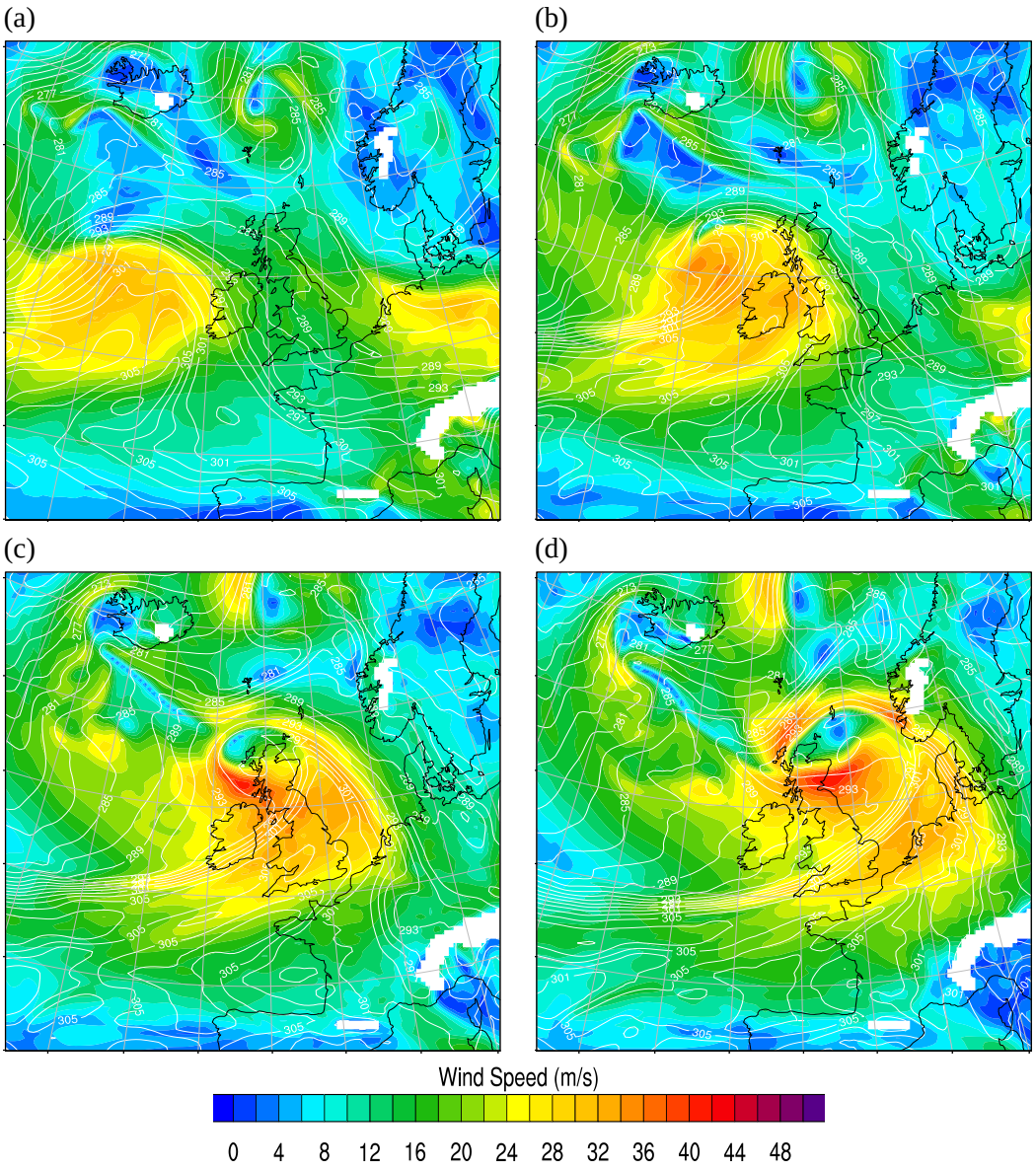

FIGURE 4.7: Domain 1 plots of wind speed (ms^{-1}) - filled colours, and θ_e (K) - white contours every 2 K, on the 850 hPa pressure level at (a) 0000, (b) 0600, (c) 1200 and (d) 1800 UTC 8^{th} December 2011.

4.2.3 Winds

4.2.3.1 ASCAT Comparison

Figure 4.8 (a) shows wind measurements from the EUMETSAT METOP satellite's ASCAT instrument. The vectors shown have a 25 km resolution, taken from an overpass at ~1134 UTC on the 8^{th} December. The ASCAT winds are calculated as 10 m winds in a neutrally stable layer based

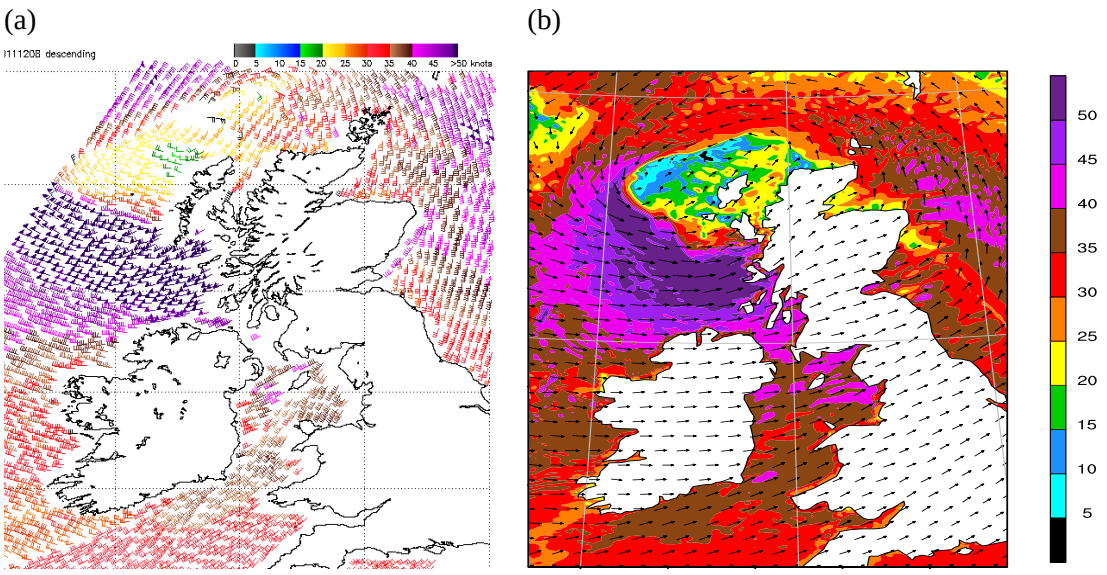

FIGURE 4.8: Comparison of ASCAT derived winds and WRF modelled winds. (a) ASCAT satellite scatterometer measured wind speeds from the 1134 UTC 8th December 2011 overpass (plot from: *http* : *//manati.star.nesdis.noaa.gov/datasets/ASCATData.php*). (b) WRF modelled 10 m winds at 1130 UTC.

on the ocean surface radar backscatter. The instrument is described by Figa-Saldaã et al. (2002). For comparison WRF 10 m wind speeds plotted at 1130 UTC are shown in Figure 4.8 (b).

The WRF simulated winds show very good resemblance to those observed with ASCAT. The general shape of the high wind region surrounding the relatively slack region in the low pressure centre is notably similar in the model to the observations, although the slack region extends slightly further south close to the Western Isles in the model. This southward shift is also noted in the SLP comparison above. The main region of highest (>50 kt) winds is observed to extend from the western coast of Scotland westwards. This spatial region and magnitude is well captured by the model excluding, perhaps, a small region near the southern tip of the Outer Hebrides. The other notable discrepancy is the lower wind speed values in the slack region, with WRF producing values as low as 5 kts compared to the 15-20 kts shown in the ASCAT plot. Despite these differences, the overall consistency in both the spatial pattern and magnitude of the winds shows that WRF is succeeding in simulating the storm. The location of the highest winds, to the south and south-west of the cyclone centre is consistent with the region where SJs and CCBs occur. These low-level winds are likely likely to be associated with the CCB as it undercuts due to its vertical extent as described in Section 2.4.2.

4.2.3.2 WRF Winds

The high winds in Cyclone Friedhelm are the main focus of this study. This section will give an overview of the development in time of the winds during the passage of the storm with a detailed analysis of the high wind regions and their dynamics in Chapter 5.

The shading in Figure 4.7 shows the development of the 850 hPa wind speeds in domain 1, as the storm deepens on its track towards Scotland. A large region of moderate winds (>20 ms^{-1}) has already developed at 0000 UTC (Figure 4.7 (a)). As the cyclone deepens to 0600 UTC, some more defined regions of higher winds (>30 ms^{-1}) begin to appear (Figure 4.7 (b)). These are located along the warm front, from ~55°N, 5°W to 50°N, 12°W, and to the south and south-west of the low pressure centre, ~5°N, 10-15°W. This region intensifies significantly and at 1200 UTC, Figure 4.7 (c) shows values of over 40 ms^{-1} located to the west of Scotland. The development in this region where, typically, SJs and CCBs occur, is discussed in greater detail below, using the domain 3 figures during this period as the resolution in domain 1 misses key features. At 1800 UTC the strong wind region to the south of the low has expanded, stretching from western Scotland into the North Sea (Figure 4.7 (d)). Given the previously documented issues examining WRF modelled winds over land (Smart and Browning, 2014) and the development to the west of Scotland shown above, the majority of this study will focus on the development of the high wind region before the storm reaches the Scottish coast.

The coarse resolution of Figure 4.7 means that some mesoscale features such as SJs may not be resolved, therefore it is important to examine the storm at higher resoluion. Figures 4.9, 4.10 and 4.11 show the development of the high wind regions on 780, 850 and 925 hPa levels, respectively, from the high resolution (3 km horizontal) domain 3. The plots show the winds every 2 hours from 0600 UTC to 1200 UTC on 8^{th} December as Cyclone Friedhelm bears down on the west coast of Scotland.

The winds on the 780 hPa level show a number of interesting features as the storm approaches Western Scotland (Figure 4.9). The yellow/orange contouring shows a broad region of relatively high winds (>20 ms^{-1}) at 0600 UTC (Figure 4.9 (a)). The warm front lies towards the eastern boundary of this region, therefore the winds induced by the warm-frontal motion are likely to dominate to the east of this region (orange colours). Evidence of the WCB along the cold front can be seen stretching north-east to south-west from 55°N 10°W, with wind speeds up to 38 ms^{-1}. The higher winds in and around this warm sector coincide with the stronger pressure gradient here,

unlike the regions further to the north of the low pressure centre. The wind speeds are relatively low to the immediate north of the low pressure centre even where the pressure gradient force is relatively high. The cyclonic circulations around the storm mean the winds here are flowing against the mean flow of the storm and from a low-momentum region. Already, there is a region of higher winds appearing just to the south of the low pressure centre where the pressure gradient is highest.

At 0800 UTC (Figure 4.9 (b)) the region of high winds on the south-west side of the low (the typical SJ/CCB region) has developed further with values now reaching >40 ms^{-1}. This region corresponds with the tightest packing of the isobars showing that the PGF is likely to be highly important in the acceleration of the winds, as well as the strong curvature around the storm centre. The cold front is evident towards the bottom of the plot stretching towards the north-east. Patchy high winds between the SJ/CCB region and cold front appear likely to be the result of convection occurring in this region similar to that seen by Browning (2004).

Between 0800 UTC and 1000 UTC (Figures 4.9 (b) and (c)) there is little movement of the exact center of the low (marked "L" in the plots). However, the pressure and wind fields have developed significantly around it. At 1000 UTC, the isobars to the west and south of the low show a very strong pressure gradient. A ribbon of very high winds (>50 ms^{-1}) extends west to east to the south of the low before orientating south-east. This ribbon is roughly 500 km in length and ~50 km in width. The ribbon sits within a larger region of high winds to the immediate south of the slack low centre region. Again the cold front/WCB winds can be seen further to the south of this. The high winds here, in particularly the ribbon, are not as obviously correlated with the regions of tightest pressure gradient suggesting that other processes are taking effect here.

At 1200 UTC Figure 4.9 (d) shows the strong wind field has progressed to the Scottish coast with the isobars distorting somewhat around the land. A small thin band of intense winds is located close to the coast. Behind this, a band of strong winds (red shading) extends north-west starting near to the high pressure gradient on the west of the low. Following the isobars the intense region at this time looks likely to be a continuation of the intense ribbon seen at 1000 UTC. The scale of these intense features means that they are only resolved at higher model resolutions and cannot be seen in the domain 1 plot (Figure 4.7 (c)).

The wind fields at 850 hPa and 925 hPa (Figures 4.10 and 4.11, respectively) both show very similar structures to those at 780 hPa, albeit generally with lower magnitudes due to the increased

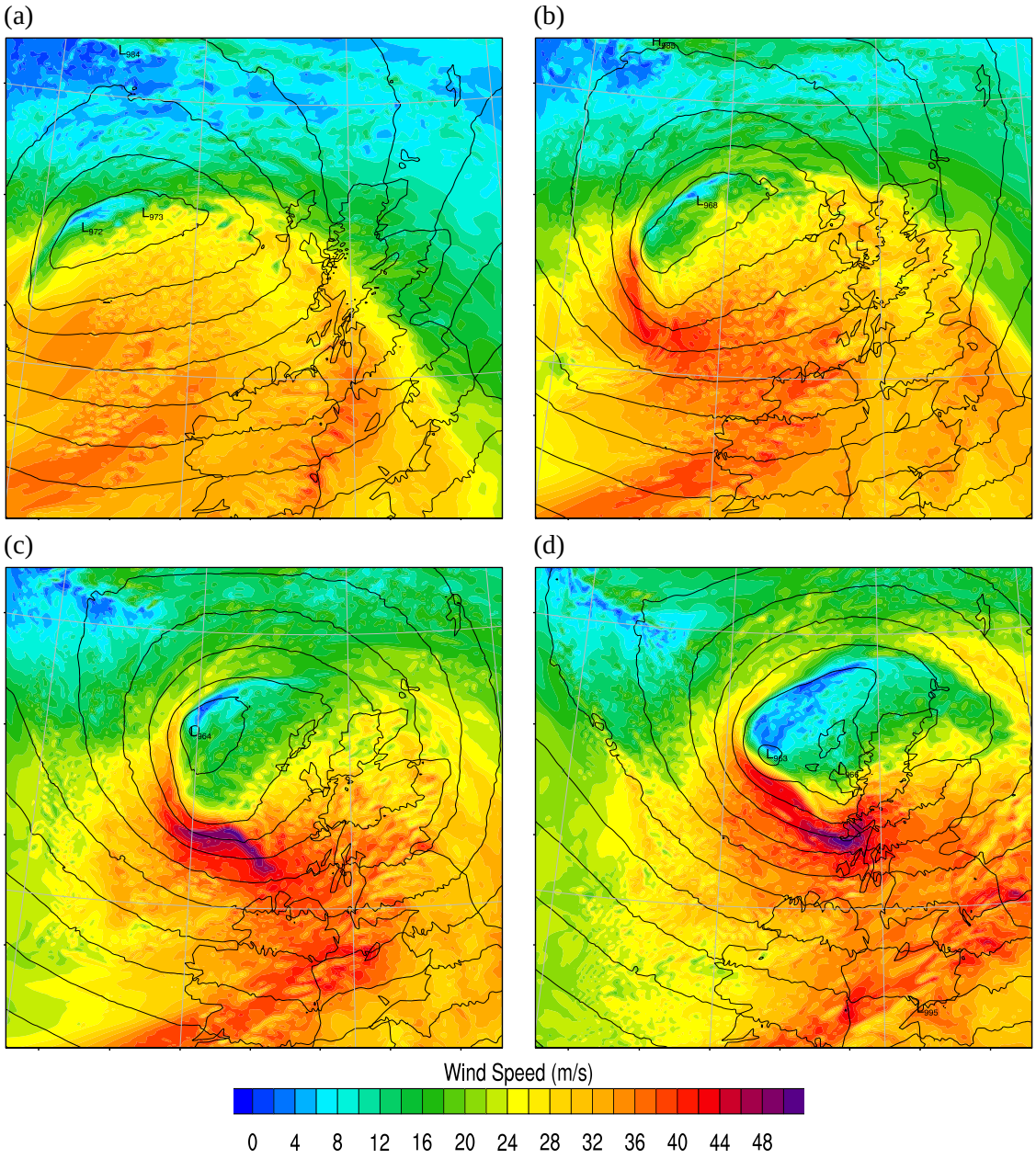

FIGURE 4.9: Domain 3 plots of 780 hPa level wind speed (ms^{-1}, shading) and SLP (black contours, every 4 hPa). Plots are shown from 0600, 0800, 1000 and 1200 UTC, (a)-(d) respectively.

friction at these levels. This is not entirely true just north of the cyclone centre however where the low-level nature of the CCB can be seen with increased winds at the 850 hPa and 925 hPa levels compared to the 780 hPa levels.

The very strong "ribbon" of winds at 1000 UTC is not evident in either of the lower-level plots, although there is a small region of purple shading in the 850 hPa plots at this time close to the strongest part of the ribbon in the 780 hPa plot. The same is true at 1200 UTC with just a small area of purple shading in the 850 hPa plot. There is also a corresponding area in the 925 hPa plot, although this is very small. This shows that this "ribbon" is a mid-level jet which may be descending to 780 hPa but unable to descend much below the 780 hPa level.

Figure 4.12 shows the time series of the maximum winds over the course of the 8^{th} December. Generally the 780 hPa winds (red line) are higher than the 850 or 925 hPa (orange and yellow lines, respectively), largely due to the lower friction at higher levels. The maximum winds show a rapid rise through the morning of the 8^{th} as the cyclone tracks towards Scotland and deepens. A caveat on the values prior to 0600 UTC is that the whole of the cyclone has not yet entered the domain. Comparison to domain 1 winds however, shows similar low-thirties and mid-thirties values at 0000 and 0600 UTC (Figure 4.7 (a) and (b)), respectively, to the time series. Between 0600 and 1000 UTC there is a rapid rise in the maximum wind speeds of $\sim$10 ms^{-1}. Two peaks are seen in the 780 hPa wind maxima at 1000 UTC and 1200 UTC. At the lower levels the 1000 UTC peak is less pronounced and the second peak occurs at 1130 with the maximum wind speed decreasing slightly by 1200 UTC. From 1200 UTC onwards the winds gradually decline on all three levels, albeit still with maximum winds of 40-45 ms^{-1} by 0000 UTC, despite the continued deepening of the storm (see Table 4.1).

The general pattern of increasing and decreasing maximum wind speeds is consistent between the three levels. This suggests that large scale forces, such as increased PGF due to the cyclone deepening, are the main drivers of the wind acceleration rather than mososcale processes which may be vertically limited in extent.

As mentioned previously Chapter 5 provides an in-depth dynamical analysis of the strong winds and other dynamical features within the storm.

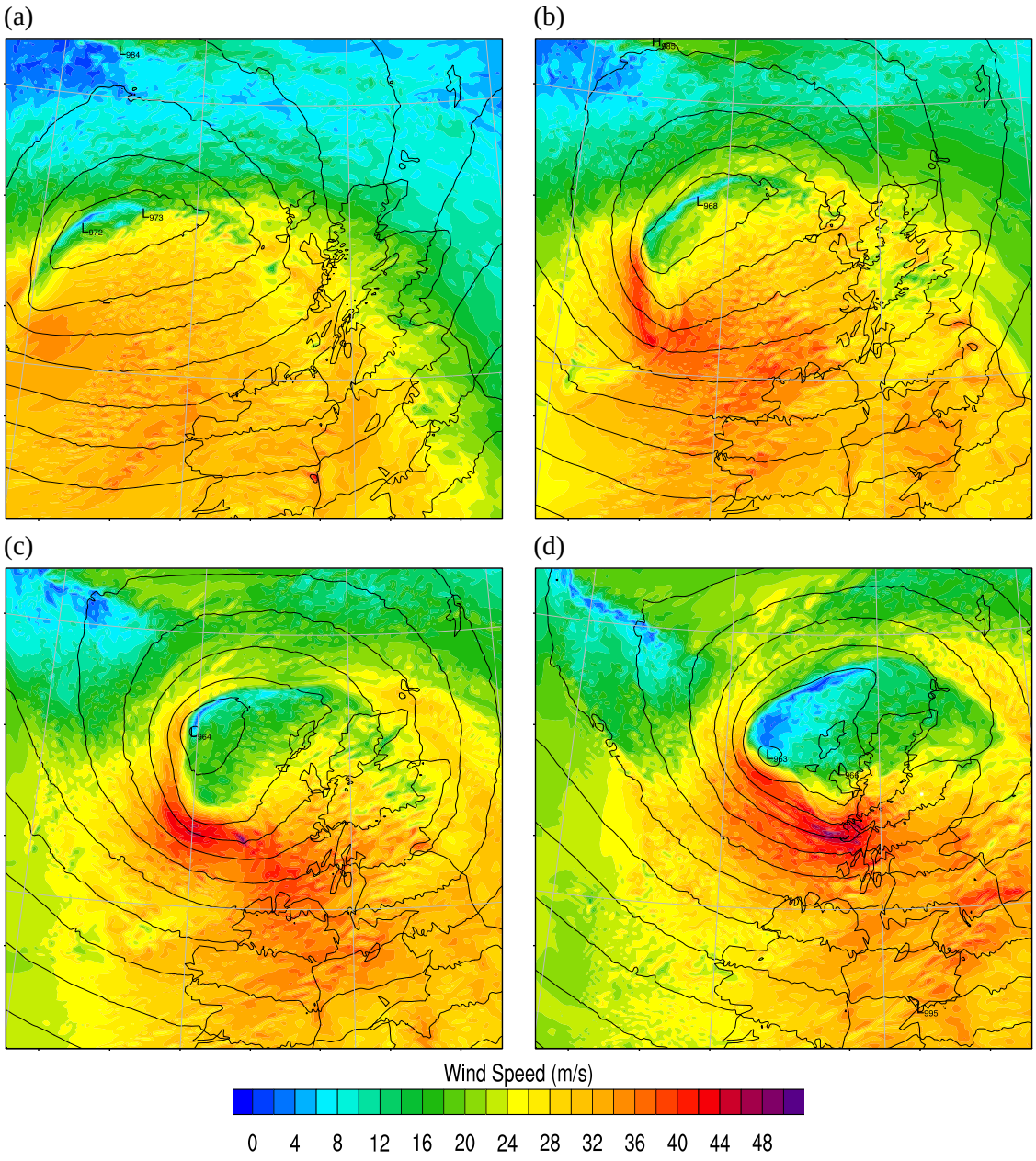

FIGURE 4.10: As Figure 4.9 but for the 850 hPa level.

4.2.4 Satellite

Infra-red (IR) satellite images are shown in Figure 4.13 (a), (c) and (e) at 0800, 1000 and 1200 UTC, respectively. These show the progression of the cloud head as it propagates across Scotland. The WRF plots (Figure 4.13 (b), (d) & (f)) show the simulated outgoing longwave radiation (OLR) which, although not an exact representation in terms of projection and colour scale, are comparable to the IR satellite images.

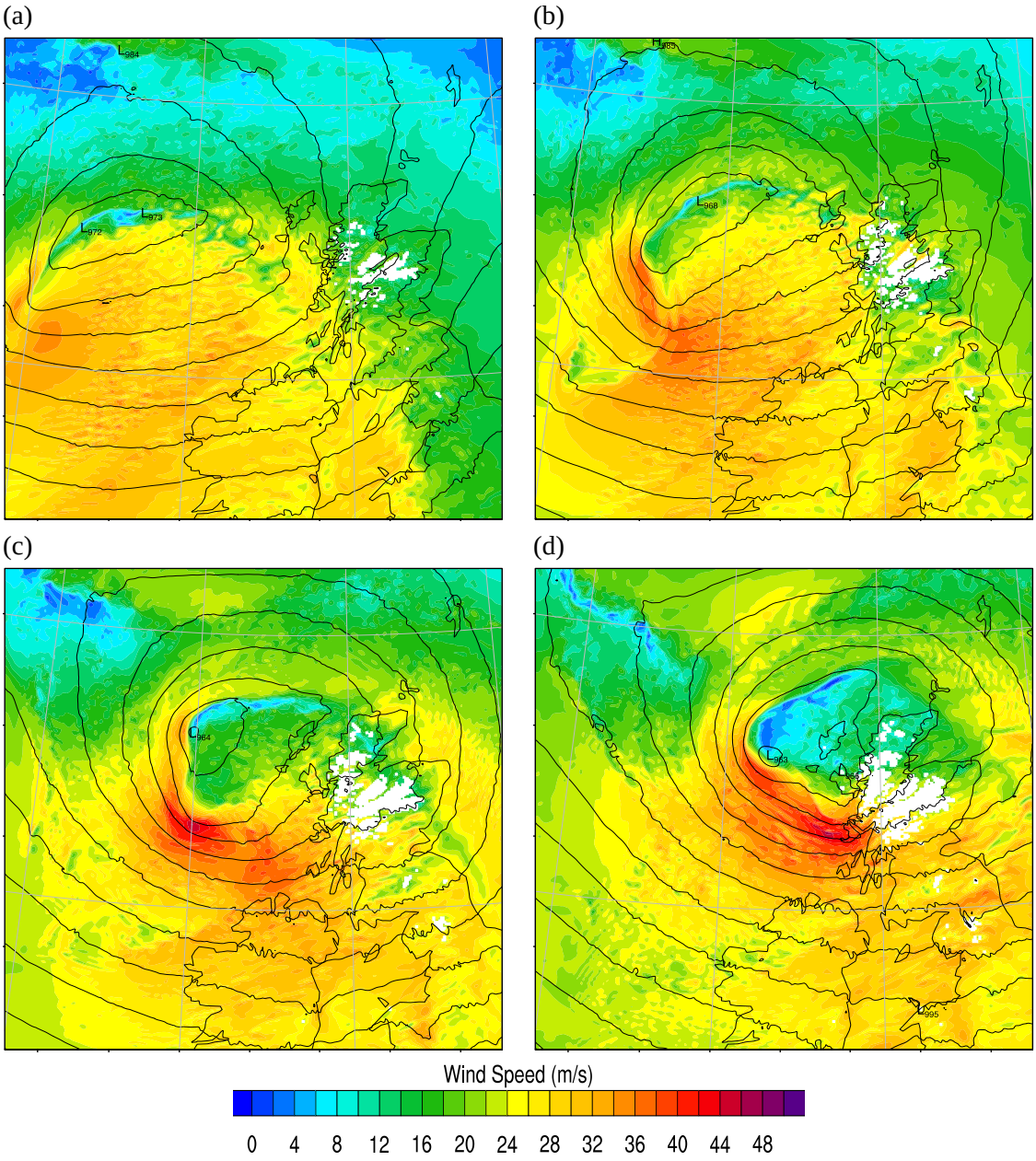

FIGURE 4.11: As Figure 4.9 but for the 925 hPa level. The white regions indicate where the 925 hPa isobar has intercepted the ground in mountainous regions.

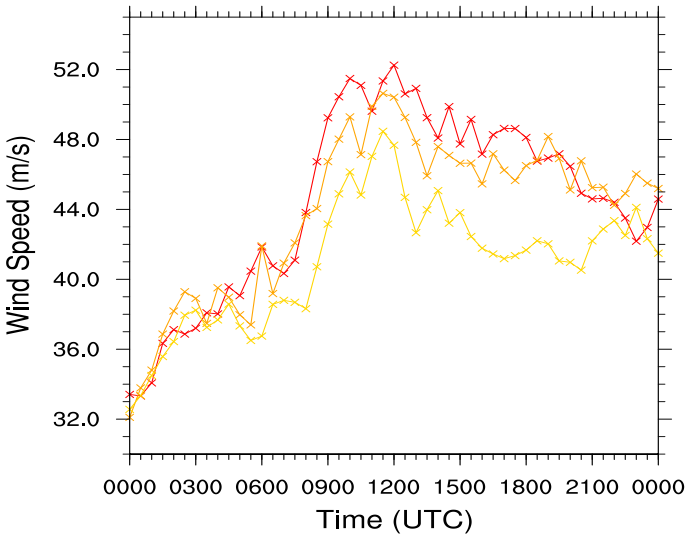

FIGURE 4.12: Time series of the maximum mean winds in domain 3 on the 8^{th} December. 780, 850 and 925 hPa pressure levels are indicated by the red, orange and yellow markers and lines, respectively.

At 1000 and 1200 UTC some banding can be seen at the tip of the cloud head (Figures 4.13 (c) & (e)), as suggested in Browning (2004) and subsequent SJ studies (Clark et al., 2005; Gray et al., 2011). This can be a sign of CSI release through slantwise convection, which may be important in the formation of SJs. The WRF clouds show some banding, mostly in the 1200 UTC plot (Figure (4.13 (f)), however, this is not as clear as in the satellite images. The banding in the satellite images is less obvious than in some of the previously studied SJ storms (e.g. Browning (2004), Smart and Browning (2014)).

The WRF OLR plots show some discrepancies to the satellite images. Firstly, the cloud head appears somewhat further south in the WRF simulation. The broken cloud on the northern edge of the dry slot extends south from around 60°N in the satellite images. In the WRF plots however, this is present at around 58°N at 0800 UTC, although the position in the WRF model does improve at 1000 and 1200 UTC. This southern shift has already been noted from both the SLP and wind field comparisons. The shape of the cloud head is also not entirely consistent between the satellite and WRF OLR images. In the WRF simulation it appears to be stretched longitudinally, this is consistent with the stretching of the isobars for the WRF simulation (e.g. Figure 4.5). The location of the cold front is slightly more northward in the WRF simulation than in reality making the dry slot smaller, it also exhibits a very sharp rear edge compared to the satellite image.

In both the WRF and satellite images convective clouds are visible within the dry slot and on the inside edge of the main cloud head. These were also seen in the Great Storm analysis by Browning

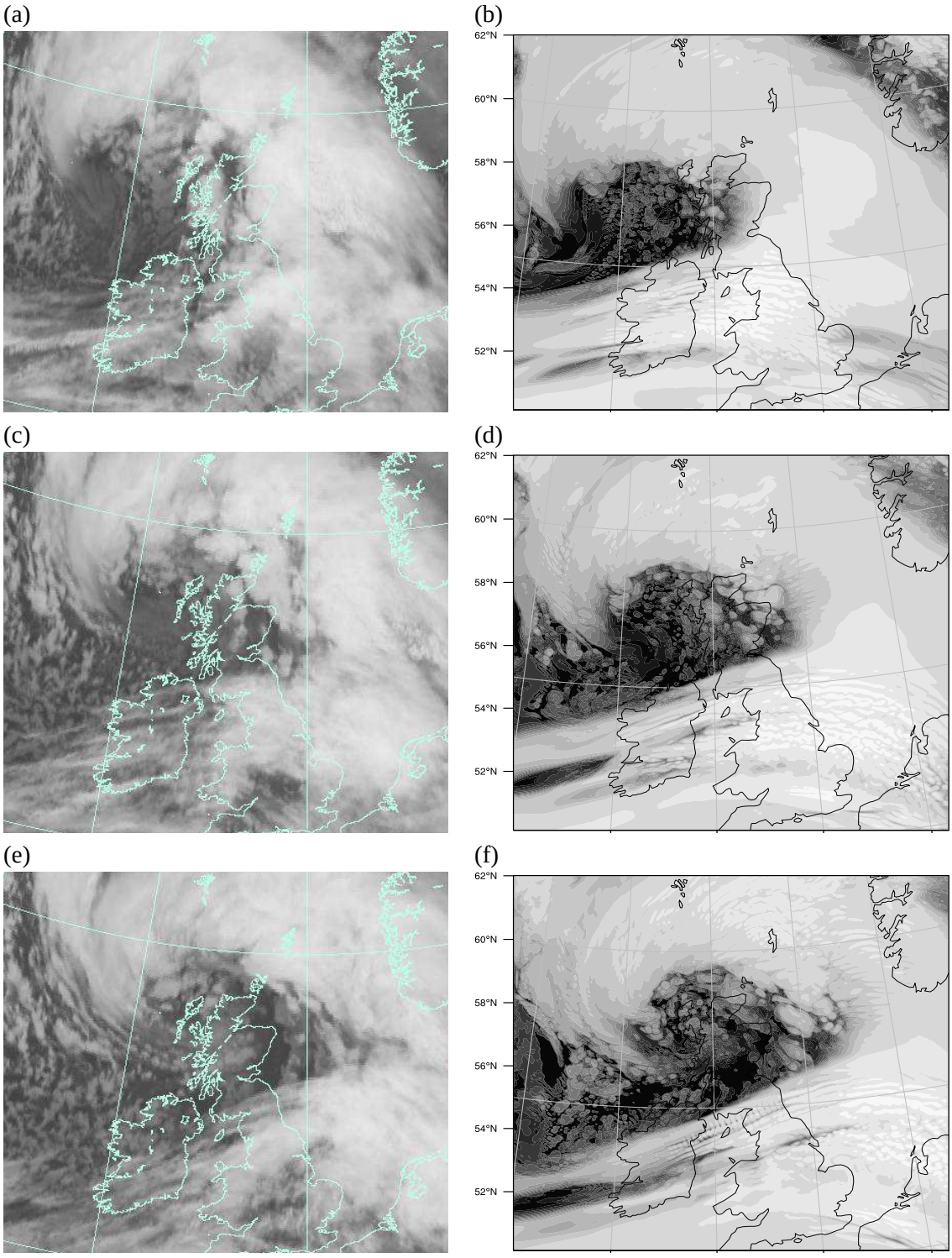

FIGURE 4.13: IR MSG satellite images at (a) 0800, (c) 1000 and (e) 1200 UTC and WRF outgoing longwave radiation (OLR) images at the same times. (Satellite images courtesy and copyright EUMETSAT/UKMO)

(2004), where downdraughts associated with them were attributed to be the cause of some of the high gusts which occurred within the dry slot. The WRF simulation is also showing more broken cloud around the inside edge of the dry slot as can be seen in the satellite images.

Although there are some differences between the satellite images and WRF OLR plots the overall shape and many of the processes in the dry slot region appear to be being recreated well by the model. As mentioned the cloud head region is of great importance in the development of the winds. The comparisons shown suggest that WRF is doing a good job of recreating this.

4.2.5 Radar

Equation 4.1 shows the Marshall-Palmer relationship from which the modelled rainfall rate is derived using the WRF simulated dBz values.

$$Rr = 0.036 \cdot 10^{0.0625 \cdot dBZ} \tag{4.1}$$

where Rr is the rainfall rate and dBZ is the modelled radar reflectivity.

The equation, 4.1, gives an instantaneous rain rate, which can be compared to the MO radar images. Due to the sampling methods and data issues of rainfall radar such as azimuth angle and attenuation, there will be differences between the model and radar, even given a near-perfect simulation. For this comparison the rain rate is calculated from the dBz diagnosed from model level 5 in order to try and achieve a good comparison to the radar. It is notable that some of the radar stations were showing scanning difficulties as Friedhelm passed over Scotland particularly between 0530 UTC and 0730 UTC (not shown), after which one of the radar stations is removed from the composite plots. For this reason the plots at 0500, 0800, 1000 and 1200 UTC are used in Figure 4.14, although some attenuation can still be seen in these images. This period also shows most of the rainfall within range of the radar stations.

The frontal structure can be clearly seen in the radar images (Figures 4.14 (a), (c), (e) and (g)) and the WRF simulated rainfall (Figures 4.14 (b), (d), (f) and (h)), albeit with some differences which will be discussed here. The structure of the warm, cold and occluded fronts shown in Figure 4.4 can be clearly seen in radar images. Overall the WRF model is picking up the general structure well, similarly to the satellite comparison above (Figure 4.13). There does appear to be a general

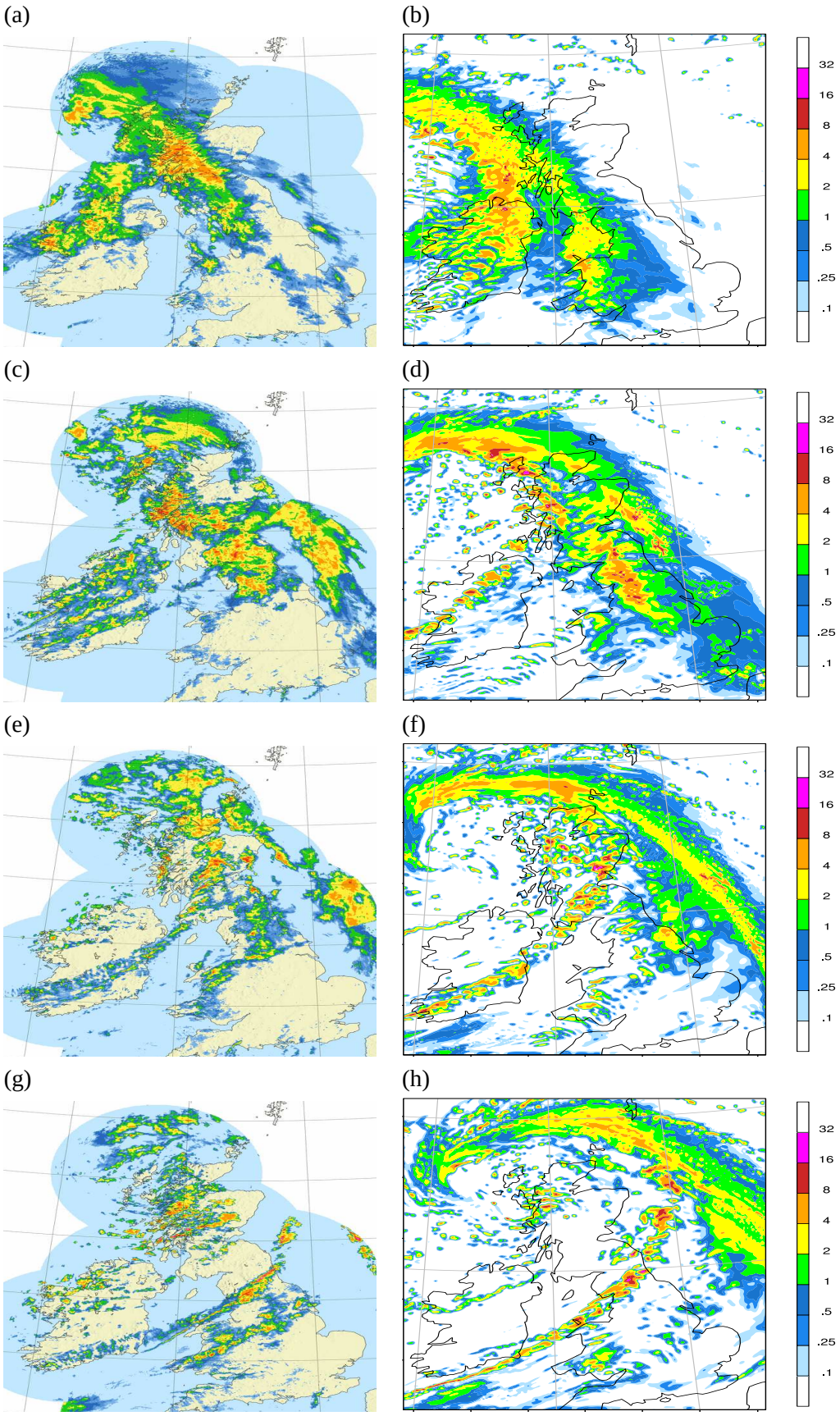

FIGURE 4.14: UKMO 1 km composite radar images at (a) 0500, (c) 0800, (e) 1000 and (g) 1200 UTC on the 08^{th} December 2011. Plots (b), (d), (f) and (h) show the corresponding times from the WRF model with rain rate calculated from the simulated reflectivity (dBz) using Equation 4.1

.

overestimation of rainfall by the WRF model, however, with larger areas showing rates >2 mm hr^{-1} (yellow shading) or above. This is accentuated by increased rainfall towards the southern ends of both the warm and cold fronts. The timing of the storm passage is slightly slower in the model with the warm and occluded fronts appearing somewhat behind the radar images, this is not so true for the cold front, however.

At 0500 UTC the warm front is positioned over central and western Scotland and north-west England with intense rain in these regions showing evidence of orographic enhancement (Figure 4.14 (a)). South of this the frontal precipitation is much weaker and increasingly broken as the front extends down towards the south-east of England. The cold front at this time stretches south-west from the triple-point situated close to the Western Isles of Scotland. The cold frontal precipitation covers a broad region over the north-west of Ireland. Again there appears to be some orographic enhancement occurring as the front hits land. There are local strong rainfall regions embedded within the front with rates of >8 mm hr^{-1}. The occlusion can be seen extending north-west from the Scottish coast. It ceases just short of the radar range as the occlusion becomes less defined. In the WRF simulation at this time (Figure 4.14 (b)) the distinction between the warm and cold frontal rainfall in the WRF model is less clear with precipitation occurring over much of the Irish Sea. This is a product of both the warm front lagging behind that in the radar and the cold front being somewhat ahead of the observed cold front.

Three hours later at 0800 UTC (Figure 4.14 (c)) the pattern of rainfall has changed dramatically. The cold front has largely disconnected from the warm front showing the frontal fracture of the Shapiro-Keyser development of the storm, at this time there appear to be three distinct precipitation bands associated with the cold front, all stretching over Ireland. A second band of precipitation, associated with the warm front, has also formed in the North Sea with what appears to be the main warm front covering much of northern England, southern and central Scotland and the Western Isles. However some doubt is cast on the exact details of the forward band given the radar artefacts at the edge of the radar range and the removal of the Hill of Dudwick radar (located ~30 Km north of Aberdeen) from the composite. Orography can still be seen playing a significant role in the intensity of the precipitation over the Scottish Highlands and Cumbrian Fells. There is a large area of rain associated with the occlusion to the north and north-west of Scotland. A large coherent region to the north of Scotland is associated with the main cloud head shown in Figure 4.13 (a). Just to the south east of this there is an area of scattered precipitation. This can also be seen in the patchier cloud in Figure 4.13 (a). The model has captured, to some extent, the forward band

of precipitation off the north-east coast although it is thinner and closer to the coast than the band in the radar (As noted above there are some doubts about the radar version of this band as well). The intense, orographically enhanced precipitation over the Pennines and western Scotland has also been reproduced by the model. On some of the other features the model appears to struggle, however. It has failed to capture the multiple bands of the cold front exhibiting only a single intense band with a broken weak band ahead of it. Again the heavy precipitation associated with the warm and cold fronts extends much further south in the model than is seen in the radar image. The occluded front also shows some considerable differences at this time. The main body of it is shifted to the south-west compared to that in the radar. It appears thinner overall in the model, largely consisting of a coherent band which is thinner than the total occlusion in the radar. Some of the rainfall intensities in precipitation are similar around the Outer Hebrides but these are part of the main band in the model rather than the more scattered regions in the radar. The tip of the occlusion still resides out of radar coverage so the overall picture is incomplete.

At 1000 UTC the radar shows some regions of precipitation over northern England and Scotland have dissipated, although areas of heavy rainfall persist (Figure 4.14 (e)). The warm front has moved further off the east coast, though some rain continues within the warm sector over the Pennines and Welsh mountains. North of Scotland there is still a large region of precipitation associated with the occluded front. The strong broken showers persist on the inside of the front with a more distinct band to the north and east of them. Compared to previous times the occlusion has weakened, particularly towards its western extent, although the radar range still fails to cover its full length. By this time the cold front had formed into a more coherent single line, stretching from central Scotland across to the south-west of Ireland. Comparatively the rainfall is resolved more accurately in the model at this time than in the preceding plots. The single line of the cold front is captured very well in terms of location, albeit with a high bias in terms of intensity. The location of the warm front in the model is slightly more eastward then in the radar, meaning the storm is somewhat stretched longitudinally. Again the warm front and occlusion show a far more coherent structure in the model, particularly in the North Sea and to the north-west of Scotland.

The rapid passage of the system means that by 1200 UTC (Figure 4.14 (g)) the warm front has largely cleared out of radar range to the east of the UK, so this feature cannot be compared to the WRF plot. The occlusion north of Scotland has dissipated further with only a few bands of precipitation still located here. However, at its tip a number of bands of very intense rainfall have formed due to the orographic effects of the Scottish coastline. The cold front has moved

south becoming an intense band across northern England with weaker precipitation extending across to the south-west tip of Ireland. A band of rain ahead of the cold front, stretching from the Pembrokeshire peninsular to the Humber estuary, contains a number of regions of intense precipitation. Although a small isolated warm front within the warm sector is shown on the MO analysis chart (Figure 4.4 (c)), at this time it's location does not correspond well with the location of the rainfall in the radar image. The cold front in the WRF model is again located well compared to the radar. An area of increased intensity across the north of England is also captured but like previous times the intensity is overestimated and the trailing end is overly-defined. The occlusion shows the same patterns as the cold front, with a far more defined and intense band to the north of Scotland. The occlusion is further westwards than that in the radar as well meaning that although some orographic precipitation is present over western Scotland, its extent and organisation is less than that in the radar plot.

4.2.6 Dropsonde Sections

During the course of the research flight into Cyclone Friedhelm a total of 21 dropsondes were released, providing a highly useful and rare dataset with which to evaluate the model. As mentioned in Chapter 3, the dropsondes from the Cyclone Friedhelm were assimilated into the ECMWF analysis data which is used for the initial and boundary conditions for the model runs presented here. In certain situations this may limit the validity of using the dropsondes as an model evaluation tool as. However, in this case the domains are large enough, and the lead-time long enough that any issue of effective "double-counting" of the dropsonde data should be mitigated.

As mentioned in Section 3.2.1, the dropsondes were released from an altitude around 7000 m and take approximately 10 minutes to descend to the surface. Due to the fall-speeds and aircraft receiving limitation the horizontal resolution on the dropsondes is on the order of 30 km, although this is somewhat variable. Given the strong winds, the dropsondes experience some drift as they descend as shown in Figure 4.15. The dropsonde sections from this flight are also used for comparison with MO UM simulations by Martínez-Alvarado et al. (2014), their results are compared to those from the WRF simulation later in this section. The dropsonde data interpolation and plots presented here were produced by Phil Rosenberg (Uni. of Leeds) as part of the DIAMET project.

The dropsondes were released on three legs of the research flight; two on the west of mainland UK in the late morning and early afternoon and one to the east of Scotland later in the evening.

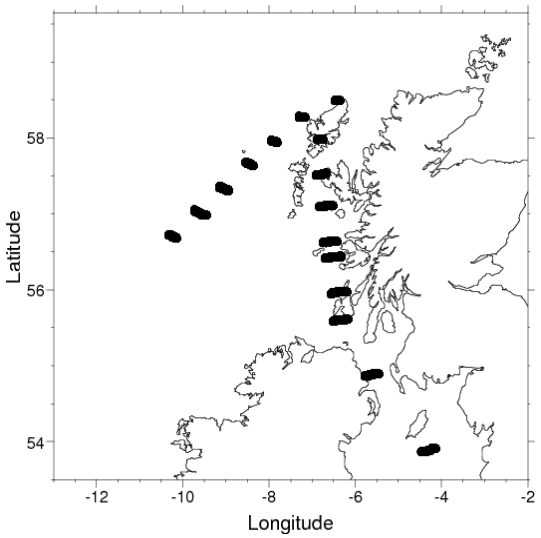

FIGURE 4.15: Map of the dropsonde drift throughout their descent. The dropsondes drift west-to-east during descent following the general wind.

TABLE 4.2: Dropsonde release times and locations.

Leg	Sonde	Time	Lon	Lat
1	1	1130	-4.47	53.83
	2	1146	-5.42	54.77
	3	1158	-6.15	55.49
	4	1203	-6.19	55.90
	5	1209	-6.32	56.37
	6	1212	-6.35	56.53
	7	1217	-6.43	57.02
	8	1223	-6.51	57.50
	9	1228	-6.51	57.85
	10	1234	-6.09	58.37
2	11	1243	-6.95	58.19
	12	1249	-7.58	57.88
	13	1255	-8.20	57.56
	14	1301	-8.81	57.25
	15	1306	-9.23	57.02
	16	1312	-9.84	56.69
	17	1318	-10.38	56.39

Given that the third leg contained only four dropsondes and occurred once the cyclone had crossed Scotland, the focus here is on the earlier of these legs. The time and approximate location of each dropsonde release is shown in Table 4.2. Figure 4.16 shows the dropsonde locations (crosses) overlaid on the WRF wind field during each dropsonde leg. The first leg (black crosses, labelled 1-10) stretched from the central Irish Sea to the northern tip of the Outer Hebrides near to the low centre, with 10 dropsondes released. According to the WRF simulation this section passed right across the region of highest winds to the south of the low. The second leg, consisting of 7 dropsondes (white crosses, labelled 11-17), stretched from the centre of the low south-west, crossing the CCB region of high winds.

There are a number of caveats to be considered when comparing dropsondes or dropsonde sections to model data, as is done here. As can be seen in Table 4.2 the temporal and spatial distribution of the dropsondes is not equal. When comparing a section to the model, the time difference between the dropsondes must be considered. The relative sparsity of the dropsondes can mean interpolation is not always correct and some features may be missed or not fully accounted for. Indeed dropsonde leg 1 (Figure 4.16 (a)) shows dropsondes 4 and 5 being released either side of the region of the modelled strongest winds, meaning their values may be underestimated in the dropsonde interpolation. The complex 4-D development of the dropsondes and the model may also cause differences to be seen. It has already been noted that some differences are present between the shape and track of the cyclone in the WRF simulation and in observations or analyses (Figure 4.6). Despite these inconsistencies dropsonde sections are an extremely useful tool for evaluating the performance of the model and the structure of the storm produced therein, given some sensible checks. The WRF sections for comparison are created at numerous times in order to check for any differences in storm velocity. Analysis of whole sections means simple misplacement and storm track errors can be identified by eye and sections moved if needed. The focus can then be on the presence and structure of features within the storm that show the model is capturing the same processes as reality.

Also used during these sections was the on-board, downward pointing lidar, which allows the cloud top height to be determined as described in Section 3.2.2. The sampling from the lidar can appear noisy but gives a good estimate of cloud top height which can be compared to the modelled clouds. It must also be noted that the lidar signal is a point measurement from directly below the aircraft, therefore, it may not exactly match with the clouds which the dropsondes may pass through, due to their drift during descent.

The initial analysis of leg 1 conducted here used a similar section as Martínez-Alvarado et al. (2014), of a straight line from dropsondes 1-10 as shown by the dashed black line in Figure 4.16. However, this section would miss some of the highest wind regions in the WRF model, which the dogleg in the dropsonde section appears to pass through. Also, this line passes over much more land than the real dropsonde paths, raising the possibility that orography and land-sea interactions may alter the atmospheric profile, particularly at lower altitudes. Therefore the section is moved 0.6° west, shown by the solid black line in Figure 4.16, in order to fit more closely with the majority of the dropsondes in the high wind region and with less influence from land.

4.2.6.1 Dropsonde Leg 1

The dropsonde section shows a low-level maximum wind speed at ~56.6°N and 1 km (~925 hPa) altitude (Figure 4.17 (a)). There is also a large region of high winds above 4 km, associated with the DI. The low-level peak is part of a larger region of high winds (>40 ms^{-1}) which extends down from the large mid-level peak of the DI. The dropsonde-WRF comparison of wind speed shows very good similarities. The large region of high winds between 56°N and 57°N is clearly visible in the WRF model (Figure 4.17 (b)). However, there are some inconsistencies; the largest magnitudes are slightly higher in altitude, at around 2 km, than those in the dropsondes. The large region of high wind magnitudes between 56° and 57°N is also lower in wind speed than the observations. The rapid decrease in wind speeds to the north of 57°N is captured in the WRF simulation. However, beyond 58°N, the WRF winds are weaker than those in the dropsonde section. In general, the WRF wind features are located more southwards than those in the dropsonde section. This is consistent with the slight southward shift in the WRF modelled cyclone shown in Figure 4.6. At the southern extent of the section, another region of winds stretching from 2 km altitude up and northwards towards the intrusion which is associated with the cold front. Again this is captured well in the WRF model, with a step in altitude visible at 3 km close to the edge of the section, albeit with lower wind speeds than in the dropsonde section.

The strong low-level wind region in the dropsonde sections and the WRF sections may be indicative of a CCB air-stream wrapping around the BBF. The winds above this are likely to have different origins and may constitute SJ features that are descending towards the surface.

The intermittent black lines in the dropsonde figures show the cloud top as determined from the aircraft on-board lidar. For comparison the white lines in the WRF plots show a cloud mixing ratio

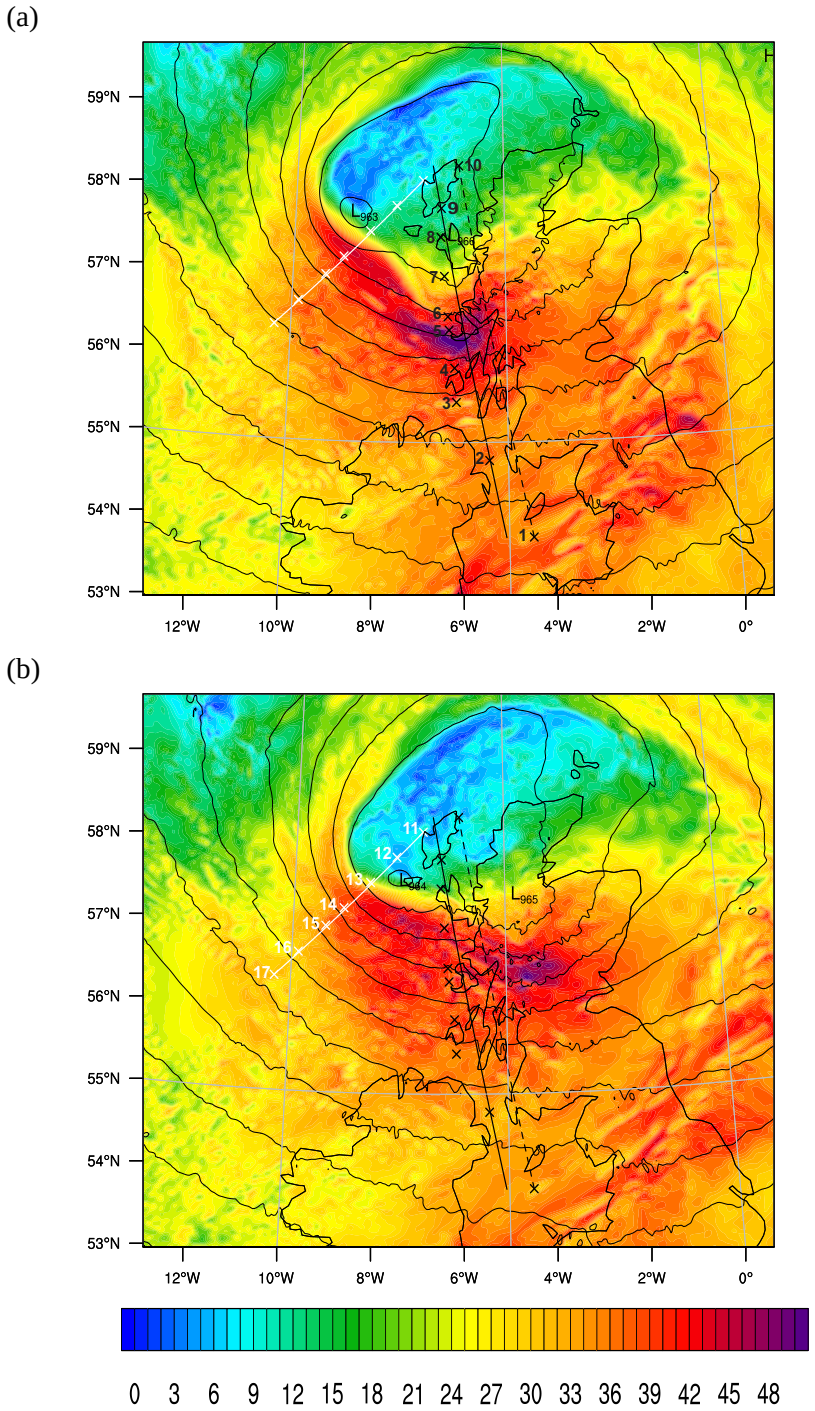

FIGURE 4.16: 780 hPa wind speed (shading and SLP (black lines) at (a) 1200 UTC and (b) 1300 UTC. Black (1-10) and white (11-17) crosses show dropsonde release locations for legs 1 and 2 respectively. Solid black (white) lines show the WRF section locations for leg 1 (2). Dashed black line shows the location of the model section used by Martínez-Alvarado et al. (2014)

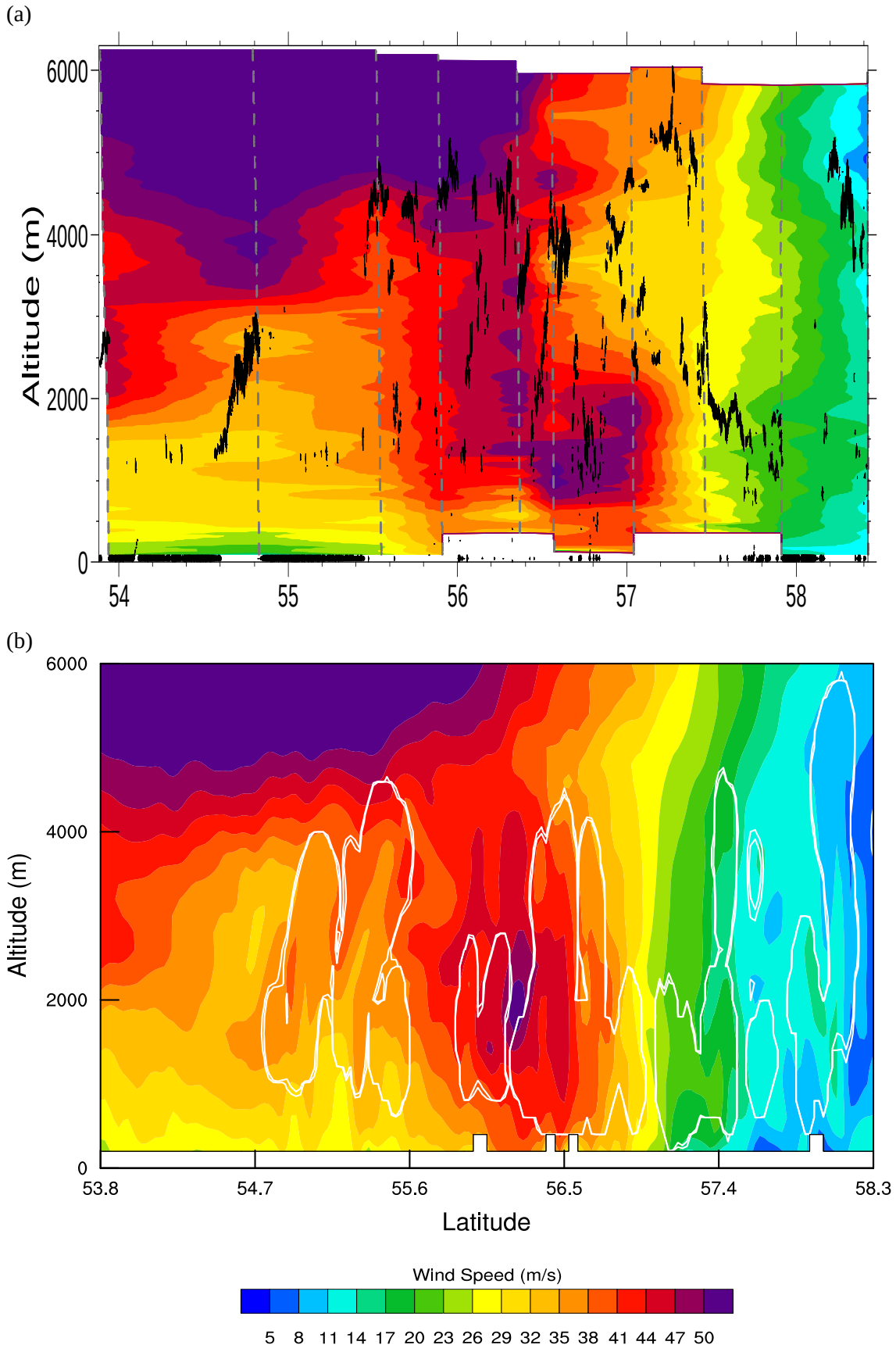

FIGURE 4.17: Top: Dropsonde section interpolated from dropsonde Leg 1 (Sondes 1-10, Figure 4.16 (a)) showing windspeed (shading) and lidar cloud tops (black peaks). Bottom: WRF simulated wind speed (shading) section for Leg 1 (black solid line Figure 4.16 (a)) at 1200 UTC with cloud mixing ratio (white lines at $1x10^{-7}$ & $2x10^{-7}$ gkg^{-1}) to indicate cloud extent.

(cloud ice + cloud water) of 1x10^{-7}-2x10^{-7}. To the southern end of the dropsonde section there is little cloud, with occasional signals near 1 km. Only one region of higher cloud can be seen near 54.8°N, which extends to ~3 km in altitude. The WRF clouds on this southern part of the leg show reasonable agreement with the lidar clouds. There is little cloud south of 55°N, beyond this however there is constant cloud until ~55.6°N, most of which is not seen in the lidar. From 55.5°N there are numerous high peaks (2-5 km) in the cloud in both the WRF model and lidar data, although the modelled cloud does not reach quite the same altitudes. In between the peaks, regions of lower cloud tops and no cloud are indicated by the lidar. Although WRF does not capture the clear regions it does show differing cloud top heights. From 57°N to the northward extent of the section the lidar shows a couple of large peaks with some lower cloud. Again this is relatively well captured in the model albeit with some overestimation of the low cloud.

The obvious feature of the θ_e section (Figure 4.18 (a)) is the region of low temperatures (~290 K) between 55° and 56.2°N, the most prominent region of which stretches from 1.5 km to 4 km altitude. Temperatures of >296 K also extend to the surface between 56°N and 57°N to the edge of the BBF at 57°N. The highest winds shown in Figure 4.18 (a), reside in this area of largely neutral stability. Cooler temperatures also stretch south towards the cold front between 1 km and 2 km. In the WRF section (Figure 4.18 (b)) the cold region between 55°N and 56°N is captured, between 2000 m and 4000 m, but not below this. The WRF section shows warm low-level temperatures between 56°N and 57.5°N, reaching over 300 K around 57°N. This is not seen in the dropsonde section although some warmer low-level temperatures are visible to the northernmost region of the section. At 56.5°N in the WRF section a vertical region of warmer air (296-300 K) is apparent, effectively marking the boundary between the high winds and the slack cyclone centre shown in Figure 4.17 (b). In the dropsonde section a warmer region is apparent above 3.5 km at 56.6°N, with a similar temperature region at 57.4°N in the lowest 2.5 km. These regions again largely bound the northern edge of the highest winds, demarcating the transition from the frontal region to the slack cyclone centre.

The wind fields in Figure 4.17 and θ_e in Figure 4.18 can be compared to the UM simulation shown in Figure 4 (b) in Martínez-Alvarado et al. (2014), reproduced in Figure 4.19 (a). The vertical region of high winds around 56.5°N is overestimated in the UM compared to the dropsonde section (see their Figure 4 (a)). This is the opposite of the slight underestimation of the winds shown here in the WRF model. The UM simulation also overestimates the extent of the high winds (>40 ms^{-1}) stretching to the south from ~56°N. The region of ~30 ms^{-1} winds extending to 3 km altitude at

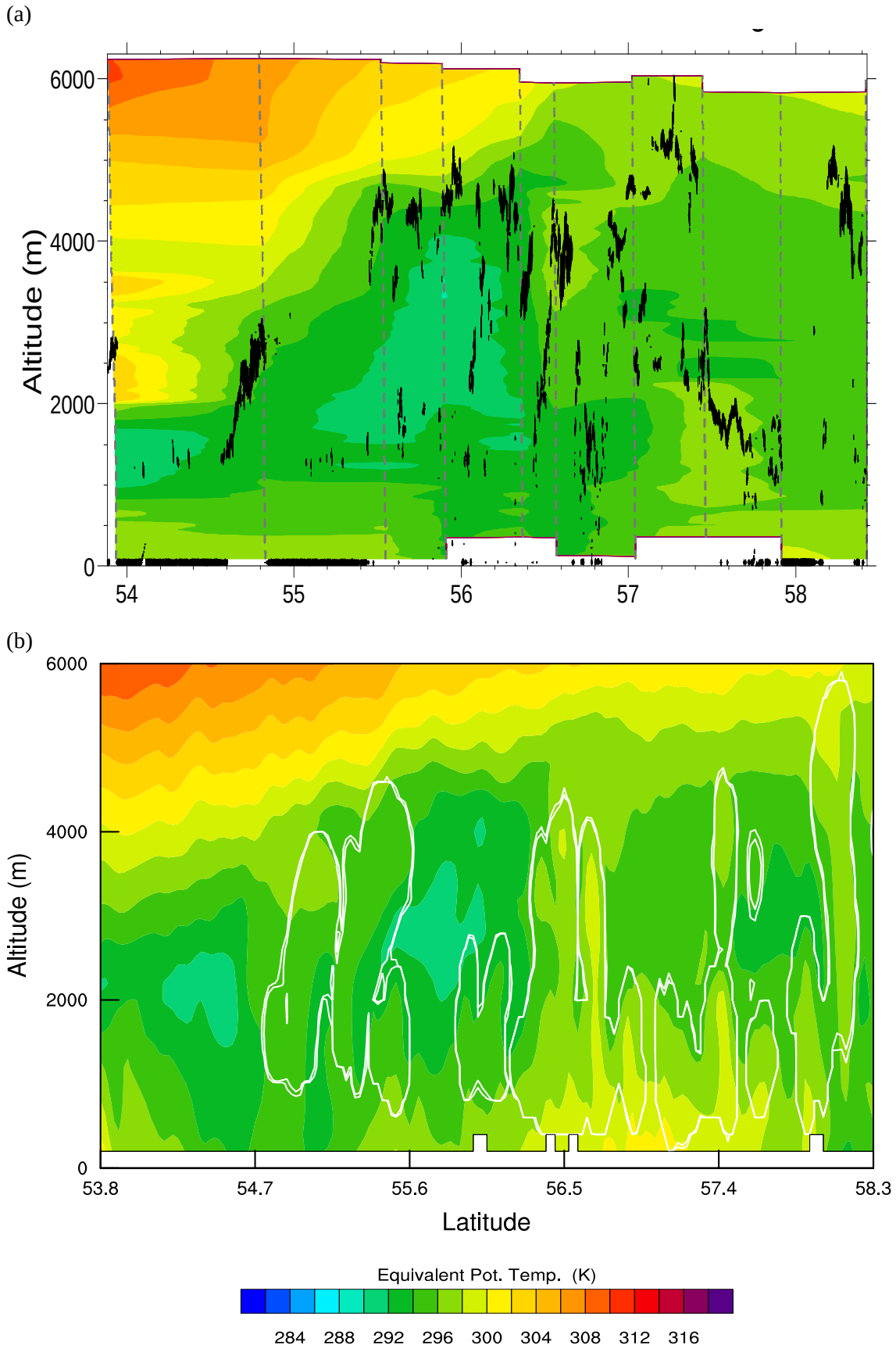

FIGURE 4.18: As Figure 4.17 but with shading showing θ_e (K).

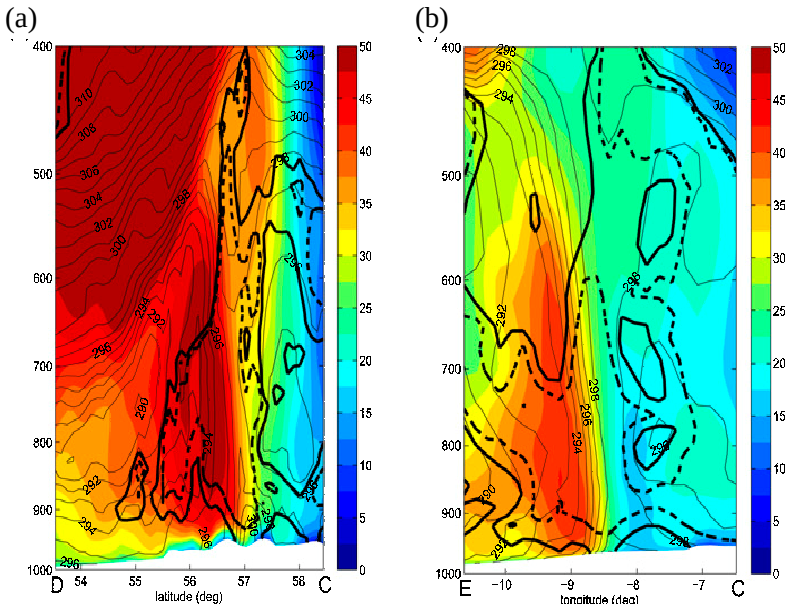

FIGURE 4.19: Figures 4 (b) and (d) (noted here as (a) and (b), respectively) from Martínez-Alvarado et al. (2014). UM Model sections for dropsonde legs 1 (a) and 2 (b). Color shades represent horizontal wind speed (ms^{-1}); thin lines show equivalent potential temperature, with a separation of 1 K; and solid (dashed) bold contours show 80% (90%) relative humidity with respect to ice.

55°N is also not well captured. However, the ground-ward extent of the DI is captured better in the UM than in the WRF simulation.

It is notable that the clouds are located much further north in the UM simulation, with large high clouds occurring north of the frontal zone. The overestimation of the clouds is also shown in the WRF simulation, however, the clouds to the south of 56°N are better represented in the WRF simulation than the UM

4.2.6.2 Dropsonde Leg 2

The second dropsonde leg extends from the cyclone centre south-west towards the Atlantic Ocean (Figure 4.16 (b)). This leg passes through the CCB region, although the model predicts the strongest winds have passed eastwards by this time. The dropsonde section shows a low-level peak in wind speeds at ~57.25°N on the edge of the frontal region (Figure 4.20 (a)). To the east of the low-level peak the winds drop rapidly towards the centre of the low. However the dropsonde spacing here means that the exact structure appears to be unresolved. Westwards, at around 2 km altitude the higher winds (<35 ms^{-1}) are present until the edge of the section. This whole region

of higher winds extends to around 4 km in height. A second, lesser, wind speed peak is present at 3 km altitude, 57°N just above the lower-level highs winds below 2 km.

The WRF plot shows some good agreement with the pattern of wind speeds, although the magnitudes are, generally, somewhat underestimated (Figure 4.20 (b)). The location of the frontal divide between the higher winds south of the BBF and the slack cyclone centre region is well captured with the WRF model showing this at ~57.6°N compared to 57.5°N in the dropsondes. Although the large region of >30 ms^{-1} winds is fairly well captured the magnitudes of the highest winds are lower in the WRF section. The cyclone centre also exhibits slower winds speeds than shown in the dropsonde section.

Figure 4.21 shows the same section as Figure 4.20 (b) but 30 minutes earlier at 1230 UTC. This section shows a better resemblance to the dropsonde section. At this earlier time the magnitude of the peak wind is close to that in the dropsonde section, although the peak is marginally too high in altitude. The areas of winds above 40 ms^{-1} do not extend as far south as the dropsonde section. These magnitudes are present to ~56.7°N in the dropsonde section whereas the WRF section shows wind speeds 5-10 ms^{-1} lower than these. Although the magnitudes are somewhat lower in the WRF section, the shape of the >25 ms^{-1} region compares well to that in the dropsondes, and the region of lower winds above 4 km to the south of the section is also captured. Although the low-level winds in the cyclone centre are again too low they are closer to those shown in the dropsondes than the 1300 UTC plot (Figure 4.20 (b)).

The lidar data from Figure 4.20 (a) suggests that the aircraft is in cloud for much of this leg, particularly between 57°N and 57.5°N. This is corroborated by the extent of the cloud in the WRF model section which extends beyond 6 km, indicative of the the frontal motion (Figure 4.21). Towards the centre of the low the lidar shows some broken cloud along with some mid- to high-level peaks. The WRF model seems to over-predict the cloud extent here similarly to the leg 1 sections.

Compared to the UM section of Martínez-Alvarado et al. (2014) the WRF section seems to compare well. The UM also seems to have a somewhat thinner more vertically elongated wind speed maximum similar to the WRF section. Unlike the WRF simulation however, the highest winds are located to the south (west) of those shown in the dropsonde section. The contouring on the UM plot makes any more detail in the highest wind region difficult to distinguish. Again in the UM the

clouds are over-predicted in the slack cyclone centre region and under-predicts the cloud height around the high-wind region.

Figure 4.22 shows the dropsonde and WRF leg 2 sections of θ_e. The dropsonde section shows distinct regions of θ_e. To the southern end of the plot a region of lower θ_e values (<290 K) is evident from ~1 km to 5 km altitude, extending from ~56.6°N to the edge of the section. The values gradually increase at all levels northwards until around 56.9°N where warmer air can be seen at both higher-levels and close to the surface. By 57.2°N values of 294 K extend from 6 km down to ~3 km, this region extends from here to the northern end of the plot. From 57.2°N and northwards there is a layer of 292 K θ_e between ~1-3.5 km. Below this another region of 294 K stretches northwards from ~57°N, within this a region of >298 K is centred around 57.6°N close to the surface.

The WRF section (Figure 4.22 (b)) shows a similar cold region between 1 and 5 km at the southern extent of the section. Between 2 and 4 km this extends around 0.1° further north than the region shown in the sections. Beyond this the θ_e field looks largely similar to the dropsonde section until around 57.1°N. From here northwards the WRF section is consistently around 4 K warmer then the dropsonde section. The structure of the θ_e is still similar despite this warm bias. This includes the band of cooler air extending from 57.4°N to 68.2°N, albeit centred ~500m lower than shown by the dropsondes. Additional structure shown in the WRF simulation here may be realistic but missed by the relatively sparse resolution of the dropsondes. This band does not appear to be as well represented in the corresponding UM section shown by Martínez-Alvarado et al. (2014), where it appears as a smaller isolated region close to the cyclone centre. A region of warmer θ_e temperatures at the surface are also seen around 57.5°N.

Unlike the wind speed sections, the WRF θ_e section at 1230 UTC (not shown) does not show a significant improvement in it's comparison to the dropsondes. This suggests a slight disparity between the evolution of the thermal structure and wind speeds when compared to that in the dropsonde sections. However, in general the key features of the storm are captured by the model

4.3 Summary

This study is, principally, a modelling study; therefore a full quantitative observation-model validation is beyond the scope of this thesis. However, to have confidence in the model results, it is

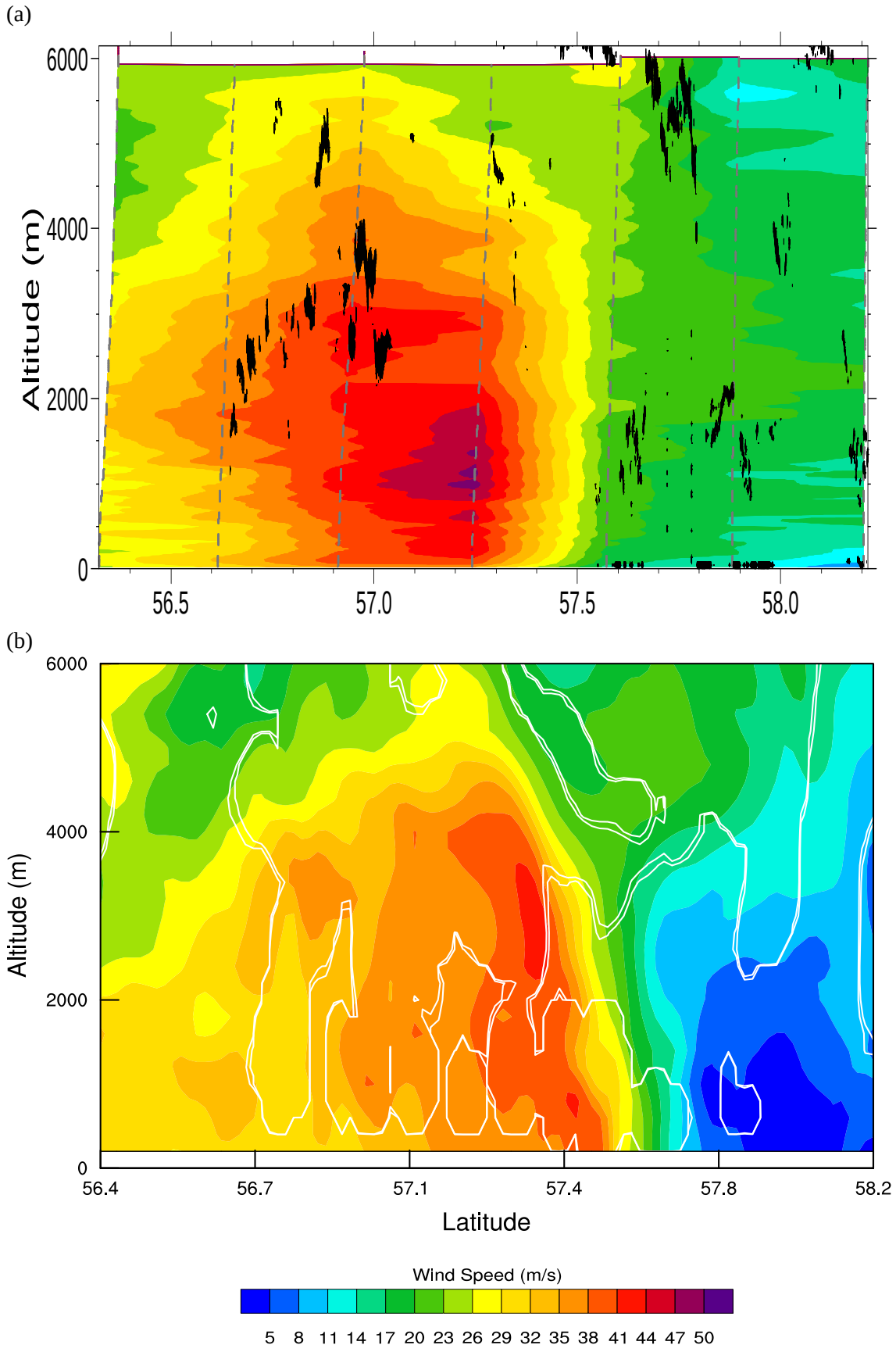

FIGURE 4.20: As Figure 4.17 but for dropsonde Leg 2 at 1300 UTC.

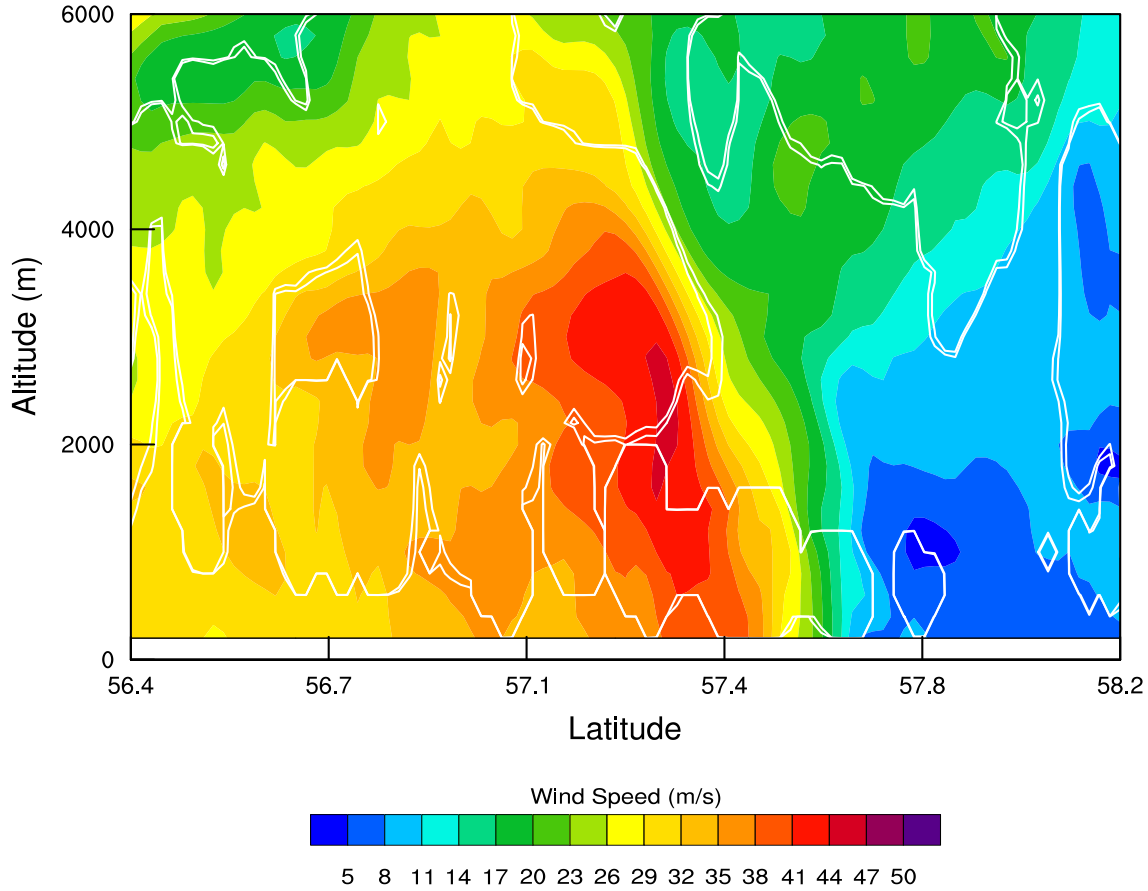

FIGURE 4.21: As Figure 4.20 but at 1230 UTC.

important to compare them to observations. A range of routinely collected observations, such as radar and satellite images, are used, along with the unique observations collected as part of the DIAMET campaign. Overall, the model does a good job of recreating the storm and it's features. As shown by Smart and Browning (2014) the WRF model has the ability to recreate sting jet storms with good accuracy depending on the initial conditions. The WRF simulation compares fairly well with the section from the previous UM-based study on this storm by Martínez-Alvarado et al. (2014).

The storm track and position are generally well replicated, although at times there is a southward shift and longitudinal stretching of the storm these should not have any major effect on the processes for further analysis. Indeed this southward shift in not particularly obvious in the dropsonde sections which give some of the best information on the internal structure of the structure of the storm. Small differences in the shape of the cloud head compared to satellite images, and frontal rain compared to radar observations are noted. In general, however, these inconsistencies are relatively small.

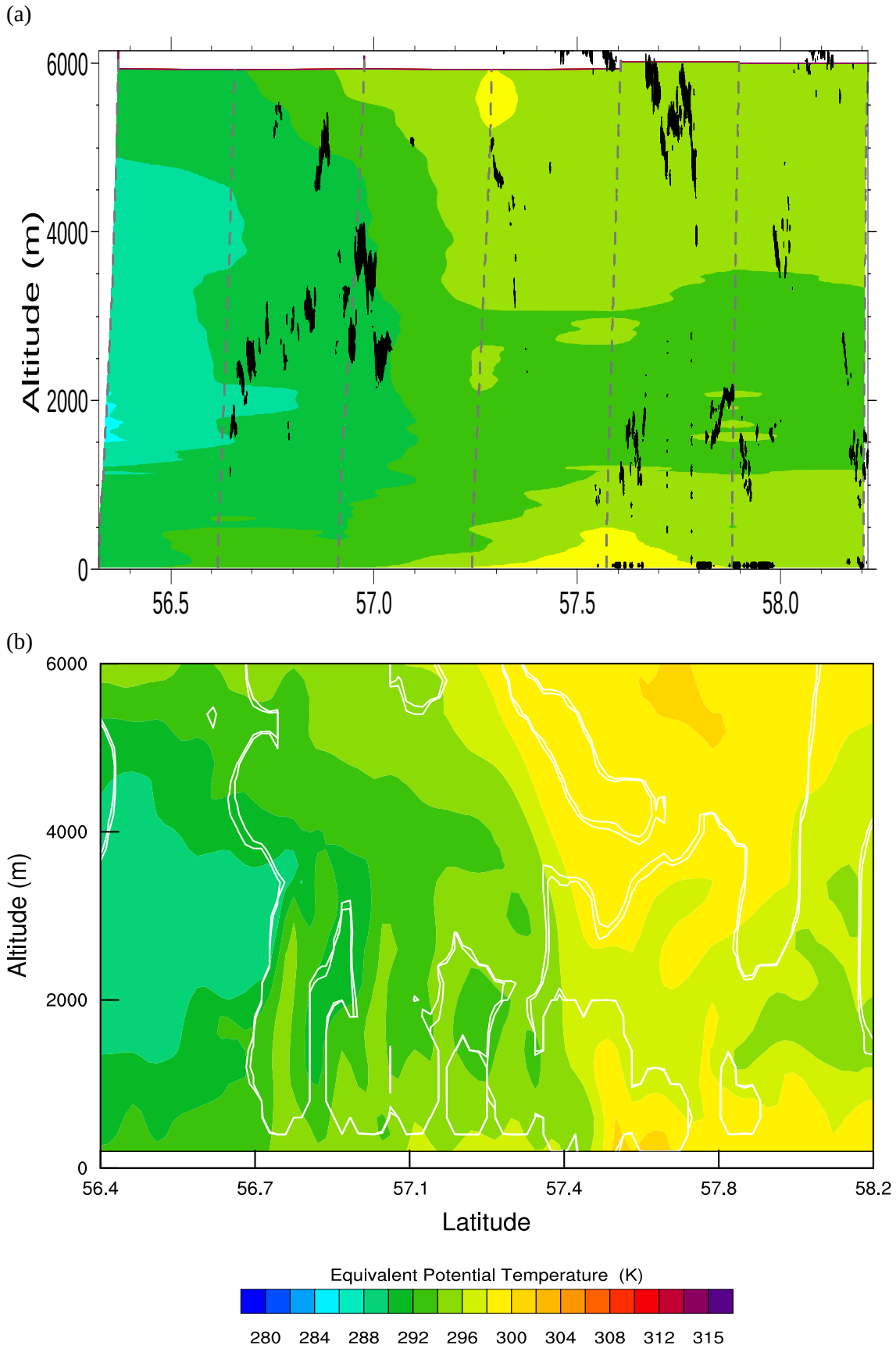

FIGURE 4.22: As Figure 4.18 but for dropsonde Leg 2

The dropsonde sections provide a useful tool to evaluate the features of the cyclone, however, as mentioned in the text there are caveats to be considered when comparing these observations to the model sections. These show generally good agreement with the model in both the wind speed and θ_e fields. Some discrepancies exist particularly in in the leg 2 comparisons. These are generally related to an over-prediction of the θ_e and some under-prediction of the wind speeds. The lidar comparisons to the modelled clouds are also good, albeit with some variation particularly towards the cyclone centre. Overall however, the general spatial pattern of the variables is shown to be well captured by the model.

As with all studies of this kind the model will not be an exact recreation of reality, but there is high confidence that the important processes and structures are recreated here.

Chapter 5

Modelled Storm Dynamics and Processes

This chapter analyses the dynamics and microphysics of the Cyclone Friedhelm control simulations and defines the key features within them. This then provides a framework with which to analyse the sensitivity tests presented in Chapter 6.

5.1 Identification of Regions of Interest

As shown in the Chapter 4 (Section 4.2.3) much of the development of the wind field occurs between 0700 UTC and 1200 UTC on the morning of the 8^{th} December. The regions of highest winds between 1000 and 1200 UTC are particularly intense, warranting specific attention. Investigating the strong winds during this period sees the added benefit of limited interaction between the storm and the land surface. Radial cross-sections extending out through the BBF are used in order to identify specific areas of high winds for further analysis and to provide a clearer 3-D picture of the storm. The radials from 1000, 1100 and 1200 UTC can be used to identify the levels and distribution of regions of interest. The earlier radials can give insight to the development of these regions. Figure 5.1 shows the locations of cross-sections taken at 1000, 1100 and 1200 UTC. The cross-section locations, marked A-A' to H-H' on each plot, are specifically selected at each time in order to examine both the strong wind regions as well as the upstream flow.

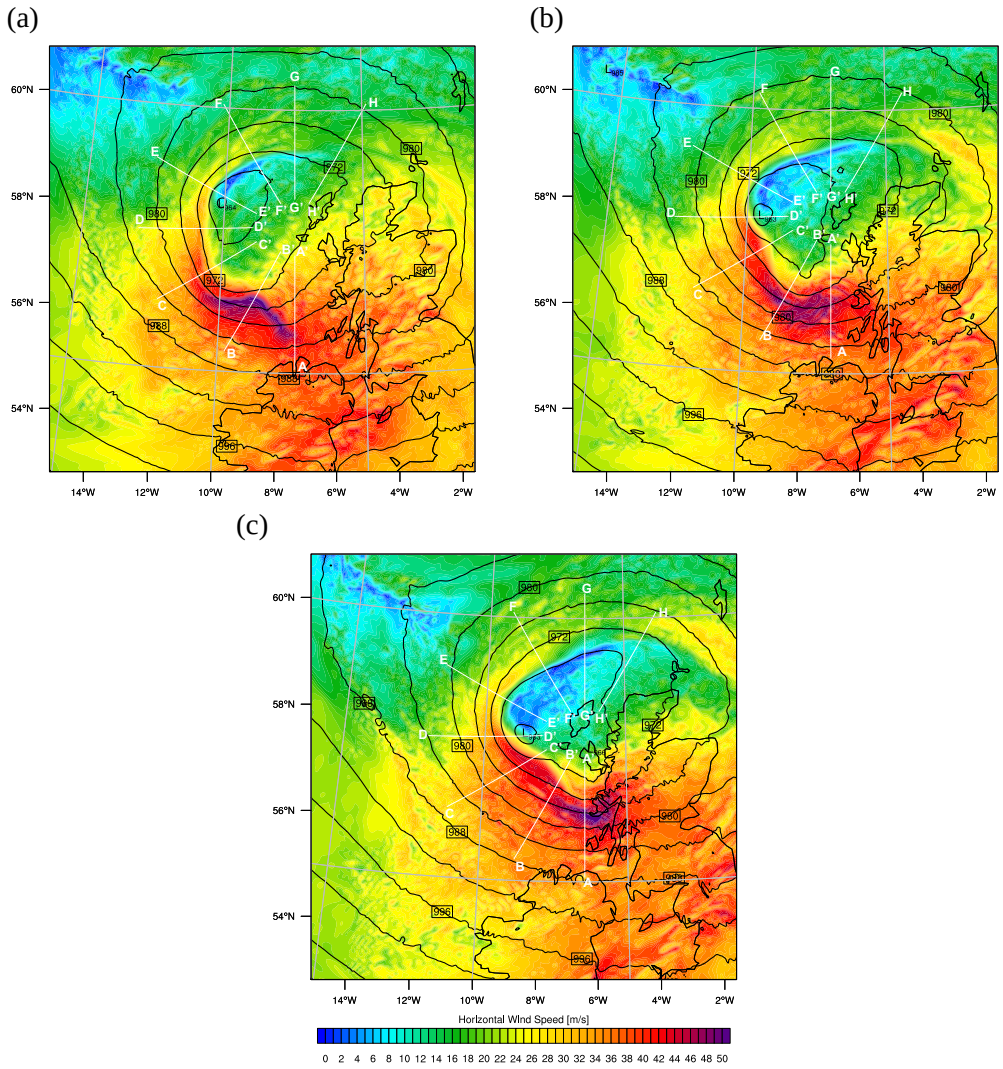

FIGURE 5.1: Wind speed (shaded) at 780 hPa and SLP (black contours) at (a) 1000 UTC, (b) 1100 UTC and (c) 1200 UTC 8th December. White lines labelled A-A' to H-H' indicate locations of cross-sections. All cross-sections consist of 80 horizontal grid points (240 km) in length.

Figure 5.2 shows the cross-sections A-A', B-B' and C-C' at 1000 UTC, from the locations in Figure 5.1 (a). These sections can be seen crossing some of the strongest wind regions to the south and south-east of the storm. Section B-B' crosses through the small region of wind speeds >50 ms^{-1}. This region can be clearly seen in the cross section plot (Figure 5.2 (b)) at around 56°N extending from 800 hPa to 730 hPa. This maximum is within a broader region of intense winds (>40 ms^{-1}) extending to the south-west and upwards. These strongest winds are bounded underneath by a level of cloud that stretches across a large portion of the cross section. Some high winds do extend into and below the cloud, but these generally have speeds below 40 ms^{-1}. There is also a region of ascent directly below the highest wind region which may be inhibiting the high

momentum from transferring towards the ground. The section C-C' (Figure 5.2 (a)), is located upstream of the highest wind region and shows quite different characteristics. Here the highest winds are lighter, generally between 35 and 40 ms^{-1}. The high winds here are located next to the frontal cloud which stretches from the near surface around 10.6°W up to 550 hPa at 11°W. The winds are largely located to the cold (western) side of the frontal cloud shown by the RH (white) and cloud (cloud water + cloud ice, grey) contours. At low-levels (950-850 hPa) high wind regions (above 40 ms^{-1}) extend eastwards within the cloud, whilst at approximately 700 hPa, the winds extend further westwards. The upper level winds are limited in vertical extent by the cloud anvil which can be seen in the grey cloud lines. Unsurprisingly the frontal cloud is dominated by ascending motion; to the west and largely concurrent with the highest winds, is a region of descent. Figure 5.2 (c) shows cross section A-A', downstream of C-C' and B-B'. The winds are marginally less intense here with the cross section passing just to the east of the "ribbon" of highest winds shown in Figure 5.1 (a). However the region of strong mid- and lower-level winds are extensive, stretching from the southern limit of the section to 56.5° N, and still relatively strong (>38 ms^{-1}). The strongest region is located at 55.6° N, between 800 and 725 hPa, with speed of 46 ms^{-1}. This region is also associated with a region of descent and a break in the cloud. Below this the higher magnitude winds extend down towards the surface and produce the strongest surface level winds in these cross-sections.

At 1100 UTC, Figure 5.1 (b) shows that the "ribbon" of high winds shown at 1000 UTC is no longer present. Cross-section B-B' passes through a small region of the most intense winds, A-A' passes through the eastern edge of a region of slightly less intense winds, while C-C' passes through the broad, less intense region upstream. Cross-section C-C' (Figure 5.3 (a)) shows the broad region of high winds (>30 ms^{-1}) extending westwards from 9.1°W. Within this, there is an area of stronger winds showing values above 35 ms^{-1}. The most intense regions are located between 9.5°W and 10.5°W, extending from 850 hPa in altitude up to 600 hPa. The highest low-level winds at 9.7°W and 10.4°W are both associated with descending air in gaps between the clouds. Figure 5.3 (b) shows more intense winds than the upstream section, C-C'. The main wind feature is a region of 46 ms^{-1} speeds at 56.4°N, between 850 and 750 hPa. This feature sits on the edge of a gap within the cloud and is, like many of the other high wind regions, co-located with a region of descent. There are numerous regions of ascent and descent around this region. Further downstream, section A-A' (Figure 5.3 (c)) shows a larger region of 46 ms^{-1} winds. The two maximum regions within this area are located on two levels: a lower region at 750 hPa and a higher region at 625 hPa. The region of 46 ms^{-1} winds is again limited by cloud below,

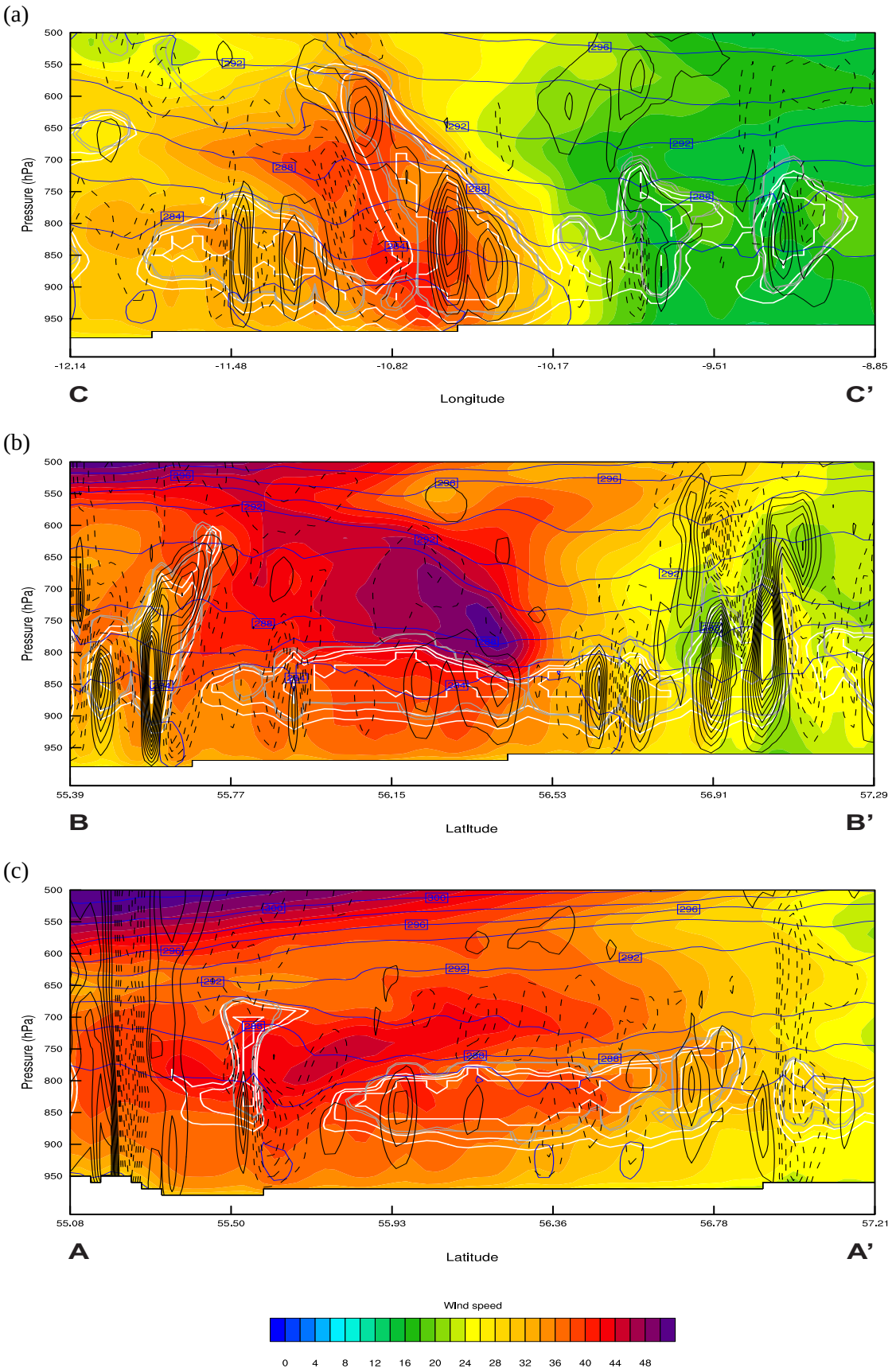

FIGURE 5.2: Cross-sections (a) C-C', (b) B-B' and (c) A-A' at 1000 UTC as marked on Figure 5.1 (a). Wind speed (shaded, ms^{-1}), θ_e (every 2 K, solid blue lines), w (every 0.1 ms^{-1}, negative dashed and zero suppressed, black lines), RH (90-100% every 5%, solid white lines) and cloud (0.005 g kg^{-1}, solid grey lines). Note that (a) is plotted against longitude, while (b) and (c) are plotted against latitude to account for the relative orientation of each cross-section as shown in Figure 5.1

although values of 36 ms^{-1} extend down close to the surface, underneath the cloud layer. The highest surface winds, at 56.7°N and 56.4°N, are again located beneath breaks in the cloud and descending motion, which allows the higher wind speeds aloft to be brought towards the ground.

By 1200 UTC the maximum wind speed region in Figure 5.1 (c) is bisected by the cross-section A-A' just to the west of Scotland. Figure 5.4 shows this section as well as the upstream sections B-B' and D-D'. In section D-D' (Figure 5.4 (a)) the highest winds reside in the frontal region at 9.5°W. There are peaks at 750-625 hPa above the cloud layer, and at 950 hPa below the cloud. The majority of this region is undergoing descent. To the west of the cross-section two regions of strong convection can be seen associated with higher cloud but much lower wind speeds. Section B-B' (Figure 5.4 (b)) shows a much broader region of winds above 38 ms^{-1} and maximum of 46 ms^{-1} at 56.7°N and 56.5°N. The regions of intense winds (>50 ms^{-1}) are located at 56.3°N in section A-A' (Figure 5.4 (c)). Occurring in a region of descent with convective cloud to the south and north, the altitude is again bound by cloud underneath.

Figures 5.2, 5.3 and 5.4 show a number of interesting features for further investigation. Regions of high winds are shown in numerous areas at different times. Low-level winds are the key area of investigation for this study; a trajectory analysis is presented in Section 5.2, in which the levels 780, 850 and 925 hPa are chosen for trajectory initiation. These levels are where a number of the low-level features occur in the cross-sections. Some patterns are already evident from the cross-sections shown in Figures 5.2-5.4. On a number of the cross-sections the highest winds (often >46 ms^{-1}) are located in dry regions, above, below or in-between the cloud. In many cases the ground-ward extent of the highest winds is limited by cloud below. Descending motion is also a common theme in the highest wind regions. Gaps in the low-level cloud are also often the location for the highest surface winds, allowing higher momentum air to be mixed downwards. The 780 hPa level is particularly chosen as this is the region of the very highest winds in the cross-sections. The lower levels obviously have greater implications for the surface conditions as well as falling within the expected vertical extend for any CCB present.

5.2 Wind Speed Trajectories, Diagnostics and Analysis

Trajectory analysis allows the evolution of the air parcels and the processes acting upon them to be investigated. Following the identification of levels from the cross-sections in Section 5.1, trajectories were initiated from the maximum wind speed location on each of the 780 hPa, 850 hPa

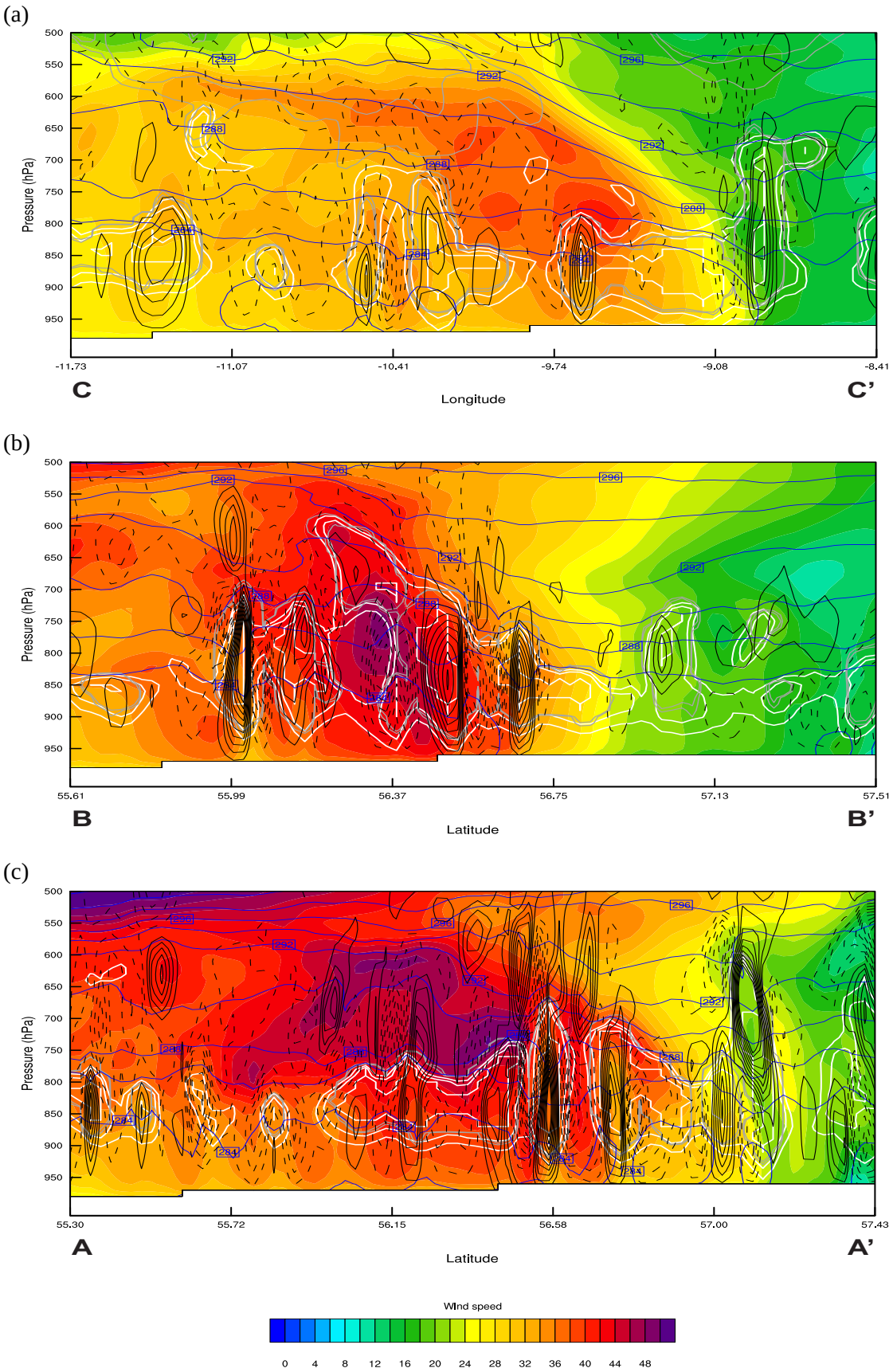

FIGURE 5.3: Cross-sections (a) C-C', (b) B-B' and (c) A-A' at 1100 UTC as marked on Figure 5.1 (a). Contours and axes as Figure 5.2.

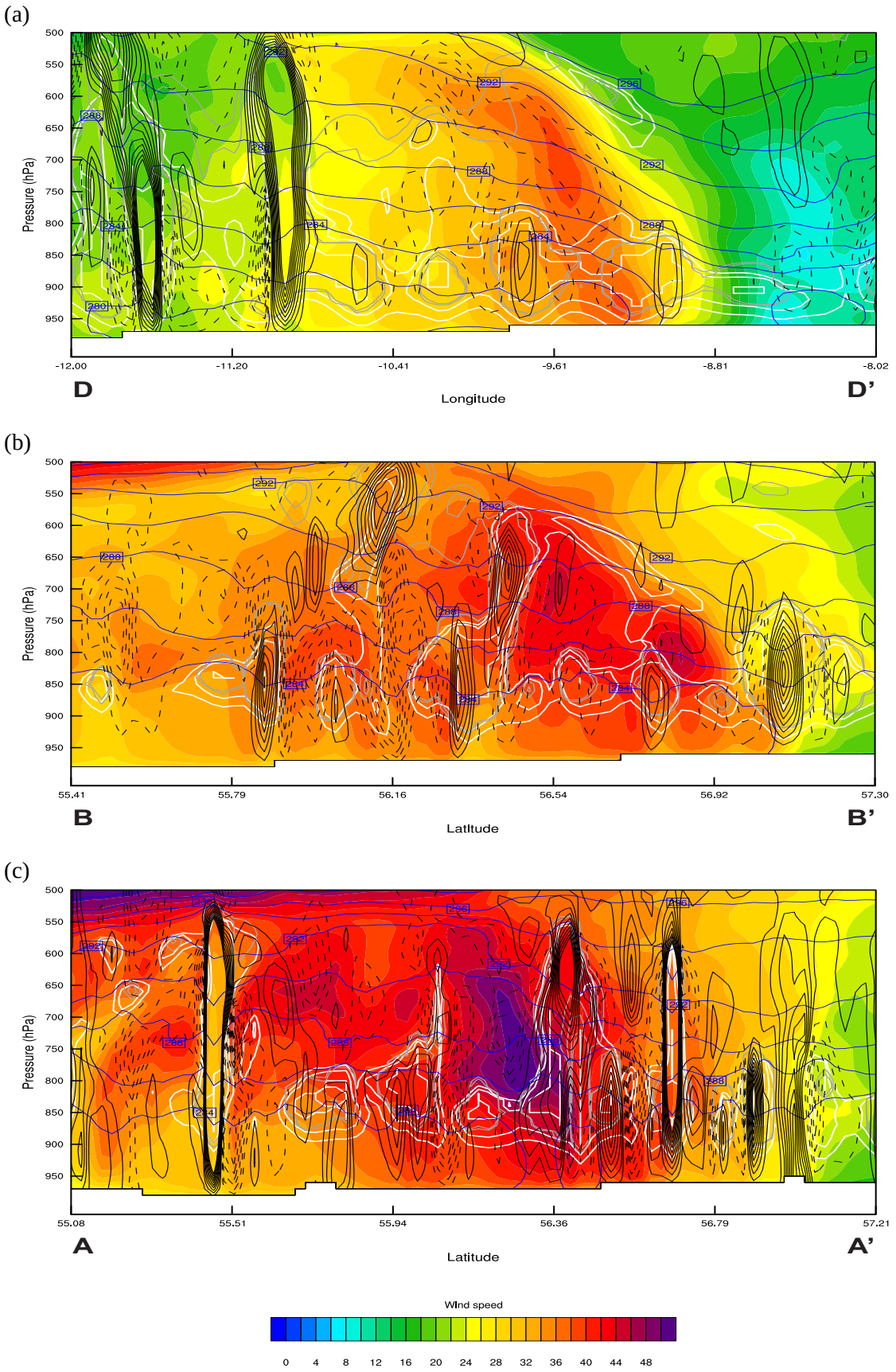

FIGURE 5.4: Cross Sections (a) D-D', (b) B-B' and (c) A-A' at 1200 UTC as marked on Figure 5.1 (a). Contours and axes as Figure 5.2.

TABLE 5.1: Maximum wind speed values and locations for trajectory initiation times and levels.

Level (hPa)	Time (UTC)	Wind Speed (ms^{-1})	Lat	Lon
780	1000	51.49	56.33	-8.68
	1100	49.62	56.33	-8.78
	1200	52.25	56.19	-6.06
850	1000	49.29	56.23	-8.44
	1100	49.90	56.33	-8.44
	1200	50.42	56.38	-6.69
925	1000	46.13	56.48	-10.01
	1100	47.03	56.36	-8.44
	1200	47.67	56.37	-6.56

and 925 hPa levels at 1000, 1100 and 1200 UTC, as summarised in Table 5.1. For clarity they will be named as tXXXX-YYY, where XXXX indicates the initiation time in UTC and YYY indicates the initiation level in hPa. 64 trajectories are started from a 12x12 km horizontal box around the point of interest. Diagnostics are calculated along these trajectories at each trajectory output time. A further description of the RIP trajectory program is presented in Chapter 3.

Figure 5.5 shows the evolution of the trajectory sets around the cyclone as it evolves from 0300 to 1500 UTC. Storm-relative trajectory plots are presented later in this section. The storm velocity for these plots is calculated from the difference in minimum SLP location at the start and end time of the trajectories (0000 UTC and 1000 UTC for the back trajectories, and 1000 UTC and 1600 UTC for the forward trajectories for a 1000 UTC trajectory initiation). However due to the evolution of the cyclone and the non-linear movement these values cause the storm-relative paths to appear slightly incorrectly. In particular the extension of the slack, low pressure centre to the north gives the impression of the trajectories crossing this region, instead of to the north of it. Therefore, the storm velocities are modified slightly to achieve storm-relative paths which better match the evolution shown in Figure 5.5. This highlights some of the potential pitfalls of assuming a steady-state or neglecting the overall evolution of the cyclone in analysis. Previous studies have used analysis of a single output time assuming that the structure will remain constant: although this may sometimes be the case, it cannot be assumed without further investigation.

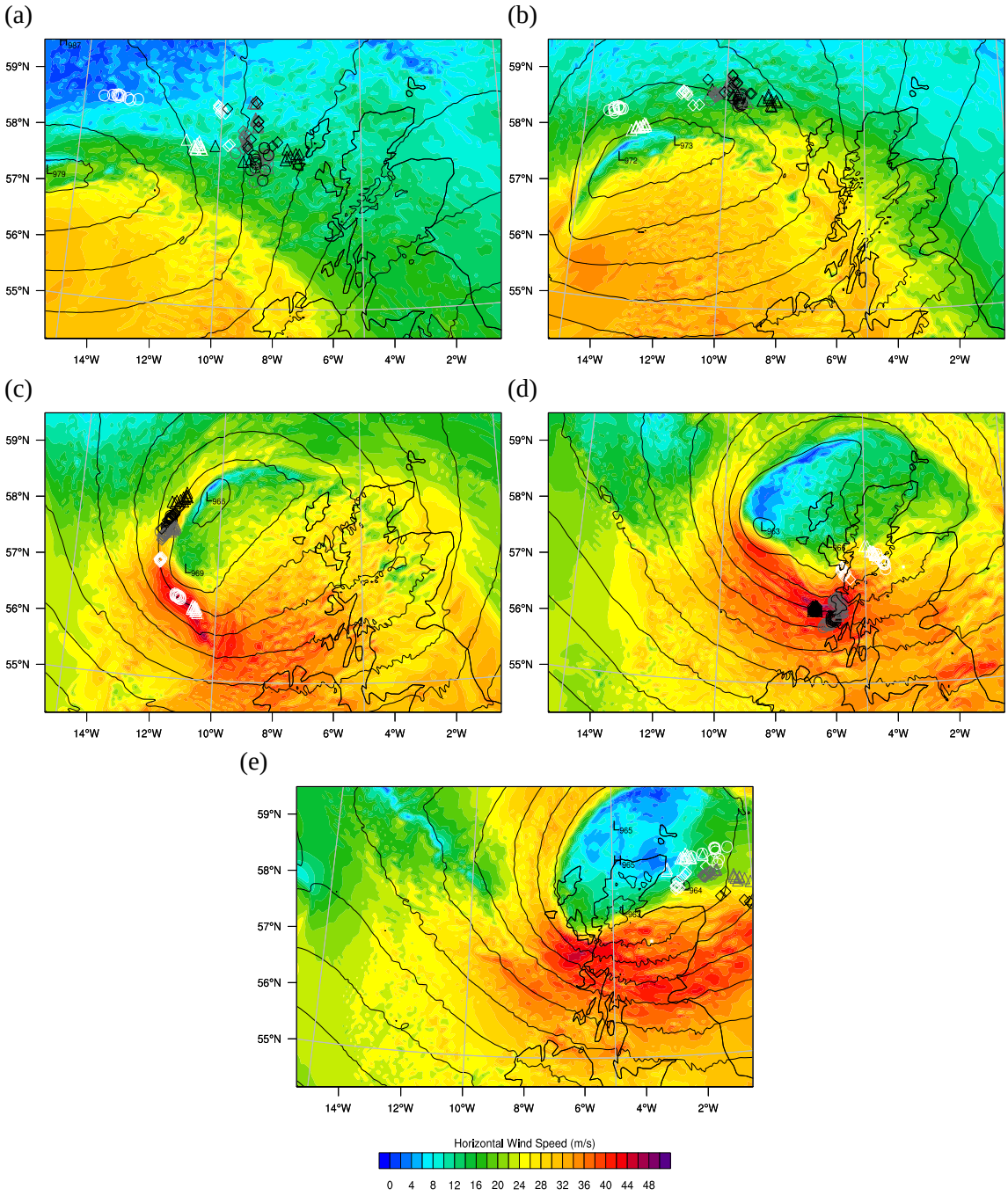

FIGURE 5.5: 850 hPa wind speed (shaded), SLP (black contours) and trajectory location shown every 3 hours from 0300 UTC to 1500 UTC ((a)-(e) respectively). White, gray and black markers indicate trajectory initialisation times of 1000, 1100 and 1200 UTC, respectively, while maker shapes indicate initialisation level: circles - 780 hPa, triangles - 850 hPa, diamonds - 925 hPa.

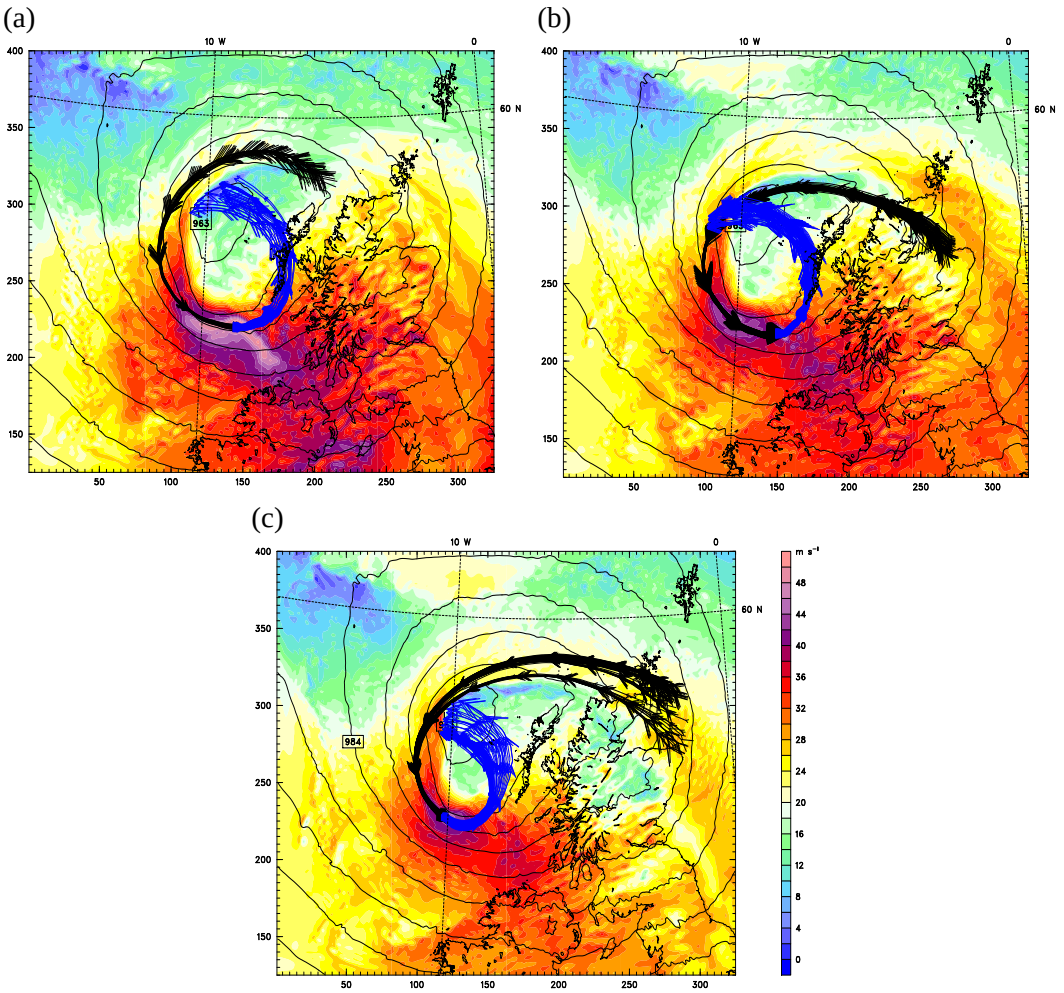

FIGURE 5.6: Storm relative trajectory paths for (a) t1000-780, (b) -850 and (c) -925 trajectories. Trajectory swarms are plotted over the horizontal wind speed on the level of trajectory initiation at 1000 UTC (filled contours, ms^{-1}) and SLP (black contours, every 4 hPa)

5.2.1 1000 UTC Trajectories

The storm relative paths of the t1000-780, -850 and -925 trajectories are shown in Figure 5.6 (a), (b) and (c) respectively. The paths of the trajectories are largely similar, with the parcels starting to the northern side of the low, before circulating around to the south by 1000 UTC. The forward trajectories then show the air spiralling into the centre of the system. Both the -780 and -850 trajectory swarms are initiated in the high wind "ribbon" to the south of the low, while the -925 trajectory initiation is further westward.

Figures 5.7, 5.8 and 5.9 show diagnostic time series for the t1000-780, -850 and -925 trajectories, respectively. The coloured lines indicate times of interest for each trajectory set. The colors are:

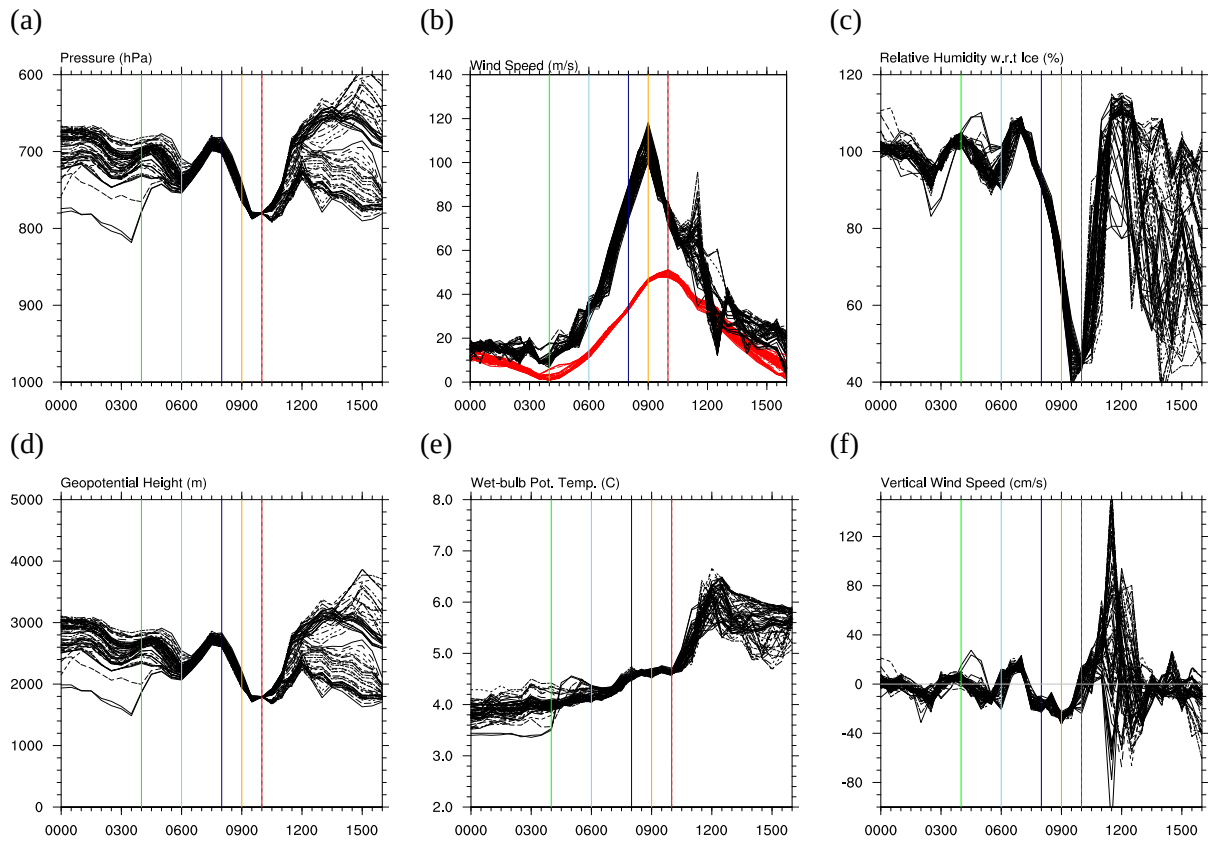

FIGURE 5.7: Diagnostics from the 64, t1000-780 trajectories: (a) Pressure (hPa), (b) horizontal wind speed (red) and geostrophic wind speed (black) (ms^{-1}), (c) RH with respect to ice (%), (d) Geopotential height (m), (e) θ_w, (f) vertical wind speed ($cm\ s^{-1}$). Coloured vertical lines represent times of interest for each trajectory: green - start of acceleration, light blue - start of ascent, navy - start of descent, orange - V_g maximum, red - wind speed maximum, grey, dashed - trajectory initiation time.

green - start of acceleration, light blue - start of ascent, navy - start of descent, orange - maximum V_g, red - wind speed maximum, grey (dashed) - trajectory initiation time.

The evolution of pressure and height are shown in Figures 5.7, 5.8 and 5.9, (a) and (d). There are some consistencies in behaviour between all the t1000 trajectories shown in these figures. The trajectories all undergo some descent in the 1-2 hours before the initiation time (dashed grey/red lines), having undergone some degree of ascent before that (light blue line). A period of strong ascent is also seen after the initiation time (dashed grey/red lines) in all the t1000- trajectories. Despite these similarities there are notable differences. The t1000-780 trajectories (Figure 5.7 (a) and (d)) are generally concentrated around 700 hPa for the first five hours of the trajectory analysis. By 0530 they have descended slightly to ~750 hPa (2200 m). At this time they undergo a two hour period of ascent (light blue line) back up to 690 hPa (2900 m), before rapidly descending (navy line) to 780 hPa (1800 m) at the initiation time, 1000 UTC (red/dashed-grey line). This descent is

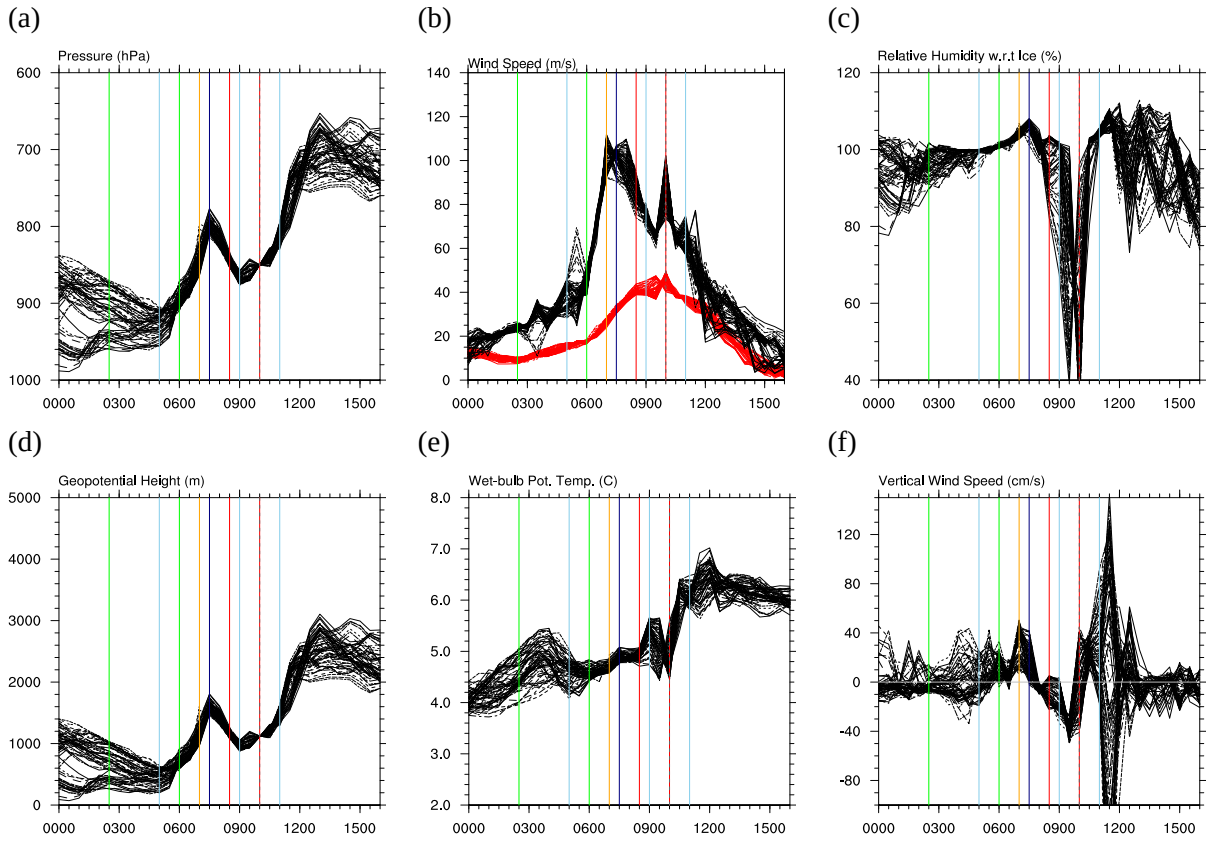

FIGURE 5.8: Diagnostics from the 64, t1000-850 trajectories: (a) Pressure (hPa), (b) horizontal wind speed (red) and geostrophic wind speed (black) (ms^{-1}), (c) RH with respect to ice (%), (d) Geopotential height (m), (e) θ_w, (f) vertical wind speed (cm s^{-1}). Coloured vertical lines represent times of interest for each trajectory: green - start of acceleration, light blue - start of ascent, navy - start of descent, orange - V_g maximum, red - wind speed maximum, grey, dashed - trajectory initiation time.

shorter and from a lower level than previous SJs have been recorded, however the rate of descent, at 1.25 Pa s^{-1}, is within the range given by Gray et al. (2011). Unlike the t1000-780 trajectories, the t1000-850 and t1000-925 ones initially start from low levels (Figures 5.8 and 5.9, (a) and (d), respectively). The t1000-850 plots show two initial air streams at 0000 UTC; one centered around 880 hPa and a smaller cluster at 960 hPa. By 0500 UTC these two streams have converged at 940 hPa (light blue line) and begin a 3.5 hour ascent. A 1.5 hour period of descent (navy line) to 860 hPa, followed by a small ascent (light blue line) takes the trajectories to the initiation point at 850 hPa. Following this there is rapid ascent as seen in the 780 and 925 trajectories. The t1000-925 trajectories show a more similar evolution to the -850 trajectories than the -780 ones, albeit at lower levels. The majority of the trajectories start below 900 hPa (1000 m), they converge before ascending at a similar level to the 850 hPa parcels, around 950 hPa, but around 3 hours later at 0800 UTC (light blue line). They then undergo a much more limited ascent to 880 hPa (navy line)

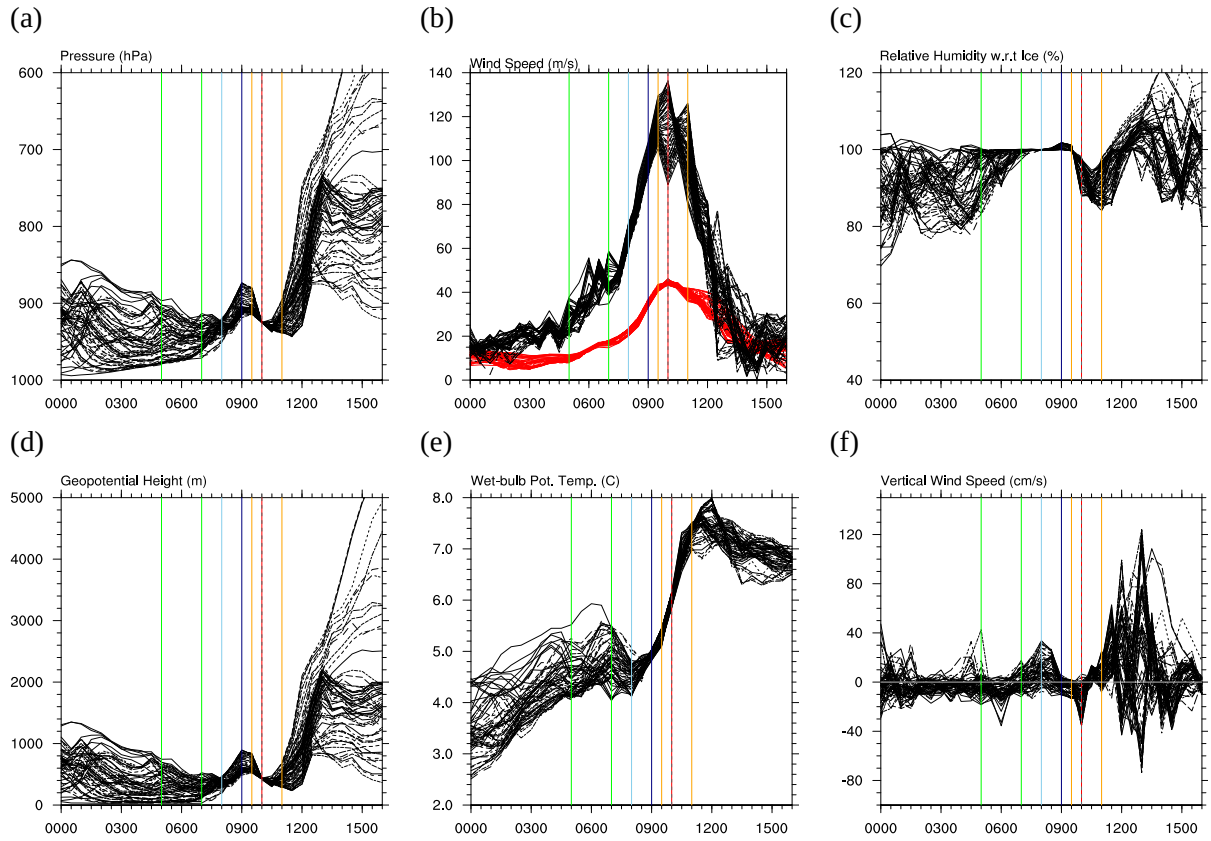

FIGURE 5.9: Diagnostics from the 64, t1000-925 trajectories: (a) Pressure (hPa), (b) horizontal wind speed (red) and geostrophic wind speed (black) (ms^{-1}), (c) RH with respect to ice (%), (d) Geopotential height (m), (e) θ_w, (f) vertical wind speed ($cm\ s^{-1}$). Coloured vertical lines represent times of interest for each trajectory: green - start of acceleration, light blue - start of ascent, navy - start of descent, orange - V_g maximum, red - wind speed maximum, grey, dashed - trajectory initiation time.

before descending to 925 hPa at 1000 UTC.

The evolution of wind speed is of key interest for this study. This is shown in Figures 5.7, 5.8 and 5.9 (b) in red, along with the geostrophic wind speed in black. The t1000-780 trajectories initially accelerate at 0400 UTC, indicated by the green line. This follows a period of deceleration to near zero wind speed from 0000 UTC. The trajectories begin to accelerate at around $2.5x10^{-3}$ ms^{-2} until 0900 UTC (orange line), then increase less quickly for a further hour, to the maximum at 1000 UTC (red line) before decreasing steadily over the rest of the time series. The slowing of the acceleration is at 0900 UTC coincident with the maximum in geostrophic wind speed (orange line). The maximum in the wind speeds occurs at the end of the rapid descent shown in Figures 5.7 (a) and (d). The t1000-850 trajectories show a slightly different evolution. Based on the gradient of the lines, there is an initial slow acceleration of $3.55x10^{-4}$ ms^{-2} from 0330 UTC (first green line) to 0600 UTC (second green line). This is followed by a quicker acceleration more akin to

the t1000-780 acceleration of $2.8\text{x}10^{-3}$ ms^{-2} until an initial peak at 0830 UTC (red line). The geostrophic wind for t1000-850 undergoes a similar two-stage acceleration, albeit starting earlier than the wind speed. The geostrophic wind speed shows a number of peaks between 0700 UTC and 1000 UTC. The first of these, indicated by the orange line, is the largest reaching up to 110 ms^{-1}; this does not include all the parcels however, with the rest going on to reach a slightly lesser peak at 0800 UTC. The geostrophic wind speed then rapidly decreases to 70 ms^{-1} at 0830 UTC before rapidly rising again at 1000 UTC (red/grey line) with a third peak reaching ~100 ms^{-1}. This pattern can be seen in a delayed reaction in the wind speed. An initial peak at 0830 UTC (red line) corresponds to the initial geostrophic peak at 0800 UTC, some of the trajectory wind speeds then rise further at 0930 UTC following the second geostrophic wind speed peak. The third wind speed peak is concurrent with the third geostrophic wind speed peak at 1000 UTC. The t1000-925 winds (Figure 5.9 (b)) show a similar two-stage acceleration to the -850 winds, however the initial acceleration is delayed until 0500 UTC (green line). This brief acceleration plateaus at 0630 UTC before mean acceleration of $1.7\text{x}10^{-3}$ ms^{-2} from 0700 UTC (second green line) until the maximum at 1000 UTC (red line). The t1000-925 trajectories record the highest geostrophic wind of the three t1000 trajectory sets with a maximum 135 ms^{-1} at 1000 UTC due to the stronger gradient in pressure at lower levels. However closer inspection of the plot suggests that only a subsection of the trajectories reach this peak, with a large number having peaked at 0930 UTC (orange line) before decreasing by 1000 UTC. A number of trajectories then increase in geostrophic wind speed again to ~120 ms^{-1} at 1100 UTC after which nearly all the trajectories see a rapid decline to below 20 ms^{-1} by 1400 UTC. The influence of the 1100 UTC (second orange line) geostrophic wind peak can be seen in the slowing of the deceleration in some of the wind speed trajectories between 1100 and 1300 UTC.

The delay between the maxima in geostrophic wind speed and actual wind speed is also present in the t1000-850 and -925 trajectories (Figures 5.8 and 5.9 (b)), albeit to different extents. This has implications for identifying the regions of highest winds from synoptic analysis charts as the highest winds may occur downstream of the highest pressure gradient. The horizontal winds all show a similar evolution to the geostrophic wind at each level but are significantly smaller in magnitude. Given the tight curvature and effects of friction at these lower levels this strong ageostrophic component is to be expected. The role of PGF and curvature will be investigated in more detail in Section 5.3.

Figures 5.7 (d), 5.8 (d), and 5.9 (d) show the RH with respect to ice (RH_i) along the trajectories.

From 0000 UTC to 0700 UTC the t1000-780 RH_i undulates between 90 and 110% as the parcels descend and ascend (Figure 5.7 (a)/(d)). Between 0700 UTC and 0930 UTC the parcels dry rapidly from 110% to 40% as they descend. The values then rise slightly to 45% by the time of the maximum winds at 1000 UTC (red/gray line). After this the parcels swiftly moisten again with many reaching saturation by 1130 UTC. This, in conjunction with the increased altitude discussed earlier indicate mixing into a region of convection. Some of the t1000-850 trajectories also show a reduction in RH_i as they descend from 0730 UTC to 0900 UTC. However, the reduction is not as uniform as shown in the -780 parcels. Others descend marginally later reaching a minimum at 1000 UTC, before, like the t1000-780 parcels, rising again to saturation by 1100 UTC. By contrast the t1000-925 parcels show a wider range during the early hours of the analysis, being spread between 80-100%. By 0600 UTC the majority have converged on 100% RH_i with the rest becoming saturated by 0730 UTC. They also show some drying during the small descent but all parcels remain above 80% RH_i before rising back to 100% and above by 1200 UTC.

Wet-bulb potential temperature (θ_w) has been used in a number of previous SJ studies to show the SJ as a distinct jet, void of any mixing as it descends from the cloud head (Baker, 2009; Clark et al., 2005; Gray et al., 2011; Martínez-Alvarado et al., 2011). Figure 5.7 (e) shows that, during the period of descent prior to the maximum winds in the t1000-780 winds, the θ_w stays constant at 4.6°C, indicating isentropic flow with no mixing. Prior to this the θ_w had stayed fairly constant around 4°C from 0000 UTC to 0700 UTC. An increase of 0.5°C is shown between 0700 and 0800 UTC immediately prior to the descent period. After the wind maximum (red line) θ_w rises to around 6°C. This again supports this flow moving into an area of convection and mixing with air from below.

The t1000-780 trajectories show some of the previously discussed (see Section 2.4.3) charactistics of a SJ:

- Descent from mid-levels
- Near constant θ_w throughout descent
- Reduction in RH_i

Although the descent is not as long or as deep as some of the SJs in the previous literature (Clark et al., 2005; Gray et al., 2011), it fits within the rate of descents used in Gray et al. (2011). One of

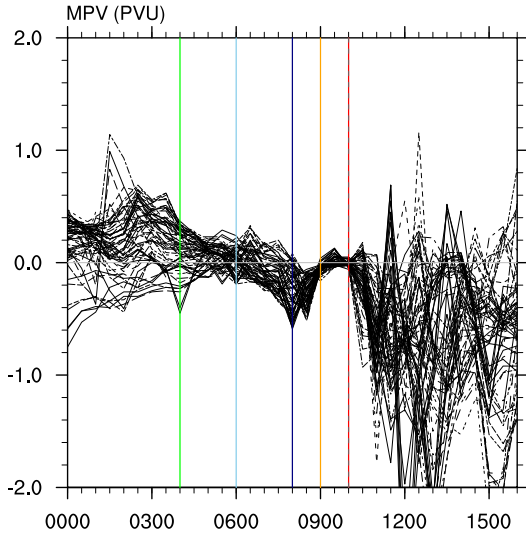

FIGURE 5.10: Time series of t1000-780 trajectory MPV.

the number of mechanisms is the role of CSI. MPV has been used in previous studies to identify regions of CSI release with negative MPV indicating CSI release. Figure 5.10 shows the trajectories having negative MPV prior to and during the descent shown in Figures 5.7 (a) and (d). CSI may only be released when the air is saturated (Schultz and Schumacher, 1999), Martínez-Alvarado et al. (2014) use a threshold of >90% RH_i for this threshold. Figure 5.7 (c) shows that the parcels are above this RH_i threshold for the period prior to the descent meaning that CSI may be released. Although it has been postulated that CSI release causes the descent of SJs (Clark et al., 2005; Gray et al., 2011; Martínez-Alvarado et al., 2011), Schultz and Sienkiewicz (2013) argue that CSI release is only a product of the descending motions and not the forcer. Schultz and Sienkiewicz (2013) instead identify secondary circulations due to frontolysis as the cause of the descent. This idea will be examined further in Section 5.5. The role of evaporation and sublimation has also been identified as a possible mechanism for driving the descent (Browning, 2004; Clark et al., 2005), however, recent studies have cast doubt on the importance of this (Baker et al., 2013; Smart and Browning, 2014). This will also be examined in more detail in Section 5.4.

The descent of the parcels in the t1000-780 and -850 swarms ceases relatively abruptly at 0930 UTC and 0900 UTC respectively. Having been initially proposed as a theory for SJ formation by Browning (2004), Schultz and Sienkiewicz (2013) show that low static stability may be a key to the descent of a SJ to the surface and suggest higher static stability may retard the descent. Figure 5.11 shows the static stability at 0900 and 0930 UTC along with the t1000-780 and -850 trajectory locations at these times. The trajectories are clearly located immediately next to and over a region

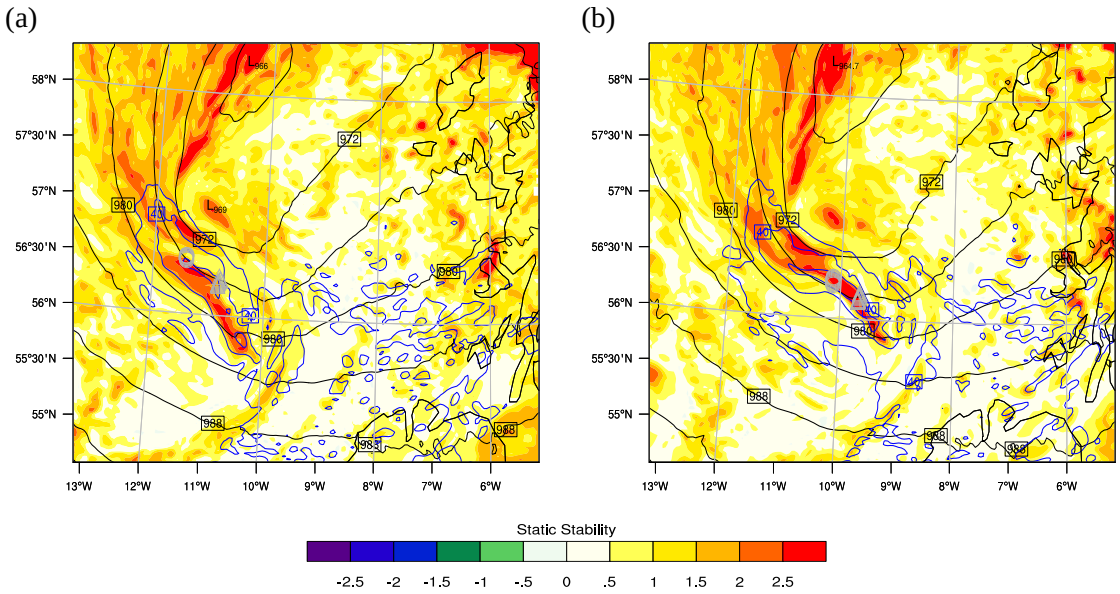

FIGURE 5.11: Static stability ($\theta_{850} - \theta_{900}$) at 0600 and 0700 UTC. Locations of the t1000-780 and t1000-850 trajectories are marked by the grey circles and triangles, respectively.

of high static stability at the two times. This supports the idea that low-level static stability may be important in the descent of SJs to the surface.

The properties of the t1000-925 trajectories do not show the charactistics of a SJ. However, they match the definition of a CCB air-stream. They remain within the lower reaches of the atmosphere as they circulate around the cyclone with high RH_i values. The more westward location of the t1000-925 hPa trajectories at 1000 UTC (Figure 5.6 (c)) compared to the t1000-780 suggests the t1000-780 SJ trajectories are descending ahead of the t1000-925 CCB trajectories.

5.2.2 1100 UTC Trajectories

The storm-relative trajectories for the t1100- trajectories are shown in Figure 5.12. In order to account for the increased northward extent of the slack low pressure centre, 1.5 ms^{-1} was added to the northward storm velocity. Compared to the the t1000- swarms they start further to the east of the cyclone, although their cyclonic evolution around the storm is similar. The maximum wind speed locations for the t1100-780 and -850 trajectories are further west than the respective t1000 counterparts.

The t1100-780 trajectory evolution exhibits important differences to the t1000 trajectories from the same level. The most noticeable of these is the differences in pressure/height along the trajectories.

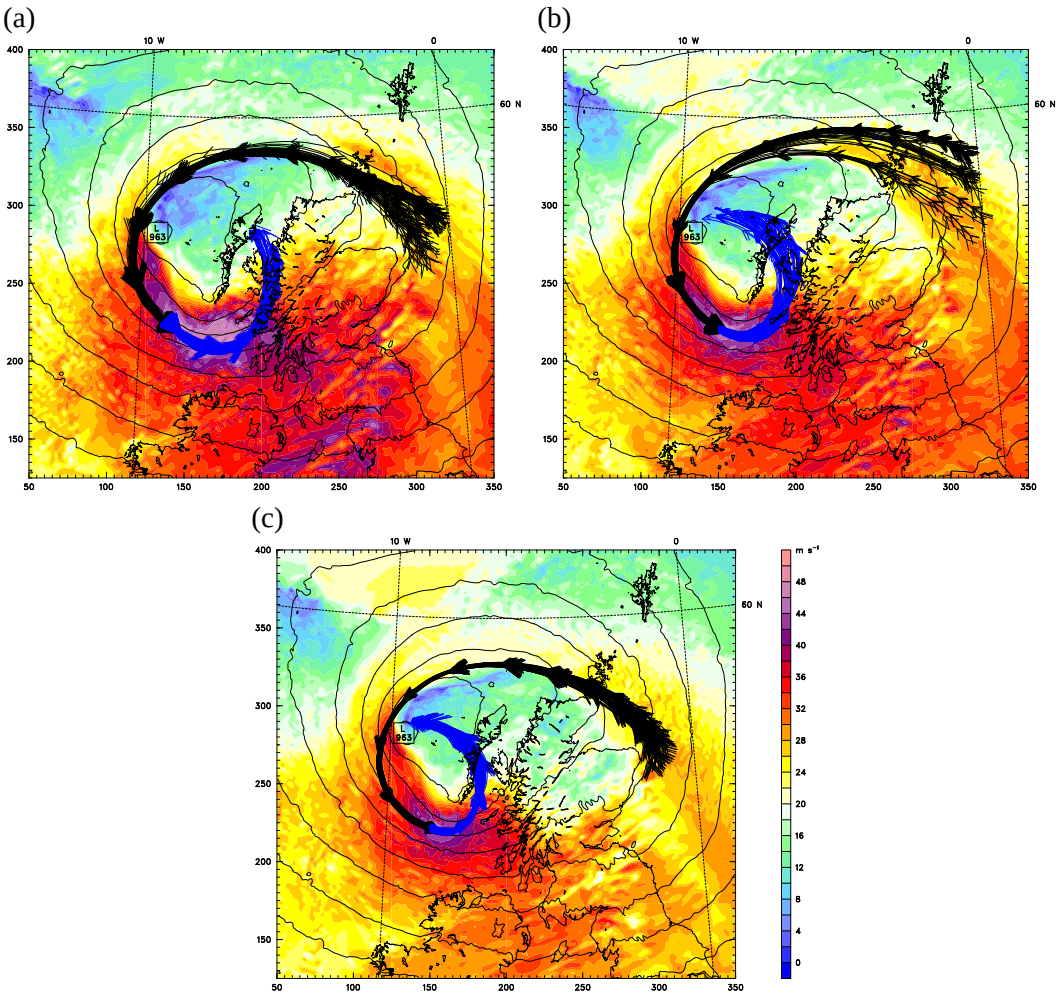

FIGURE 5.12: Storm relative trajectory paths for (a) t1100-780, (b) -850 and (c) -925 trajectories. Trajectory swarms are plotted over the horizontal wind speed on the level on trajectory initiation at 1000 UTC (filled contours, ms^{-1}) and SLP (black contours, every 4 hPa)

Unlike the t1000-780 parcels, these begin lower with pressure values above 860 hPa height at 0000 UTC. At 0500 UTC (light blue line) they begin to ascend. Some of parcels undergo a small amount of descent (~20 hPa, 400 m) for an hour before the initiation time at 1100 UTC (grey dashed line). This is in stark contrast to the higher altitude followed by descent of the t1000-780 trajectories. The t1100-850 trajectories show a similar altitudinal evolution, albeit being slightly lower and ascending later and more rapidly than the t1000-850 trajectories. The ascent of the t1100-850 trajectories continues after 1100 (grey dashed line) with some reaching above 600 hPa (~4 km) by 1600 UTC, whereas the -780 parcels remain around 780-820 hPa for the remainder of the analysis. The t1100-925 trajectories again show slightly different behaviour: they undulate around 900 hPa (~700 m) from 0000 UTC until congregating at 925 hPa 1100 UTC. After this they undergo a rapid period of ascent until 1530 UTC before descending slightly. Both the -850

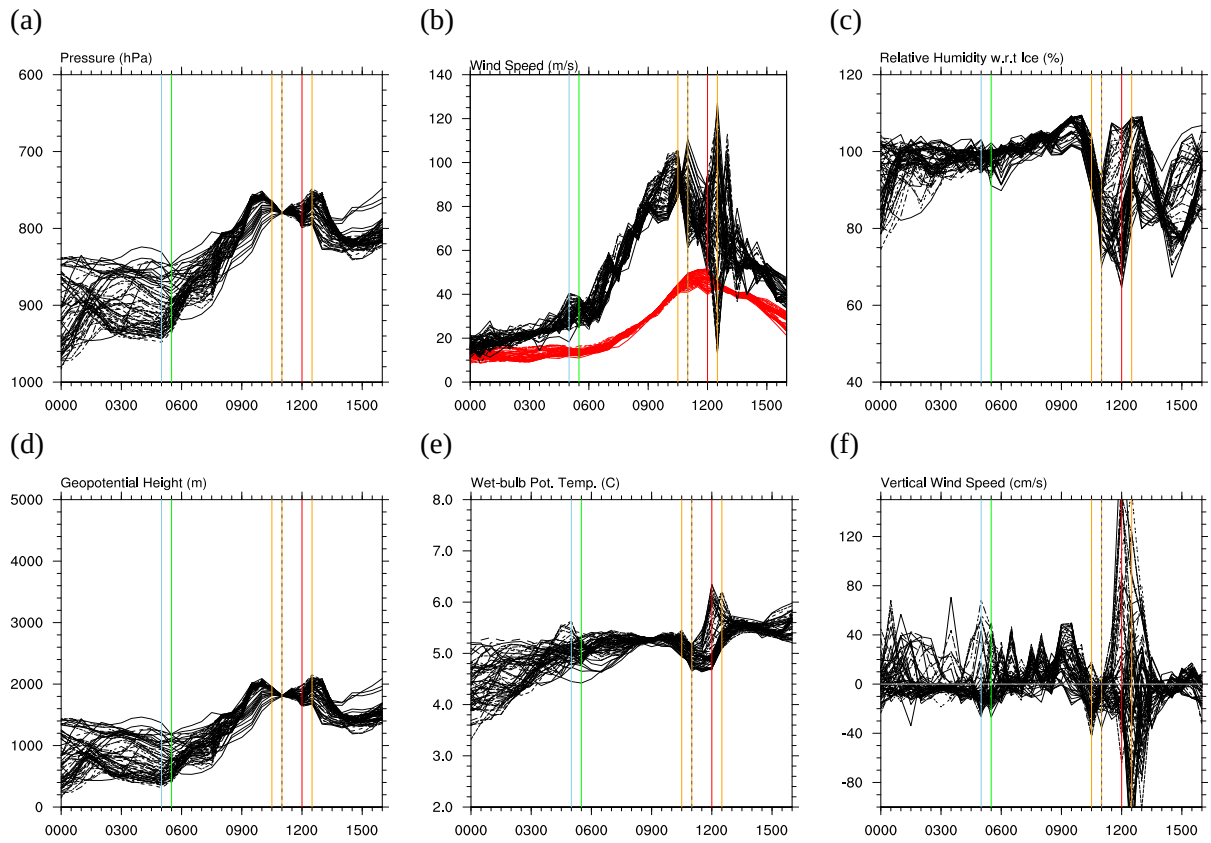

FIGURE 5.13: Diagnostics from the 64, t1100-780 trajectories: (a) Pressure (hpa), (b) horizontal wind speed (red) and geostrophic wind speed (black) (ms^{-1}), (c) RH with respect to ice (%), (d) Geopotential height (m), (e) θ_w, (f) vertical wind speed ($cm\ s^{-1}$). Coloured vertical lines represent times of interest for each trajectory: Green - start of acceleration, light blue - start of ascent, navy - start of descent, orange - V_g maximum, red - wind speed maximum, grey, dashed - trajectory initiation time.

and -925 trajectory sets show ascent after the 1100 UTC initiation time, whereas the -780 parcels stay at a relatively constant altitude. The different paths of the trajectory swarms show the reason for this with the -850 and -925 trajectories being initiated closer to the cyclone centre and moving into this area of large-scale ascent quicker than the -780 trajectories (Figure 5.12). The altitudes of the 1100 UTC initiated trajectories are indicative of CCB air-streams, remaining low as they move around the cyclone centre. The t1100-780 trajectories rise slightly higher than might be expected but are clearly distinct from the mid-level air-streams of the SJ shown in t1000-780.

The wind speeds of the t1100-780, 850, and 925 (Figures 5.13 (b), 5.14 (b) and 5.15 (b)) begin to accelerate between 0500-0530 UTC (green lines). The -925 trajectories show a slight slowing in acceleration at 0700 UTC before continuing again at 0730 UTC, marked by the second green line (Figure 5.15 (b). The peak in wind speed (red line) in the t1100-780 trajectories occurs at 1200 UTC. Prior to this there are two separate peaks in the geostrophic wind speed at 1130 and 1100

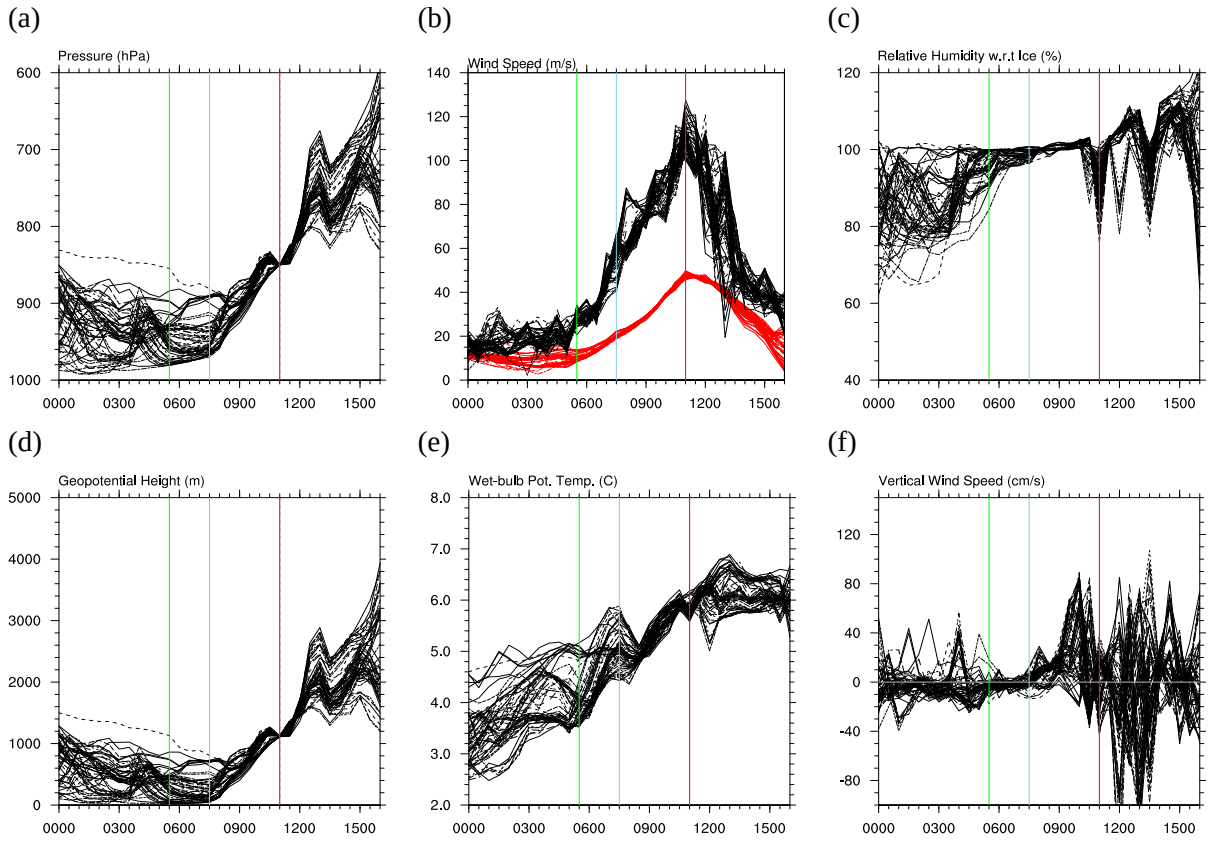

FIGURE 5.14: Diagnostics from the 64, t1100-850 trajectories: (a) Pressure (hpa), (b) horizontal wind speed (red) and geostrophic wind speed (black) (ms^{-1}), (c) RH with respect to ice (%), (d) Geopotential height (m), (e) θ_w, (f) vertical wind speed (cm s^{-1}). Coloured vertical lines represent times of interest for each trajectory: Green - start of acceleration, light blue - start of ascent, navy - start of descent, orange - V_g maximum, red - wind speed maximum, grey, dashed - trajectory initiation time.

UTC (orange lines). The geostrophic wind on the trajectories spreads significantly at 1230 UTC with a number of trajectories reaching the overall maximum along all the trajectories, around 125 ms^{-1}, while others drop to as low as 15 ms^{-1}. By 1300 UTC they have merged towards 60 ms^{-1} and continue to gradually reduce over the rest of the analysis time. To a lesser extent the t1100-850 and -925 trajectories also show a increased spread and some considerably low values in the geostrophic wind at 1230 UTC. In both the t1100-850 and -925 trajectories the peak in geostrophic wind speed in coincidental with the peak in winds speed at 1100 UTC.

RH_i in the t1100-780 trajectories is constant around 90-100% from 0100 UTC until 1000 UTC. It then undergoes a decrease over an hour. Some of the trajectories then moisten again while others continue to descend to as low 65% by 1200 UTC when the maximum winds speed occurs. The t1100-850 and -925 both show a spread of ~65-100% in RH_i values over the first few hours of the analysis. They then become largely saturated until ~1030 UTC with many trajectories showing

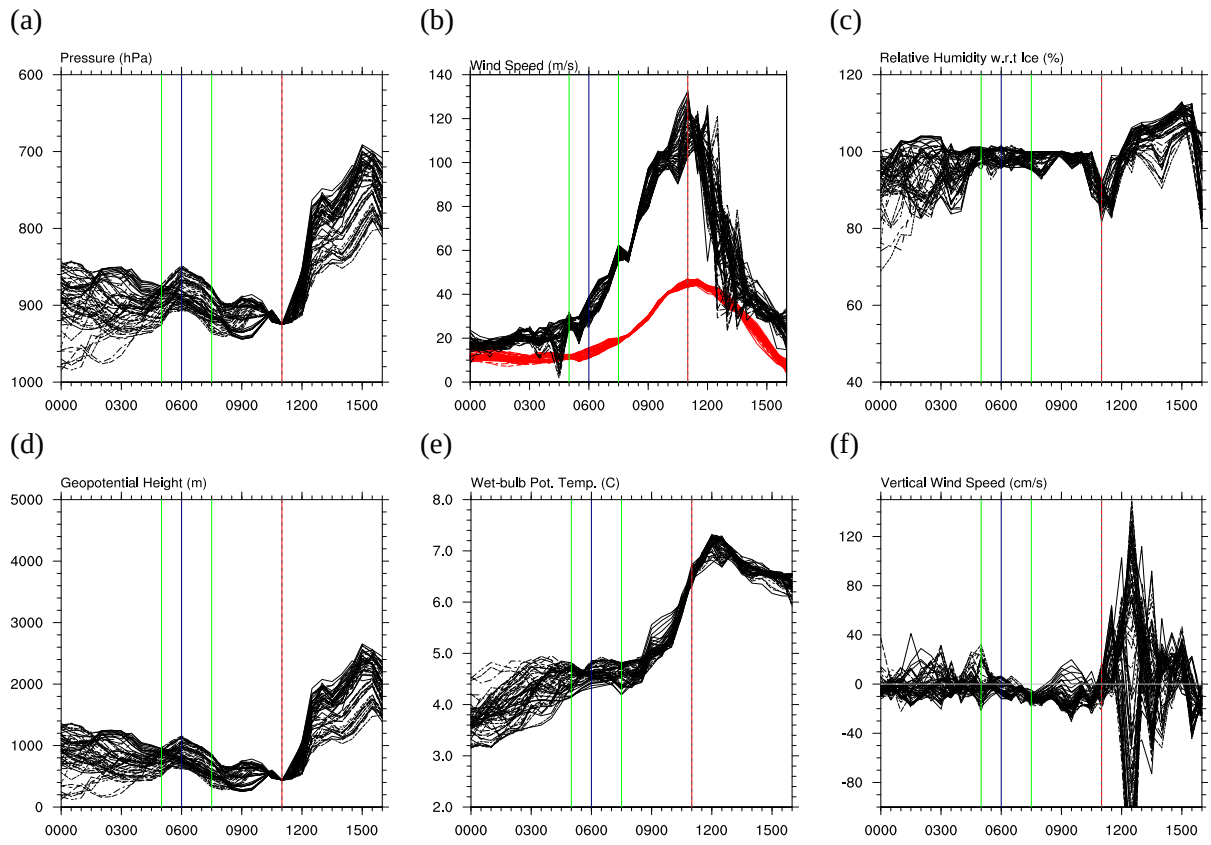

FIGURE 5.15: Diagnostics from the 64, t1100-925 trajectories: (a) Pressure (hpa), (b) horizontal wind speed (red) and geostrophic wind speed (black) (ms^{-1}), (c) RH with respect to ice (%), (d) Geopotential height (m), (e) θ_w, (f) vertical wind speed (cm s^{-1}). Coloured vertical lines represent times of interest for each trajectory: Green - start of acceleration, light blue - start of ascent, navy - start of descent, orange - V_g maximum, red - wind speed maximum, grey, dashed - trajectory initiation time.

some drying before reaching their respective wind maximums, albeit not as pronounced as the t1100-780 air parcels. This drying of the air prior to the wind speed maximum is consistent with the t1000- trajectories and suggests this process may contribute to enhancing the maximum wind speed.

Rising θ_w in some of the t1100-780 trajectories between 0000 UTC and 1600 UTC indicated mixing is taking place. The flow then becomes isentropic until 1030 UTC when the θ_w falls slightly before rising again around 1130 UTC. By contrast the t1100-850 show a fairly continuous increase in θ_w over the majority of the trajectory analysis, with a flattening off after 1200 UTC (Figure 5.14 (e)). The t1100-925 trajectories show an initial increase in θ_w before plateauing around 4.5°C from 0600 UTC until rising rapidly up to 7°C between 0900 UTC and 1200 UTC (Figure 5.15 (e)). This is indicative of the mixing via convection with the ascent as seen in Figures 5.15 (a) and (d).

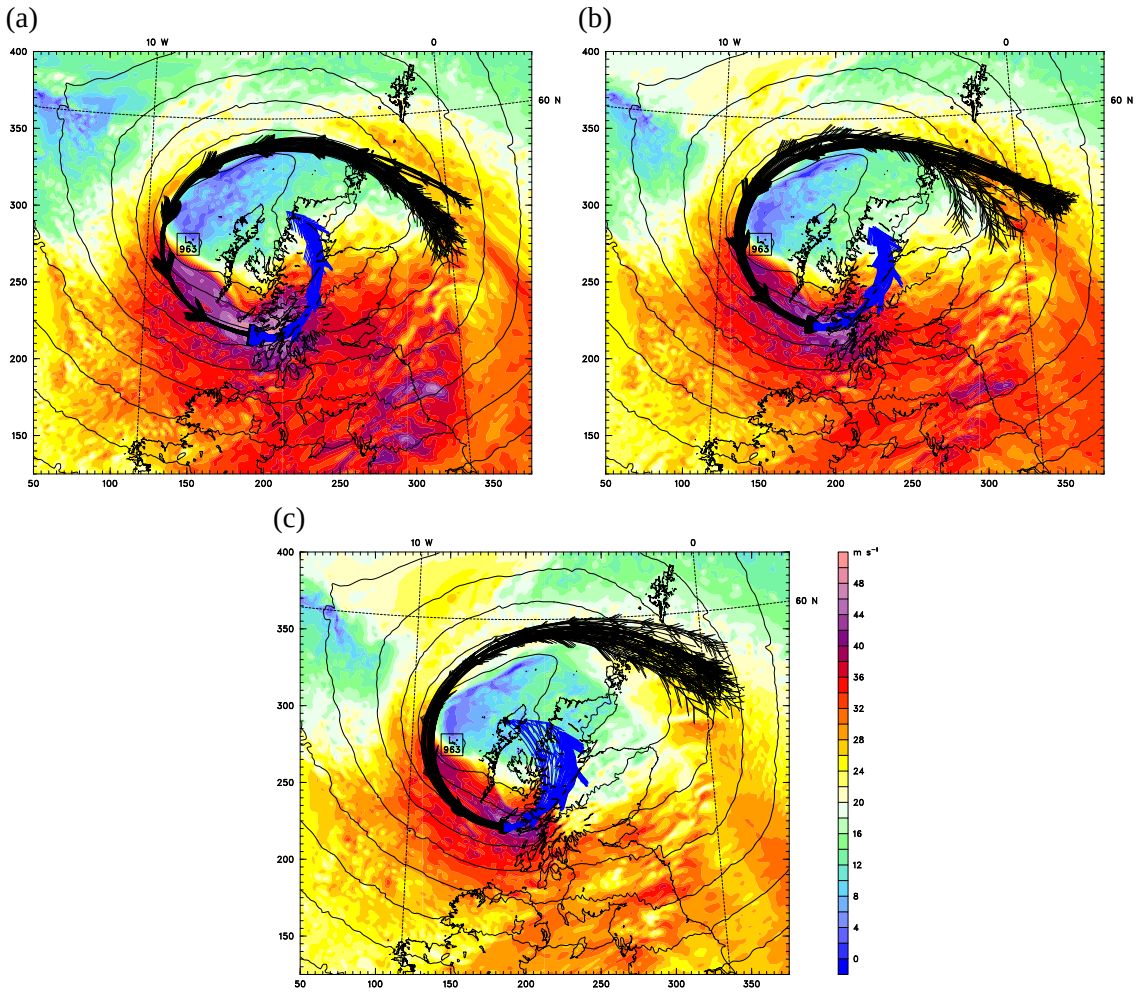

FIGURE 5.16: Storm relative trajectory paths for (a) t1200-780, (b) -850 and (c) -925 trajectories. Trajectory swarms are plotted over the horizontal wind speed on the level on trajectory initiation at 1000 UTC (filled contours, ms^{-1}) and SLP (black contours, every 4 hPa)

5.2.3 1200 UTC Trajectories

The t1200-780 trajectory diagnostics shown in Figure 5.17 show a very strong likeness to the t1100-780 diagnostics described previously (Figure 5.13), again resembling a CCB feature for most of their path. In the pressure and altitude plots (Figures 5.17 (a) and (d)), the split in trajectory heights between 0200 UTC and 0630 UTC shows the result of the two slightly different streams shown in Figure 5.16. At 0530 UTC (first light blue line) the lower of these two sets begin to ascend from around 980 hPa (400 m), at 0700 UTC (second light blue line) they merge with the rest of the trajectories around 860 hPa (1000 m) and all ascend towards the initiation level of 780 hPa (~1800 m). As in the t1100-780 trajectories, some overshoot this level and descend slightly in the hour prior to the trajectory initiation at 1200 UTC (red/grey dashed line). Figures 5.18 (a) and (d) show

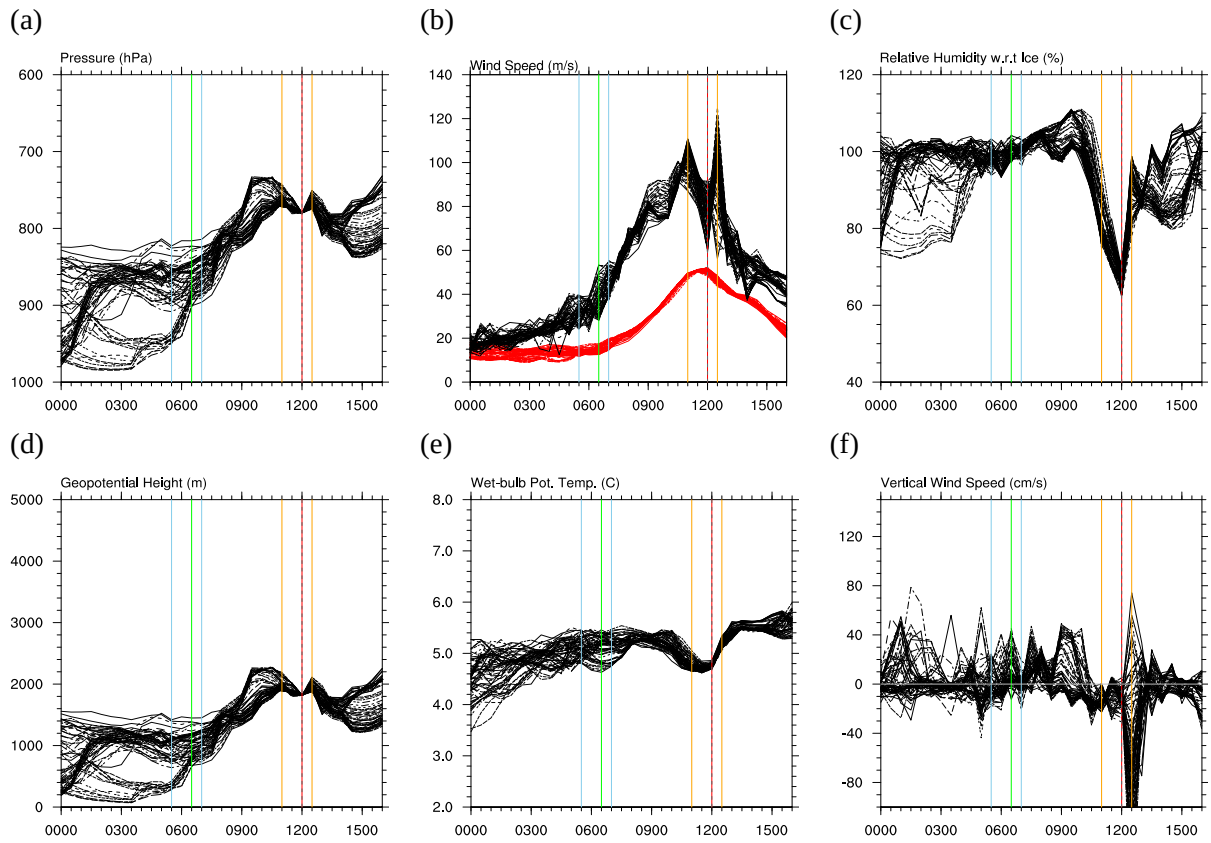

FIGURE 5.17: Diagnostics from the 64, t1200-780 trajectories: (a) Pressure (hpa), (b) horizontal wind speed (red) and geostrophic wind speed (black) (ms^{-1}), (c) RH with respect to ice (%), (d) Geopotential height (m), (e) θ_w, (f) vertical wind speed ($cm\ s^{-1}$). Coloured vertical lines represent times of interest for each trajectory: Green - start of acceleration, light blue - start of ascent, navy - start of descent, orange - V_g maximum, red - wind speed maximum, grey, dashed - trajectory initiation time.

two different air streams make up the trajectories for this region. The larger swarm is confined to low levels, generally above 900 hPa (<1000 m) until 0539 UTC (light blue line) at which point they begin to ascend. A smaller group flows at ~780 hPa (1600 m) for the initial ten hours of the analysis. At 1000 UTC (navy line) the trajectories start to descend for 1.5-2 hours. Some of the trajectories then rise slightly to the initialisation level at 1200 UTC (red/gray dashed line). A two hour period of rapid ascent then ensues before slowing before a slight fall, then continuing to rise until the end of the analysis period. The t1200-925 trajectories are initially spread between 1000 hPa and 820 hPa at 0000 UTC; between this time and the trajectory initiation at 1200 UTC, they steadily congregate towards the 925 hPa level. As with the t1200-850 trajectories there is rapid ascent after 1200 UTC (red/gray-dashed line). Figure 5.5 (d) shows that these trajectories are located almost on top of each other at 1200 UTC. Also, at this time the trajectories are located immediately to the west of the Scottish coast. Thus, orographic ascent over the coastline would

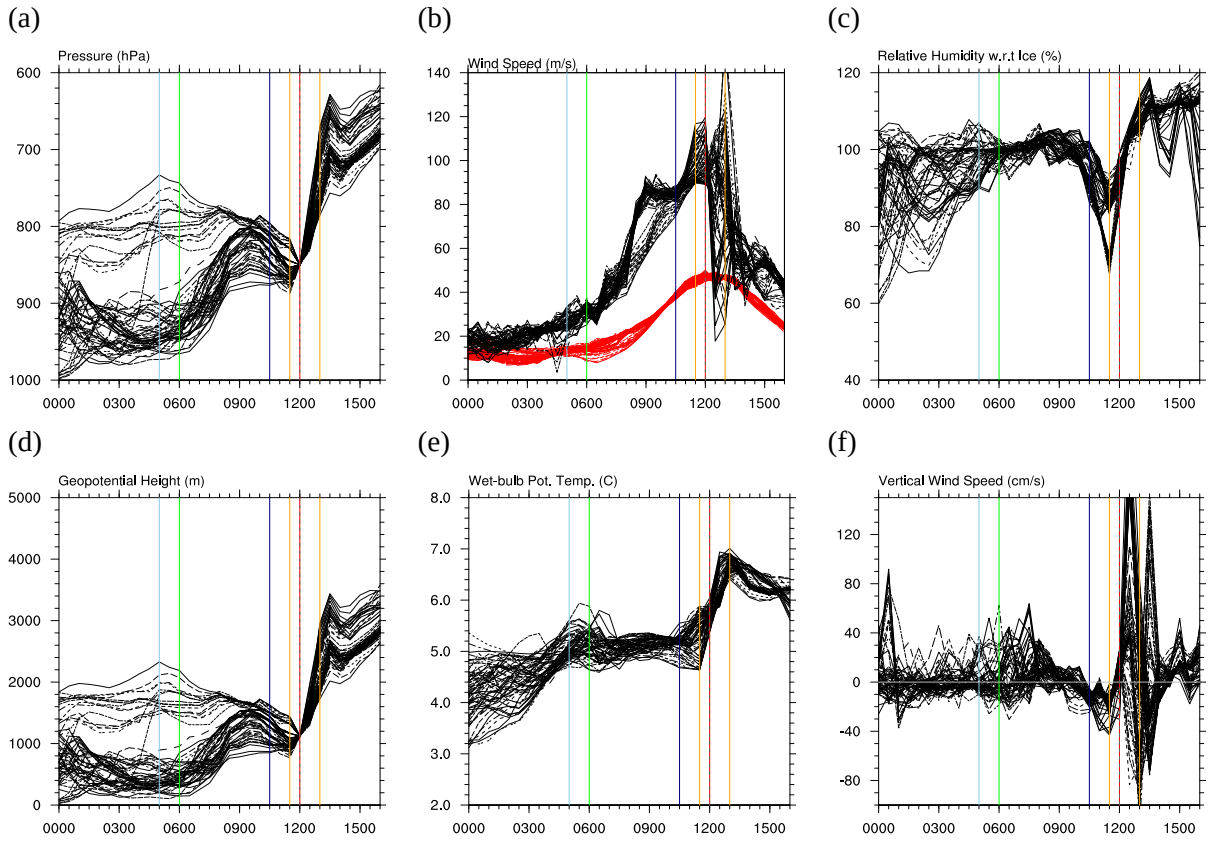

FIGURE 5.18: Diagnostics from the 64, t1200-850 trajectories: (a) Pressure (hpa), (b) horizontal wind speed (red) and geostrophic wind speed (black) (ms^{-1}), (c) RH with respect to ice (%), (d) Geopotential height (m), (e) θ_w, (f) vertical wind speed (cm s^{-1}). Coloured vertical lines represent times of interest for each trajectory: Green - start of acceleration, light blue - start of ascent, navy - start of descent, orange - V_g maximum, red - wind speed maximum, grey, dashed - trajectory initiation time.

explain the rapid ascent beyond 1200 UTC.

All of the wind speed plots of the t1200- trajectories show similar evolution (Figures 5.17, 5.18 and 5.19 (b)), suggesting that the CCB is now the dominant driver of the high winds. Acceleration of the air parcels starts between 0600 and 0700 UTC (green lines). A peak in wind speed is seen at 1200 UTC (red/grey dashed line) in all of the plots, although the t1200-925 trajectories see a second peak at 1330 which is not present in the -780 and -850 plots. The geostrophic wind speed shows peaks in the t1200-780 at 1100 UTC, slightly earlier than the 1130 UTC initial peaks in both the -850 and -925 trajectories (orange lines). Secondary peaks in the geostrophic winds speed at 1230 UTC in the -780 and -925, and at 1300 UTC in the -850 trajectories are also present (second orange lines). In the -850 plots there is a very large spread in the values at this point, whereas the other t1200- plots show more consistent peaks. These secondary peaks are at the time of the

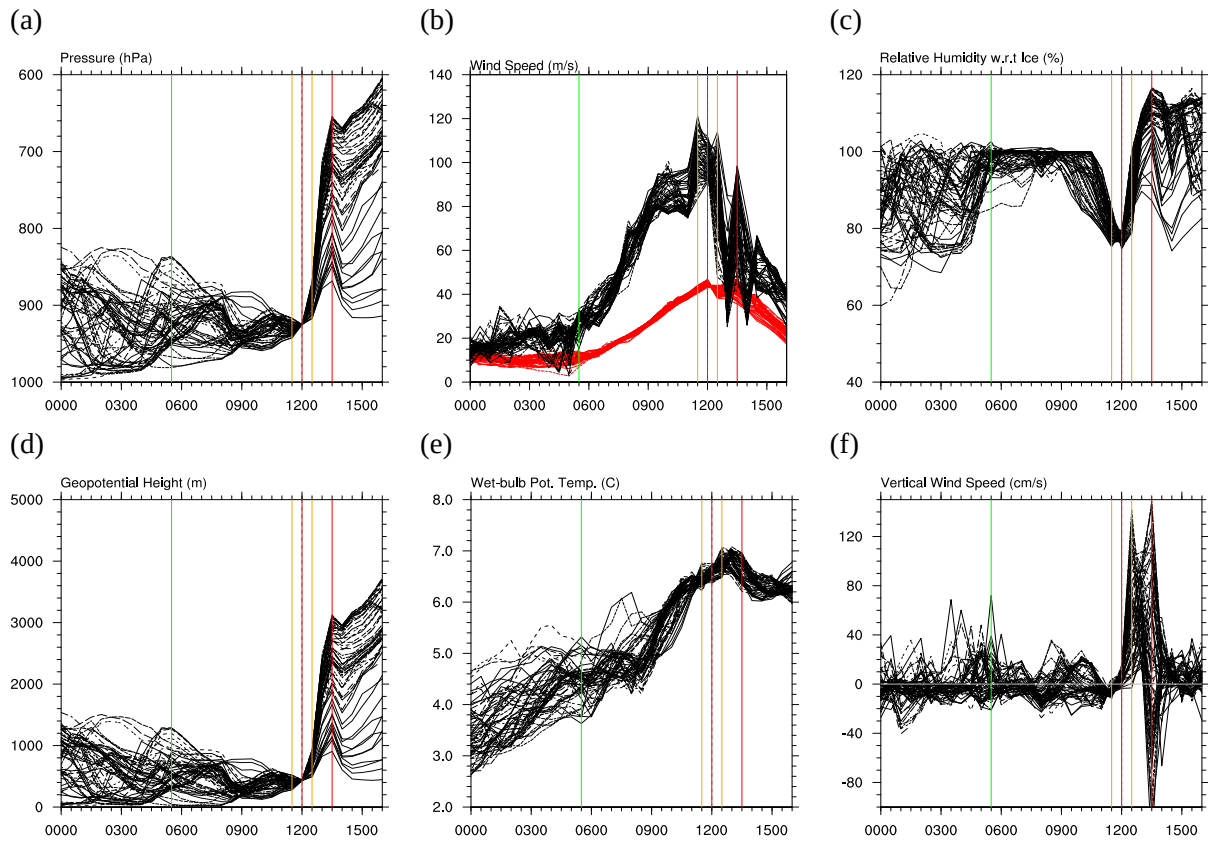

FIGURE 5.19: Diagnostics from the 64, t1200-925 trajectories: (a) Pressure (hpa), (b) horizontal wind speed (red) and geostrophic wind speed (black) (ms^{-1}), (c) RH with respect to ice (%), (d) Geopotential height (m), (e) θ_w, (f) vertical wind speed ($cm\ s^{-1}$). Coloured vertical lines represent times of interest for each trajectory: Green - start of acceleration, light blue - start of ascent, navy - start of descent, orange - V_g maximum, red - wind speed maximum, grey, dashed - trajectory initiation time.

interaction with the Scottish coast and therefore presumably due to pressure changes as the air mass rises over the coastline.

Again there is a consistent story emerging with regards to the RH_i. In all three of the t1200-trajectory swarms there is a distinct minimum in the RH_i at the time of maximum winds. The t1200-780 parcels show the most drying, falling from supersaturation to around 65%. The t1200-925 trajectories show a decrease from around 100% to 75%, while the t1200-850 parcels show a split with some falling to 70% but the majority only falling to 90%. This is a consistent pattern in many of the trajectory plots shown. In order to look into the possible effect of this drying on the trajectories Section 5.4 will analyse the latent heating diagnostics from the model for this run. Chapter 6 will investigate the importance of this through sensitivity simulations.

The θ_w evolution of the t1200-780 trajectories shows a small but steady mean increase over the first

8 hours of the analysis from ~4.5°C to ~5°C. Between 0800 UTC and 1000 UTC the θ_w remains largely constant before decreasing by around 0.4°C by 1200 UTC. The t1200-850 trajectories also increase in θ_w until 0600 UTC then remain constant until 1100 UTC. Following this period, θ_w then rises rapidly to 6.5°C by 1300 UTC as the air rapidly ascends. The -925 parcels show a more continuous rise in θ_w along the majority of the analysis time suggesting that mixing is present at lower levels.

5.3 Dynamical Flows and Force Balance

5.3.1 Geostrophic Wind and Pressure Gradient Force

As seen in the trajectory diagnostics (Figures 5.7-5.19) the wind speeds are much lower than the geostrophic wind. Equations 5.1 and 5.2 show the formulation of geostrophic wind components on a given pressure level.

$$u_g = -\frac{g}{f}\frac{\partial z}{\partial y}, \tag{5.1}$$

$$v_g = \frac{g}{f}\frac{\partial z}{\partial x}, \tag{5.2}$$

where, g is the gravitational acceleration, f is the Coriolis, and z is the geopotential height. The lower actual winds compared to the geostrophic winds is to be expected, as the geostrophic wind does not take into account the effects of curvature or friction on the air. The geostrophic wind does however show that the pressure gradient force (PGF) is likely to be important in the acceleration of the high winds.

Figure 5.20 highlights the calculated geostrophic winds and the differences between the geostrophic balanced wind and the actual horizontal wind. As also seen in the trajectory analysis, the geostrophic wind reaches speeds in excess of 100 ms^{-1} (Figures 5.7-5.19). The difference plots (Figures 5.20 (b), (d) and (f)) show the actual wind speed being more the 30 ms^{-1} slower than the geostrophic wind across much of the plot area, and over 100 ms^{-1} slower in the strongest regions. This gives an indication of the role of the PGF in the development of the high winds. However it is also noted

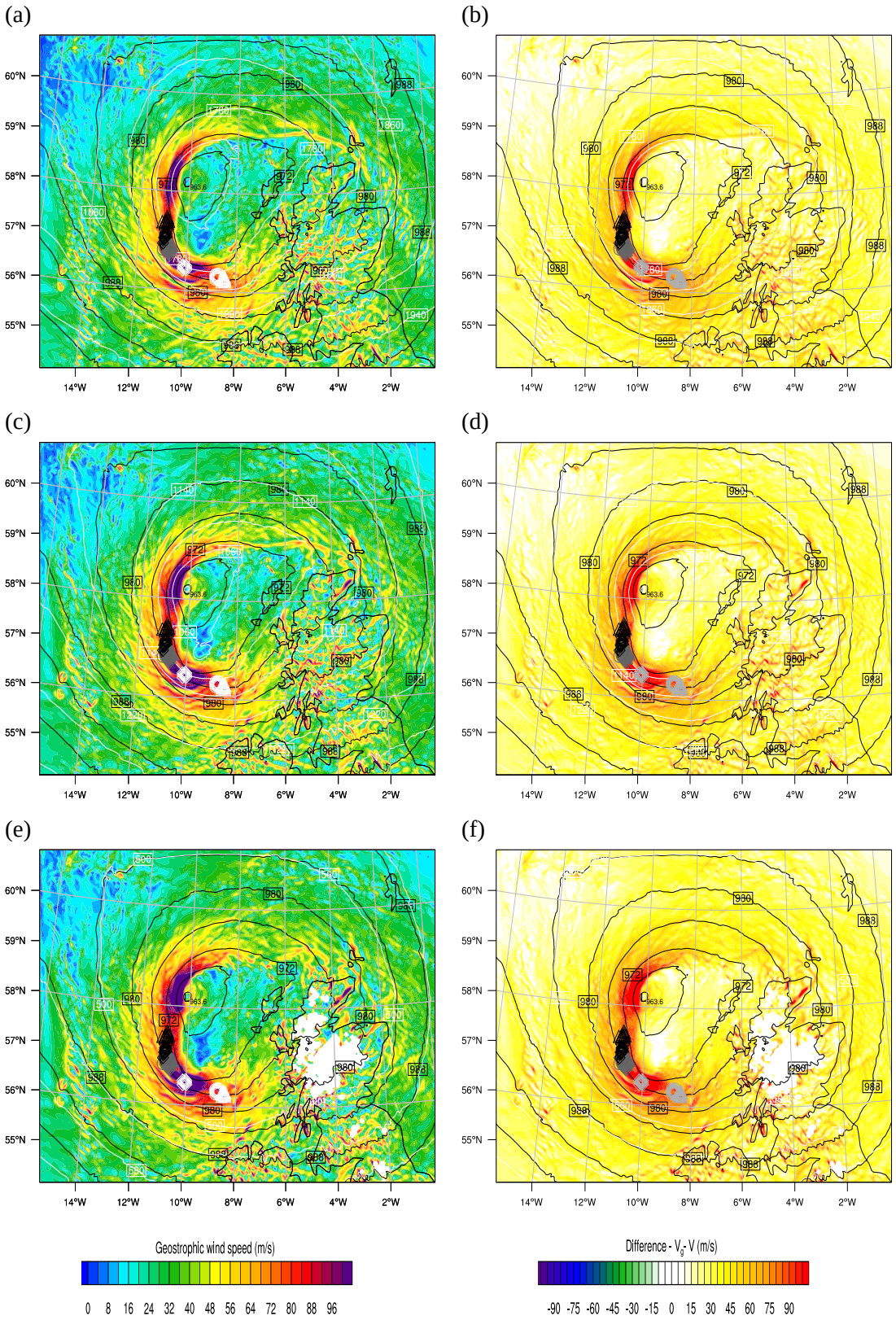

FIGURE 5.20: Geostrophic wind speed on (a) 780 hPa, (c) 850 and (e) 925 hPa levels and difference to actual wind speed $V_g - V$ on corresponding levels (b, d, f, respectively). Black lines are SLP and white z on the levels of the winds. White, gray and black markers indicate trajectory from initialisation times of 1000, 1100 and 1200 UTC, respectively, while maker shapes indicate initialisation level: circles - 780 hPa, triangles - 850 hPa, diamonds - 925 hPa.

earlier that there is a lag between the geostrophic maximum and the highest wind speeds along many of the trajectories.

The PGF (Equation 5.3) can be computed from the WRF model output on height levels using centre finite difference calculations to get the gradient of P (∇P) in the x- and y-direction.

$$PGF = -\frac{1}{\rho}\nabla P \tag{5.3}$$

The contribution of the PGF to the along-flow momentum can then be calculated using:

$$\frac{V \cdot \nabla P}{|V|} \tag{5.4}$$

where, V is the horizontal wind. This allows us to see the pure contribution of the pressure gradient to the wind speed and identify if there are regions where other processes contribute to the wind speeds.

Figure 5.21 shows the along-flow PGF acceleration for the t1000 trajectories and Figure 5.22 shows the same diagnostic for the t1100 parcels. The role of the PGF in the acceleration can be seen in all the plots with the green lines occurring as the PGF begins to increase. In the t1000-780 trajectories the maximum wind speed occurs as the along-flow PGF moves from positive to negative (Figure 5.21 (a) - red/gray-dashed line)). In the t1000-850 and t1100-850 the peak winds occur slightly before the PGF becomes negative showing other forces must be becoming dominant. Figures 5.21 (c) and 5.22 (c) show the -925 trajectories highest along-flow PFG prior to hitting the coastline, reaching up to 0.008 ms^{-2}. This increased PGF is counter-weighted by the increased friction at this level helping to retard the flow. This is highlighted by the maximum wind speeds on this level (red lines) occurring when the PGF is still positive showing that other forces must be outweighing the PGF. The peaks in geostrophic wind speed (orange lines) are often located marginally later than the peak in along-flow PGF: this would suggest that although the pressure gradient is higher, a portion of it is acting against the flow. The t1000 trajectories all show some degree of descent during the analysis (see Section 5.2.1). Figure 5.21 shows that the start of the descent (navy lines) in these cases is co-located with a peak in the along-flow PGF.

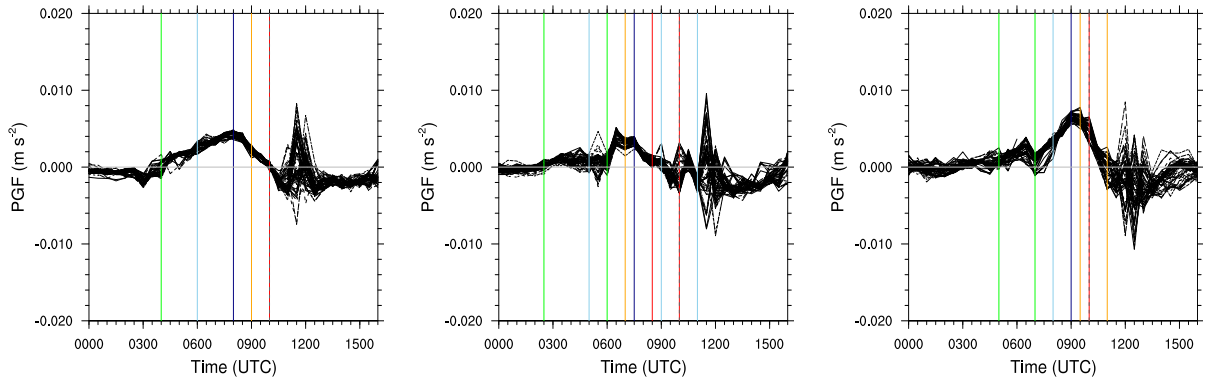

FIGURE 5.21: Along-flow PGF component on t1000 (a) -780, (b) -850 and (c) -925 trajectories. Coloured lines as Figures 5.7, 5.8 and 5.9, respectively

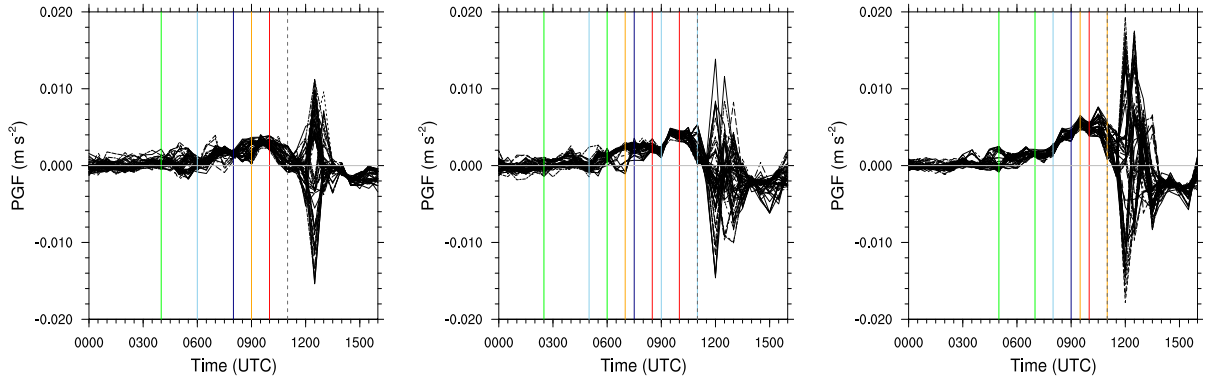

FIGURE 5.22: Along-flow PGF component on t1100 (a) -780, (b) -850 and (c) -925 trajectories. Coloured lines as Figures 5.13, 5.14 and 5.15, respectively

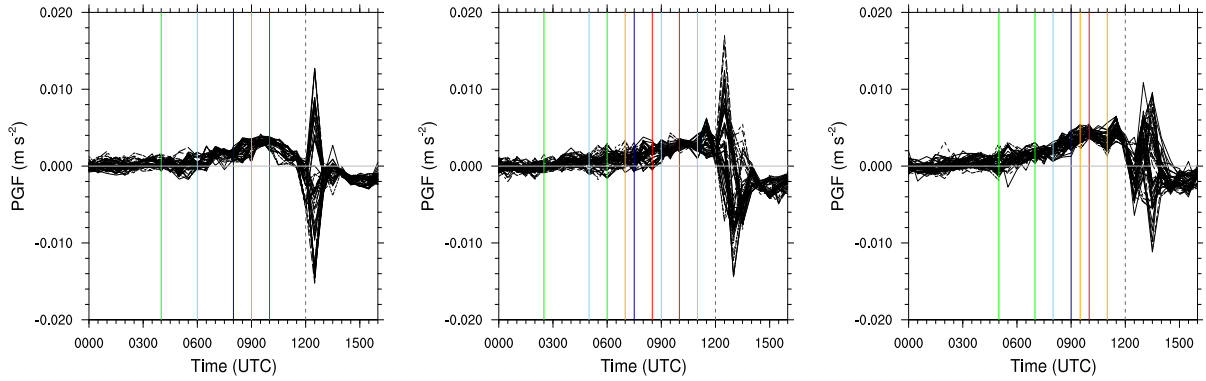

FIGURE 5.23: Along-flow PGF component on t1200 (a) -780, (b) -850 and (c) -925 trajectories. Coloured lines as Figures 5.17, 5.18 and 5.19, respectively

5.3.2 Gradient Wind

5.3.2.1 Gradient Wind Methodology

As shown in the trajectory analysis above, the storm winds are not in geostrophic balance. This is hardly surprising given the curvature of the flow as it travels around the storm. The geostrophic wind, is the balance of the Coriolis with the PGF, defined as:

$$V_g = \frac{-1}{f}\frac{\partial \Phi}{\partial n} \tag{5.5}$$

where f is the Coriolis parameter, and $\delta\Phi / \delta n$ is the geopotential gradient following the flow. However, in a storm such as Cyclone Friedhelm, the centrifugal force will play a significant role in the force balance due to the tight curvature of the isobars. The effect of curvature can be analysed by rearranging the horizontal momentum equation with the radius of curvature (R):

$$\frac{V^2}{R} + fV = -\frac{\partial \Phi}{\partial n} \tag{5.6}$$

where R is the radius of curvature (Holton, 1992). Using the quadratic equation to solve for the gradient winds (V_{gr}) yields:

$$V_{gr} = -\frac{fR}{2} \pm \left(\frac{f^2R^2}{4} - R\frac{\partial \Phi}{\partial n}\right)^{\frac{1}{2}}, \tag{5.7}$$

where, for a given level $\partial\Phi / \partial n$ can be replaced by $-fV_g$.

Mathematically there are a number of solutions to Equation 5.7 depending on the sign of the components of the equation. However, some of these would give non-physical answers and are therefore impossible. The possible solutions are shown in Table 3.1 in Holton (1992), which is reproduced here in Table 5.2. The terms R>0 and R<0 indicate cyclonic and anticyclonic flow respectively, while the "Positive root" and "Negative root" in Table 5.2 refer to the ± sign in Equation 5.7.

The complication with this approach for a storm such a Cyclone Friedhelm, is the calculation of the radius of curvature (R). In an idealised situation such as a symmetrical tropical cyclone, the concentric circles of increasing pressure would show a perfect linearity with increasing radius in

TABLE 5.2: Possible solutions to the V_{gr} equation 5.7.

Sign $\partial\Phi/\partial n$	R>0	R<0
Positive	Positive root: **Non-physical** Negative root: **Non-physical**	Positive root: **Antibaric flow** (anomalous low) Negative root: **Non-physical**
Negative	Positive root: **Cyclonic flow** (regular low) Negative root: **Non-physical**	Positive root: **Anticyclonic flow** (anomalous flow) Negative root: **Anticyclonic flow** (regular high)

any direction from the centre of curvature. As can be seen in Figure 5.6 this idealised situation is clearly not the case here. The unsymmetrical distribution of the pressure/geopotential height would give a differing curvature centre point (CCP), depending on the region of interest. Here a new method is utilised to estimate R for a given area of the storm - in this case the region of highest winds to the south and south-west of the cyclone centre. Here the gradient wind is to be calculated on pressure levels so the geopotential height (z) is used for the calculations, if the gradient wind was required on a height level pressure (P) could be substituted in for z.

The novel method used to calculate the radius of curvature and gradient wind is as follows:

- Define the area of interest

This is the region where the gradient wind will be calculated, marked as box B (solid dark grey box) in Figure 5.24 (a).

- Set region for estimated CCP

This region is defined based on a guess by eye of the likely CCP, this box may be large if this is uncertain. Box A is shown in Figure 5.24 (a) as the dashed dark grey box.

- Calculate R against z

For each prospective CCP gridpoint in box A the distance to each gridpoint in box B is calculated (R) and saved, along with the z for each of the gridpoints in box B.

- Plot R against z and calculate correlation

Scatter plots of the saved R and z data from each potential CCP are produced and r^2 calculated for the R against z data

- Select CCP

The CCP can then be chosen form the gridpoint in box A which shows the highest r^2 correlation between R and *z*.

- Calculate V_{gr}

The selected CCP can then be used to calculate the radius of curvature for each point in box B and input into the V_{gr} equation 5.7.

Boxes A and B are not necessarily limited in size although computation costs are higher if large boxes are used. If these boxes start to edge out of the cyclonic geopotential or pressure region the resultant CCP may be less accurate. Due to the non-circular nature of the pressure or *z* surfaces the sizes and locations of the boxes will alter the values obtained. Generally concentrating on a smaller area where there will be less change in the P/*z* field, and therefore a better fitting CCP, should yield a more accurate V_{gr}.

The example from 1000 UTC (Figure 5.24) shows the effect of using different boxes. The larger boxes marked as A and B in Figure 5.24 (a) are compared to the A' and B' boxes, also in Figure 5.24 (a), which focus on a smaller region to the south of the cyclone centre.

The smaller boxes, A' and B' (Fig. 5.24 (c)), produce a better R-*z* relationship with an r^2 value of 0.99 compared to 0.95 where the larger boxes (A and B) are used (Fig. 5.24 (b)). This means the smaller boxes should give a more accurate V_{gr} value. Figure 5.25 shows V_{gr} within the smaller, B' box, using the centre point from the larger boxes and smaller boxes (Figures 5.25 (a) and (b)), respectively). Figure 5.25 (c) shows the difference between the two V_{gr}) fields, which is high in some regions. This highlights the main caveat of this deduction of a centre point of the curvature where the circulation is not symmetrical. Despite this, the method should give a reasonable estimate of V_{gr}.

The location of box A is important in allowing a reasonable centre point for the curvature for a given box B. The location for box A can be easily selected by eye as has been done in Figure 5.24. However, a poorly placed "A" box will affect the radius of curvature and likely produce an erroneous gradient wind distribution. Although choosing a reasonable location for box A is important, extending the size of the box should have no effect on the outcome of the centre point. Therefore if the centre point location is dubious a larger box A can be used to cover all possibilities, although this would be computationally more expensive.

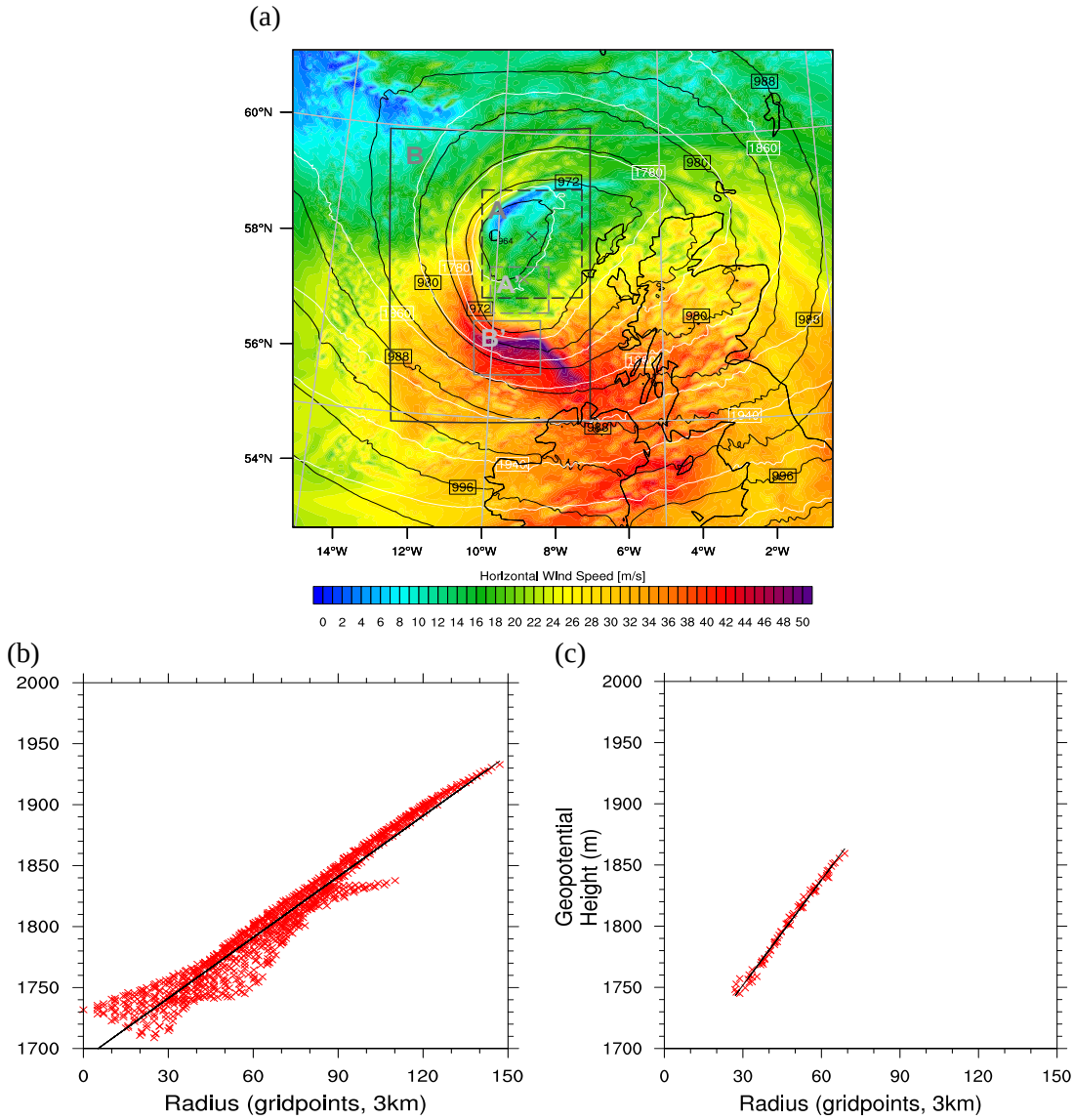

FIGURE 5.24: Gradient wind calculation boxes and CCPs: (a) plotted over wind speed on 780 hPa (shaded) with SLP and 780 hPa level *z* shown by the black and white contours, respectively. Solid grey lines indicate the boxes for which Gradient wind will be calculated, while dashed grey lines show the regions selected as possible centre points. Grey crosses mark the calculated centre points for the respective boxes as denoted by the colours. Panels (b) and (c) show the best correlating R vs. *z* scatter plots for the A and A' boxes in (a) respectively.

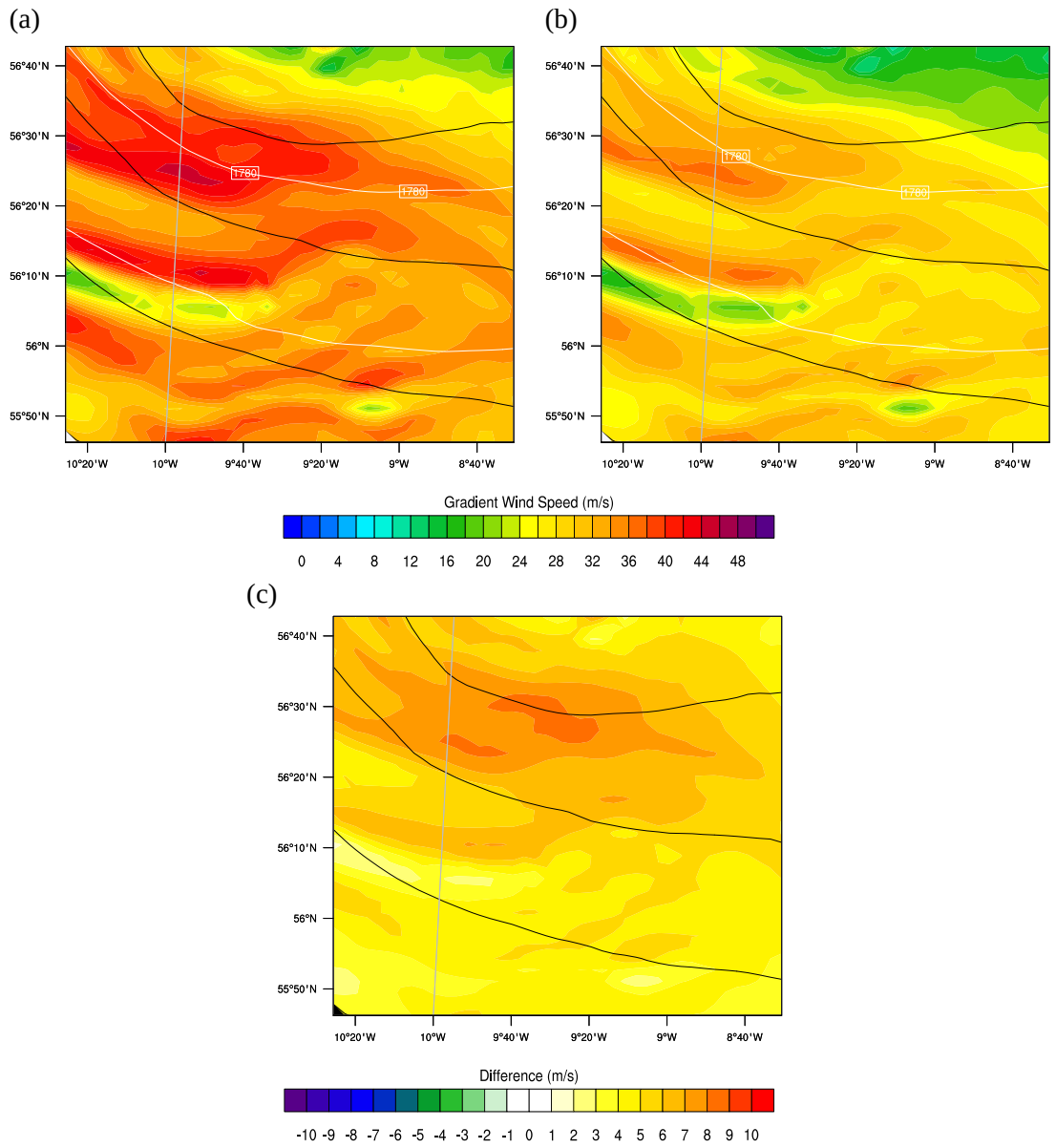

FIGURE 5.25: V_{gr} at 780 hPa calculated from the CCP of (a) boxes A/B (dark gray boxes in Figure 5.24 (a)), (b) boxes A'/B' (light gray boxes in Figure 5.24 (a)). Plot (c) is the difference (a)-(b)

5.3.2.2 Gradient Wind Results

Using the method described in Section 5.3.2.1, the gradient wind can be calculated for Cyclone Friedhelm. Here, in order to provide a broad picture of the flow, large boxes are used. As shown previously this reduces the accuracy of the radius of curvature which will directly affect the gradient wind results. However, the results should still give a reasonable approximation of the gradient flow. Table 5.3 shows the centre of curvature locations and r^2 values for the gradient wind plots at 1000, 1100 and 1200 UTC on pressure levels of 780, 850 and 925 hPa.

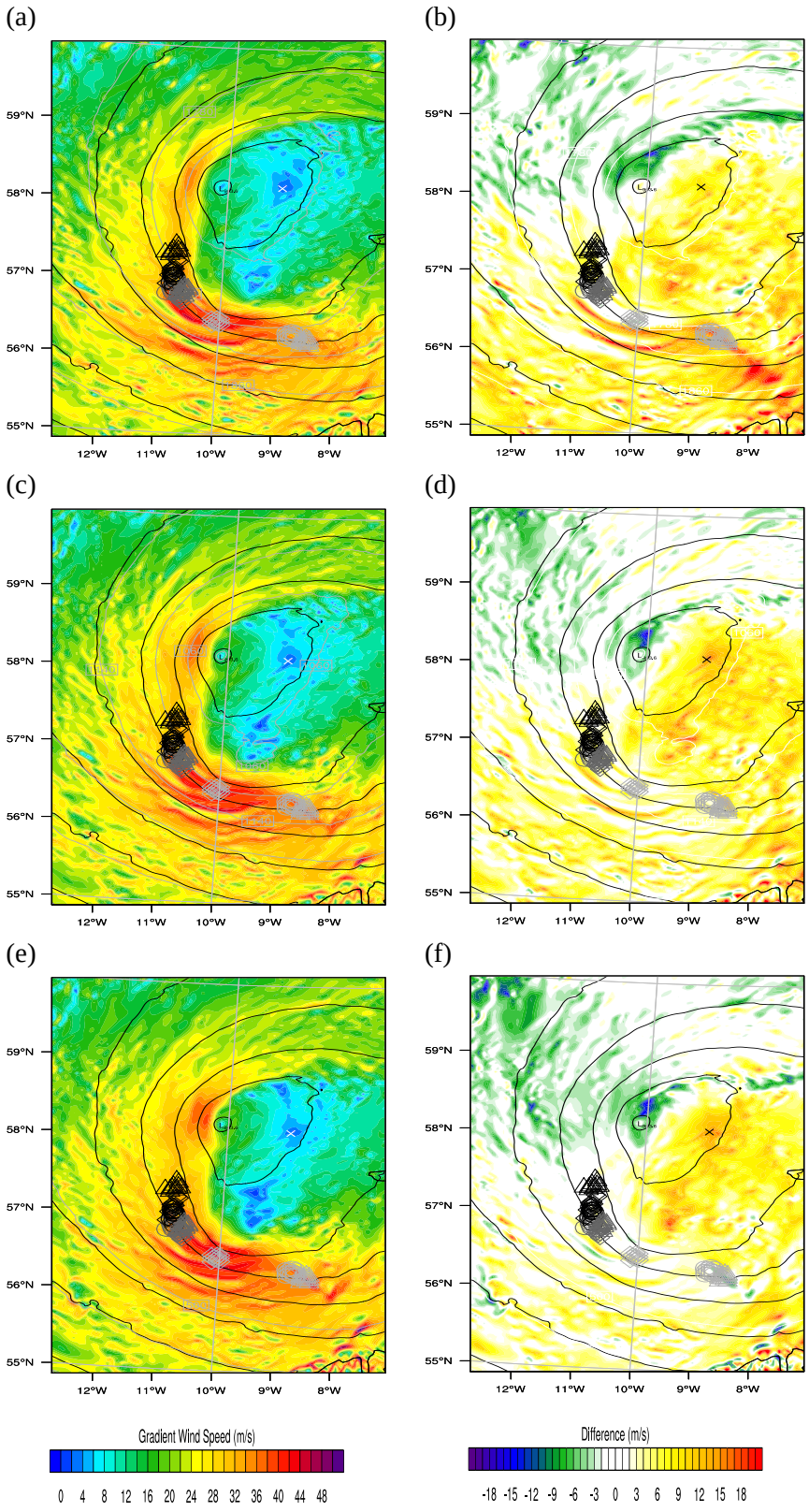

FIGURE 5.26: Gradient wind at 1000 UTC on (a) 780 hPa, (c) 850 hPa and (e) 925 hPa. Panels (b), (d) and (f) show the difference (V-V_{gr}) on the respective levels. SLP and geopotential height are shown by the black and white contours respectively. Light grey, grey and black markers indicate trajectory from initialisation times of 1000, 1100 and 1200 UTC, respectively, while marker shapes indicate initialisation level: circles - 780 hPa, triangles - 850 hPa, diamonds - 925 hPa. White/black cross indicates the computed centre of curvature.

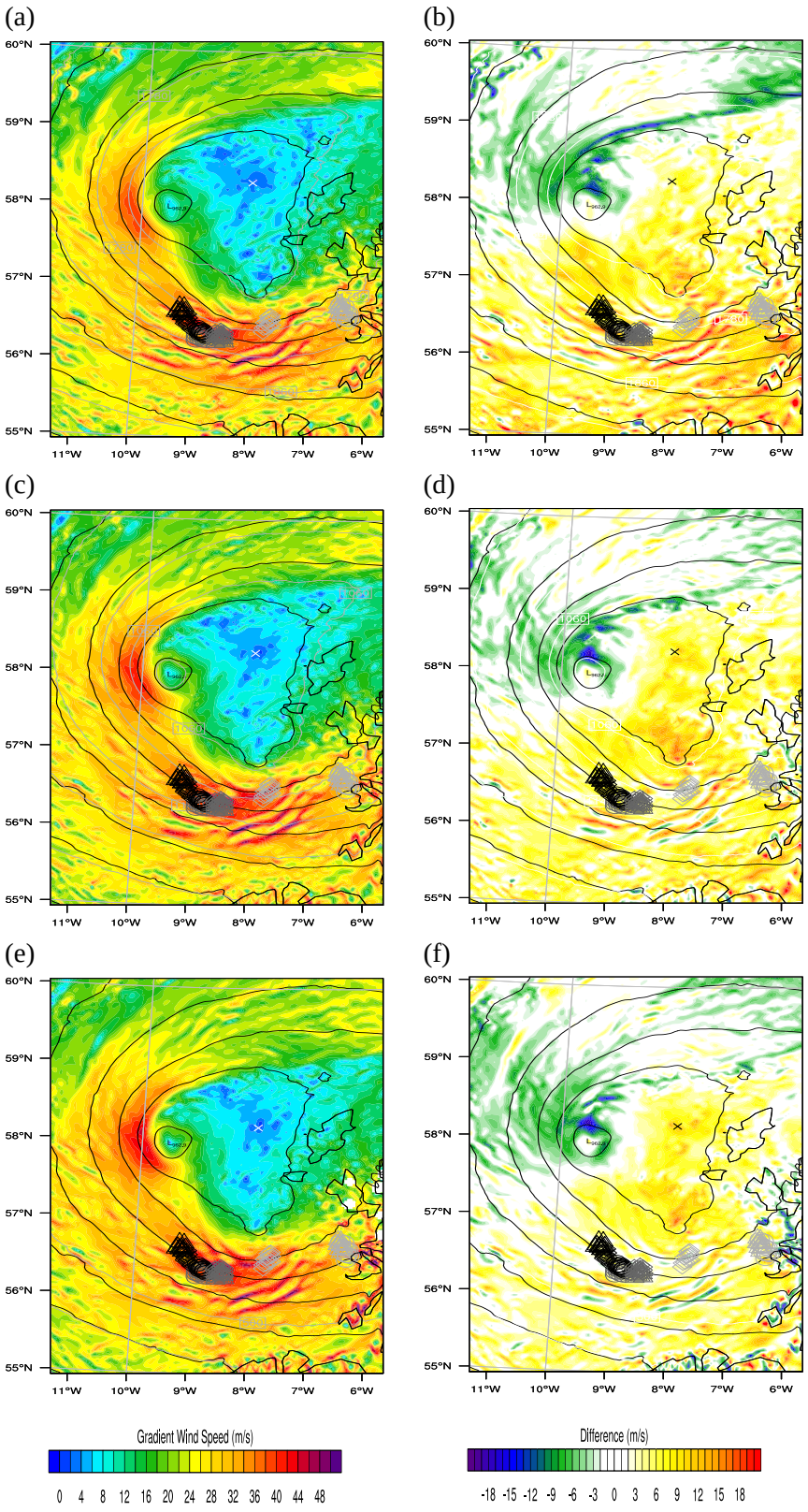

FIGURE 5.27: Gradient wind at 1100 UTC on (a) 780 hPa, (c) 850 hPa and (e) 925 hPa. Panels (b), (d) and (f) show the difference (V-V_{gr}) on the respective levels. SLP and geopotential height are shown by the black and white contours respectively. Light grey, grey and black markers indicate trajectory from initialisation times of 1000, 1100 and 1200 UTC, respectively, while marker shapes indicate initialisation level: circles - 780 hPa, triangles - 850 hPa, diamonds - 925 hPa. White/black cross indicates the computed centre of curvature.

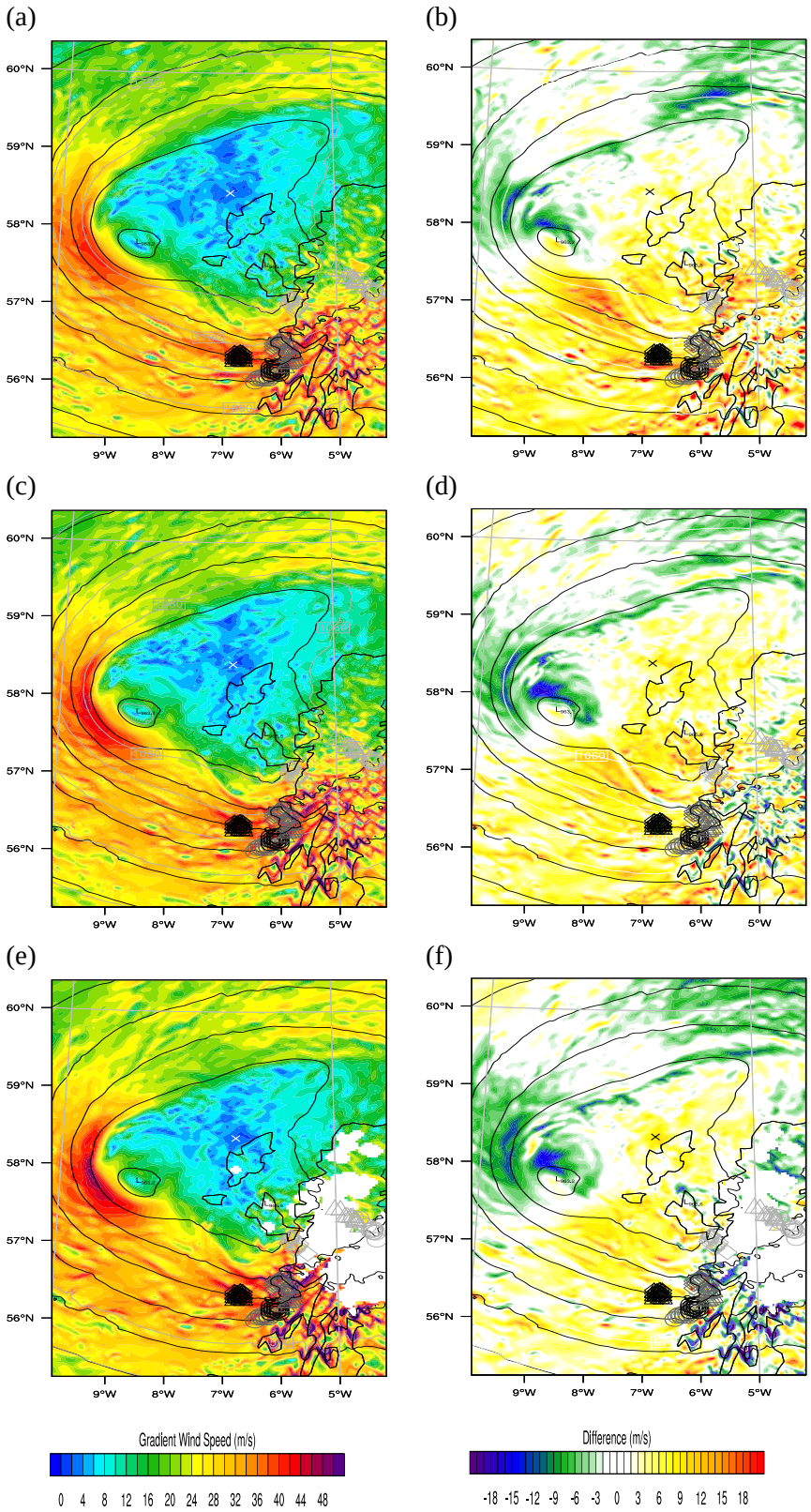

FIGURE 5.28: Gradient wind at 1200 UTC on (a) 780 hPa, (c) 850 hPa and (e) 925 hPa. Panels (b), (d) and (f) show the difference (V-V_{gr}) on the respective levels. SLP and geopotential height are shown by the black and white contours respectively. Light grey, grey and black markers indicate trajectory from initialisation times of 1000, 1100 and 1200 UTC, respectively, while marker shapes indicate initialisation level: circles - 780 hPa, triangles - 850 hPa, diamonds - 925 hPa. The white or black cross indicates the computed centre of curvature.

TABLE 5.3: Gradient Wind Calculation Values. Lat and Lon indicate the location of the CCP and r^2 shows the correlation of the R against *z* for this CCP

Level (hPa)	Time (UTC)	Lat	Lon	r^2
780	1000	58.21	-9.01	0.946
	1100	58.31	-7.99	0.941
	1200	58.45	-6.92	0.912
850	1000	58.16	-8.90	0.946
	1100	58.28	-7.94	0.940
	1200	54.43	-6.87	0.911
925	1000	58.11	-8.85	0.947
	1100	58.20	-7.88	0.942
	1200	58.37	-6.81	0.916

The effect of curvature in the idealised flow can be seen in the gradient wind plots (Figures 5.26-5.28). Compared to the geostrophic wind (Figure 5.20) the gradient flow is significantly closer to the real wind values. Figures 5.26 (a), (c) and (e) show the gradient wind on 780, 850 and 925 hPA respectively at 1000 UTC. Regions of strong gradient wind (>40 ms^{-1}) exist to the south and south-west of the cyclone centre. A second intense region to the north-west of the centre is also present. The t1000- trajectory swarms are initiated at this time. The t1000-780 and -850 sets can be seen towards the south-east of the low (light-grey circles and triangles, respectively). These reside in a region of moderately strong gradient wind with values of ~35 ms^{-1}. The t1000-925 trajectories are more westward (light-grey diamonds) and are situated within a region of strong gradient flow (~40 ms^{-1}). The V-V_{gr} difference plots (Figures 5.26 (b), (d) and (f)) indicate that these regions show different levels of balance. The -780 trajectories are situated on a ribbon of super-gradient flow with V-V_{gr} values up to 20 ms^{-1} (Figure 5.26 (b)). At the 850 hPa level the parcels are still in a super-gradient region but the magnitude is lesser at around 8 ms^{-1} (Figure 5.26 (d)). By contrast the -925 trajectories sit in a region of largely balanced flow (Figure 5.26 (f)). Much of the flow to the south and west of the cyclone centre is super-gradient although the magnitude is generally less than 10 ms^{-1}. The t1000-780 trajectories however reside in a relatively small region of far higher super-gradient flow.

Figures 5.27 (a), (c) and (e) show that by 1100 UTC the main region of high (>40 ms^{-1}) gradient wind has propagated around to the south of the cyclone centre. The secondary region to the north-west has also moved southwards and strengthened slightly. The trajectories initiated at this time are indicated by the gray markers. All of these are located in a region of ~40 ms^{-1} gradient wind to the south of the cyclone. The V-V_{gr} difference plots for each level shows that again the upper

two levels (Figures 5.27 (b) and (d)) are more super-gradient than the 925 hPa level trajectories (Figure 5.27 (f)). The magnitude of the V-V_{gr} difference is not as high at any of the levels as that seen for the t1000-780 trajectories in Figure 5.26 (b).

At 1200 UTC the southern region of high gradient wind has moved to the west coast of Scotland and is becoming influenced by the orography here (Figure 5.28). Again, the second region to the west has intensified, reaching 50 ms^{-1}. The t1200 trajectories (black markers) are again located within the broad region of super-gradient flow to the south and west of the cyclone (Figures 5.28 (b), (d) and (f)). Over the land some regions are showing sub-gradient balance due to the effects of the orography. As with the previous times shown the upper levels show a greater magnitude of super-gradient flow compared to the lower levels.

The difference plots show that the gradient wind is lower than the actual wind to the south of the cyclone. There is some error associated with the unsymmetrical flow and the choice of CCP location as shown in Figures 5.24 and 5.25. Indeed, Figure 5.25 shows an increased accuracy of CCP producing a lower gradient wind speed suggesting that the flow may be even more unbalanced than indicated in the plots. Although many of the trajectories exhibit super-gradient flow at their peak, the t1000-780 trajectories are shown to be more unbalanced. This may be due to the descent of higher momentum air from above to the 780 hPa level.

5.3.3 Bernoulli Function

The Bernoulli theorem states that for steady, non-frictional flow, under adiabatic conditions the Bernoulli number (B) will remain constant. Schär (1993), following Gill (1982), define the Bernoulli equation as:

$$B = \frac{1}{2}\mathbf{U}^2 + c_pT + gz, \tag{5.8}$$

where B is a constant, **U** is the 3-D velocity vector, c_p is the specific heat capacity at constant pressure and gz is the geopotential (Φ). The term $c_pT + gz$ is also known as the Montgomery Potential (M). The equation shows that an ideal gas undergoing isothermic descent under adiabatic conditions would show an increase in wind speed in order to retain the balance. If these assumptions were true, the Bernoulli equation could describe the acceleration of the SJ parcels as they descend from the cloud head.

The Bernoulli function and its constituent parts has been calculated along the t1000-780 trajectories which exhibit SJ characteristics, as shown in Figure 5.29. These trajectories show strong acceleration as they descend between 0800 UTC and 1000 UTC (Figure 5.7), if the Bernoulli principle holds then the function would remain constant with the descent balancing the increase in wind speed. Figure 5.29 (a), however, shows the Bernoulli function is not constant along the flow indicating that the assumptions of steady-state are not valid in this case. The variations in the Bernoulli function are largely due to the cpT function (Figure 5.29 (d)), which shows a higher increase than the lessening of ϕ function during the descent period. The $\frac{1}{2}\mathbf{U}^2$ function is of a much smaller magnitude than the other terms of the equation (Figure 5.29 (e)), and so contributes little to the overall Bernoulli function.

That the storm is still deepening over the course of the trajectories, although the deepening has slowed somewhat by the time of the trajectory descent, provides an explanation for the failure of the Bernoulli function in this case. Equation 5.8 also assumes adiabatic motion, the presence of moisture here may also be a factor in the balance not holding true, the effect of moisture processes and latent heating are investigated in Section 5.4. In other cases where a greater degree of balance may be achieved the Bernoulli function may in part explain the acceleration coincident with the descent of the SJ parcels and therefore may be of interest for future studies.

5.4 Latent Heating and Cooling Processes

As described in Chapter 3 the Morrisson microphysics scheme used here outputs latent heating diagnostics. These variables account for all of the latent heating processes from the microphysics scheme. A number of papers have identified the possible role of evaporative cooling as a mechanism for the high winds in sting jets (e.g. Browning (2004); Clark et al. (2005)), although some recent studies have cast doubt on this hypothesis (Baker et al., 2013; Slater et al., 2014; Smart and Browning, 2014). The diagnostics used here allow the investigation of this hypothesis for the high winds within Cyclone Friedhelm.

As shown above the t1000-780 trajectories show some of the characteristics of a SJ. The trajectories show rapid descent along with significant drying (Figure 5.7 (a), (d) and (c)). As previously mentioned, cooling through evaporation and sublimation has previously been proposed as a driver for SJ descent. Figure 5.30 (a) shows the latent heating rate from the microphysics scheme diagnostics. The descent after 0800 UTC (navy line) shows evidence of some cooling in Figure

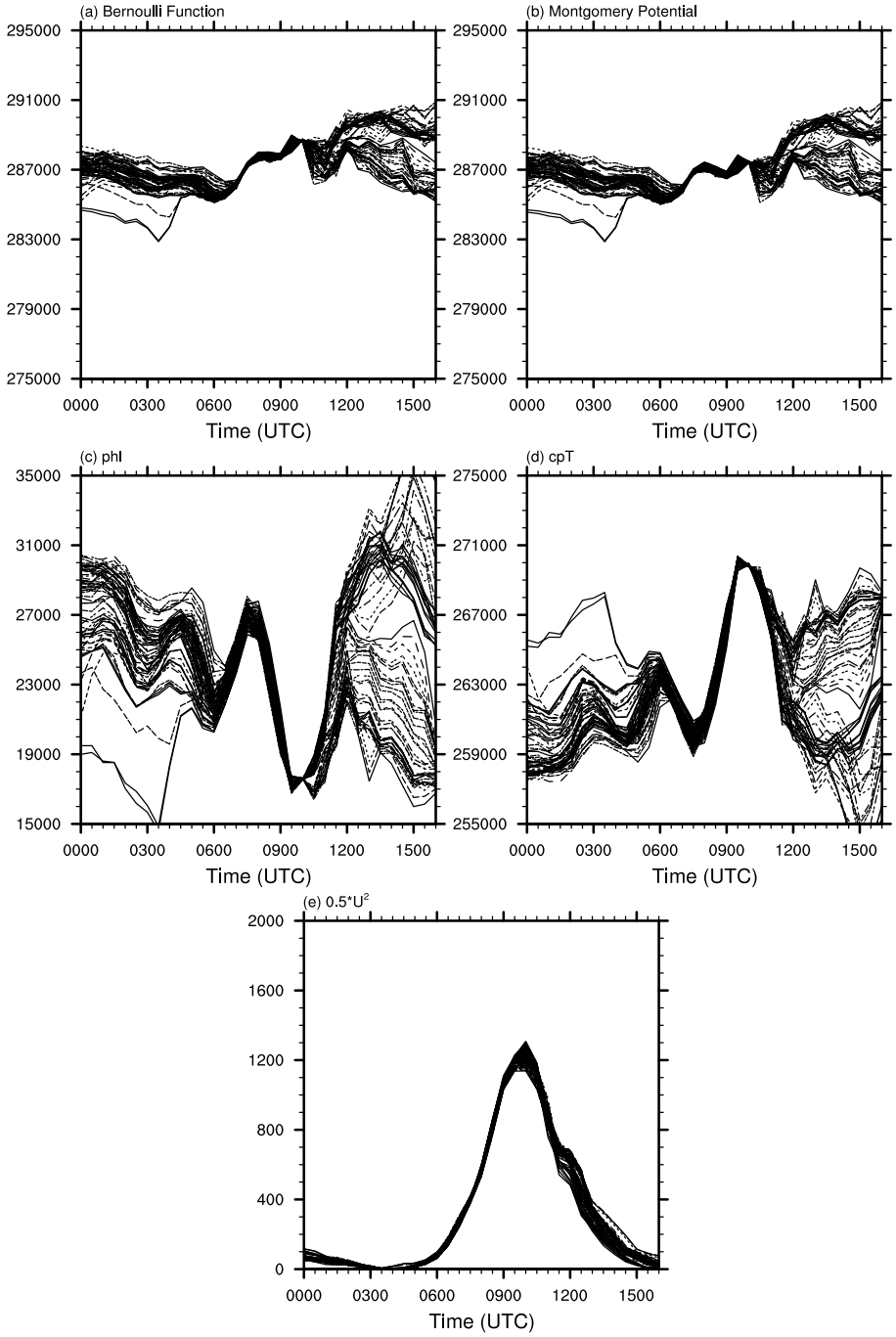

FIGURE 5.29: Bernoulli Function and equation terms along the t1000-780 trajectories. (a) Bernoulli number (B); (b) Montgomery Potential M; (c) Φ (zg); (d) c_pT; (e) $\frac{1}{2}\mathbf{U}^2$. Y-axis spacing on (a)-(d) is equal for comparison, spacing on (e) is reduced by a factor of 10.

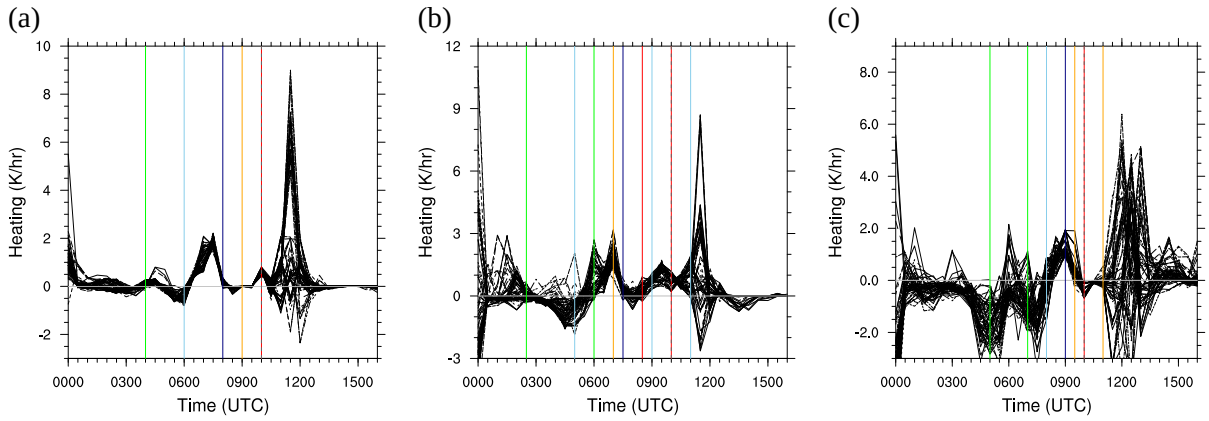

FIGURE 5.30: Time series of latent heating rate (K/hr) for trajectory swarms (a) t1000-780 (b) t1000-850 and (c) t1000-925. Coloured lines are as Figures 5.7, 5.8 and 5.9, respectively.

5.30 (a), however the magnitude of this is small with values reaching -0.5 K hr^{-1}. The periods of strong ascent at 0800 UTC (light blue line) and after 1100 UTC (red/grey-dashed line) can clearly be seen in the plots with strong latent heating from condensation occurring. The t1000-850 trajectories also undergo a period of strong descent (Figure 5.8), however only some of the trajectories show any latent cooling at this point (Figure 5.30 (b)). This lack of latent cooling in both the t1000-780 and -850 during the periods of descent may account for the high static stability shown in Figure 5.11 that inhibits further descent. At 0500 UTC there is greater cooling immediately before the trajectories ascend and undergo a strong degree of latent heating through condensation. The relatively low level of the trajectories at this time means evaporation/sublimation of hydrometeors as they fall through the layer is the cause for the cooling here. The t1000-925 trajectories show the highest levels of latent cooling during the analysis, particularly at 0700 UTC, 0930 UTC and around 1200 UTC (Figure 5.30 (c)). This is mainly due to the sublimation of snow falling through the trajectories at low level at the earlier times and evaporation of droplets at the later times.

The t1100- and t1200-850 and -925 trajectory ensembles (Figures 5.31 and 5.32 (b) and (c)) show general cooling for much of the analysis as they travel underneath the precipitating frontal region. The swarms of these which undergo ascent tend to see some latent heating from condensation. The t1200-850 parcels (Figure 5.32 (b)) also see latent heating as they descend from 1000 UTC -(blue line) to 1200 UTC (red line).

Unlike the other trajectory streams the t1200-850 trajectories see a latent heating effect as they descend immediately prior to the maximum wind speed.

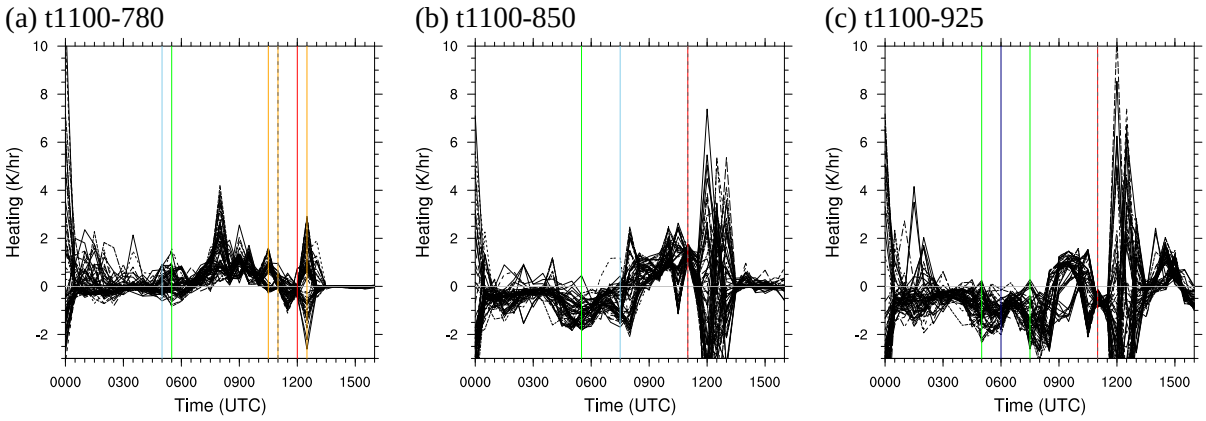

FIGURE 5.31: Time series of latent heating rate (K/hr) for trajectory swarms (a) t1100-780 (b) t1100-850 and (c) t1100-925. Coloured lines are as Figures 5.13, 5.14 and 5.15, respectively.

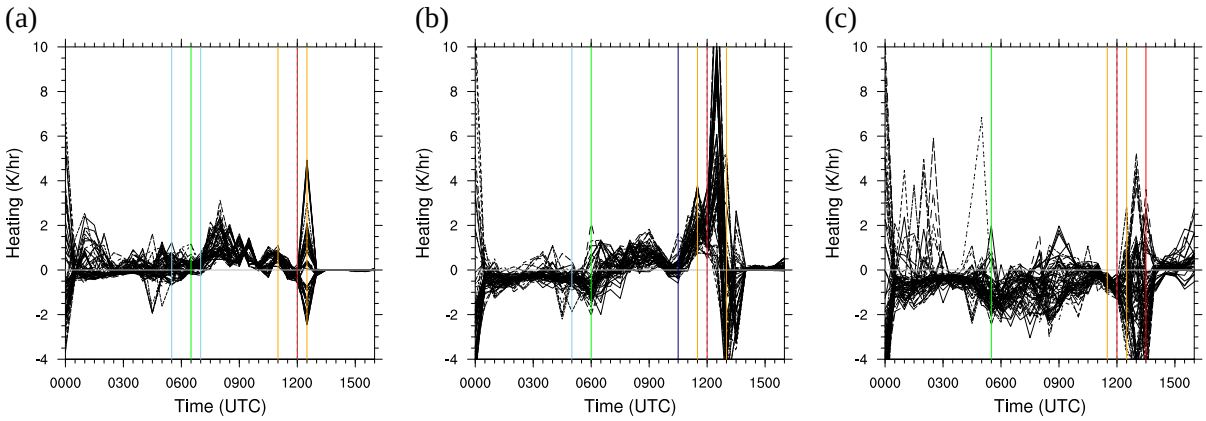

FIGURE 5.32: Time series of latent heating rate (K/hr) for trajectory swarms (a) t1200-780 (b) t1200-850 and (c) t1200-925. Coloured lines are as Figures 5.17, 5.18 and 5.19, respectively.

5.5 Frontogenesis

As discussed in Section 2.4.3, Schultz and Sienkiewicz (2013) identified the secondary circulations associated with a frontolytic region at the end of the bent back front, to be the possible cause of the descent of the sting jet. Here Cyclone Friedhelm is examined within this context to investigate the possibility that descent of the strong 780 hPa winds shown in Figures 5.6 and 5.7 is due to the presence of frontolysis.

As described in Schultz and Sienkiewicz (2013), following Petterssen (1936) frontogenesis (F) can be described as:

$$F = \frac{d}{dt}|\nabla_H \theta| \tag{5.9}$$

where,

$$\frac{d}{dt} = \frac{\partial}{\partial t} + u\frac{\partial}{\partial x} + v\frac{\partial}{\partial y} \tag{5.10}$$

$$\nabla_H = \mathbf{i}\frac{\partial}{\partial x} + \mathbf{j}\frac{\partial}{\partial y} \tag{5.11}$$

Therefore the frontogenesis is the Lagrangian rate of change of the magnitude of the gradient of θ. This form of the frontogenesis considers only the horizontal θ gradient. Equation 5.9 can be written as (Keyser et al., 1988; Schultz and Doswell, 1999):

$$F = \frac{1}{|\nabla_H \theta|}\left[\frac{\partial \theta}{\partial x}\frac{d}{dt}\left(\frac{\partial \theta}{\partial x}\right) + \frac{\partial \theta}{\partial y}\frac{d}{dt}\left(\frac{\partial \theta}{\partial y}\right)\right], \tag{5.12}$$

where,

$$\frac{d}{dt}\left(\frac{\partial \theta}{\partial x}\right) = -\frac{\partial u}{\partial x}\frac{\partial \theta}{\partial x} - \frac{\partial v}{\partial x}\frac{\partial \theta}{\partial y} \tag{5.13}$$

and,

$$\frac{d}{dt}\left(\frac{\partial \theta}{\partial y}\right) = -\frac{\partial u}{\partial y}\frac{\partial \theta}{\partial x} - \frac{\partial v}{\partial y}\frac{\partial \theta}{\partial y}. \tag{5.14}$$

Equations 5.13 and 5.14, therefore assume adiabatic motion. Following Schultz and Zhang (2007) equation 5.9 can be expanded to:

$$F = \frac{1}{|\nabla_H \theta|}\left[\frac{\partial \theta}{\partial x}\left(-\frac{\partial u}{\partial x}\frac{\partial \theta}{\partial x} - \frac{\partial v}{\partial x}\frac{\partial \theta}{\partial y}\right) + \frac{\partial \theta}{\partial y}\left(-\frac{\partial u}{\partial y}\frac{\partial \theta}{\partial x} - \frac{\partial v}{\partial y}\frac{\partial \theta}{\partial y}\right)\right] \tag{5.15}$$

Following Equation 5.15, positive frontogenesis is therefore defined as regions where the θ is instantaneously sharpening while negative frontogenesis (frontolysis) indicated regions were the isotherms of θ are spreading. Due to the high resolution within the inner domain there are large areas of small-scale noise in the frontogenesis field. Therefore the frontogenesis plots, to follow, are smoothed to remove this noise and make the key features clearer. The smoothing is done by passing the data through a 9-point smoothing function in NCL. This is done 20 times in order to reduce the noise, while retaining the large-scale features.

The t1000-780 and -850 trajectories show the most clear descent prior to highest winds (Figures 5.7 and 5.8). As described earlier, the t1000-780 trajectories descend slightly between 0700 UTC and 0800 UTC before descending rapidly thereafter whereas the t1000-850 trajectories undergo

rapid descent immediately at 0730 UTC. Figures 5.33 (a) and (b) show the locations of these trajectories in relation to the frontogenesis at 0700 UTC when the transition from ascent to descent takes place. At 700 hPa the frontogenesis shows a strong band extending across the northern edge of the cyclone centre and around the north-western side. To the inside of this there is a band of frontolysis, which is particularly strong in two regions to the north and west of the cyclone center. The lower-level frontogenesis field differs to this. The frontogenetic band is broken by regions of frontolyis rather than the latter residing as a band to the inside. Both sets of trajectories are located in the proximity of the frontal region at their respective levels with the t1000-780 parcels on to the cold side of the frontogenetic region at around 700 hPa (Figure 5.33 (a)) and the t1000-850 parcels further south-east in the frontolytic region at around 850 hPa (Figure 5.33 (b)). The t1000-780 trajectories lag slightly behind the t1000-850 trajectories at both times, which could explain why they descend slightly later. The locations of the trajectory ensembles can be seen in the two cross-sections (Figures 5.33 (c) and (d)). The t1000-780 cross section (Figure 5.33 (c)) shows the strong frontogenetic region with the trajectories located on its western side, to the east is a strong frontolytic region. Unlike the SJ shown in Schultz and Sienkiewicz (2013) the t1000-780 trajectories are towards the cold side of the frontal region. The t1000-850 trajectories reside more within the frontal region. The frontogenesis extends from the surface to above 550 hPa, a large strong region is prominent at the surface from 13°W to 12.3°W. The frontolytic region is limited in its lower vertical extent by this strong low-level frontogenetic region meaning it only extends from ~820 hPa upwards. There are strong vertical motions associated with the frontal region, these are centred around the transition between frontogenesis and frontolysis. The t1000-850 cross-section (Figure 5.33 (d)) shows that marginally downstream of Figure 5.33 (c) the frontolysis has become dominant. The t1000-850 trajectories are located near the lower reaches of the strongest frontolytic region at ~860 hPa. At this point they are still associated with a region of relatively strong ascent which extends westwards and up to the edge of the frontolytic region. The vertical motions in both the 0700 UTC cross-sections are more complex than those shown in Schultz and Sienkiewicz (2013) with multiple regions of ascent and descent on both sides of the main frontal region.

By 0800 UTC the trajectories have propagated with the flow and now reside to the south-west of the cyclone centre (Figures 5.34 (a) and (b)). Generally, the frontogenesis on the western side of the cyclone has weakened with frontolytic regions becoming more prominent at both 700 hPa (Figure 5.34 (a)) and 850 hPa (Figure 5.34 (b)). The t1000-780 trajectories still reside around 700 hPa; they have moved closer to the frontolytic region and reside on the inside of the frontogenesis (Figure 5.34 (a)). The t1000-850 trajectories are at an altitude of around 820 hPa at this time, marginally

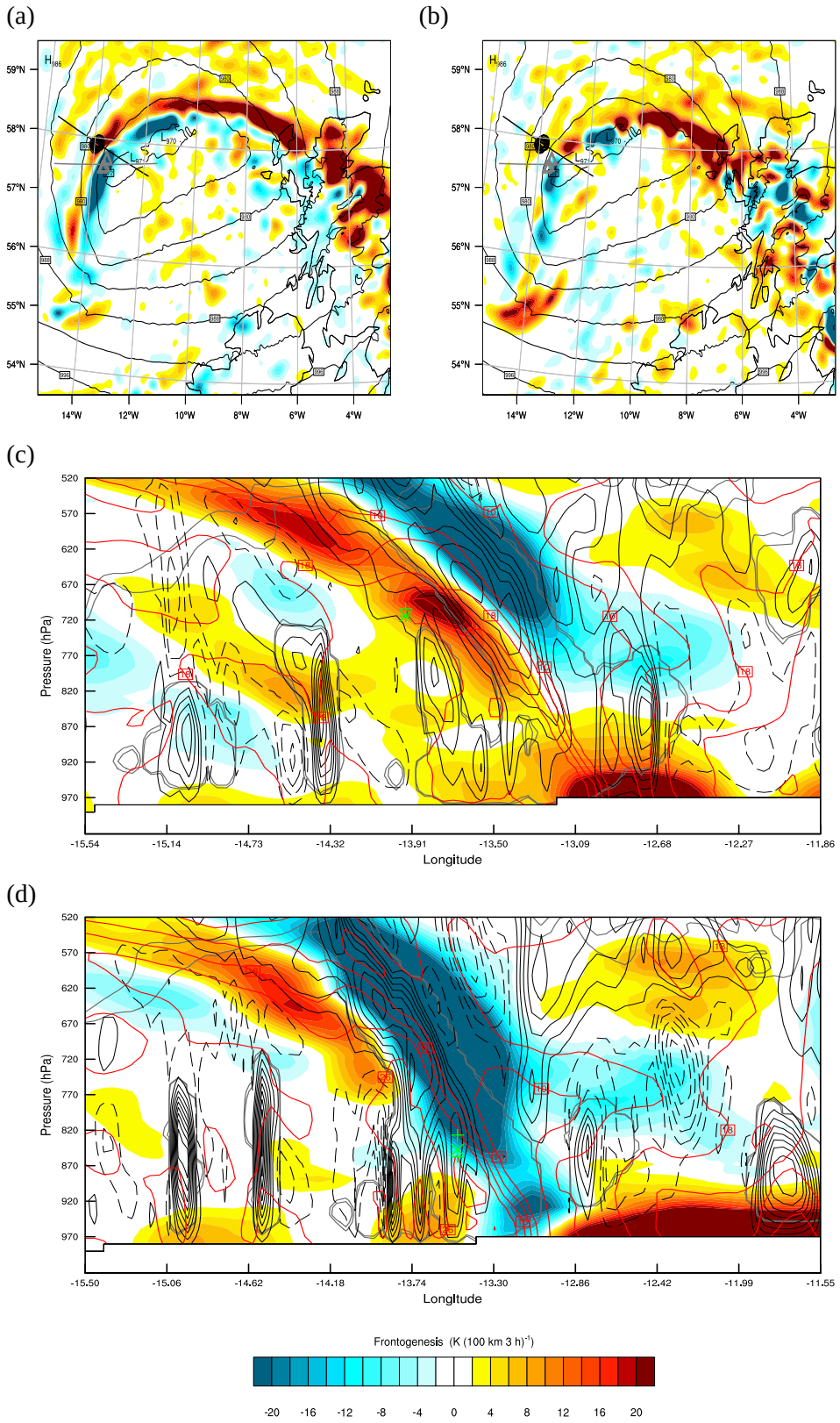

FIGURE 5.33: Frontogenesis at 0700 UTC. (a) and (b) show frontogenesis (shading) on the 700 and 850 hPa levels, respectively, with SLP (black contours). Black circles denote the locations of the t1000-780 trajectories with the black line indicating the location of the cross section shown in (c). Grey triangles and line indicates the t1000-850 trajectory location and the cross section in (d). (c) and (d) show frontogenesis (shading) on the cross-sections indicated by the black and gray lines in (a) and (d), respectively. Red contours indicate horizontal wind speed (every 4 ms^{-1}), black lines show vertical wind speed (every 0.1 ms^{-1}, negative dashed, zero suppressed) and grey contours indicate the cloud mixing ratio (0.005 and 0.001 g kg^{-1}). Green cross indicates mean trajectory pressure, with pluses showing maximum and minimum trajectory pressure.

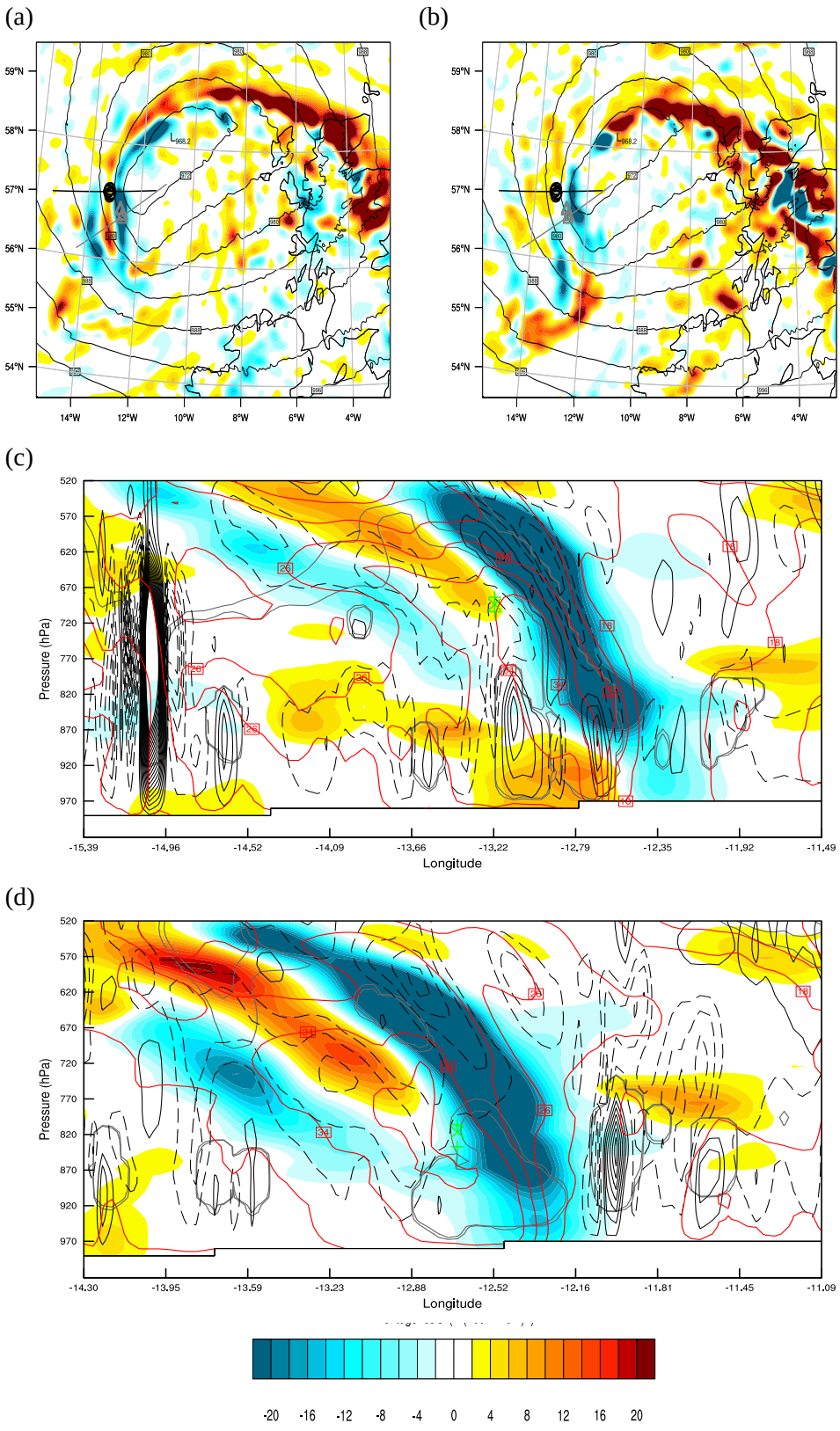

FIGURE 5.34: As Figure 5.33 but for 0800 UTC.

higher than the frontolysis field shown in Figure 5.34 (b). They are in a region dominated by frontolysis at this level. The cross-section for the t1000-780 trajectories shows these located at the bottom tip of a relatively weak region of elevated frontogenesis (Figure 5.34 (c)). They are located in regions of ascending air at this point. In contrast to Figure 5.33 (c) the frontolysis is stronger here and the frontogenesis is weakening. Although a region of frontogenesis exists at lower levels and is associated with some ascent and convection, large regions of descent have formed on the cold side of the front and on the western edge of the strong frontolytic region. Further along the cyclonic flow, the t1000-850 cross-section (Figure 5.34 (d)) shows a strong band of frontolysis dominates and frontogenesis around the frontal region limited to above 770 hPa. The t1000-850 trajectories are located on the western edge of the frontolysis at ~820 hPa. These are close to the highest winds of ~38 ms^{-1} located just to the west and south of the trajectories. The vertical motion shows large-scale descent located within the frontolysis region and to the cold side. There is also some descent close to the east of the frontolysis region interrupted by a small region of convection at 12.2°W.

The situation presented here is somewhat unlike that shown by Schultz and Sienkiewicz (2013), where the secondary circulations show ascent on the cold side of the frontal region (see Figure 2.6). The frontolytic reversal of the vertical motions as shown by Keyser and Pecnick (1985) which occur in the case of Schultz and Sienkiewicz (2013), with large scale ascent on the cold side and descent on the warm side, are not seen here. Instead the picture is complicated by numerous regions of low-level ascent as well as large-scale descent on the cold side even in the frontolytic regions. Figure 5.33 shows the t1000-780 trajectories being slightly upstream of the -850 ones, meaning that they reach the frontolytic region and descend slightly later. This shows that movement from frontogenetic to frontolytic regions could be the cause for the descent of the SJ like trajectories here although the mechanisms are unclear. However the t1000-850 trajectory cross-sections show that there is some adjustment time needed for the large scale descent to occur within the frontolytic region.

5.6 Potential Vorticity

The storm shows a strong, distinct band of high diabatic PV associated with the bent-back front. This is shown in Figure 5.35, along with contours of the high wind speeds and the trajectory locations. The strong PV ribbon extends around the north and western sides of the cyclone at 0600

UTC (Figure 5.35 (a)) with the trajectories located away from this region further to the north. A large "blob" of PV is located to the south-west of the cyclone centre which is associated with a small region of higher winds. The PV ribbon stretches around the cyclone centre and towards the centre at its south-western-most region. At 0800 UTC the trajectories have propagated towards the cyclone centre and are located just to the cold side of the PV band. The larger region of stronger winds has developed to the south and south-west of the cyclone centre. By 1000 UTC (Figure 5.35 (c)) the PV band has begun to circle around the southern side of the cyclone. At this time the t1000- trajectories are at their respective initialisation locations (light grey markers). The regions of highest winds reside to the outside of the regions of highest PV. This is similar to the idealised simulation results in Figure 7 of Schemm and Wernli (2013), reproduced here in Figure 5.36. By 1200 UTC (Figure 5.35 (d)), the southern region of PV has weakened with the highest values of PV largely restricted to the north-west side of the cyclone centre. A weaker region extends to the south of the cyclone exhibiting values of 2-3 PVU. It is near this area in which the t1100- and t1200- trajectories reside. Again these high wind locations and their related trajectories are located to the outside of the high PV regions. The northern and eastern regions of the high-PV ribbon have also weakened, this suggests an increase in the frontal fracture and a movement of the CF and WCB southwards lessening the low-level PV generation caused by the WCB ascent (Schemm and Wernli, 2013).

Figure 5.37 shows the evolution of the strong PV band. As shown in the plots the band is clearly exhibited throughout the lower levels of the atmosphere, although it less well-defined at the lower levels where diabatic heating gradients are lesser. The band propagates steadily eastwards with the storm motion, however, the shape of the band changes dramatically at times. Over the first four hours shown (0600 UTC - blue to 1000 UTC - yellow) the band grows and extends around the west and south-west of the cyclone 700 hPa (Figure 5.37 (a)). However, at 1100 UTC (orange contour) the main region of PV retreats back towards the north-west side with a cut-off region moving further to the south and east. Following this the high PV band begins to extend around the west and south-west of the cyclone. At 850 hPa (Figure 5.37 (c)) the cut-off and retreat of the south-western end of the band occurs at 0700-0800 UTC (Dark and light green contours). From 1000 UTC (yellow contours) onwards the band regrows towards the south-west and south again. The cut off region at 850 hPa continues for some time propagating with the flow to the south of the cyclone.

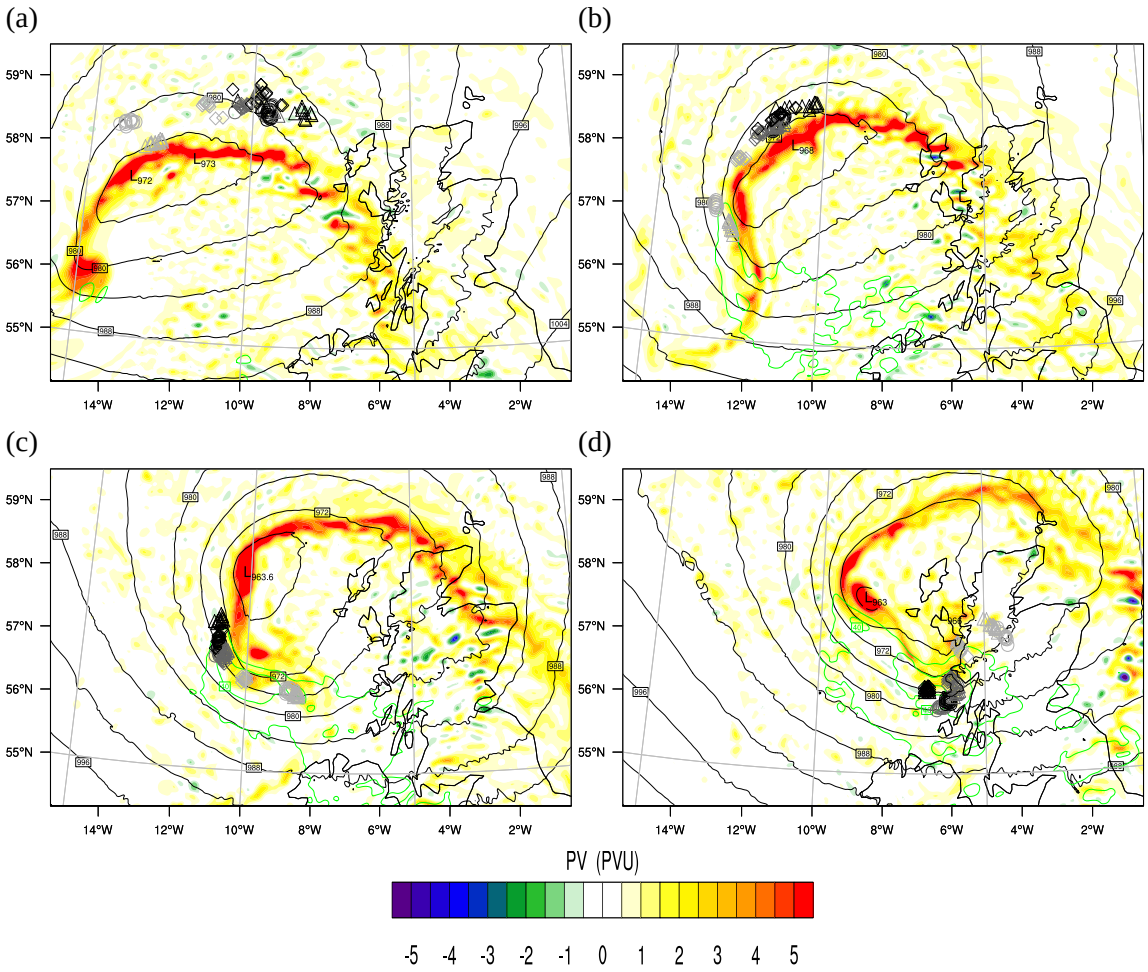

FIGURE 5.35: 850 hPa PV (shaded), wind speed (green contours, every 5 ms^{-1} from 35 ms^{-1}) SLP (black contours, every 4 hPa) and trajectory location shown every 2 hours from 0600 UTC to 1200 UTC ((a)-(e) respectively). White, gray and black markers indicate trajectory initialisation times of 1000, 1100 and 1200 UTC, respectively, while maker shapes indicate initialisation level: circles - 780 hPa, triangles - 850 hPa, diamonds - 925 hPa. The PV and wind speed have been passed through a smoother 5 and 2 times respectively to reduce the small scale noise.

5.6.1 Relationship of Potential Vorticity to Absolute Vorticity

As stated in Section 2.2.3, PV is a measure of the vorticity and static stability. Therefore PV is related to the momentum of the air through the vorticity equation. Figure 5.38 shows how the absolute vorticity (η) relates spatially to the PV and the high winds. The regions of high η correlate strongly with the regions of high PV. The highest winds therefore, reside to the outside of the strong η and PV ribbon. The strongest regions of high η are consistently located to the northern region of the band, particularly to the north-western and north-eastern sides of the cyclone centre. These are the same regions that are also associated with some of the highest PV values. These "corners" of the cyclone show strong poleward motion enhancing the $\partial v/\partial x$ cyclonic contribution

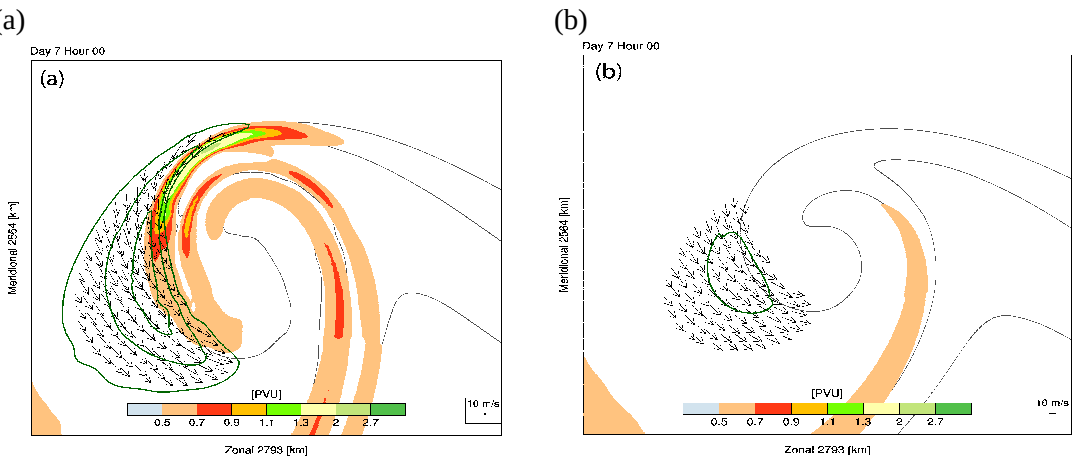

FIGURE 5.36: Figure 7 from Schemm and Wernli (2013): Low-level vertically averaged (1000-850hPa) PV and wind for (a) the moist idealized simulation and (b) a dry simulation. Also shown are the 290-, 295-, and 300-K isentropes at 850 hPa and the region of strong low-level wind 30, 35, and 40 ms^{-1}; green contours)

to the vorticity. The highest winds however are located further downstream of these high vorticity regions.

There are two regions of highest η to specifically note. One high η region propagates around the system over the times shown in Figure 5.38. At 0600 UTC this can be seen as two closely located regions zonally stretched at ~57.75°N, centred around 10°W (Figure 5.38 (a)). Two hours later, Figure 5.38 (b) shows that these are still centred around 10°W although the storm has moved eastwards. The western region of this η region has begun to rotate cyclonically, and is now orientated south-south-west to north-north-east. By 1000 UTC (Figure 5.38 (c)) this region is located on the north-west corner of the cyclone centre as the cyclone centre has moved further eastwards. The western part of the region has rotated further with a near exactly north-south orientation. At 1200 UTC (Figure 5.38 (d)) this region has propagated slightly westwards to ~9°W and has weakened. The western region has continued to rotate rapidly and is orientated north-west to south-east. It has weakened somewhat with values of around 140 $10^{-5}s^{-1}$. The eastern region (now located marginally more westwards) has shrunk but is still strong with values over 200 $10^{-5}s^{-1}$.

The second notable region is to the north-west of the cyclone centre at 0600 UTC (Figure 5.38 (a)). This regions propagates west with the cyclone and moves south with the flow, being located to the west of the cyclone centre in Figure 5.38 (b). It has weakened somewhat by this time with values ~160 $10^{-5}s^{-1}$. At 1000 UTC it moves further to the south-west of the cyclone centre and had spread out and weakened to ~100 $10^{-5}s^{-1}$. This region then breaks off from the main band

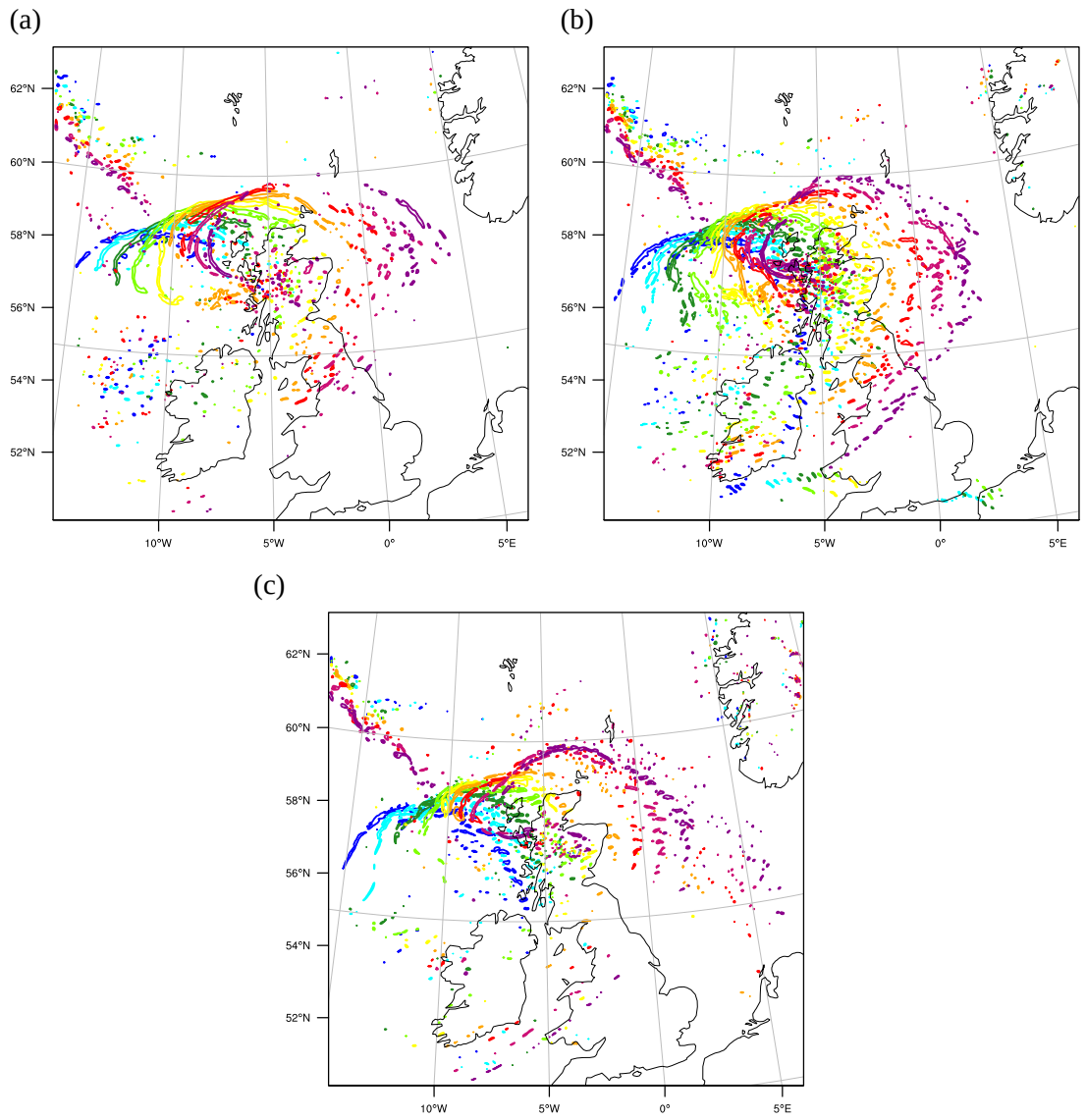

FIGURE 5.37: Evolution of PV hourly from 0600 UTC to 1400 UTC on (a) 700 hPa, (b) 800 hPa and (c) 900 hPa. Coloured contours show PV=5 PVU where colour denotes time as follows: Blue = 0600 UTC, Cyan = 0700 UTC, Dark green = 0800 UTC, Green = 0900 UTC, Yellow = 1000 UTC, Orange = 1100 UTC, Red = 1200 UTC, Pink = 1300 UTC, Magenta = 1400 UTC.

of high η and is located close to the Scottish coast along with the t1100- and t1200 trajectories at 1200 UTC (Figure 5.38 (d)).

Around the south-west corner the reduction in the η decreases the curvature of the flow allowing an increase in the wind speed and a subsequent wind maximum. In this case this occurs marginally downstream of the largest PGF region due to the convergence of the isobars being coincidental with the highest curvature.

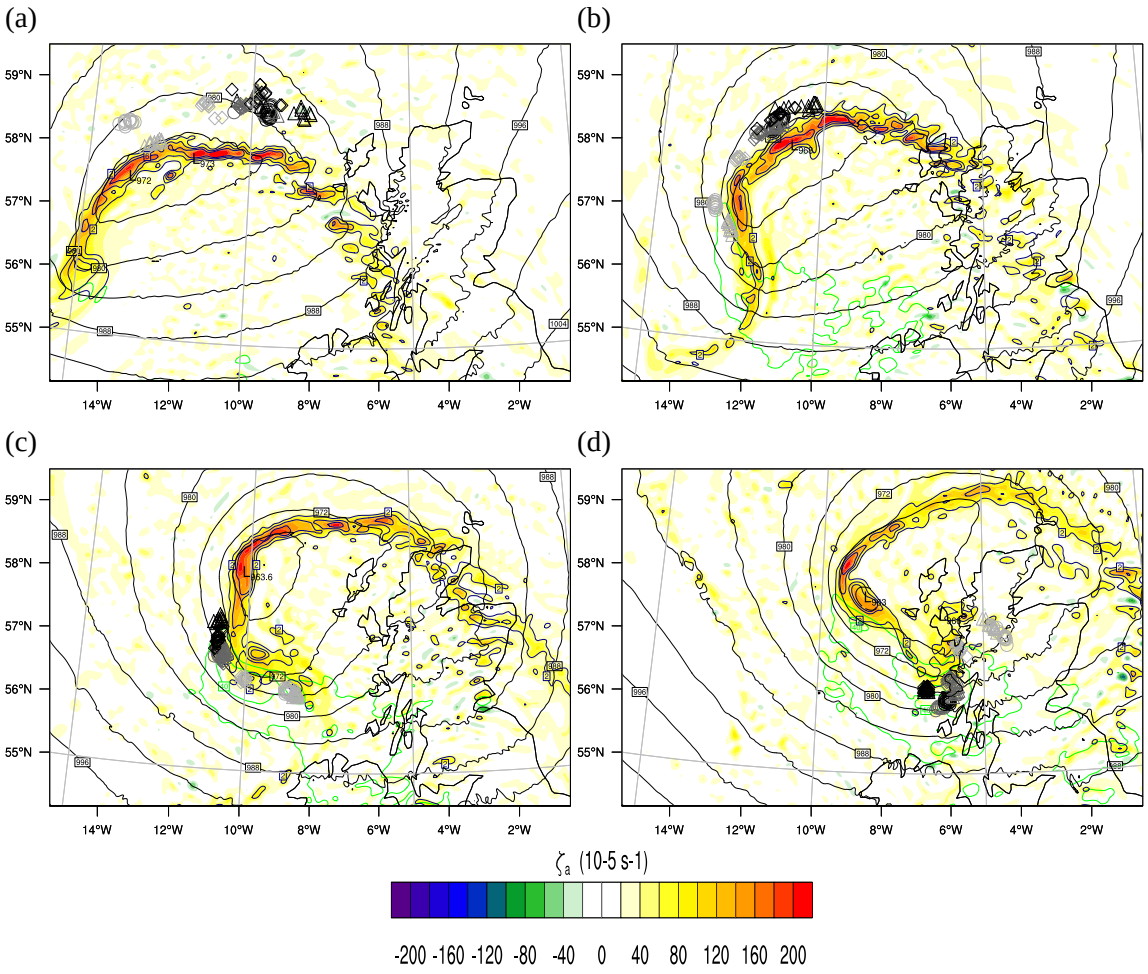

FIGURE 5.38: 850 hPa η (shaded), wind speed (green contours, every 5 ms^{-1} from 35 ms^{-1}), PV (blue contours, every 2 PVU from 2 PVU) and SLP (black contours, every 4 hPa) and trajectory location shown every 2 hours from 0600 UTC to 1200 UTC ((a)-(d) respectively). light-grey, dark-gray and black markers indicate trajectory initialisation times of 1000, 1100 and 1200 UTC, respectively, while maker shapes indicate initialisation level: circles - 780 hPa, triangles - 850 hPa, diamonds - 925 hPa. The η and wind speed have been passed through a smoother 5 and 2 times respectively to reduce the small-scale noise.

5.7 Summary

This chapter defines the evolution of the wind field in cyclone Friedhelm and the important processes in developing the high winds. This then provides a framework for the analysis of sensitivity runs which are presented in Chapter 6.

The trajectory analyses focus on trajectories initiated from the proximity of the maximum wind speed location on the 780, 850 and 925 hPa levels at 1000, 1100 and 1200 UTC on the 8th December as Friedhelm approached the UK. As shown above the t1000-780 trajectories show a number of the characteristic of SJs, such as: descent from mid-levels, conserved θ_w and decreasing RH_i.

Other trajectory swarms show clear evidence of CCB characteristics, these occur lower in the atmosphere and reach similar, if slightly lower maximum wind speeds that the SJ trajectories.

A number of key themes emerge from the trajectory analysis. Descent prior to maximum wind values is seen in a number of trajectory swarms. The descent of the trajectories is often limited by low-level cloud and mixing of the air parcels into regions of convection. High static stability under the trajectories is shown to inhibit the descent and supports the previous work of Schultz and Sienkiewicz (2013). This indicates that this could be another possible simple forecasting tool for the prediction of surface-reaching SJs.

In nearly all the 780 and 850 hPa initiated trajectories there is drying of the parcels prior to the maximum winds. If considering the t1000-780 SJ trajectories in isolation this would appear to support the suggestion of Browning (2004) that latent cooling through evaporation may help drive the descent of the SJ and intensify the low-level winds. However, a number of the trajectory sets which do not descend also show similar levels of drying. The drying of the air parcels is indicative of them exiting the cloud head and moving into the frontal fracture region as shown in previous studies (Browning, 2004; Clark et al., 2005; Martínez-Alvarado et al., 2011).

Another consistent feature is the delay between the maximum geostrophic wind and the maximum actual wind. The along-flow PGF plots show that the winds continue to accelerate until the along-flow PGF begins to decline. In some cases such as the t1000-780 trajectories the wind only decelerate once the PGF begins to act against the flow. In others the winds to decrease prior to this.

A new method for the calculation of gradient wind is also presented in Section 5.3.2.1. This relatively simple computation allows the calculation of the gradient wind for a region of interest in a non-symmetric system. The results here show that the wind is not in gradient wind balance with super-gradient values to the south of the cyclone centre and sub-gradient values to the north.

The latent heating diagnostics along the trajectories show no particular theme within the evolution if the high winds. It is evident latent cooling is a regular occurrence in lower-level trajectories as hydrometeors fall through the atmosphere undergoing evaporation and sublimation as they descend. However they still provide a useful tool for analysing the processes which affect the trajectory swarms individually.

Section 5.5 clearly shows that the movement from the large scale frontogenetic regions to those of frontolysis coincides with the start of descent. This appears to support the theory of Schultz and Sienkiewicz (2013), that SJ descent is caused by frontolytic flow. However, the trajectories shown here are located further to the cold side of the frontal region than those in Schultz and Sienkiewicz (2013). The vertical motion in this region does not resemble the secondary circulations shown by Schultz and Sienkiewicz (2013). The region of transition from frontogenesis to frontolysis is complex in terms of the distribution of these factors and the associated air motion. Regions of low level frontogenesis are seen remaining below regions of strong frontolysis, inhibiting the descent. Therefore, using frontogenesis from a single plane may not be an entirely robust way for forecasting SJs and descending motion as was hoped by Schultz and Sienkiewicz (2013). However, there may still be merit in this as a framework for forecasting, but further analyses of different storms must be carried out in order to ascertain this.

A strong PV band is exhibited at low- and mid-levels around the BBF. This region is co-located with high values of vorticity. The highest winds are located to the outside of this region where the PV band ends on the south-west side of the cyclone. The relationship of the diabatic low-level PV to the cyclone deepening will be examined in Chapter 6.

Chapter 6

Sensitivities to Latent Heating and Microphysics

In this chapter the WRF sensitivity runs are analysed within the physical framework set out in Chapter 5. The aim is to answer three main questions:

- Does the lack of graupel or hail affect the modelled storm development?
- What effect does latent cooling have on the high winds of the control simulation?
- How big is the influence of latent heating on the storm development?

6.1 Inclusion of Graupel or Hail in the Microphysics Scheme

The microphysics scheme can include one large ice category which can be switched to graupel or hail, or indeed off entirely, as in the control simulations. As mentioned in Chapter 3 the control simulations presented in Chapters 4 and 5 were completed without the inclusion of either graupel or hail in the microphysics scheme. In this section, high-resolution simulations are presented to briefly examine the effect of including these large ice particles in the simulation. These simulations were run on the ARCHER HPC system and are therefore compared to a control simulation which was also run on this system, rather than the HECToR-run simulations presented in Chapters 4 and 5. To avoid confusion with the simulations shown in Chapter 5, these runs will be referred to as ARCH-CTRL, ARCH-GRAUP and ARCH-HAIL.

6.1.1 Effect on Wind Speeds

The influence of graupel on the wind speed is presented in Figure 6.1. In general, there is little difference between the ARCH-CTRL and the ARCH-GRAUP simulations. The 780 hPa level plots (Figure 6.1 (a-c)) show a slight southward shift in the regions of highest winds stretching east from 10°W. Most of the differences shown in the ARCH-CTRL plots (Figures 6.1 (b, e, h)) are small scale, and magnitude differences are typically between 5-10 ms^{-1}. The largest change is to the north and north-west of the cyclone centre in the proximity of the 968 hPa isobar, where a pronounced difference is apparent at lower levels with differences of ± 15 ms^{-1}. This region is small and is largely confined to the lower levels with much lower differences ($\sim \pm 5$ ms^{-1}) at 780 hPa. The larger changes at lower levels are likely due to the effects of graupel descending from the frontal region, causing changes to the thermodynamic and latent heating characteristics.

The influence of hail on the wind speeds compared to the control simulation is shown in Figure 6.2. Here, the general pattern of differences is largely similar to those shown for graupel in Figure 6.1, although the magnitude of the differences are smaller. The high difference region to the north and north-west is smaller in the hail comparison than the graupel, with the area of higher winds in the ARCH-HAIL simulation located further to the south. The smaller difference in the ARCH-HAIL simulation may be a result of less hail being produced than graupel, due to the stronger updraughts needed.

The wind speeds in the CCB/SJ region to the south-west of the cyclone centre shows little influence from the inclusion of graupel or hail. On all three levels shown in Figures 6.1 and 6.2 there are only minor wind speed differences in this region and these are within the variability of the system to the computing changes.

Figure 6.3 (a) shows the 1000 UTC UKMO composite radar image also shown in Chapter 4, panels (b)-(c) show the model derived rainrate for the same time for the ARCH-CTRL, -GRAUP and -HAIL simulations, respectively. In all the simulations the precipitation is stronger and more concentrated in distinct frontal bands in the model compared to the radar image. The location of the cold front in the ARCH-CTRL simulation (Figure 6.3 (b)) compares well to the radar image (Figure 6.3 (a)) extending from the south-west tip of Ireland to the triple-point in north-eastern Scotland. This shows better agreement than the location of the CF in the graupel and hail plots (Figures 6.3 (c) and (d), respectively) where the triple-point is located further south. As with the

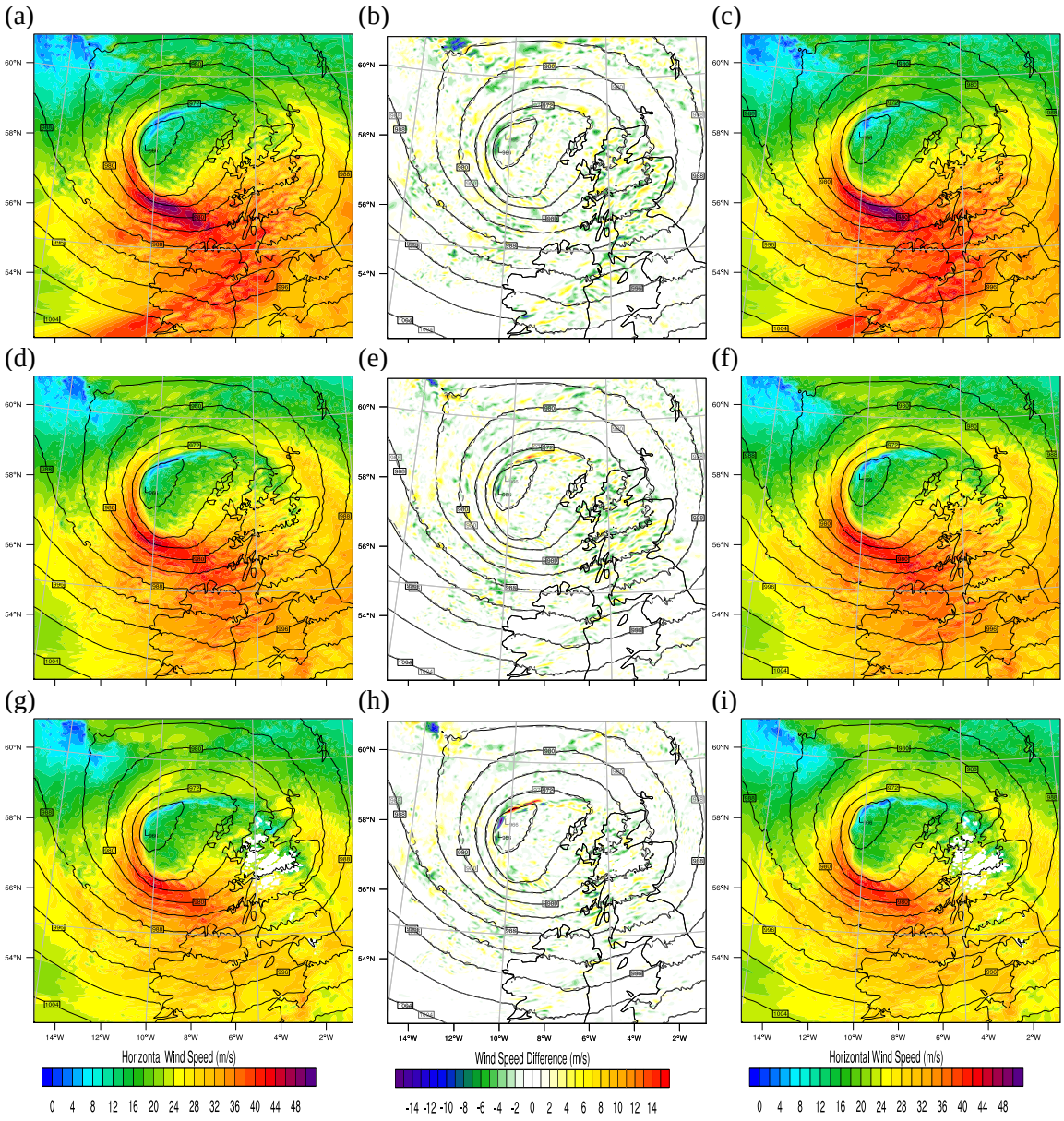

FIGURE 6.1: ARCH-CTRL and ARCH-GRAUP wind speed and SLP plots at 1000 UTC. Plots (a), (d)and (g) show ARCH-CTRL on 780, 850 and 925 hPa respectively while (c), (f) and (i) show corresponding levels for the ARCH-GRAUP simulation. Wind speed difference and SLP comparison is shown in the middle column (b), (e) and (h).

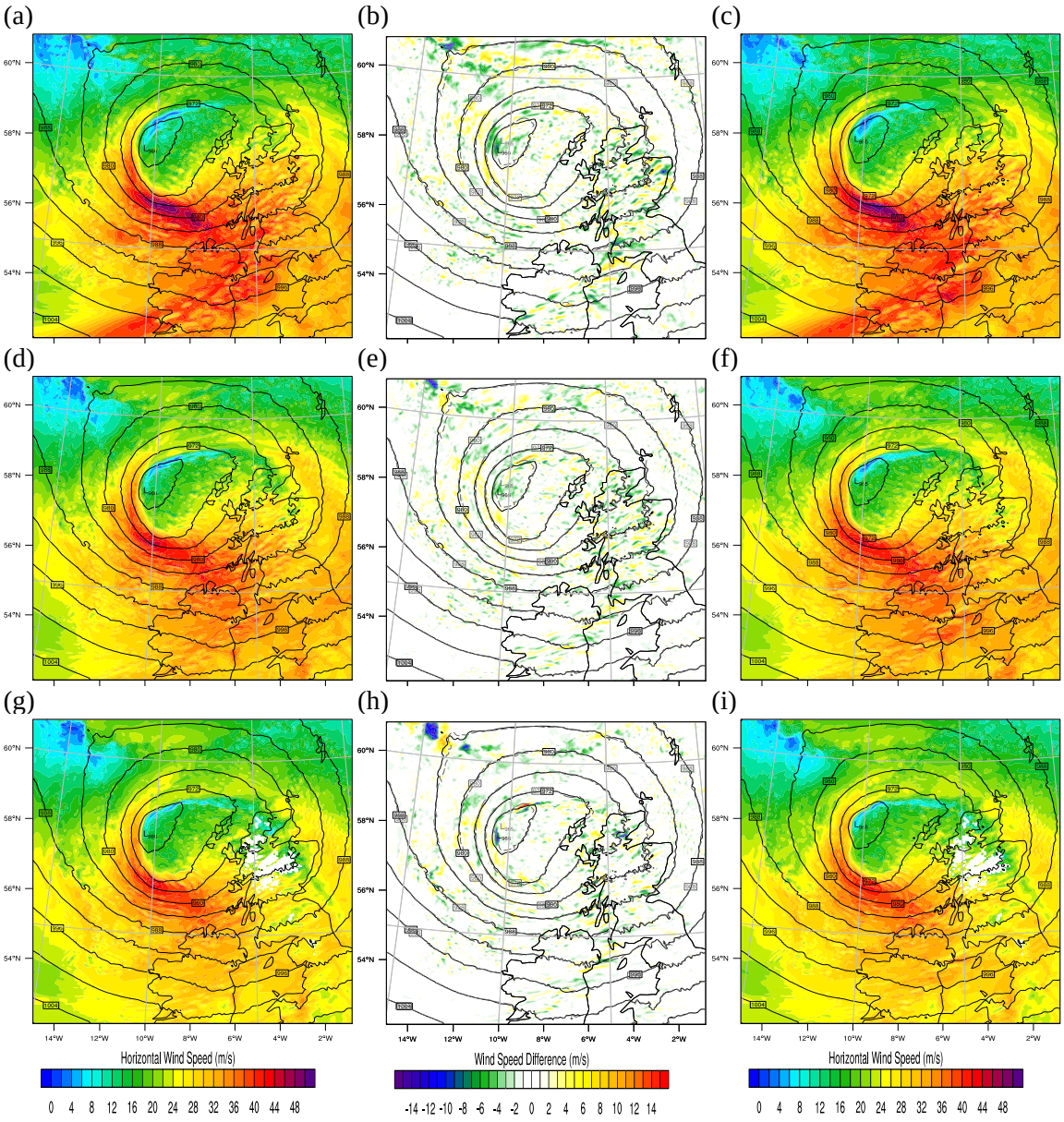

FIGURE 6.2: ARCH-CTRL and ARCH-HAIL wind speed and SLP plots at 1000 UTC. Plots (a), (d)and (g) show ARCH-CTRL on 780, 850 and 925 hPa respectively while (c), (f) and (i) show corresponding levels for the ARCH-HAIL simulation. Wind speed difference and SLP comparison is shown in the middle column (b), (e) and (h).

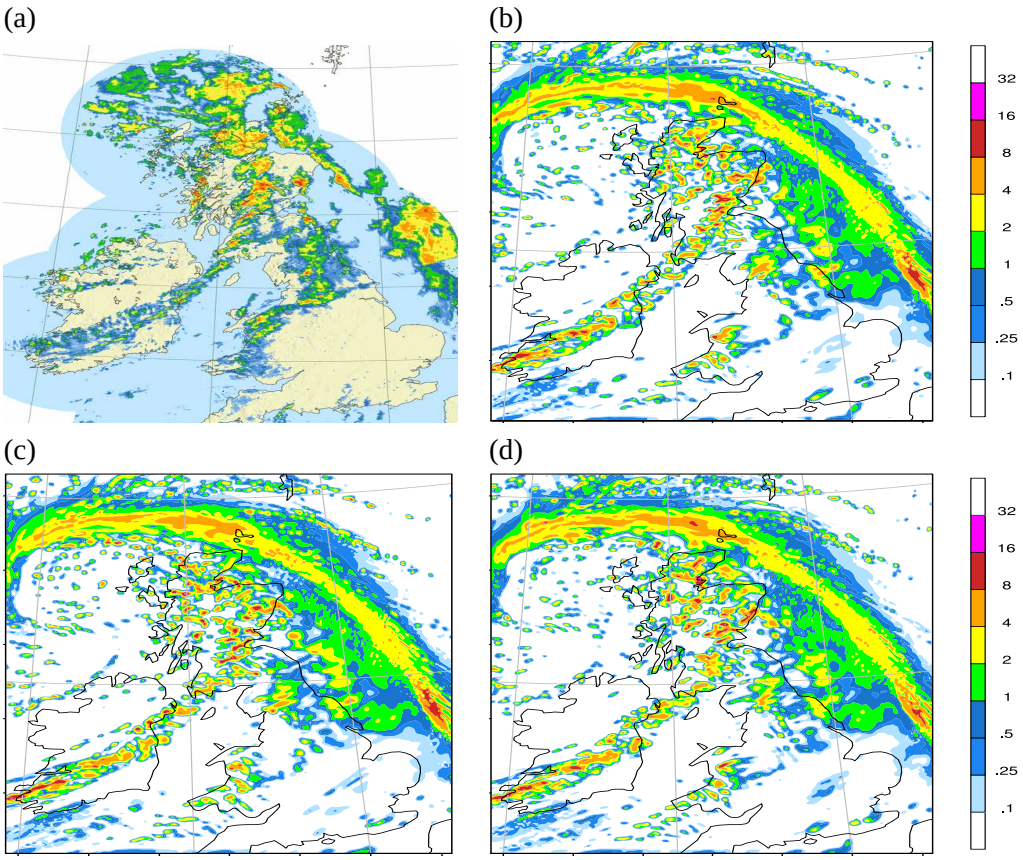

FIGURE 6.3: Comparison of radar at 1000 UTC to model derived rainrate. Plot (a) shows the UKMO 1 km composite radar image(© Crown Publishing), (b), (c) and (d) show the ARCH-CTRL, graupel and ARCH-HAIL simulations, respectively.

.

comparison in Chapter 4 the warm front and BBF is clearer and more distinct in the model than the radar image.

The southern movement of the cold front may be due to increased cooling under the frontal zone due to sublimation and melting of the hydrometeors. This would be particularly pronounced in the triple-point region due to the increased ascent here.

Previous work has shown that ice microphysics can be important in influencing the mesoscale dynamics of systems (Clough et al., 2000; Forbes and Clark, 2003; Parker and Thorpe, 1995) The plots show that in this case the, however, the inclusion of graupel or hail in the microphysics scheme does not have a large effect on the storm dynamics compared to the natural variability of the system. The lack of difference in the SLP pattern, storm intensity and winds all indicate that ice microphysics relating to hail or graupel do not play a major role in the evolution of the storm.

These finding suggest that the large-scale dynamics are the key drivers of the features exhibited by cyclone Friedhelm.

6.2 Effect of Latent Cooling on Winds

In this sensitivity test the latent cooling is removed from the simulation, hereafter referred to as the no-lc simulation. As mentioned in Chapter 3, this is achieved by removing the cooling parameters from the temperature tendency which feeds back from the WRF microphysics scheme to the gridpoint. The role of latent cooling through evaporation of hydrometeors during the descent of a sting jet has been hypothesised since Browning (2004). However despite other earlier studies identifying it as a feature of a sting jet (e.g. Clark et al. (2005)), recent work has suggested it is not necessary for the descent of the sting jet (Baker et al., 2013; Smart and Browning, 2014), although it may assist in mixing the SJ to lower levels through lowering the static stability (Schultz and Sienkiewicz, 2013).

Table 6.1 shows the maximum wind speeds and locations on the 780, 850 and 925 hPa levels from 1000-1200 UTC in the no-lc simulation. When compared to Table 5.1, the pattern of wind speeds is largely comparable between the control and no-lc simulations. However some notable differences arise; the no-lc simulation exhibits a higher peak wind speed at 1000 UTC on the 780 hPa level, which is also located slightly eastwards relative to the control. At all other times and levels the wind speeds are lower in the no-lc simulation than the control simulation. As shown in Chapter 5 the t1000-780 trajectories initiated from the maximum winds speed on this level/time showed the properties of being a sting jet. Given the differences in the wind speeds shown here it raises the question of the effect of the latent cooling on these winds.

6.2.1 Trajectories

The no-lc trajectory diagnostics from both the no-lc maximum wind speed (MWS) location (Figure 6.4) and the control run MWS location (Figure 6.5) show considerable differences to those in the control t1000-780 trajectories. Both the no-lc trajectory sets exhibit a broad range of pressures and geopotential heights at the start of the diagnostics. At 0000 UTC, the no-lc MWS trajectories are spread between 980 hPa and 700 hPa (0-2900 m) with clusters at 960, 840 and 710 hPa (200, 1400 and 2600 m) (Figure 6.4 (a) and (d)). Initially the 960 hPa nad 840 hPa trajectories show

TABLE 6.1: Maximum wind speed values and locations for trajectory initiation times and levels.

Level (hPa)	Time (UTC)	Wind Speed (ms^{-1})	Lat	Lon
780	1000	53.76	56.35	-8.88
	1100	49.95	56.42	-7.23
	1200	51.75	56.32	-5.86
850	1000	46.33	56.40	-9.17
	1100	47.94	56.21	-7.41
	1200	50.20	56.48	-6.64
925	1000	44.98	56.52	-9.72
	1100	45.24	56.41	-8.35
	1200	46.83	56.46	-6.50

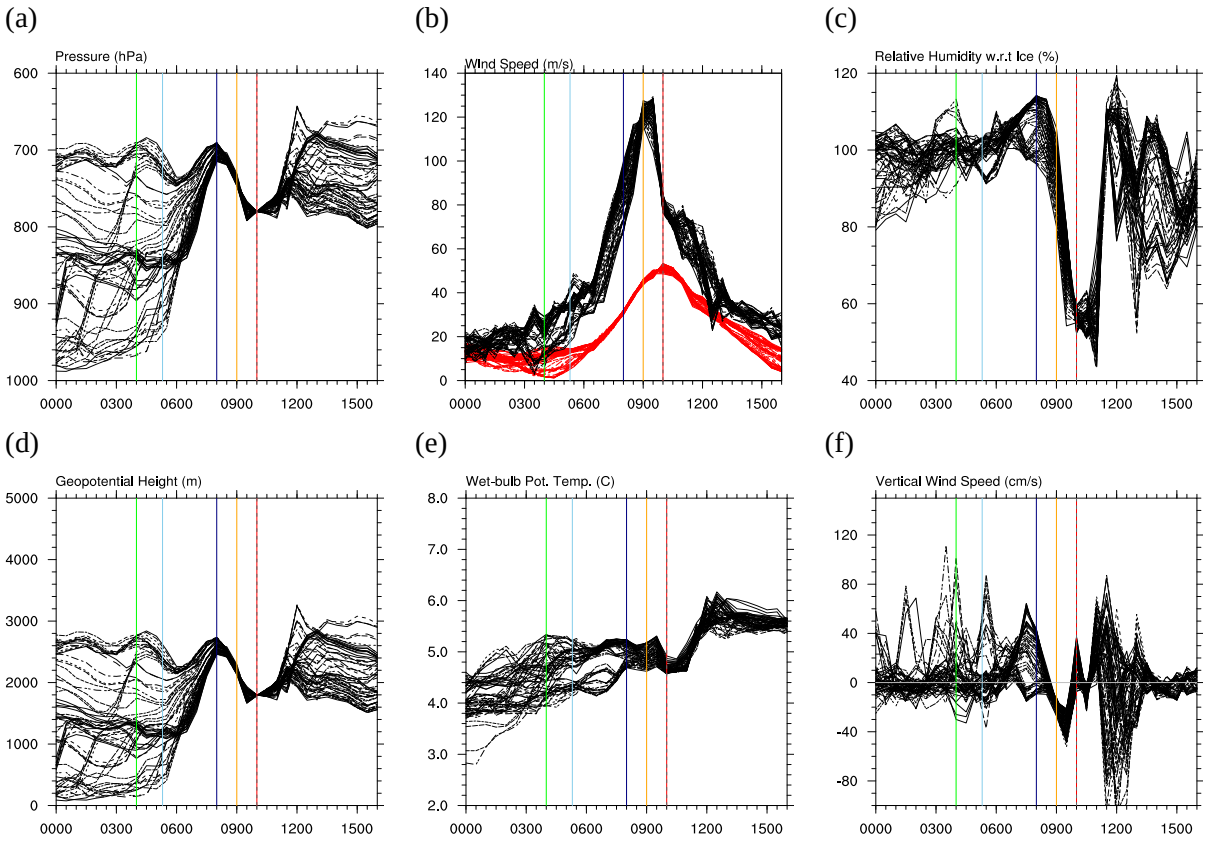

FIGURE 6.4: Trajectories initiated from the maximum wind speed location at 1000 UTC on 780 hPa in the no-lc simulation. Coloured vertical lines represent times of interest for each trajectory: green - start of acceleration, light blue - start of ascent, navy - start of descent, orange - V_g maximum, red - wind speed maximum, grey, dashed - trajectory initiation time.

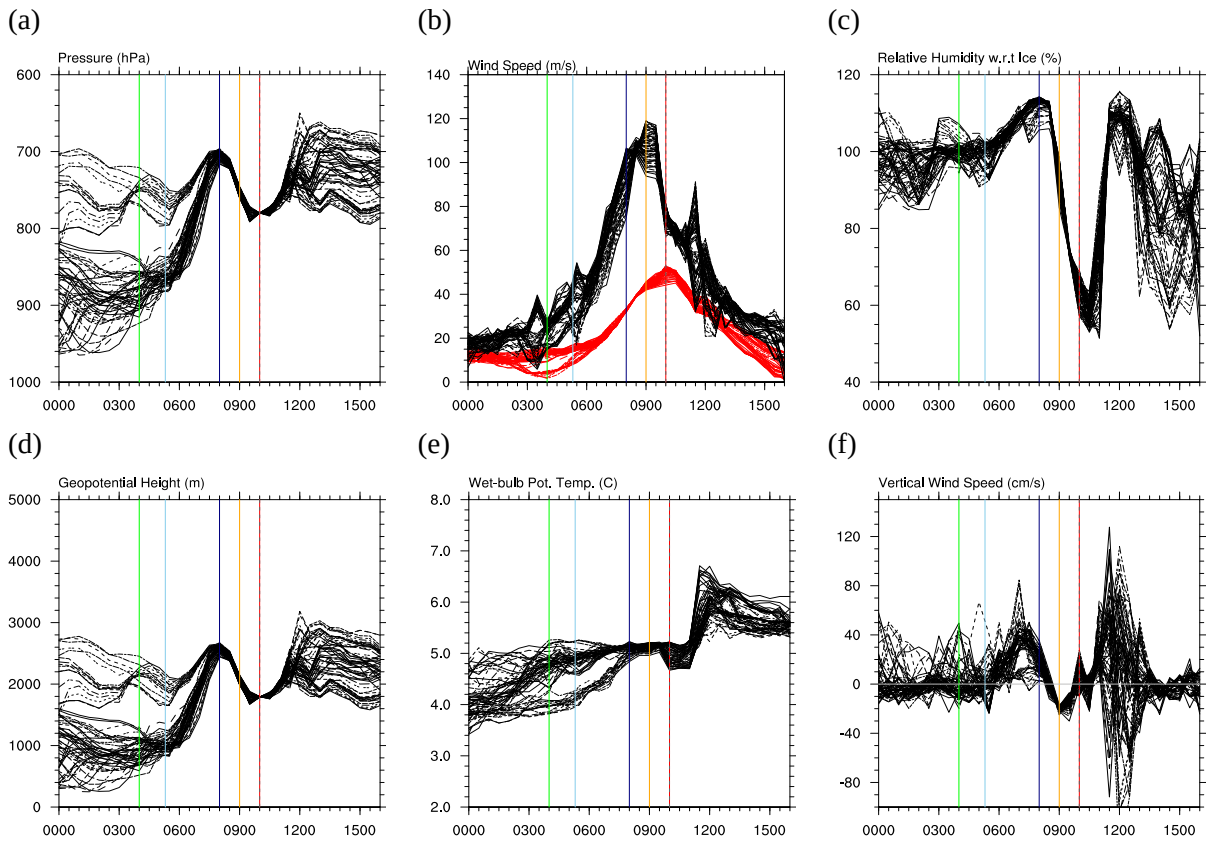

FIGURE 6.5: Trajectories initiated in the no-lc simulation from the maximum wind location on 780 hPa from the high-resolution control simulation presented in Chapter 5. Coloured vertical lines represent times of interest for each trajectory: green - start of acceleration, light blue - start of ascent, navy - start of descent, orange - V_g maximum, red - wind speed maximum, grey, dashed - trajectory initiation time.

similarities to the CCB airstreams shown, for example, in the t1000-850 trajectory plots in Chapter 5. The no-lc trajectories from the control MWS location show a different evolution with two distinct clusters at 960-820 hPa (150-1600 m) and 820-700 hPa (1600-2800 m) (Figure 6.5). The lower of these two clusters contains around three times the number of trajectories as the higher one and, again, is more consistent with the vertical location of a CCB until the rapid ascent at 0530 UTC (light blue line). Generally the trajectories stay within ±50 hPa of their initial pressure level until 0500 UTC. However, in the no-lc MWS trajectories, some can be seen ascending over this initial period indicating flow through areas of frontal convection. At 0500 UTC (light blue line) the trajectories in both sets begin to ascend rapidly, although some have already begun to slowly ascend prior to this. The lower-level trajectories converge on 700 hPa level (2600 m) by 0800 UTC, when both the initiation swarms start to descend again (dark blue line). The trajectories then descend as a coherent stream to ~780 hPa by 0930 UTC. The descent in both of these trajectory sets is similar to that in the control t1000-780 trajectories from Chapter 5, those trajectories, however,

are located around 700 hPa throughout the period prior to descent.

The other diagnostics of the no-lc trajectories show similarities to the control ones. The wind speed shows acceleration from 0300 UTC (green line), peaking at 1000 UTC at the time of the trajectory initiation (red/grey line) (Figures 6.4 and 6.5 (b)). This, along with the geostrophic wind speed peaks (orange lines) occurring ~1 hour prior to the maximum wind speed, are also both characteristics of the t1000-780 SJ trajectories.

The trajectories show that the SJ properties identified in the control simulation in Chapter 5 are present despite the removal of latent cooling. However, the evolution of the trajectories prior to the SJ descent does vary from that of the control in that the majority ascend from lower levels prior to descending. These results support the recent studies of Baker et al. (2013) and Smart and Browning (2014) that questioned the role of latent cooling, or lack thereof, in the development of a SJ, There is still a question over the role of latent cooling in the mixing of the SJ's high momentum air to the surface. This hypothesis cannot be examined here due to the limited descent of the SJ in this case.

6.3 Large-scale sensitivity to Latent Heating

This section will examine the large-scale sensitivities of Cyclone Friedhelm to latent heating. Here, a larger domain is used compared to that used in Chapters 4 and 5, which covers the majority of the North Atlantic and allows the whole development of the storm to be modelled. This requires running at a lower resolution of 27 km, although 100 vertical levels are still used. These domains and simulations will be referred to as "NA domain" runs. At this resolution, the cumulus parameterisation (Cu) would normally be switched on in order to capture the sub-grid convective processes. However, this parameterisation contributes to the heating profile where it is triggered. Thus, in order to remove the effects of latent heating the cumulus parameterisation must be switched off as well. A simulation with latent heating on but Cu off is also run and compared to the CTRL in order to separate the effects of this. Table 6.2 summarises the simulation used to analyse the latent heating effects.

TABLE 6.2: Latent heating sensitivity runs

Run	Cu	LH
CTRL	Y	Y
NO-CU	N	Y
NO-LH	N	N

6.3.1 Control Development and Evaluation

The NA simulations were not used for the model evaluation presented in Chapter 4, therefore a brief comparison of the NA domain control simulation with the observations presented in Chapter 4 is shown here.

Figure 6.6 shows the evolution of Cyclone Friedhelm as it approaches and crosses the UK in the WRF NA domain control simulation. At 1200 UTC on the 7th December, the storm has just begun to develop at around 35°W 64°N in the central Atlantic (Figure 6.6 (a)). At 0000 UTC 8th December the storm has developed to a central pressure of 986 hPa (Figure 6.6 (b)). Driven by the strong jet stream shown in Chapter 4, it has tracked to around 20°W, and moved northwards to 61°N. By this time the winds associated with the cyclone develop and the cold front appears as a strong band at around 35 ms^{-1}. Twelve hours later the storm is located to the north-western coast of Scotland (Figure 6.6 (c)). Now, the strongest winds (>40 ms^{-1}) are located to the south and south-west of the cyclone centre. The 35 ms^{-1} winds associated with the warm and cold fronts are also present to the east and south of the low. The storm tracks across Scotland and into the North Sea by 0000 9th December (Figure 6.6 (d)). The SLP evolution compares favourably to that shown in the UKMO synoptic charts presented in Chapter 4; there is slight southward bias to the storm location which was also present, albeit to a lesser extent, in the high-resolution runs. It is notable that the winds show continued development and some higher speeds later in these simulations than shown in the high-resolution runs presented in Chapters 4 and 5.

The 850 hPa winds and θ_e shown in Figure 6.7 show a similar evolution to that of the smaller domain shown in Figure 4.7). Comparing the NA domain 850 wind speed at 1200 UTC (Figure 6.7 (c)) to the corresponding domain 3 wind speed in the high-resolution run (Figure 4.7) shows good agreement between the two, albeit with some slight differences. Generally the highest winds are produced to the south-west of the cyclone centre in the CCB/SJ region (Figure 6.7 (c)). The low pressure centre in the NA domain run is located marginally eastwards (~100 km) compared

(a) 1200 7^{th} Dec.

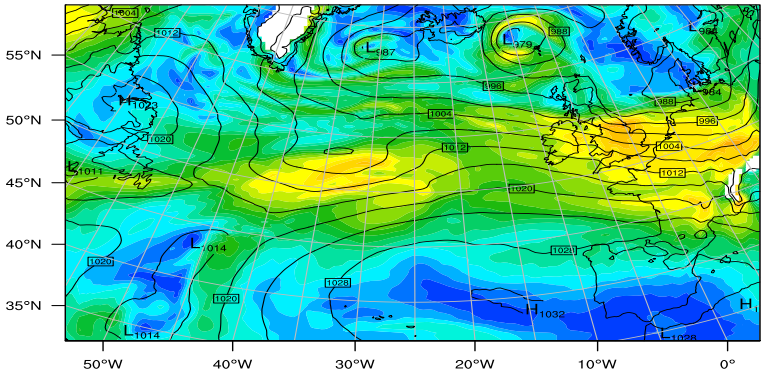

(b) 0000 8^{th} Dec.

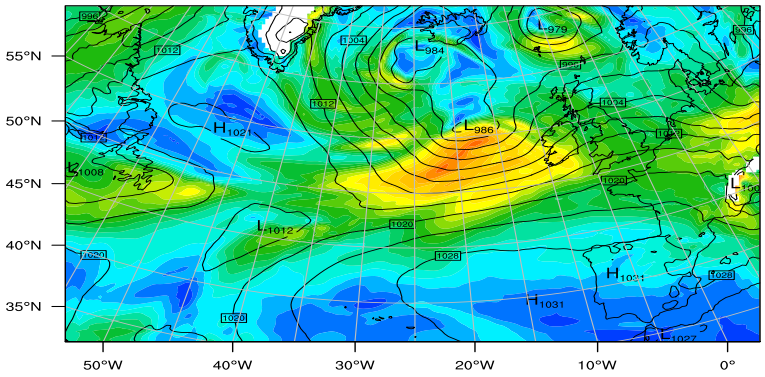

(c) 1200 8^{th} Dec.

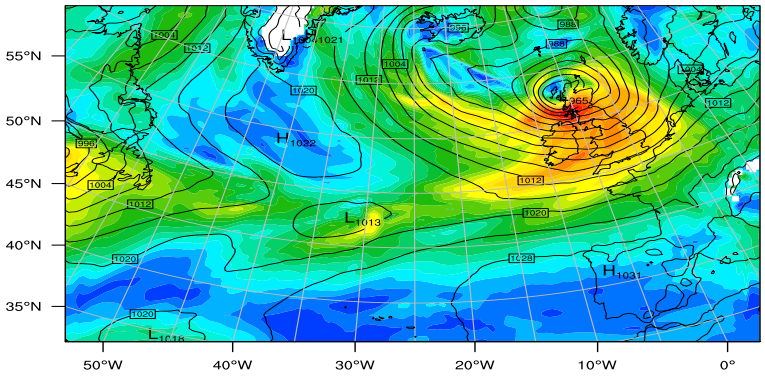

(d) 0000 9^{th} Dec.

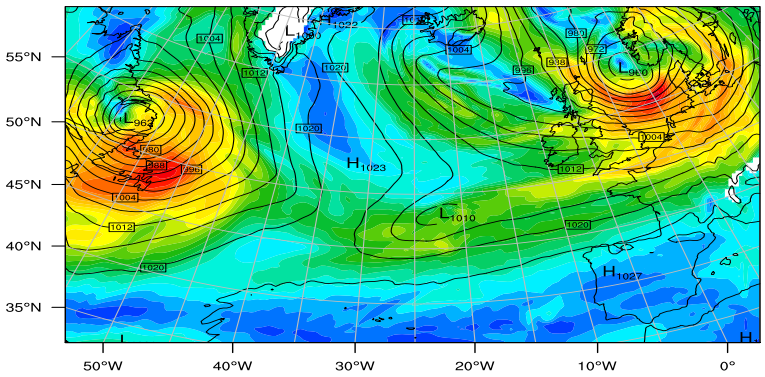

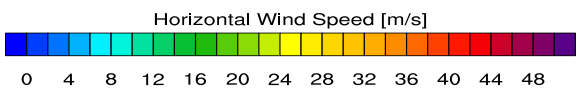

FIGURE 6.6: Evolution of Cyclone Friedhelm Wind speed (shading) and SLP (black contours) every 12 hours from 1200 UTC 07 December 2011 to 0000 09 December 2011.

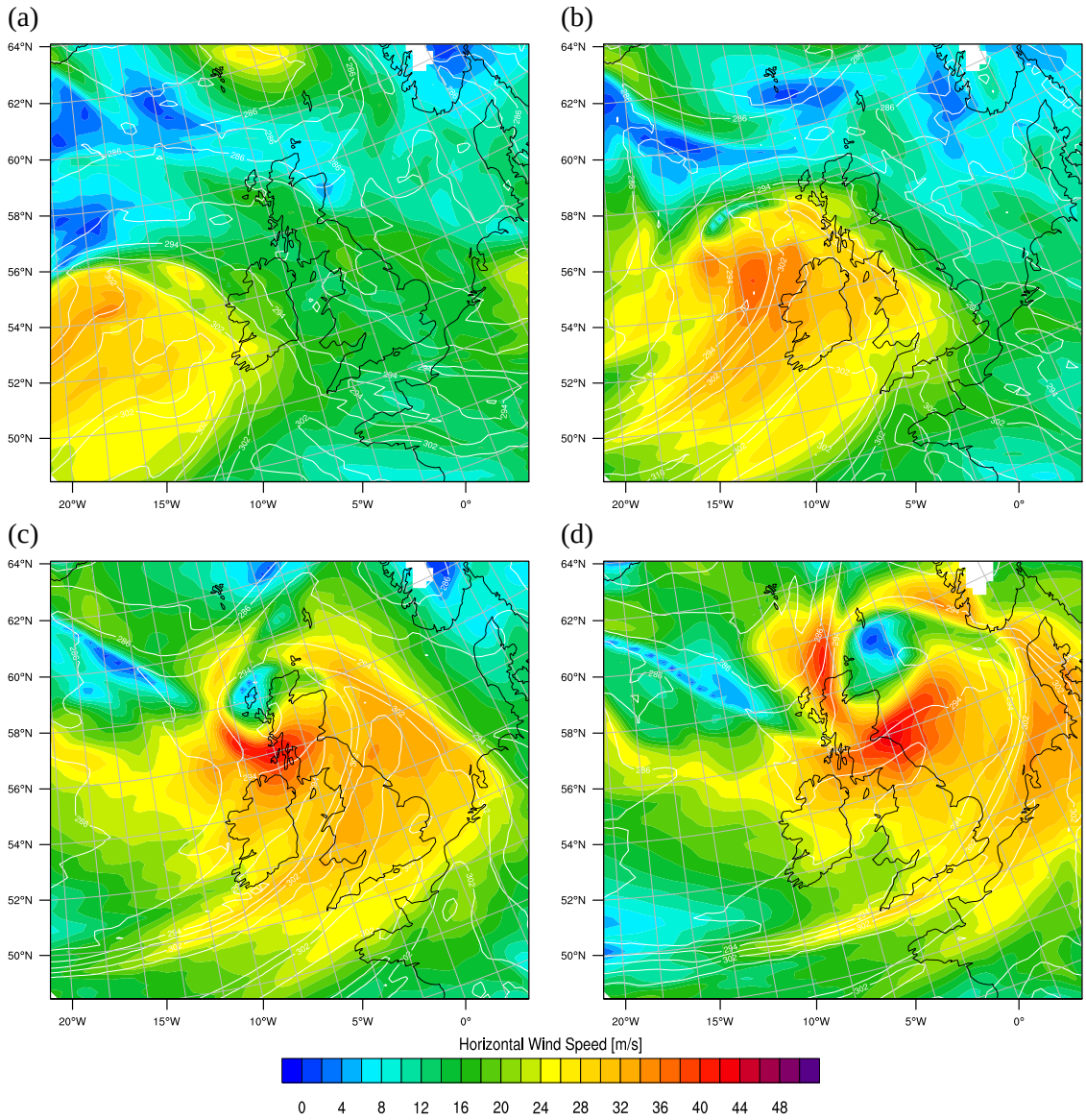

FIGURE 6.7: NA domain Wind speed (ms^{-1}) (shading), and θ_e (K) (white contours), on 850 hPa level at (a) 0000, (b) 0600, (c) 1200 and (d) 1800 UTC 8^{th} December 2011.

to the high-resolution run. The areas of maximum wind speed are also located slightly further south. As would be expected, some of the small scale intense wind features are not seen in the lower-resolution simulation, as they are sub-grid scale and are therefore effectively smoothed out by the model.

Figures 6.6 and 6.7 show that the NA domain is successfully simulating the storm when compared to the higher resolution WRF simulation and the observations. Given the long spin-up time with the model initiation occurring prior to the storm formation, this shows the model is able to produce the cyclogenesis accurately. The resolution used here means some of the small-scale features in

the high-resolution runs will not be reproduced. However, the aim of this section is to investigate the large-scale effects of latent heat on the overall wind field and storm evolution and so, it is not essential to reproduce these small-scale features.

6.3.1.1 Cumulus Parameterisation Sensitivity

At 27 km horizontal resolution, the Cu parameterisation would normally be engaged in order to account for the sub-grid scale updrafts and downdrafts, and their associated heating and moisture fluxes. As mentioned above, in order to examine the total effect of latent heating the Cu parameterisation must be switched off as well as the microphysics latent heating processes. A brief analysis of the NO-CU simulation compared to the CTRL is presented here, with further analysis and comparison to the NO-LH simulations presented in Section 6.3.2.

Figure 6.8 shows the wind fields and difference of the CTRL and NO-CU simulations as they pass Scotland. The SLP field in Figures 6.8 (a) and (b) show the NO-CU simulation being only 1 hPa deeper than the CTRL run. Overall, the SLP at the centre of the cyclone shows very good agreement and is within ±2 hPa as the storm moves across the UK. Further analysis of the tracks and deepening is presented with the latent heating sensitivity analysis in Section 6.3.2. The pressure distribution shows some differences, however. As shown in the difference plot (Figure 6.8 (c)), the low pressure centre is located slightly westwards in the NO-CU simulation. Away from the cyclone, the pressure fields are largely similar, indicating the influence of convection around the frontal cyclone on the pressure pattern. Figure 6.9 shows the difference plot zoomed onto the centre of the storm; this shows there is also a westward stretching of the pressure field. The 968 hPa isobar for the NO-CU simulation extends out beyond the 976 hPa isobar of the CTRL run on the western side of the cyclone. There is also some shift and extension to the north in the NO-CU simulation as well. This causes a movement of the high wind speeds on the west of the cyclone centre to be located more westwards, creating the dipole in the difference plots (Figure 6.8 (c)). The NO-CU simulation also shows stronger winds stretching into the cyclone centre; comparison of Figures 6.8 (a) and (b) shows that this is largely due to the larger size and magnitude of the slack wind region in the low centre (<10 ms^{-1}) in the CTRL simulation. The higher winds to the south of the cyclone centre have extend further eastwards in the NO-CU simulation. Analysis of the SLP field here shows that this region is less curved than the corresponding region in the CTRL run; this lack of curvature may act to slow the deceleration of the winds as they pass beyond the region of maximum PGF. Despite these differences, the wind fields are largely consistent.

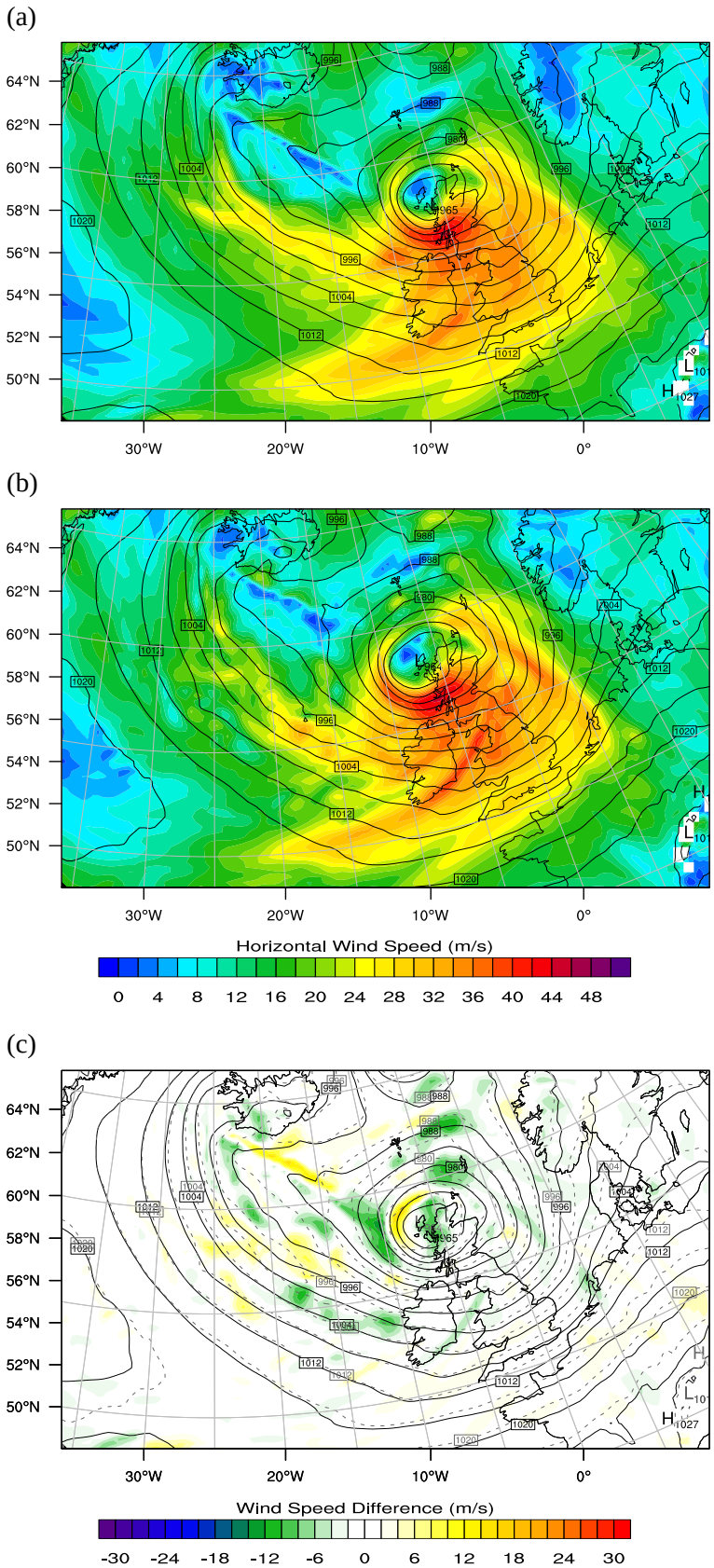

FIGURE 6.8: 780 hPa horizontal wind speed (ms^{-1}) at 1200 UTC for (a) CTRL and (b) NO-CU simulations. (c) shows the difference (CTRL-NO-CU) with SLP lines for the ctrl (solid, black) and NO-CU (dashed, grey) runs.

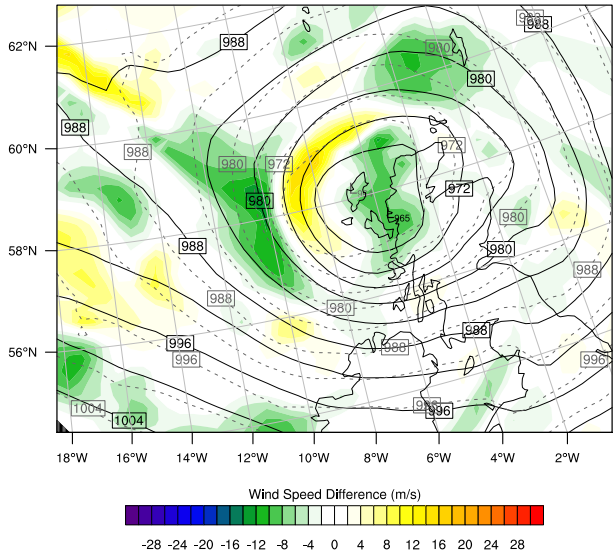

FIGURE 6.9: As Figure 6.8 (c) but zoomed in on the centre of the storm.

The location of the SLP and western cyclonic winds in the NO-CU run suggest a slowing of the cyclone track may be the cause of at least part of the differences. Given the relatively long lead time and the distance from any boundary forcing, this is more likely than it might be on a smaller, shorter run (Froude, 2009). In order to quantify if this is indeed the case, Figure 6.10 shows the same difference plot at Figure 6.9 but with the NO-CU simulation plotted one hour later (i.e. 1200 UTC for the CTRL and 1300 UTC for the NO-CU). The differences to the west of the cyclone are lessened by the time offset although the higher winds to the north-west and south in the NO-CU run are still evident to a lesser magnitude. The differences to the north-east of the cyclone have increased, however. The location of the minimum SLP of the NO-CU run is now located to the north-east of the CTRL. There is little difference between the values of the minimum SLP (the NO-CU being 1 hPa deeper) but the pressure distributions are different. Much like at 1200 UTC, the 968 hPa region is larger in the NO-CU run but this time extends further to the north and west of the 1200 UTC CTRL. These results suggest that although there is some influence of different temporal evolution, there are also some dynamical differences caused by the lack of Cu parameterisation.

Overall the figures show that switching off the cumulus scheme does have some small effects on the development of the cyclone and its associated winds and pressure fields. The large-scale forcing and processes are sufficient enough to achieve a realistic simulation of the cyclone despite the lack of parameterised convection. The simulations are similar enough that a NO-LH run will be valid to investigate the effects of LH, without the removal of the cumulus scheme playing a major role

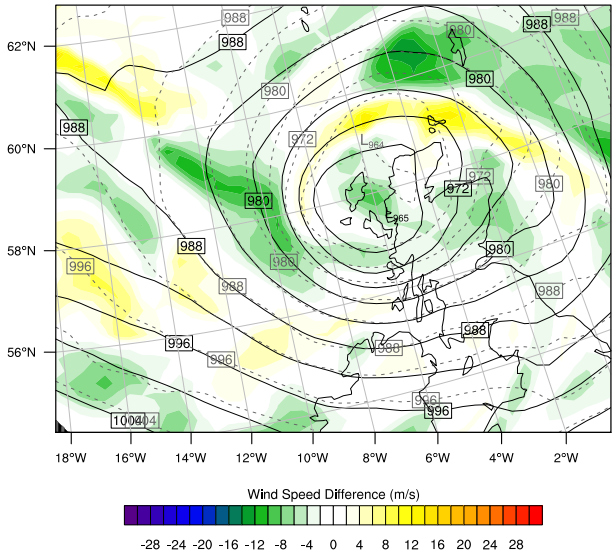

FIGURE 6.10: As Figure 6.9 but showing the difference of the CTRL at 1200 UTC and NO-CU at 1300 UTC.

in any differences. As the NO-CU simulation is robust, this can also be used as a comparison for the NO-LH simulation in addition to the CTRL simulation.

6.3.2 Latent Heating Sensitivity

6.3.2.1 Track and Deepening

Figure 6.11 (a) shows the track of Cyclone Friedhelm in the control and two sensitivity simulations. All three show a remarkably similar track from the mid-Atlantic towards the UK. The CTRL and NO-CU tracks show strong agreement from ~30°W until ~15°W where they diverge slightly with the NO-CU taking a more northward path. The NO-LH run contrasts slightly with the other two; it stays consistently to the south until it reaches the coast of Scotland. The location also lags behind that in the other two simulations from the start. This suggests that the lack of latent heat release slows the initial formation and progress of the cyclone. The evolution of the minimum SLP and maximum 780, 850, and 925 hPa wind speeds are shown in Figures 6.11 (b), (c) and (d), respectively. At the initiation of the track, the minimum SLP is around 5 hPa lower in both the CTRL and NO-CU runs than in the NO-LH run. The CTRL and NO-CU pressures then decrease almost identically to around 970 hPa by 0600 UTC on the 8^{th}. The deepening then slows somewhat with the NO-CU reaching a minimum SLP of ~960 hPa at 1800 UTC and the CTRL reaching ~959 hPa at 1800 UTC. Conversely, the deepening of the NO-LH run is much slower, SLP decreases

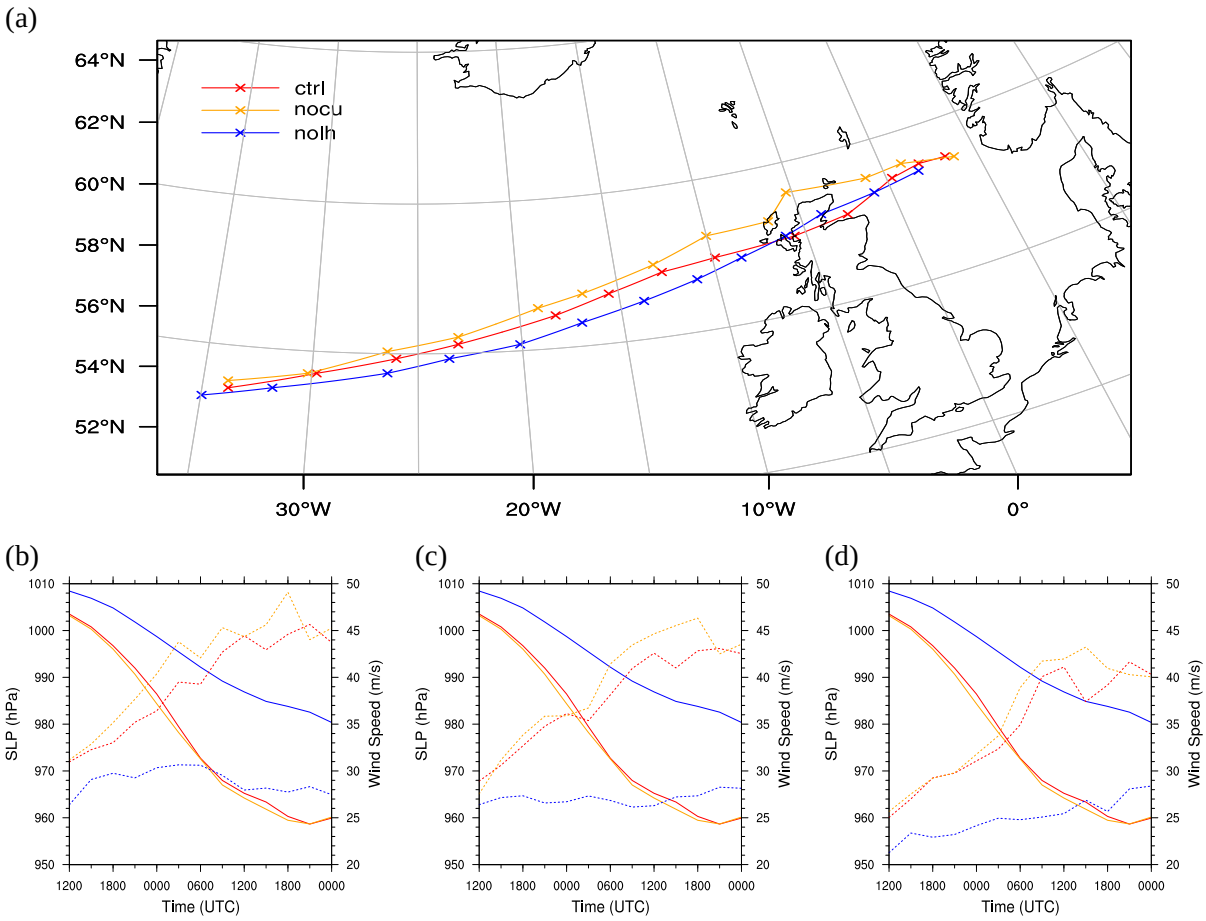

FIGURE 6.11: (a) Tracks of minimum SLP for the CTRL (red), NO-CU (orange) and NO-LH (blue) simulations. Tracks start at 1200 UTC 7^{th} December with crosses marked every 3 hours until 0000 UTC 09^{th} December. Evolution of cyclone minimum SLP (solid lines) shown in (b), (c) and (d) with maximum cyclone wind speeds on 780, 850 and 925 hPa, respectively (dashed lines). Colours are as in (a). Maximum cyclone wind speed in calculated form a 40x40 grid point box centered on the minimum SLP.

steadily to ~985 hPa by 1500 UTC on the 8^{th}, then by another 5 hPa by the end of the track at 0000 UTC on the 9^{th}. This clearly shows a significant effect of latent heating on the overall deepening of the storm, with little effect from the lack of convection scheme.

The maximum cyclone wind speeds are shown in Figures 6.11 (b), (c) and (d). These were obtained from a 40x40 gridpoint box centred on the minimum SLP, therefore, the maximum may be associated with parts of the CF or the BBF. Large differences are shown in the cyclone winds speed evolution. Generally, the CTRL and NO-CU winds are significantly higher than those in the NO-LH simulation. At 780 hPa the NO-LH maximum winds initially rise from 22 ms^{-1} to ~30 ms^{-1}, reaching a maximum of 31 ms^{-1} around 0300 UTC 8^{th} December. They then decrease to ~28 ms^{-1} for the rest of the track. By contrast, the CTRL and NO-CU maximum winds are

already at 31 ms^{-1} at 1200 UTC on the 7^{th}. They then diverge with the NO-CU accelerating faster, reaching 43 ms^{-1} by 0300 UTC on the 8^{th}. In contrast, the CTRL maximum only reaches these speeds around 6 hours later at 0900 UTC. At 1200 UTC the NO-CU maximum winds increase again to ~47 ms^{-1}, while the CTRL winds show a delay of around 3 hours before they too rise to 45 ms^{-1}.

At the 850 hPa level the NO-LH maximum cyclone winds stay relatively constant around 26-27 ms^{-1}, with a slight rise after 1200 UTC on the 8^{th} to 29 ms^{-1}. Again, both the CTRL and NO-CU winds show significantly higher magnitudes. The earlier peaks in the NO-CU winds are again evident both in the 850 and 925 hPa plots, reaching 45 ms^{-1} at 1200 UTC and 43 ms^{-1} at 0900 UTC, respectively. Meanwhile, the CTRL winds peak at 44 ms^{-1} at 1800 UTC on 850 hPa and 42 ms^{-1} at 2100 UTC at 925 hPa. The 925 hPa winds show the biggest increase on any level of the NO-LH maximums over the period of the track, rising from an initial 21 ms^{-1} to a maximum ~29 ms^{-1} at 2100 UTC on the 8^{th}.

All three levels show the NO-CU maximum wind speed reaching higher magnitudes than the CTRL. This is evident from the start of the time series at upper levels but only later at lower levels. Less mixing of slow momentum air from lower levels effectively causing friction at higher levels.

Given the differences and evolution of SLP between the CTRL/NO-CU and NO-LH this is not surprising. It has been shown in Chapter 5 that the PGF plays a dominant role in the development of the high winds around the cyclone. With less deepening the NO-LH storm does not develop the same pressure gradient as the CTRL/NO-CU storms significantly retarding the development of the high winds.

The slight slowing of the NO-LH cyclone track in the early stages of the storm, as a result of lessened convection and upper-level divergence may hinder the interaction with the upper-levels. If the upper- and lower-level anomalies are in a less favourable configuration, this in turn will lessen the deepening of the cyclone (Froude, 2009; Hoskins et al., 1985)

6.3.2.2 Wind Speed Differences

Figure 6.12 shows the evolution of the 780 hPa wind speed and SLP as Cyclone Friedhelm passes Scotland in the three simulations. The two left hand columns of the CTRL and NO-CU show strong similarities, as shown previously. Both exhibit strong winds (>40 ms^{-1}) along the cold front

initially and a developing strong wind region to the south and south-west of the low. In addition, strong winds to the east along the warm front can also be seen. The overall region of high winds to the south and south-west of the cyclone is marginally broader in the NO-CU simulation than the CTRL and develops quicker as seen in Figure 6.11.

In contrast to both the CTRL and NO-CU plots, the NO-LH simulation shows significant differences. As shown in the track plot (Figure 6.11 (a)), the storm propagates slower than the other simulations and is located further south. The lesser deepening compared to the CTRL/NO-CU runs is clearly visible in the isobars and produces a much weaker pressure gradient. This is evident to the northern side of the low where, at 1200 UTC, the NO-LH simulation shows a gradient of ~10 hPa from the storm centre to Iceland. In contrast, the NO-CU simulation pressure difference is more than twice as large. This leads to the weak winds north of the storm of around 5 ms^{-1} compared to regions of 20-30 ms^{-1}. To the south of the cyclone the pressure gradient is greater but still considerably less than the CTRL/NO-CU runs. This leads to the development of a region of stronger winds to the south and south-west of the storm which only reach a maximum of ~25 ms^{-1}. The maximum winds are more often seen in the cold frontal region rather than the CCB/SJ region, in the NO-LH simulation. The southward displacement of the NO-LH storm means that low-level winds to the south of the storm may be influenced by the increased friction of Ireland. At the 780 hPa level this effect should be lessened; indeed there is little change in wind magnitude in the CTRL simulation as it passes over Scotland at this level.

6.3.2.3 Influence of PV

The role of PV in atmospheric sciences has been widely studied as summarised in Section 2.2.3. Given its important role in large-scale cyclogenesis and on smaller scales it is analysed here in the context of its influence on the cyclone generation and evolution and on the high winds.

Figures 6.13-6.15 show the evolution of the upper level PV anomalies in the CTRL, NO-CU and NO-LH simulations, respectively. The plots show θ contoured on the 2 PVU iso-surface, indicating the height of the dynamical tropopause. The CTRL and NO-CU simulations show very similar tropopause evolution (Figures 6.13 and 6.14), while the NO-LH shows some differences, albeit subtle. At 1800 UTC on the 7^{th} the initial upper-level disturbance can be seen as a depression in the tropopause height (decrease in θ) on the left of the plot over the central Atlantic (Figure 6.13 (a)). At this time there is little difference between any of the simulations with the exception

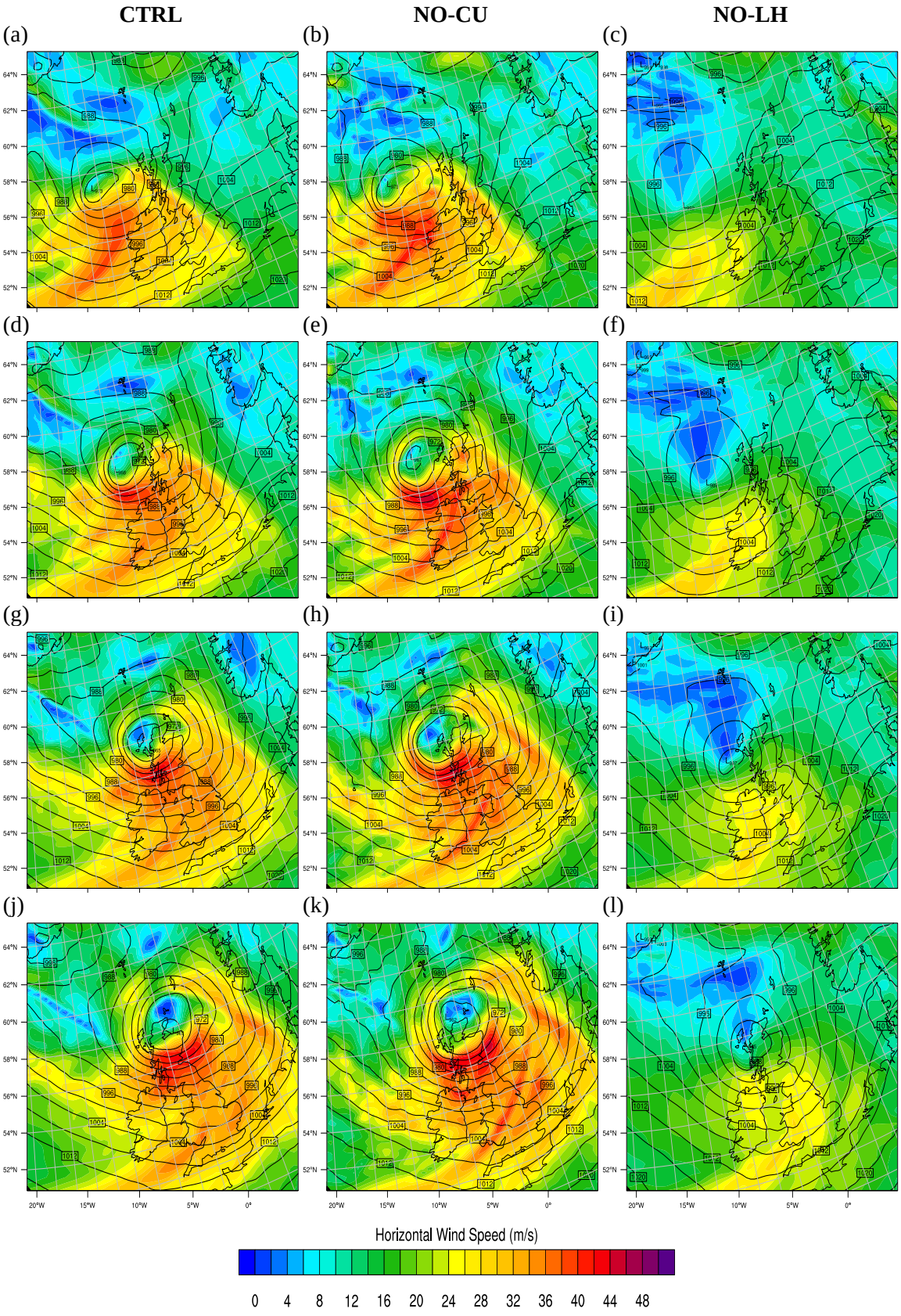

FIGURE 6.12: Evolution of the 780 hPa wind speed in the CTRL (a, d, g, j), NO-CU (b, e, h, k) and NO-LH (c, f, i, l) simulations. Rows show plots at the same times of 0600, 0900, 1200 and 1500 UTC, top-bottom.

the amplitude of the wave in the tropopause ridge being slightly greater in the CTRL and NO-CU (Figures 6.13 (a) and 6.14 (a)) compared to the NO-LH (Figure 6.15 (a)). At 0000 UTC on the 08^{th} the trough has moved eastwards and the decreased θ shows the descent of the feature behind the surface cyclone (Figure 6.13 (b)). A slight ridge of lower θ, orientated east-to-west immediately to the south of the main trough, delimits the intrusion behind the cold front from the main upper-level trough. The cold-frontal intrusion appears deeper by this time in the NO-LH simulation (Figure 6.15 (b)) than in the other two runs. By 0600 UTC on the 08^{th} the storm continues to deepen as shown previously; in the upper levels the trough can be seen extending to the south and turning cyclonically. The NO-LH plot at this time shows a larger region of the cooler θ (<300 K, green and blues). The CTRL and NO-LH simulations show a higher tropopause particularly at the northern end of the upper-level ridge with θ values above 304 K. At 0600 UTC on the 08^{th} the tropopause trough has deepened further in all three simulations (Figures 6.13-6.15 (d)). However, the NO-LH run shows the tropopause to be more depressed at the centre of the cyclone with a wider trough and a deeper intrusion along the cold front. This would suggest that the lack of vertical motion sustained by the latent heating is allowing the upper-level PV anomaly to descend further. This may then be compensating to a small degree for the lack of LH.

Figures 6.13-6.15 show a clear upper-level PV anomaly/trough associated with the cyclone. The presence of this feature prior to, and during the most rapid deepening of the storm suggests that this is the initiator of the cyclogenesis, while also playing a role in the deepening. Hoskins et al. (1985) show that cyclones generally form to the east of the upper-level anomaly as is the case here. However, the anomaly is also present in the NO-LH simulation where the deepening is significantly lower than the CTRL/NO-CU simulations. This would then indicate that a combination of the upper-levels and low-level anomalies are essential for the deepening seen in the CTRL/NO-CU runs.

A side-on view of the θ contoured, 2 PVU iso-surfaces is shown in Figure 6.16 at 0600 UTC (top row) and 1200 UTC 08^{th} Dec. (bottom row), for the three simulations. These highlight the extent of the depression of tropopause behind the cyclone. The tropopause fold is deeper in the NO-LH simulation (Figure 6.16 (c) and (f)) than in the other two simulations as shown by the larger prominence of green/blue colors. The deeper tropopause fold is likely a result of the lessened convection as a result of the lack of latent heating, effectively reducing the buoyancy of the troposphere.

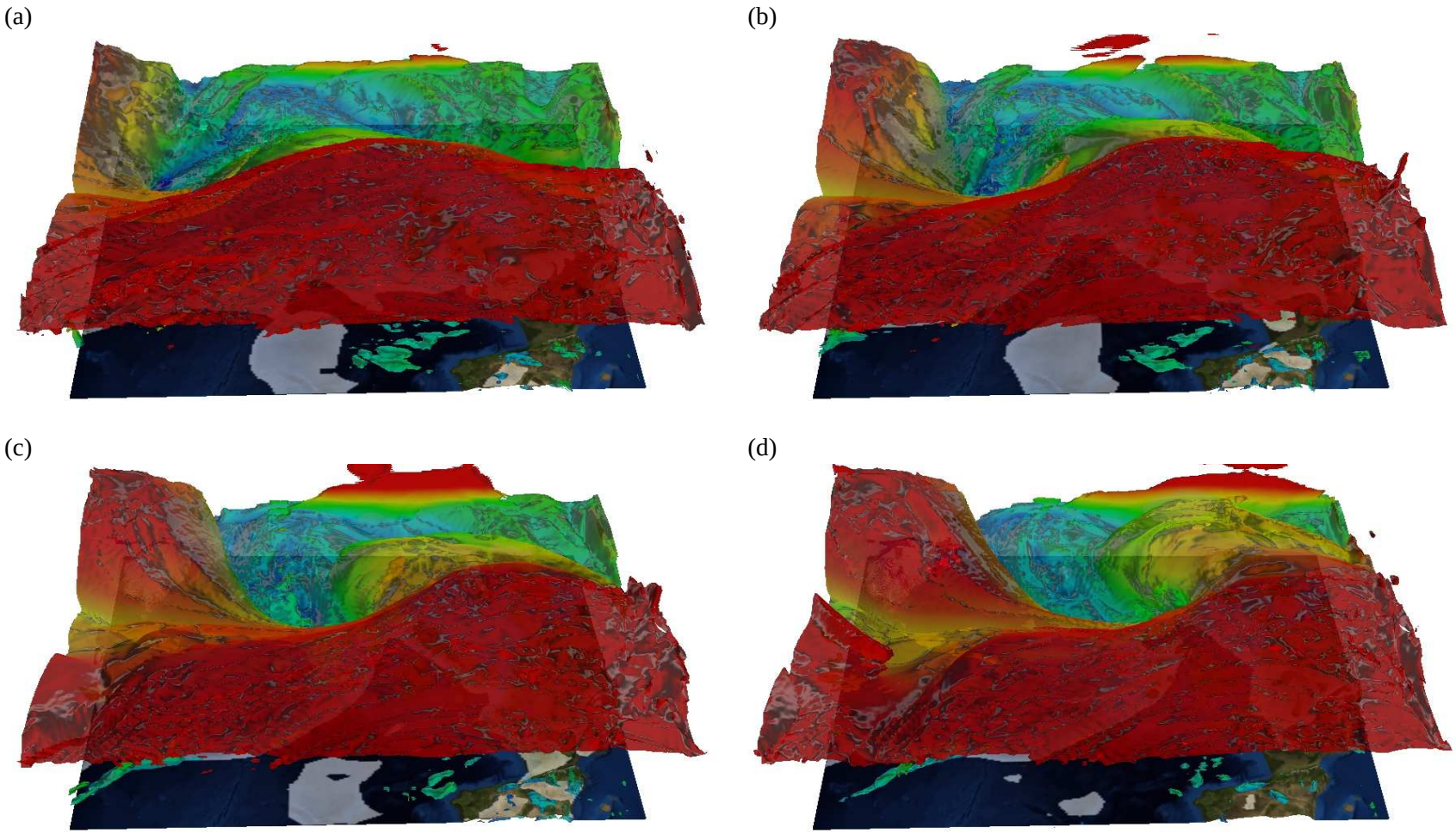

FIGURE 6.13: θ contoured onto the 2 PVU surface indicating the dynamic tropopause in the CTRL simulation. Panels (a)-(d) are plotted from 1800 UTC on the 7^{th} every 6 hours.

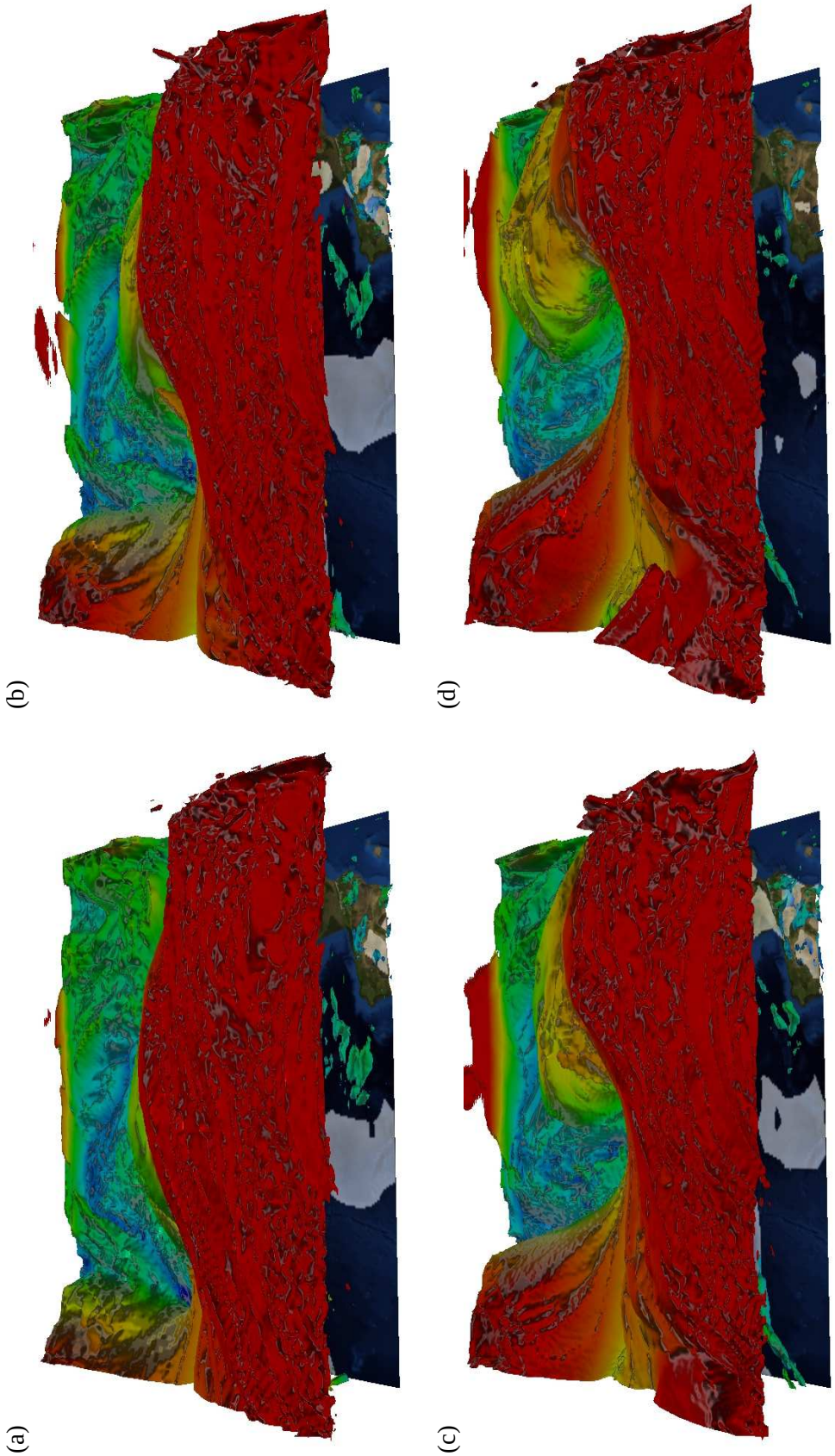

FIGURE 6.14: As 6.13 but for the NO-CU simulation.

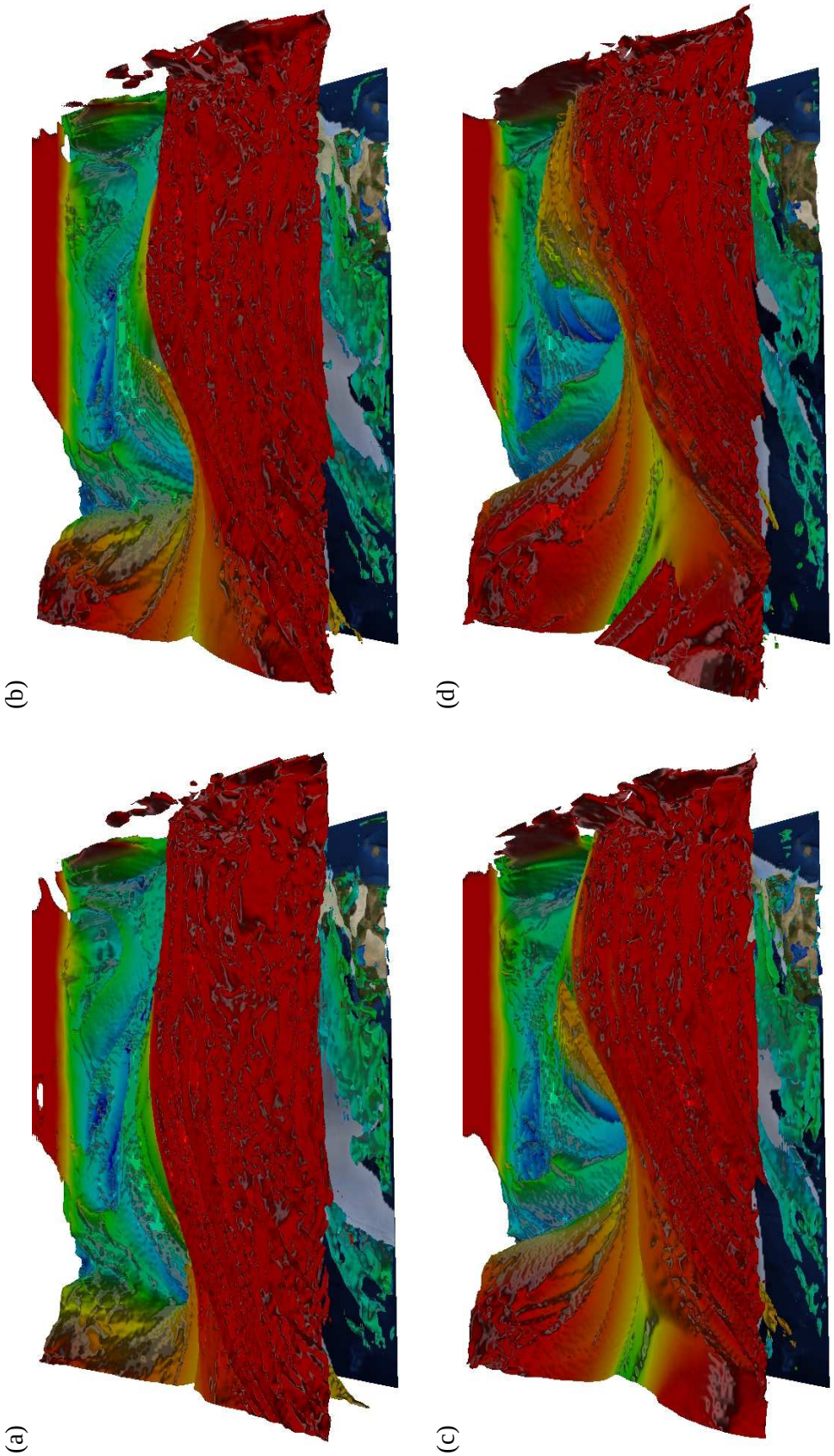

FIGURE 6.15: As 6.13 but for the NO-LH simulation.

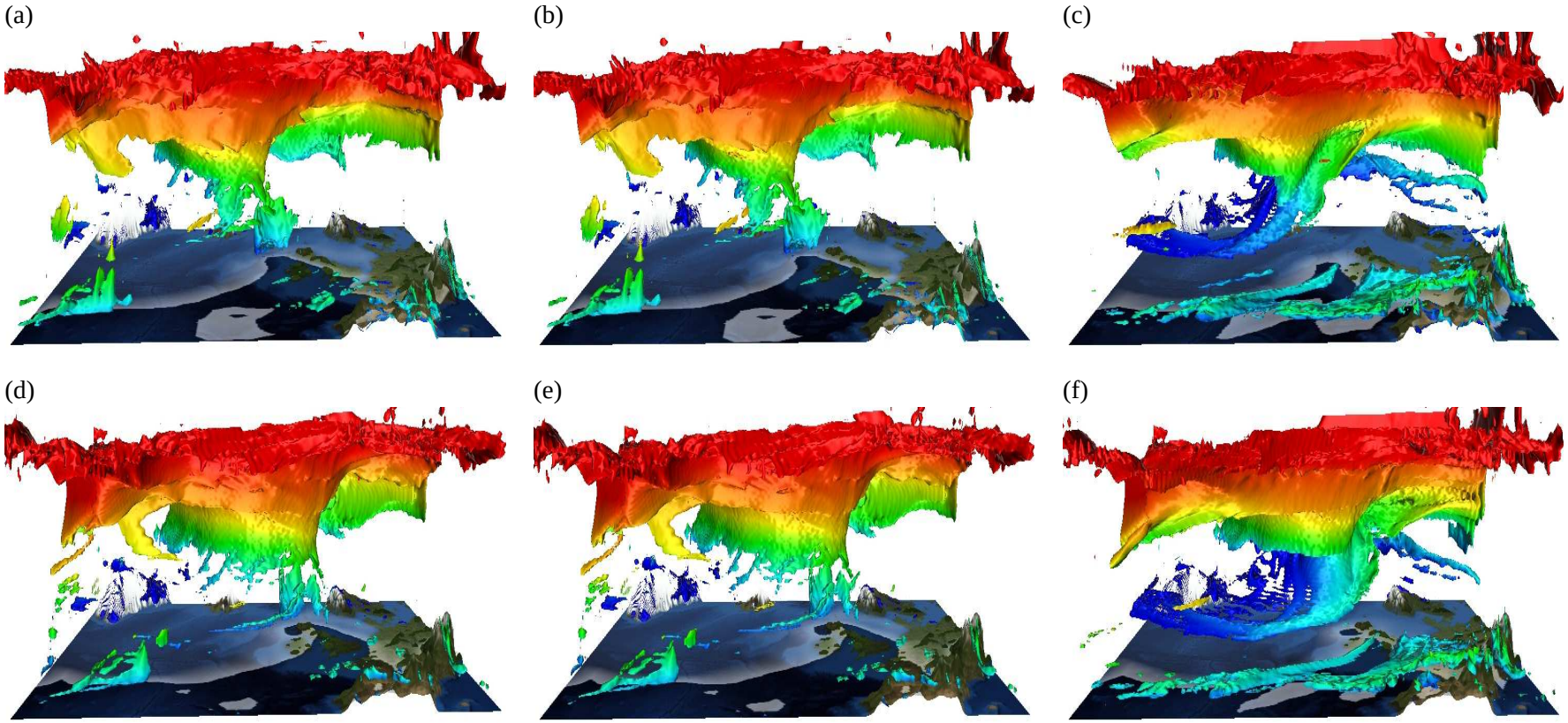

FIGURE 6.16: Side-on view of the θ shaded 2 PVU surface. Top row shows CTRL (a), NO-CU (b) and NO-LH (c) at 0600 UTC on 8^{th}. Bottow row (d, e, and f) shows the same runs at 1200 UTC. Surface is shaded from 2 m θ = 284 K to indicate the cyclone position.

(a) (b)

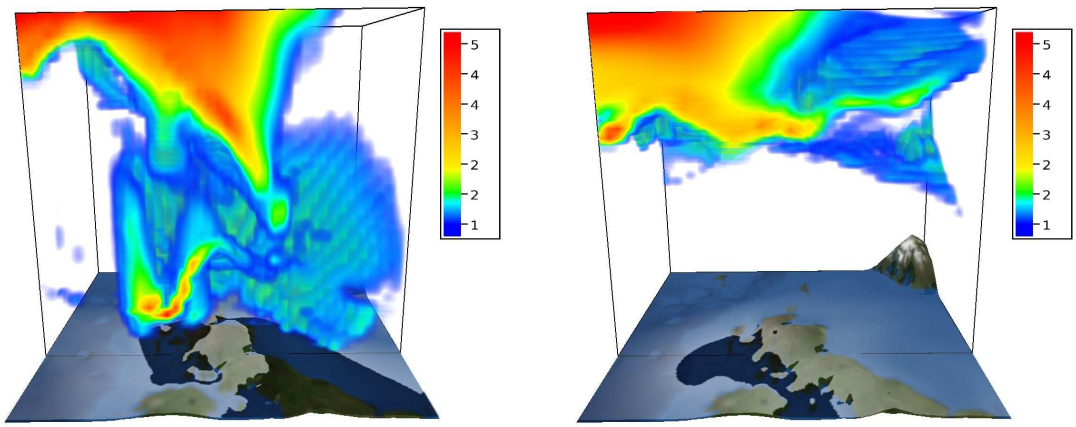

FIGURE 6.17: PV around the cyclone centre at 1200 UTC. PV (PVU) contoured according to label bar, with values <1 PVU opaque. Surface is shaded from 2 m θ = 284 K to indicate the cyclone position.

Figures 6.16 (a), (b), (d) and (e) also highlight the development of a low-level high PV region to the north of the cyclone centre in the CTRL and NO-CU simulations. By contrast the lack of latent heating in the NO-LH simulation mean no low-level PV anomaly forms (Figures 6.16 (c) and (f)). The extent of the diabatically produced PV around the cyclone centre can be seen in Figure 6.17. As shown in Figure 6.16, there is an intense band around the north edge of the storm produced by latent heating in the cloud head. The contouring in Figure 6.17 (a) shows that relatively high PV stretches from low levels and joins the upper-level anomaly, creating a well aligned PV tower. These have been identified in a number of intense storms and can key in the development of the storm (Bosart et al., 1996; Hoskins and Berrisford, 1988; Uccellini et al., 1987; Wernli et al., 2002; Whitaker et al., 1988). By contrast, Figure 6.17 (b) shows the lack of PV tower in the NO-LH simulation. The highest low-level values of 2-5 PVU in Figure 6.17 (a) correspond to the strong CCB extending around the BBF in this region where PV is generated through diabatic heating in the cloud head above.

Wernli et al. (2002) show that for the storm Lothar, the low-level PV was the main driver of the initial cyclogenesis. The evolution of the PV shown in Figure 6.18 and the tropopause plots (Figures 6.13-6.15) show that in this case the low-level PV anomaly forms after the cyclone has begun to develop. The upper-level anomaly is, therefore, key to the initial cyclogenesis in this case, however the lower level anomaly is important in the increased deepening seen in the contrast of the CTRL/NO-CU to the NO-LH simulations.

The plots in Figure 6.19 show the PV on 850 hPa and its spatial relationship to the high winds as the storm crosses the UK. The magnitudes of PV are smaller in the NA runs than in the high-resolution simulations due to the lack of small scale diabatic heating that can be resolved at this resolution. Again, Figure 6.19 highlights the lack of diabatically generated low-level PV and the lower wind speeds in the NO-LH simulation (Figs. (c, f, i, l)). Conversely, the CTRL (Figs. (a, d, g, j)) and NO-CU (Figs. (b, e, h, k)) show the strong PV extending around the BBF with the high winds to the south of the low pressure centre. In relation to the PV, the winds are located similarly to that shown by Schemm and Wernli (2013) reproduced in Figure 5.36, namely, to the outside and slightly downstream of the maximum PV region.

As well as through latent heating, PV can also be generated through friction in frontal regions (e.g. Schemm and Wernli (2013); Stoelinga (1996)). Schemm and Wernli (2013) show that friction has a larger effect in the CCB than WCB region, it is still less then the LH-induced PV increase. Figures 6.18 and 6.19 support that in this case, as no low-level PV is present in the NO-LH simulation despite friction still being present.

As shown by Hoskins et al. (1985), condensation in rising air can help to couple with the upper levels and increase the development of both the upper- and low-level cyclonic anomalies. They also show that the positive feedback between upper and lower anomalies is enhanced where the low-level anomaly is ahead of the upper-level one. In this case the NO-LH cyclone develops slower and later, partially due to the lack of condensational heating. This may then limit the coupling with the upper levels, whilst also limiting the connection with the high jet stream winds causing the initial propagation to be slowed. A later coupling to the jet stream may then be responsible for the more southern track of the NO-LH storm.

6.3.2.4 Circulation and Kinetic Energy

The differences in PV, wind speed and their respective locations raise questions about the relationships therein. In order to examine the relative large- and small-scale vorticity, two terms are defined. The first, Circulation Kinetic Energy (CKE) is defined as:

$$CKE = \frac{1}{2}\left(\frac{1}{L}\int \zeta \, dA\right)^2, \qquad [m^2 s^{-2}] \tag{6.1}$$

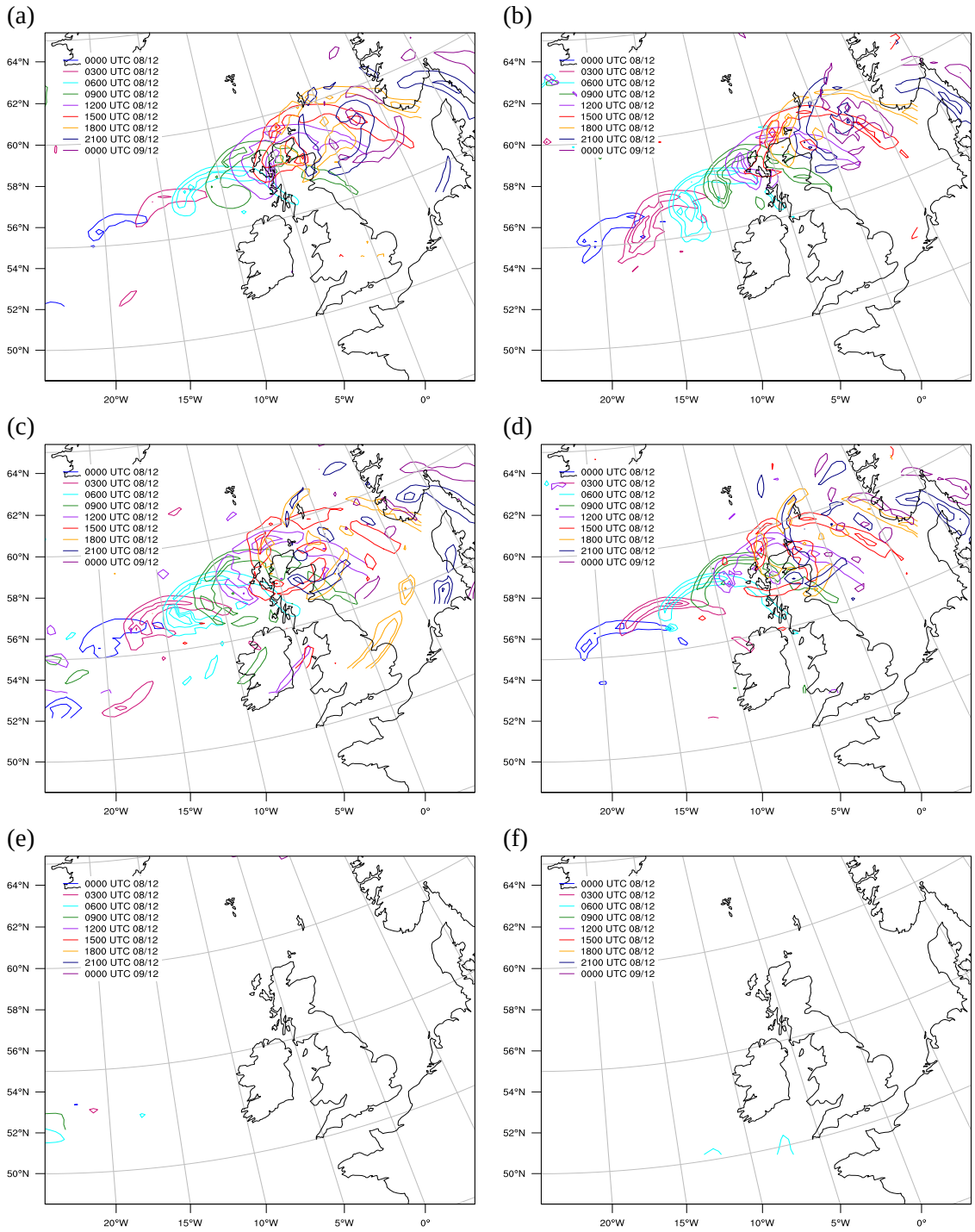

FIGURE 6.18: Evolution of PV in the CTRL; (a) and (b), NO-CU; (c) and (d) and NO-LH; (e) and (f) on 780 hPa (left column) and 850 hPa (right column). The PV is shown for a 40x40 gridpoint box around the minimum SLP at each time to remove the noise and small scale PV features not associated with the BBF. Contours are marked 1.5 to 3.5 PVU every 1 PVU from 000 UTC 8th Dec. to 0000 UTC 9th Dec every 3 hours as marked in the legend.

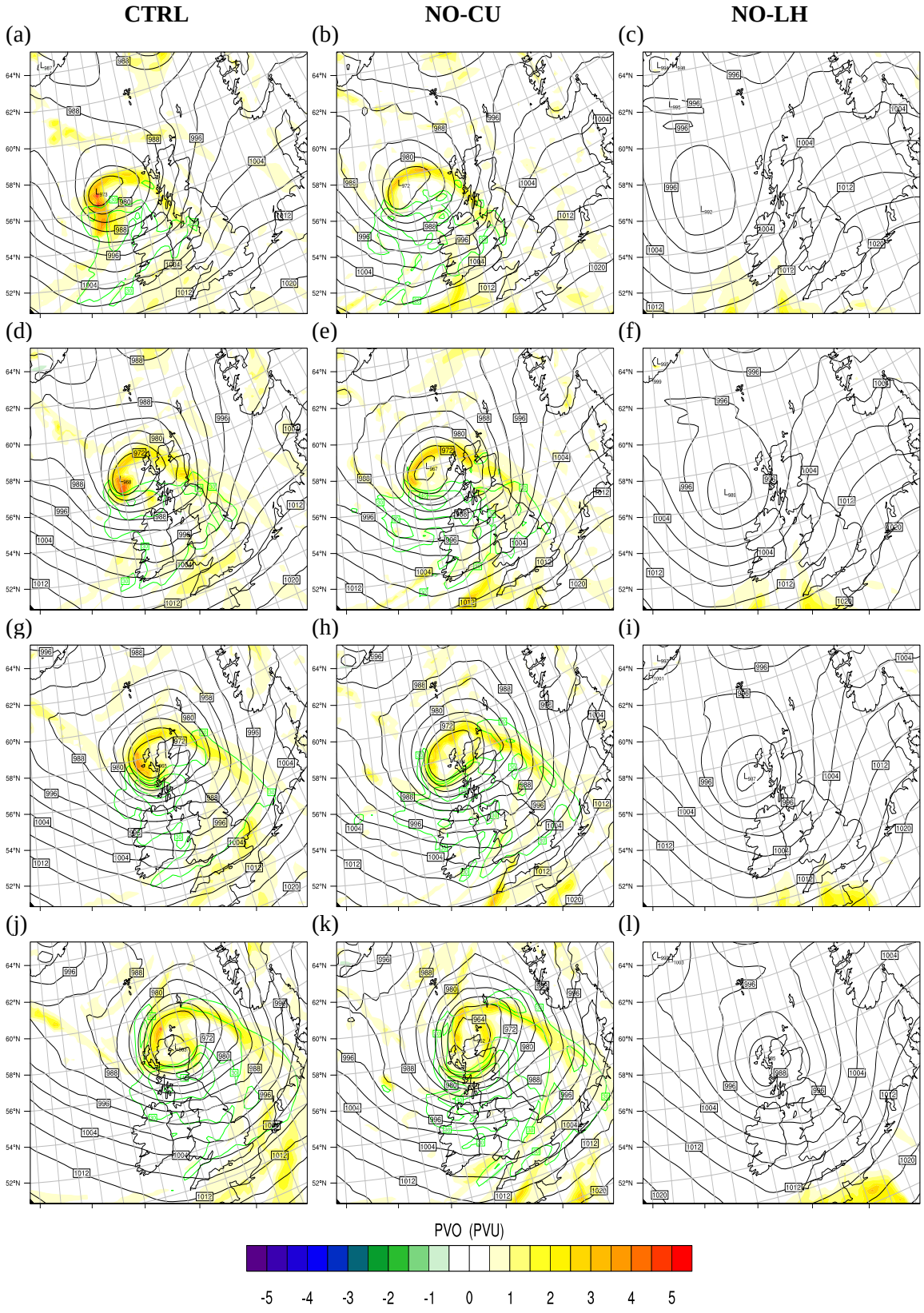

FIGURE 6.19: As Figure 6.12 but with shading showing PV and green contours indicating wind speed at 35, 40 and 45 ms^{-1}.

where L is the length bounding the area of interest, ζ is the relative vorticity and A is the area. CKE is therefore defined as the energy per unit mass, with units of m^2s^{-2}, and is the kinetic energy of the large scale circulation. ζ is related to the large-scale circulation through Kelvin's Circulation Theorem (Holton, 1992; Martin, 2006). It is also related to the high winds on a small-scale but independent to the large-scale circulation. The CKE equation allows the circulation over the large scale area of the storm to be analysed and compared to the energy on smaller scales.

The second term is the Wind Kinetic Energy (WKE):

$$WKE = \frac{1}{A}\int \frac{1}{2}\mathbf{U}^2 \, dA, \qquad [m^2 s^{-2}] \tag{6.2}$$

where A is area and $\mathbf{U}$ is the horizontal wind speed. The WKE defines the kinetic energy per unit mass of the small-scale circulations of the winds within the area. This allows us to compare the large- and small-scale circulations within the cyclone.

The time evolution of CKE and WKE are compared in Figure 6.20. There is a clear distinction between the energy within the CTRL and NO-CU simulations compared to the NO-LH simulation. On all three levels the CTRL and NO-LH show a steady increase in the CKE and WKE over time. By contrast, the NO-LH simulations shows an increase in the CKE from 0000 UTC until 0900 UTC at which point it plateaus and begins to decline slightly. The NO-LH WKE however, shows a different evolution. At 780 hPa (Figure 6.20 (a)) it starts at 160 m^2s^{-2} and gradually declines until 1000 UTC where the decline ceases and the values remain relatively constant around 130 m^2s^{-2}. At the lower levels of 850 hPa (Figure 6.20 (b)) and 925 hPa (Figure 6.20 (c)) the WKE starts with values around 135 m^2s^{-2} and remain relatively constant throughout the period shown. This shows that although the total circulation around the cyclone (CKE) increases, the small-scale energy of the winds decreases or remains largely constant in the NO-LH simulation. The contrast of the increasing CKE and WKE over time in both the CTRL and NO-CU simulations shows the energy added to both the large-scale circulation and local energy by the release of latent heat.

As noted previously, ζ can be related to the high winds on a local scale as well as the large-scale circulation. This would suggest a correlation between the CKE and WKE. Figures 6.21 (a), (b) and (c) show CKE plotted against WKE for the 780, 850 and 925 hPa levels, respectively. Generally, CKE values rise with WKE values in the CTRL and NO-CU. This is best observed at the 780 and 850 hPa levels (Figures 6.21 (a) and (b)). At the 780 and 850 hPa levels the NO-CU simulation

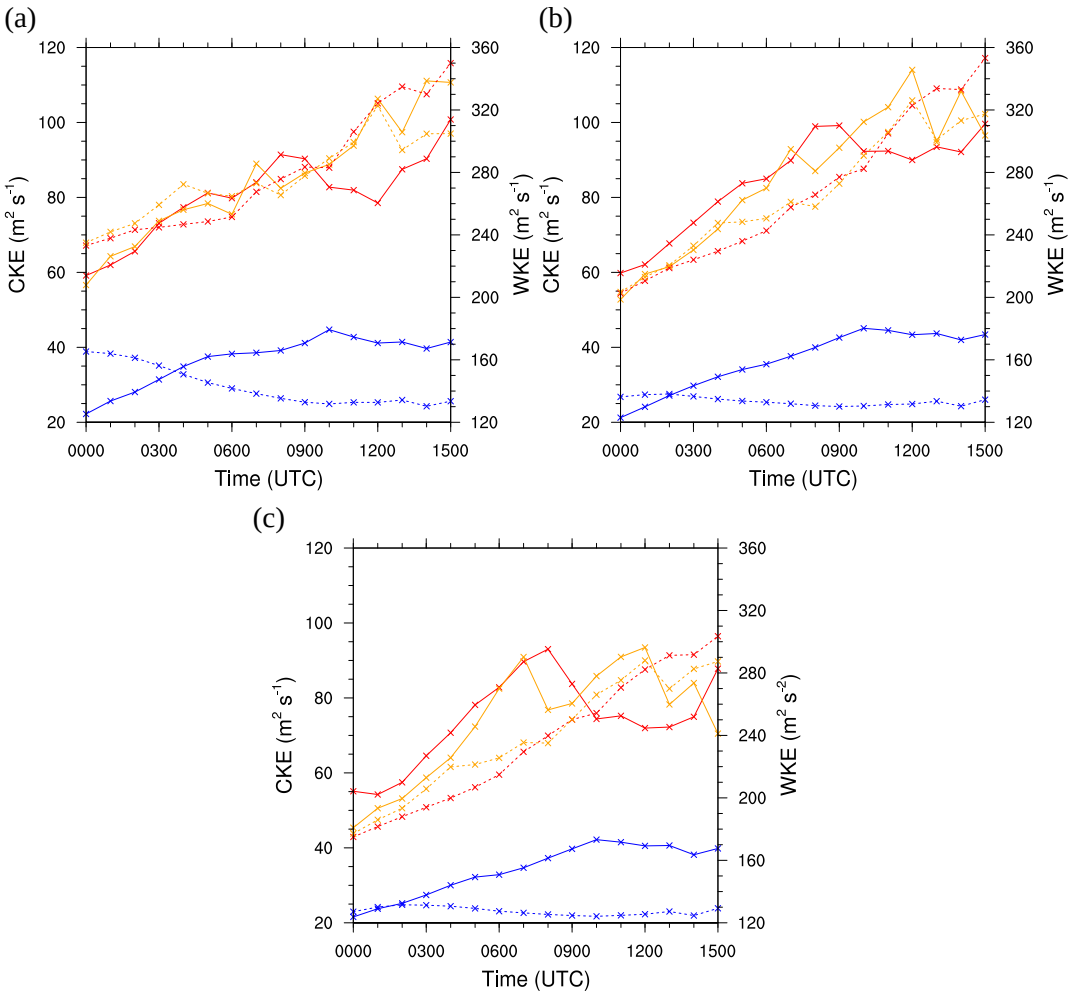

FIGURE 6.20: Time series of CKE (solid lines) and WKE (dashed lines) on (a) 780, (b) 850 and (c) 925 hPa levels. Coloured lines/markers indicate CTRL (Red), NO-CU (orange) and NO-LH (Blue) simulations.

shows good correlation between the CKE and WKE with r^2 values of above 0.9. However, there is some spread of the data compared to the regression lines showing that an exact 1:1 relationship between the large- and small-scale circulations does not exist. Corroborating the pattern fron the time series in Figure 6.20, the NO-LH simulation shows WKE falling with increasing CKE at the 780 hPa level (Figure 6.21 (a)) while it remains fairly constant at the lower-levels. The low-level 925 hPa plot (Figure 6.21 (c)) shows much lower correlation in all three simulations due to the influence of friction and land induced perturbations to the flow. However a general trend of rising CKE with WKE is shown by both the CTRL and NO-CU simulation.

Figure 6.20 suggests a relationship between the deepening of the storm and the circulation energy, particularly in the CTRL and NO-CU cases. The relationship between CKE and SLP is shown in Figures 6.22 (a), (c) and (e) on the 780, 850 and 925 hPa levels respectively, while WKE is plotted

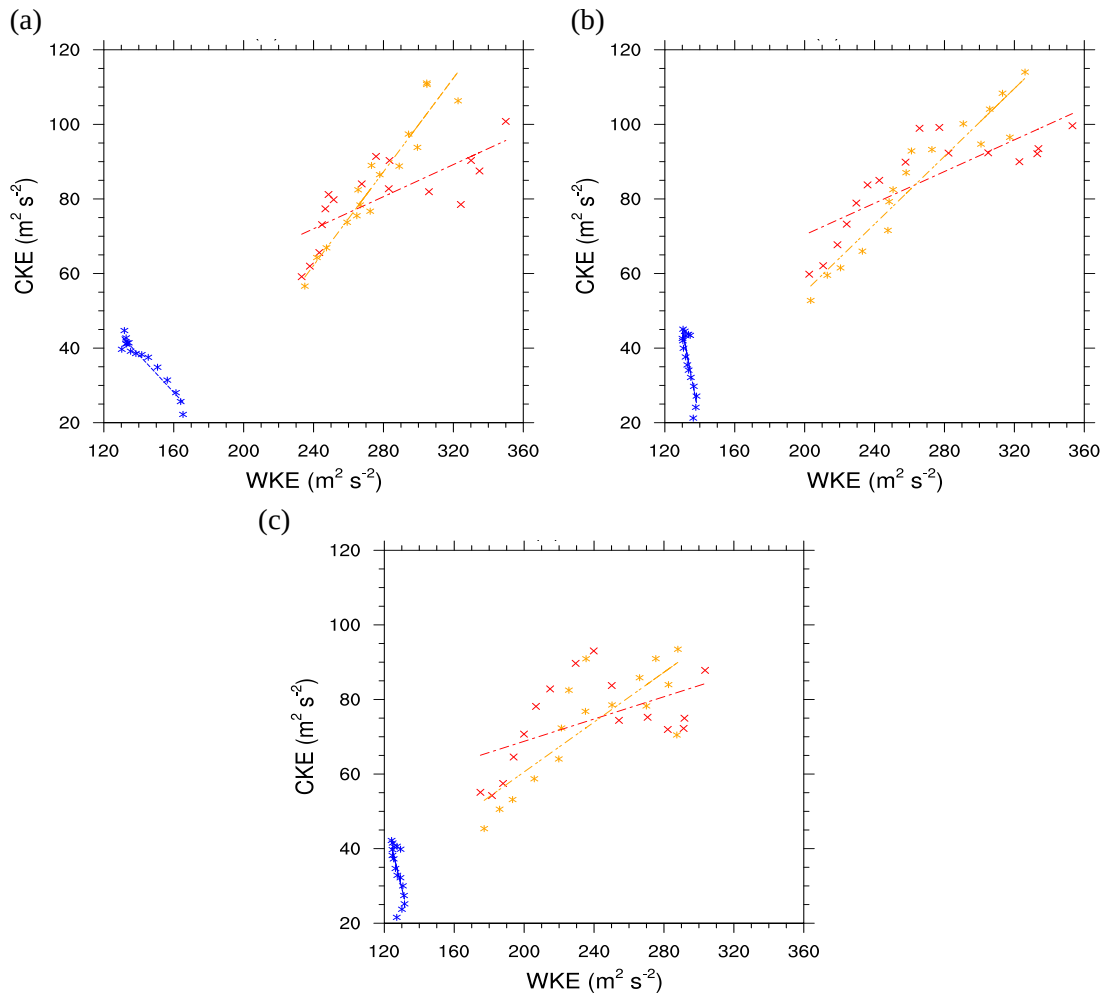

FIGURE 6.21: Scatter plots with lines of best fit of CKE against WKE. Marker and line colours correspond to CTRL - red, NO-CU - orange and NO-LH - Blue. (a), (b) and (c) show CKE from the 780, 850 and 925 hPa levels, respectively.

against SLP in (b), (d) and (f) for the corresponding levels. The statistics for the correlation and best fit lines are shown in Table 6.3 for the CKE plots and Table 6.4 for the WKE lines. A clear relationship can be seen at the 780 hPa and 850 hPa levels between the CKE and minimum SLP. The 925 hPa level, however does not show the same level of regression in the CTRL and NO-CU simulations. The lower regression in these two simulations is mainly caused by a bigger spread in CKE at lower minimum pressures, when the storm is at its deepest. This level intersects the surface at this time in the CTRL and NO-CU runs meaning that the high values of vorticity will be missing. This is further highlighted by the close relation of the NO-LH r^2 value at this level where there are fewer missing values. All three simulations show a similar relationship between CKE and SLP at 780 and 850 hPa in particular. This can be seen by the relatively good fit by a single line-of-best-fit created for all the data points. There is a systematic strengthening of the gradient

TABLE 6.3: Line of best fit equations and r^2 values for the CKE and minimum SLP data plotted in Figures 6.22 (a, c, e). "All run" values equate to the grey line calculated from the data from all three of the simulations.

CKE					
Level	**Run**	**r^2**	**Level Reg. Equation**	**All Run r^2**	**All run Equation**
780	CTRL	0.792	-1.313x+1356.99	0.932	-0.098x+105.77
	NO-CU	0.889	-2.054x+2079.71		
	NO-LH	0.824	-1.328x+1352.68		
850	CTRL	0.895	-1.616x+1656.18	0.957	-0.104x+112.38
	NO-CU	0.915	-2.380x+2396.68		
	NO-LH	0.928	-1.675x+1697.21		
925	CTRL	0.511	-1.120x+1163.19	0.876	-0.081x+88.71
	NO-CU	0.697	-1.7x+1724.36		
	NO-LH	0.914	-0.103x+1485.31		

of the best fit lines in the NO-CU and NO-LH runs compared to the CTRL. This suggests that the vertical motions produced by the convection scheme act to limit the large-scale circulation for a given central pressure.

The comparison of WKE to the minimum SLP for the CTRL and NO-CU simulations shows a similar agreement to that of the CKE - that the WKE increases with decreasing SLP. Unlike the CKE-SLP relationship however, the NO-LH does not show a similar WKE-SLP relationship to the CTRL and NO-CU. At the lower two levels (Figures 6.22 (d) and (f)) the WKE is largely constant for any given SLP. At 780 hPa the WKE increases with increasing pressure showing lower small-scale circulation energy as the cyclone deepens. The release of latent heat within the cyclone is therefore, essential for increasing the energy of the small-scale circulations as the cyclone deepens. Figures 6.22 (b), (d) and (f), along with the best-fit line data shown in Table 6.4, indicate that the influence of SLP on WKE is greater at lower altitudes with higher line gradient at 850 and 925 hPa compared to the corresponding 780 hPa gradient for each simulation.

6.3.2.5 Varying the Latent Heating Switch Off Time

The comparisons so far in this section have been on simulations with latent heating either on or off from the model initiation at 1200 UTC on the 06^{th} Dec. meaning that latent heat is missing from before the initiation of the storm. In this section simulations are performed using the WRF restart function. The model is run using the NO-CU setup, creating restart dumps at regular intervals.

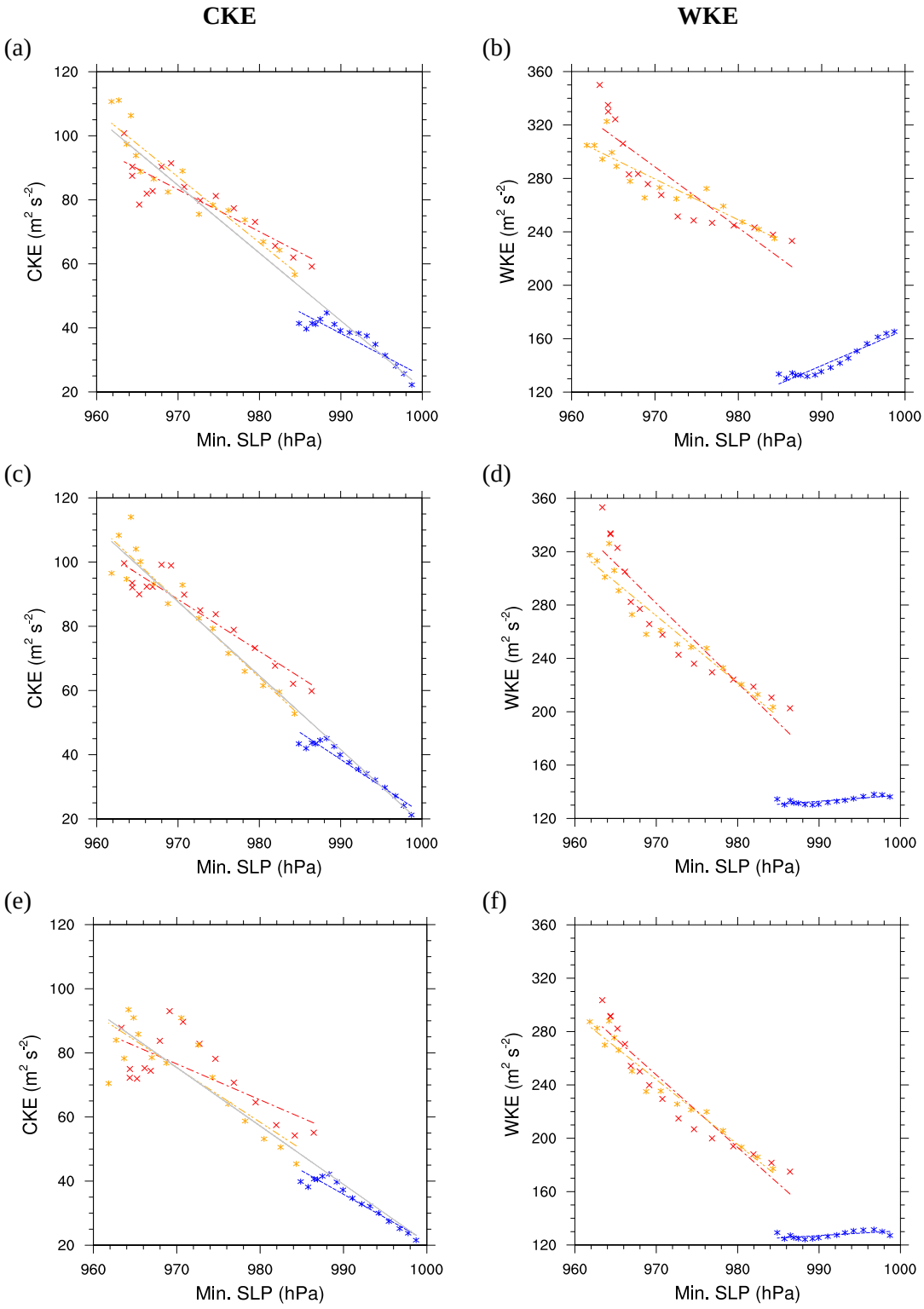

FIGURE 6.22: Scatter plots with lines of best fit of CKE against the minimum cyclone pressure for the CTRL (red), NO-CU (orange) and NO-LH (Blue). (a), (b) and (c) show CKE from the 780, 850 and 925 hPa levels, respectively. Grey lines indicate the line of best fit across the data from all 3 simulations.

TABLE 6.4: Line of best fit equations and r^2 values for the WKE and minimum SLP data plotted in Figures 6.22 (b, d, f).

WKE			
Level	**Run**	**r^2**	**Level Reg. Equation**
780	CTRL	0.790	-4.555x+4707.13
	NO-CU	0.849	-3.059x+3246.78
	NO-LH	0.914	2.769x+-2512.13
850	CTRL	0.846	-5.973x+6074.87
	NO-CU	0.930	-5.045x+5165.64
	NO-LH	0.573	0.455x+-317.662
925	CTRL	0.912	-5.436x+5520.84
	NO-CU	0.963	-4.865x+4962.85
	NO-LH	0.393	0.358x+-227.446

Latent heating is then switched off and the simulation restarted at the chosen times of 0600 UTC (hereafter LHo-0600 run) and 0000 UTC (LHo-0000), both on the 8^{th}.

The track of the NO-CU simulation and the two LHo simulations are shown in Figure 6.23 (a). The first latent heating switch off occurs at 0000 UTC, at this time the storm is centred at ~18°W. There is some delay before the LHo-0000 line (dark green) splits from the NO-CU track. At 0600 UTC the LHo-00 minimum SLP has slowed and is lagging behind the NO-CU marker at ~14°W and ~13°W respectively. However, by the next marker, 0900 UTC it is in an almost identical position to the NO-CU.

Both the LHo tracks are to the south of the NO-CU from 1500 UTC onwards. This mimics the more southerly track in the early evolution of the NO-LH simulation shown in Figure 6.11 (a), although by the end of the track the CTRL moves south of the NO-LH. The removal of latent heating does, therefore, appear to have some effect of forcing the cyclone on a more southerly path. This effect only seems to be apparent for a limited time as shown by the switch in the NO-LH and CTRL in the latter stages.

The evolution of the minimum SLP and maximum wind speed for the 780, 850 and 925 hPa levels are shown in Figures 6.23 (b), (c) and (d), respectively. The minimum SLP quickly deviates from the NO-CU simulation as soon as the latent heating is switched off, with the deepening significantly slowed. Some deepening still occurs without the latent heating due to the influence of the upper-level trough. The continued deepening is limited, with the minimum SLP largely plateauing after 1200 UTC in the LHo simulations, while the NO-CU continues to deepen. From the tropopause plots, shown in Section 6.3.2.3, it can be seen that at this time the upper-level PV

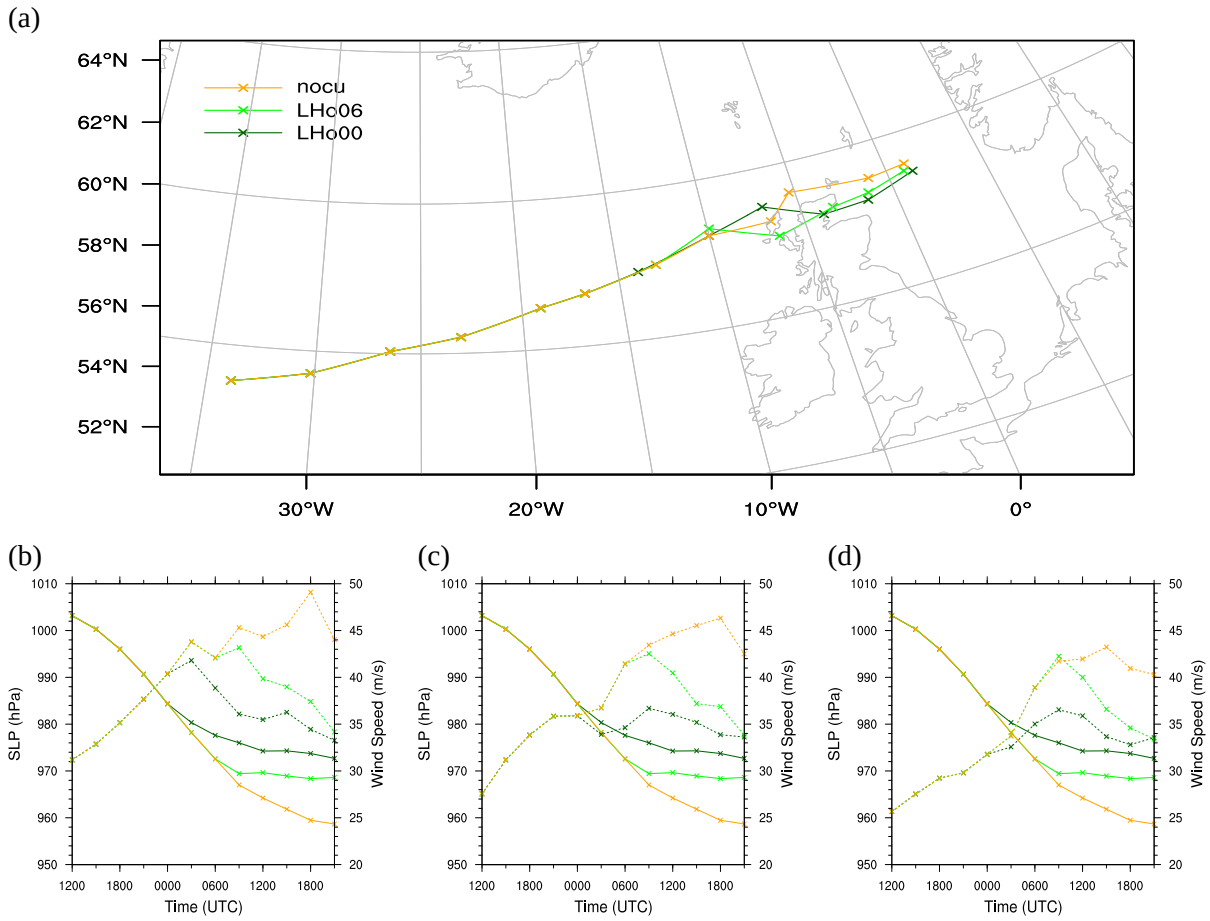

FIGURE 6.23: As Figure 6.11 but for the NO-CU (orange) and LHo-06 (green) and LHo-00 (dark green) simulations.

anomaly begins to overtake the surface cyclone meaning it becomes less conducive for deepening (Hoskins et al., 1985). The continued deepening of the NO-CU SLP then suggests that the latent heating is responsible for this once the upper-level anomaly has overrun the surface storm.

The maximum wind speed evolution varies depending on the level (dashed lines, Figures 6.23 (b)-(d)). On 780 hPa the maximum wind speed continues to increase for the 3 hours after the latent heat is switched off, albeit at a slower rate than the NO-CU run. The LHo-0000 reaches a peak wind speed of 42 ms^{-1} at 0300 UTC and the LHo-06 peaks at 43 ms^{-1} at 0900 UTC. After these peaks the wind speeds decrease. The LHo-0000 rapidly decreases to ~36 ms^{-1} by 0900 UTC, then, excluding a slight rise at 1500 UTC, decreasing more gently to ~33 ms^{-1} by 2100 UTC. The LHo-0600 decreases by 3 ms^{-1} over the first 3 hours after its peak before then decreasing by a further 5 ms^{-1} over the following 9 hours. The 850 hPa LHo-0000 wind maxima show a different evolution after the latent heating switch off. They undergo an initial deceleration before increasing again after 3 hours. The maximum in both the LHo wind speeds is at 0900 UTC at 36 ms^{-1} for the

LHo-0000 and 42 ms^{-1} for the LHo-0600. They decelerate at different rates with both maxima at 2100 UTC being around 34 ms^{-1}. At 925 hPa the LHo-0000 maximum wind continues to increase until 0900 UTC; the LHo-0600 maximum wind also continues to accelerate until 0900 UTC when both begin to decrease from maximums of ∼36 ms $^{-1}$ and 43 ms^{-1}, respectively (Figure 6.23 (d)). The LHo-0000 decelerates relatively gently to just below 33 ms^{-1} at 1800 UTC before accelerating by ∼1 ms^{-1} at 2100 UTC. The LHo-0600 decreases more rapidly ending at 2100 UTC marginally lower than the LHo-0000 speed.

The differing rates of deceleration in the maximum wind speeds suggest a relaxation of the system moving back towards some sort of balance as the SLP deepening subdues. Meanwhile, the continued deepening of the NO-CU storm maintains the imbalance causing the winds to continue accelerating.

The differences in the magnitudes and spatial distribution of the wind speeds in the LHo-0600 and LHo-0000 simulations compared to the NO-CU simulation are shown in Figures 6.25 and 6.24, respectively. The wind speed differences in the LHo-0600 simulation are highest to the north and east of the storm along the warm front and BBF. Differences in the regions of highest winds, to the south of the cyclone centre, are lower than those associated with the warm and BBFs. The differences are greatest at the 780 hPa level (Figure 6.25 (b)), and generally lower in the 850 and 925, hPa levels (Figures 6.25 (e) and (h)). One exception to this point is a region to the west of the cyclone centre at ∼10°W 58°N where differences are highest at the 850 hPa level.

As would be expected the switching off of latent heating earlier has a larger effect on the wind field. In the LHo-0000 comparison with he NO-CU simulation (Figure 6.24) the magnitudes of the differences are much larger than for the LHo-0600 differences shown in Figure 6.25. Differences of >10 ms^{-1} are shown on all sides of the cyclone at the 780 and 850 hPa levels (Figures 6.24 (b) and (e)). At 925 hPa (Figure 6.24 (h)) the magnitudes of the differences are generally lower barring the region to the west of the cyclone centre which was also identified in Figure 6.25.

The two LHo- wind speed difference figures indicate common areas where latent heating is particularly important in developing the winds. These areas are to the north-east of the cyclone and along the warm front at all levels, and to the west of the cyclone centre at the 850 and 925 hPa levels. The region to the north-east of the cyclone centre is the region of intersection of the cold front and BBF where the WCB lifts over the warm front. The influence of the condensation and PV generation here has a strong impact on the downstream flows (Schemm and Wernli, 2013).

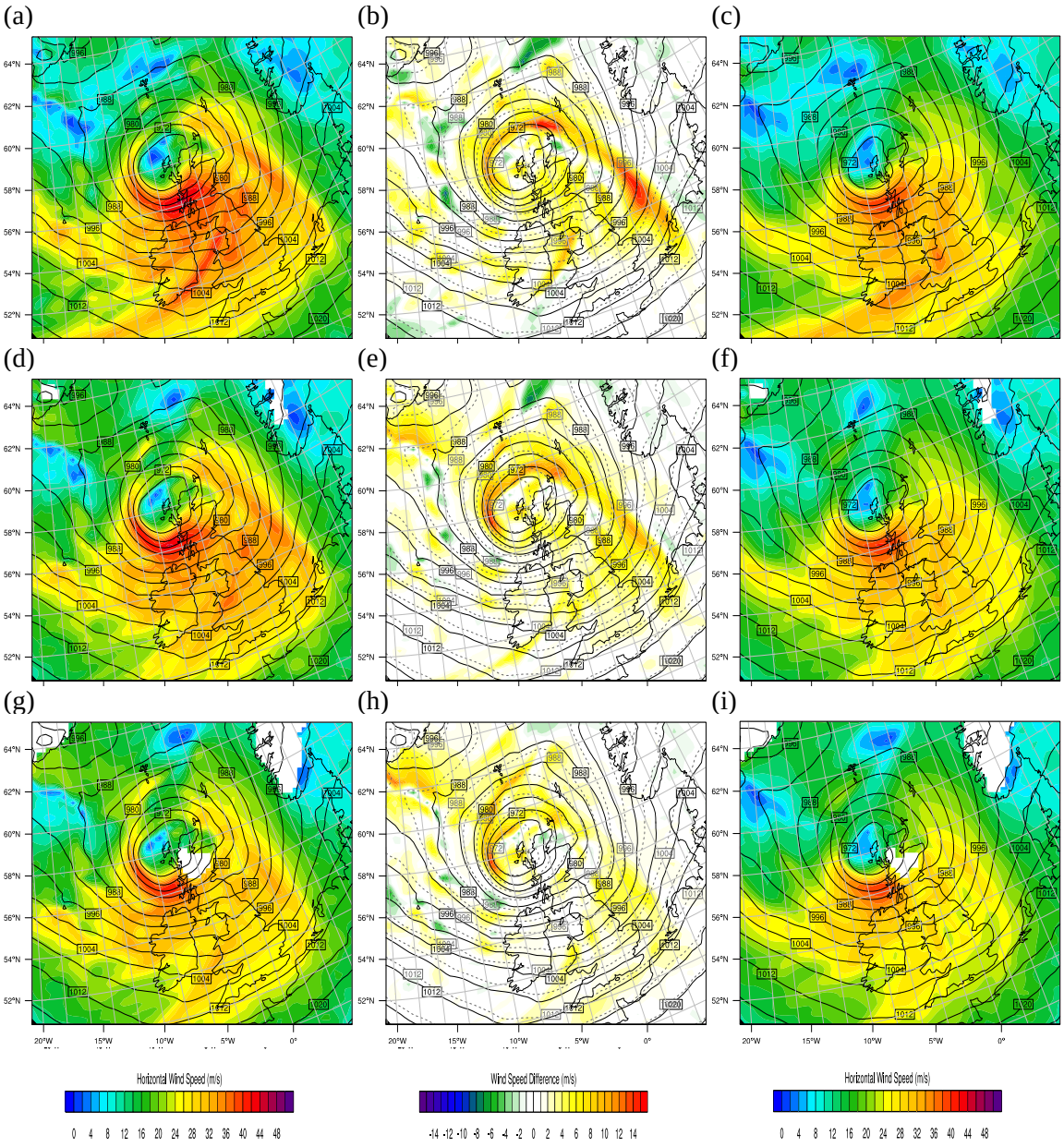

FIGURE 6.24: NO-CU and LHo-0600 simulation wind speeds and SLP plots at 1200 UTC. Plots (a), (d)and (g) show NO-CU on 780, 850 and 925 hPa respectively while (c), (f) and (i) show corresponding levels for the LHo-0600 simulation. Wind speed difference and SLP comparison is shown in the middle column (b), (e) and (h).

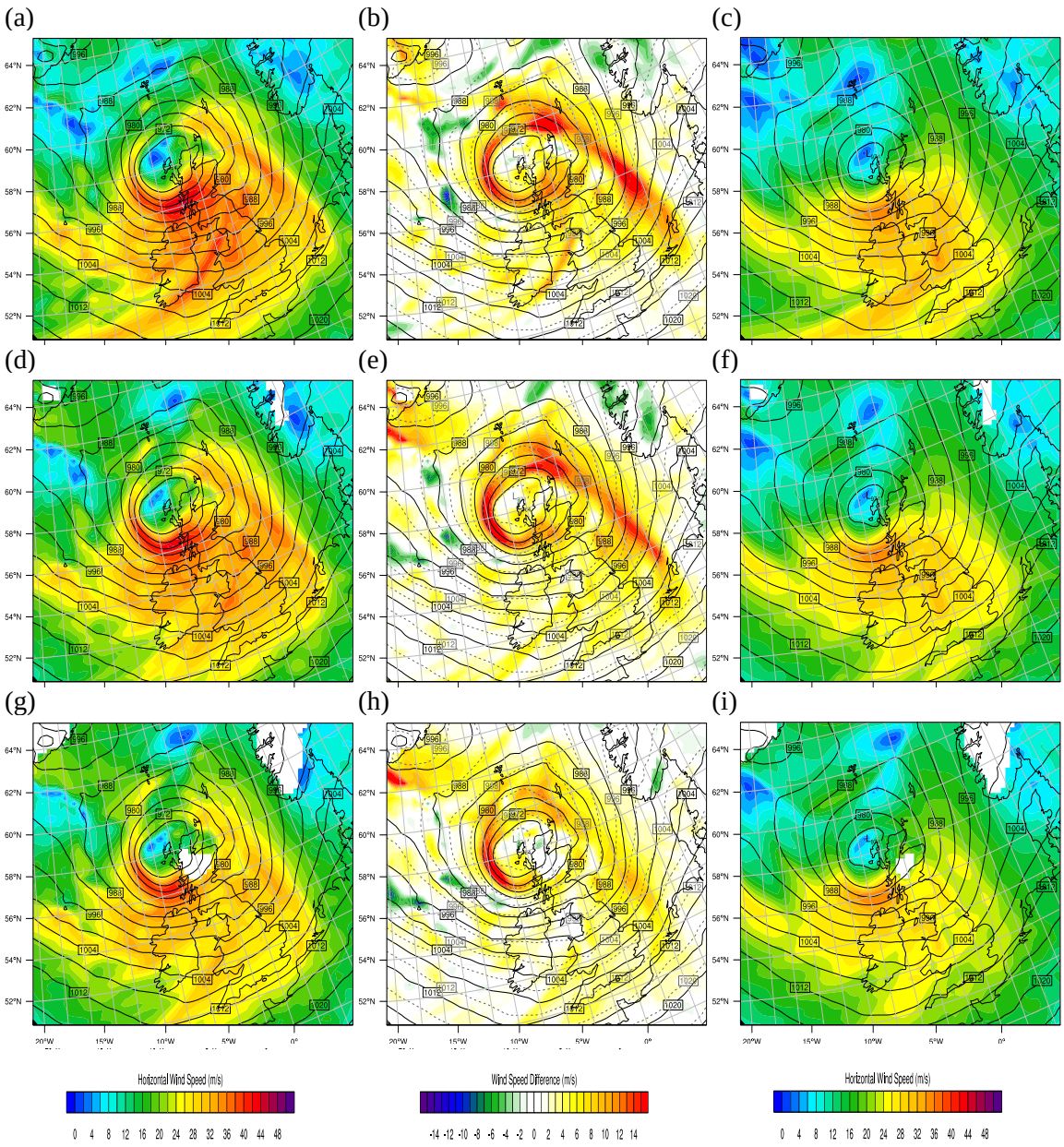

FIGURE 6.25: NO-CU and LHo-0000 simulation wind speeds and SLP plots at 1200 UTC. Plots (a), (d)and (g) show NO-CU on 780, 850 and 925 hPa respectively while (c), (f) and (i) show corresponding levels for the LHo-0000 simulation. Wind speed difference and SLP comparison is shown in the middle column (b), (e) and (h).

The region to the west of the cyclone centre in the 850 and 925 hPa wind differences is close to the location of the end of the PV ribbon (Figure 6.18 (d)). This suggests that the latent heating influence on the strength of the low-level PV ribbon is of importance for the development of high wind speeds in this region.

Figure 6.26 shows the effect of latent heat removal on PV in both the LHo-0000 and LHo-0600 compared to the NO-CU simulation. The role of latent heating in developing the low-level PV

anomaly is evident from the large differences in the PV field when it has been removed. The removal of latent heating at 0000 UTC (Figures 6.26 (a) and (c)) causes larger differences compared to the NO-CU PV, with larger regions of >2.5 PVU difference than the LHo0600 run (Figures 6.26 (b) and (d)).

To the west of the cyclone centre, there is a strong region of difference in the PV fields. At 850 hPa in both the LHo-0000 and LHo-0600 (Figures 6.26 (c) and (d) respectively) this region is located at ~9°W 58°N, just to the east of the noted wind speed differences in Figures 6.24 and 6.25. At the 780 hPa level there is a corresponding region of strong difference located slightly to the south and east (Figures 6.26 (a) and (b)). This region, however, is not associated with a large wind speed difference.

6.4 Summary

As the simulation presented in Chapter 5 and the no-lc simulation in this chapter were run without the inclusion of graupel or hail a sensitivity test has been run to investigate if this has any effect on the modelled storm. In terms of both winds and precipitation there is little notable effect from the inclusion of either graupel or hail.

Following the disagreement as to the influence of latent cooling on the development of SJs within the past literature (see Section 2.4.3), a simulation is presented where latent cooling is removed. This shows that latent cooling has little effect on the overall wind speed distribution but does change the evolution of trajectories.

Latent heating is shown to have a large effect on the development of the storm. Removal of the latent heating causes a much shallower low to develop with corresponding weaker winds. The track of the cyclone is largely unaffected by the lack of latent heating. The lesser deepening of the storm is largely due to the low-level diabatic PV anomaly not forming. The coupling with the upper levels may also play a role through the slower initial speed of the cyclone without latent heating.

When the latent heating is switched off later during the simulations the storm rapidly slows the deepening rate as the lack of latent heating reduces the production of low-level PV along the BBF. The wind speeds also drop as the deepening rate slows.

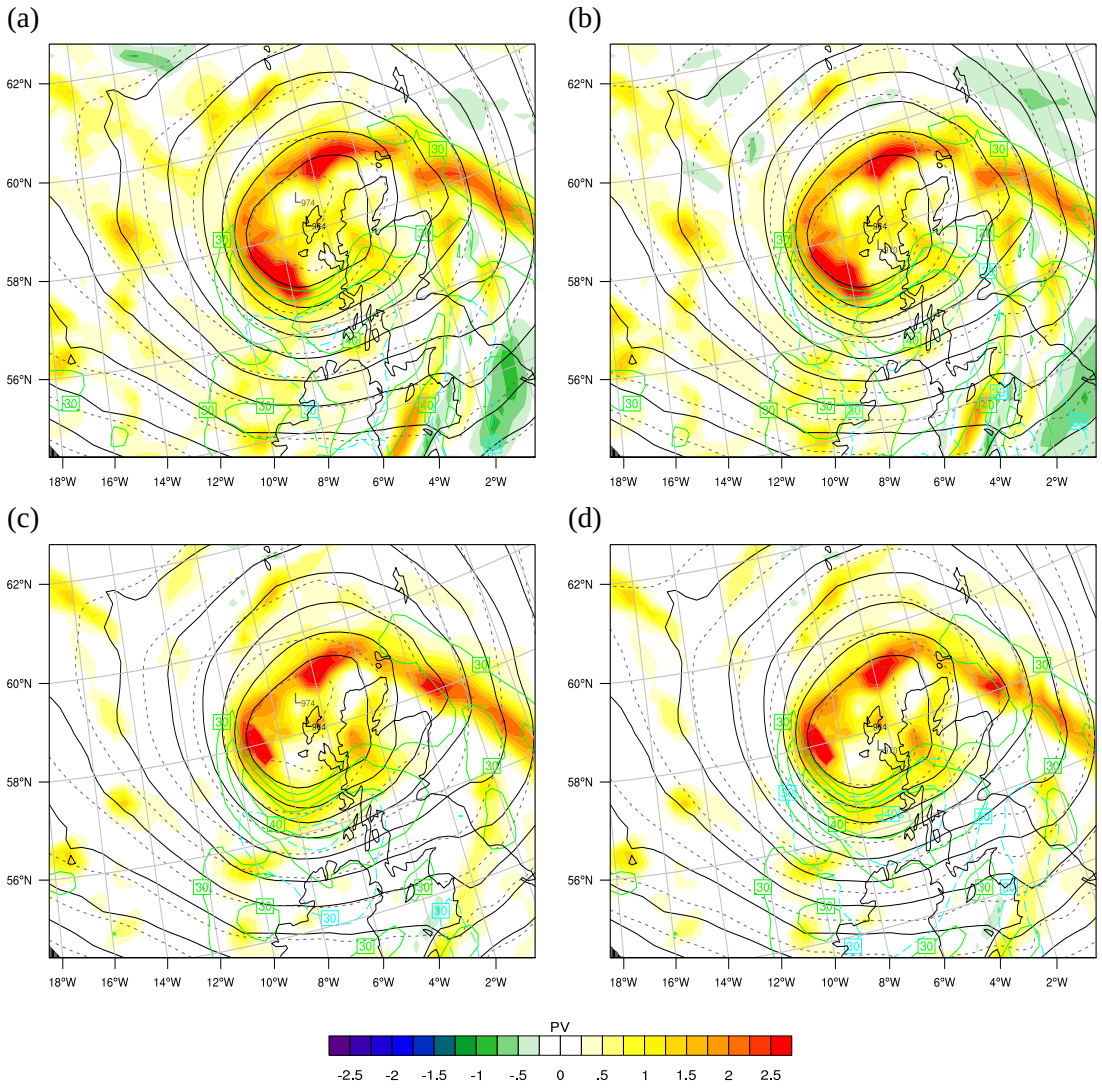

FIGURE 6.26: PV differences between the NO-CU simulation and the LHo-0000 (a and c) and the LHo-0600 (b and d) on 780 hPa (top row) and 850 (bottom) hPa level at 1200 UTC 8^{th} Dec. Wind speeds contoured every 5 ms^{-1} from 30 ms^{-1} for NO-CU (green) and the respective LHo (blue). SLP contoured in black for the NO-CU and dashed grey for the LHo simulations.

Novel diagnostics for investigating the energy of the circulation and wind speeds are presented. The CKE provides a measure of the energy of the large-scale circulation around the cyclone. WKE shows the influence of the small-scale circulations as a result of wind speed. Some correlation is shown between these two variables in the simulations with latent heating. Both variables show good correlation with the minimum cyclone SLP with the values of the CKE and WKE increasing as the storm deepens.

Chapter 7

Conclusions and Further Work

This chapter brings together the conclusions and findings of Chapters 4-6. It also presents ideas for future work that have arisen through the results presented here and gaps in the literature.

As stated in Chapter 1, the overarching aims of this thesis are to:

- **Understand the dynamical development of the high winds in Cyclone Friedhelm.**
- **Determine the influences of diabatic processes on the high winds, specifically:**
  - **The role of latent cooling on the high winds**
  - **The role of latent heating in the storm development**

7.1 Conclusions

7.1.1 Evaluation of WRF Modelling

In a modelling study such as this, it is important to have confidence that the model is able to replicate the processes and features of the cyclone. Chapter 4 provides an evaluation of the high-resolution WRF simulation, used for the dynamical analysis in Chapter 5. The WRF model is shown to replicate the development of Cyclone Friedhelm well in comparison to operational analysis and observations. The unique dataset provided by the dropsondes provides an additional platform from which to compare the model performance. Again the model recaptures many of the key features.

Comparison to MO analysis shows generally good agreement in both the deepening of the cyclone and the track. The track of the WRF cyclone shows a slight southerly bias until the storm has passed over Scotland. The southerly shift in the track is also noticeable in the ASCAT-WRF wind comparison. Barring this, however, the winds compare very well with both the spatial location and magnitudes of the low-level winds well represented in the WRF simulation. The WRF cloud and precipitation fields are compared to satellite imagery and radar data, respectively. These show a degree of zonal stretching in the WRF simulation and some overestimation of the precipitation along the BBF. The overall shape of the storm is well resolved and the timings largely consistent with those shown in the observations. This provides strong confidence in the subsequent analysis of the dynamics of the cyclone.

7.1.2 Dynamics of Cyclone Friedhelm

7.1.2.1 Identification of a Sting Jet

Trajectories are initiated on three levels to investigate the evolution of high wind speed regions throughout the evolution of the storm. One ensemble of trajectories, named t1000-780, shows evidence of being a SJ. These parcels show strong descent to the 780 hPa level, whilst exhibiting near-constant θ_w, acceleration and a reduction in RH_i. Although the trajectories originate from further towards the cold side of the BBF than some of those in previously studied storms, they appear relatively consistent with the track of the SJ identified in the UM analysis of cyclone Friedhelm by Martínez-Alvarado et al. (2014).

7.1.2.2 Influences on Sting Jet Trajectories

Having identified specific SJ trajectories these are analysed within the context of the theories presented in Section 2.4.3. Each of these theories and the main findings are presented below.

CSI release prior to Sting Jet descent

The SJ trajectories shown in Chapter 5 are shown to exhibit some negative MPV prior to descent. This supports the case made by a number of previous studies that CSI is a factor in the development of SJs. However, there is debate about its importance and influence. It has been shown in the

idealised studies of Baker et al. (2013) and Slater et al. (2014) that CSI is not needed to form SJs. However the number of studies which have found evidence for CSI on SJ trajectories suggests there is at the very least a correlation between the presence of these phenomena. The evidence here adds another example of SJ trajectories exhibiting some CSI release prior to, and during the SJ descent.

Frontolysis during Sting Jet Descent

Following the suggestion by Schultz and Sienkiewicz (2013), the influence of frontolysis on the descent of the SJ feature is examined. A frontolytic region is present at the end of the BBF in this case, in support of Schultz and Sienkiewicz (2013) the identified SJ trajectories begin to descend as they pass from the frontogenetic to the frontolytic region. However, unlike in the Schultz and Sienkiewicz (2013) case, the frontolytic region does not exhibit the perceived reversal in vertical motions. The SJ descends on the cold side of the frontal region, rather than the warm in the case of Schultz and Sienkiewicz (2013) where the textbook frontolytic circulations show descent. This is likely due to the complexities of the moist processes and the continued growth of the clouds in the frontolytic region through latent heat release.

Latent Cooling effect on sting jet trajectories

The role of evaporation influencing the SJ has been suggested in a number of papers (Browning, 2004; Clark et al., 2005; Martínez-Alvarado et al., 2011, 2010), although others have shown little or no influence (Baker et al., 2013; Slater et al., 2014; Smart and Browning, 2014). Latent cooling has little effect on the strength of the winds but does influence the evolutions of the SJ trajectories. Indication from the pattern of winds on different levels suggest that the drivers are similar, i.e. large-scale motion. This is supported by the no-LC simulation showing similar wind speed properties albeit with a different parcel evolution.

SJs appear to be varied in their initial forcing, evolution, descent and strength. Schultz et al. (1998) argue that rather than attempting to find a single conceptual model for the evolution of cyclones it may be better to focus attention on the evolution and structure in different settings. Similarly, it could be argued for describing SJs as a broad model for a jet descending from the cloud head. Focus on the influences and prevalence of different forcing and outcomes may be a more fruitful focus for future research efforts rather than attempting to strictly define them based

on the presence of some specific criteria. The forecasting of SJs is of key importance for the safety of the general public. The work carried out here shows that the use of multiple diagnostics is key to understanding and predicting the life-cycle of a SJ. The forecasting of descent potentially requires the identification of frontolytic and CSI regions while the overall descent and probability of strong surface SJ winds can be informed by the application of low-level stability diagnostics. Trajectories may also play a key role in forecasting SJs accurately but can be computationally intensive to simulate. Knowledge and availability of this range of techniques and diagnostics may be key for forecasters attempting to identify and accurately predict the impact of SJ features.

7.1.2.3 CCB Trajectories

As well as the SJ airstreams identified from the t1000-780 trajectories a number of the other trajectory sets showed strong characteristics of CCB flow. These were seen both at the lover levels from the t1000- trajectory initiations and at all levels at the later times of 1100 and 1200 UTC. The CCB trajectories showed high winds of similar but slightly lower magnitudes to the SJ trajectories and were driven by the strong PGF around the cyclone center. Similarly to the SJ trajectories the maximum wind speeds shown by the CCB occurred around one hour later than the maximum of the PGF/geostrophic wind. Due to the limited vertical descent of the SJ trajectories in this case, the CCB is the key source of the low-level and surface winds. As with previous studies this highlights the need for greater understanding of the influences on both the SJ and CCB development and the relative magnitudes of both these phenomena to realise the risk of these explosive cyclones.

7.1.2.4 Unbalanced Nature of the High Winds

As would be expected in a highly curved, deepening storm such as cyclone Friedhelm, the geostrophic balance is not maintained. The peak winds are strongly sub-geostrophic, showing ageostrophic components of 60 ms^{-1} or more. Consistently, the trajectories show that the highest wind speed values occur after the peak geostrophic wind speeds. This lag varies slightly but is generally on the order of one hour. The calculation of along-flow PGF on the trajectories shows that at higher levels the peak wind occurs when the along-flow component of PGF is close to, or falls below zero, i.e. it begins to act against the flow. At lower levels the wind speed maxima occur closer to the maximum along-flow component of PGF maximum as higher friction at these levels retards the flow more rapidly.

The gradient wind, which accounts for the curvature of the flow, shows a better resemblance to the actual wind. The gradient wind is calculated in a novel way which allows for relatively easy calculation of the centre and radius of curvature. Although showing a much better estimate to the real wind than the geostrophic balance, the gradient wind still shows differences to the actual wind. To the southern side of the cyclone centre the actual wind is systematically super-gradient, while to the north it is sub-gradient. It is also noted that focusing on a smaller region, and therefore achieving a more accurate radius of curvature, decreases the magnitude of gradient wind, indicating that the actual wind is more super-gradient to the south of the cyclone than is shown.

The locations of the trajectories in relation to the gradient wind shows that the SJ trajectories are more super-gradient on a given level than the CCB ones. This is indicative of higher momentum air descending to levels where it is more unbalanced.

The Bernoulli equation is tested on the SJ trajectories in order to investigate whether this theory fits the acceleration during the descent of the SJ. The trajectory analysis shows that the Bernoulli number is not conserved during the descent, due to the influences of both friction and the continued deepening of the storm. It would be of interest to test this theory on other cases where the storm may be in a more steady-state.

The investigation of the balances here suggest that attempting to describe rapidly evolving cyclones such as Friedhelm in terms of an idealised balance may result in large errors compared to the observed flows. However, these should not be discounted entirely; cases where the cyclone is more balanced, perhaps due to a more steady state situation, may allow useful conclusions to be drawn from these theories.

7.1.3 Role of Latent Heating

As shown in Section 2.3.1, a number of past studies have examined the role of latent heating in the development of extratropical cyclones. These sensitivity tests presented here allow these effects to be analysed for this storm in the context of the other analyses.

Effect on Deepening

The NA domain run, with a horizontal resolution of 27 km, was able to capture the evolution of the cyclone. This was also true when the cumulus parameterisation was switched off. These

simulations were then used to examine the influence of latent heating on the large-scale cyclone development.

The effect of latent heating on the development and track of the cyclone is examined in Chapter 6. As shown in a number of previous studies latent heating is responsible for a significant portion of the deepening of the storm. The presence of latent heating enhances the deepening of cyclone Friedhelm by ~20 hPa in the WRF simulation. The lack of deepening following the removal of latent heating is attributed to the lack of a low-level diabatically-generated PV anomaly and subsequent PV tower.

The reduced deepening of the system has a dramatic impact on the winds. With a much lower PGF the wind speeds around the cyclone are significantly lower. This effect is largest in the south-west, SJ/CCB region, where the PGF has a larger influence on the wind speeds. This means that the highest winds within the storm system are located along the WCB and cold front for a longer period of time before higher winds generate in the south-west sector.

Wind speed Changes with Varying the Latent Heating Switch Off

Varying the time that latent heating is switched off shows interesting results in the development of PV and high winds. The latent heating is switched off 12 and 18 hours after the initiation at 0000 and 0600 UTC on the 8^{th} December. This switches the latent heating off as the storm is still deepening but prior to the highest wind speeds occurring. This causes small deviations in the track from the full latent heating simulation but these are relatively minor. Switching off the latent heating at these times has a significant impact on the deepening of the cyclone, slowing the deepening rapidly. It is notable however that the upper-level forcing continues to deepen the systems to some degree.

The removal of latent heating and reduction in deepening also causes the maximum cyclone wind speeds to initially slow their acceleration before decelerating, despite the storm continuing to deepen, albeit at a lesser rate. This shows that the rate of deepening plays a major role in the magnitude of maximum wind speeds.

7.1.3.1 Kinetic Energy

Diagnostics examining the kinetic energy of the large- and small-scale circulations are presented, the CKE and WKE, respectively. When each of these is plotted against the minimum cyclone pressure a strong negative correlation is shown indicating that the circulation at both local- and large-scales increases with decreasing SLP. When the CKE and WKE are compared there is a relatively good correlation. The NO-CU simulation shows better correlation between the two variables than the CTRL simulation. This suggests that the vertical motion and associated heating cause disturbances to the relationship between the large-scale circulation and that on the local-scale.

7.1.4 Summary of Key Conclusions

A number of key conclusions are outlined above, and are summarised here:

- WRF simulations of cyclone Friedhelm and trajectory analysis show evidence of a SJ
  - SJ descends upon passing to frontolytic zone at the end of the BBF
  - SJ shows evidence of CSI during period before the descent
  - SJ descent occurs in the region of frontolytic flow
  - Latent cooling does not affect the wind fields but alters the prior evolution of the SJ trajectories
- Winds within the cyclone do not conform to idealised balances such as geostrophic and gradient.
  - Geostrophic wind speeds peak around one hour prior to the maximum actual winds
  - Super-gradient flow is shown to the south side of the cyclone centre, sub-gradient to the north
- Latent heating plays a major role in the development of the cyclone.
  - Diabatically produced low-level PV anomaly is key to the explosive development of the storm
  - The high winds are linked to the deepening rate of the cyclone through the low-level PV generation

This thesis covers a number of aspects relating the dynamics of the high-winds in the CCB and SJ region of an extratropical cyclone, as well as their sensitivity to diabatic processes. Investigation of SJ trajectories in the context of the previous literature supports certain theories, namely the presence of CSI and frontolysis prior to descent, and provides greater insight into the variation of this phenomena. Novel approaches to calculating both the gradient wind and diagnostics of circulation can be used in future studies to test their robustness and provide future insights into the dynamics of extratropical cyclones.

7.2 Future Work

A robust theory for the initial forcer of SJ descent is still unclear. As Schultz and Sienkiewicz (2013) state CSI is not a cause of descent, and while the secondary circulations in the frontolytic region are shown to drive the descent in their case it is not as clear in cyclone Friedhelm. Further analysis of other cases should help clarify this situation, and could prove worthwhile in allowing an easy identification of potential SJ cases. The use of ensembles to identify the probability of SJ descent and magnitude may also be a useful branch of future research. Modern ensemble model systems such as the Met Office Ensemble Prediction System (MOGREPS) are capable of resolving SJs and may provide a valuable tool for forecasters if SJ conditions and diagnostics can be identified. Assessing the mechanisms which may cause SJs to descend to the surface, where they can cause significant damage, is a key area for assessing their impacts. Identifying the likelihood of SJ descent to the surface may be of significant use and impact. Given the evidence presented here and elsewhere low-level stability appears to be highly influential in this process, quantifying this and potentially providing kinematic forecasting tools, such as level of cloud in the dry slot, may lead to much improved forecasting and warnings of damaging SJs.

The identification of which of the cyclonic jets will be strongest is not always clear. Further work is needed in determining the key processes in the formation of each of the high-wind jets, contributing a useful addition to scientific knowledge and forecasting ability. The possible interaction of different jets such as the CCB and SJ is also an area which has not been the focus of research. Studies, including this one, investigating SJs have tended to focus purely on the SJ and/or CCB jets, but some have commented on the possibility of SJs descending into the CCB as the BBF develops further around the cyclone. Any interaction of the two jets may increase low-level winds and my be of interest to operational forecasting services.

The relatively easy method for calculating the gradient wind presented in this thesis provides the basis for further analysis of individual cyclones. Specifically it can be used to investigate whether the pattern of sub-gradient wind and super-gradient wind to the north and south of the cyclone centre, respectively, as shown in cyclone Friedhelm, is consistent in other cyclones.

The Bernoulli equation was applied to the SJ trajectories in cyclone Friedhelm to investigate if this theory can account for the acceleration of the SJ winds as they descend. Although this does not hold true in this case, due to both the unsteady nature of the deepening cyclone and the possible role of friction, it may play a role in other storms. Whether the Bernoulli function is relevant to SJs at all, should be the subject of future work.

Further examination of CKE and WKE in other storms would be a potentially interesting and potential fruitful avenue. This method could, feasibly, be applied to lower-resolution analysis products such a ECMWF analysis to explore the possibility of any link between CKE and important phenomena or intensity of cyclones.

The rate of deepening is shown to be important in the development of the highest wind; identifying if there is a fixed relationship between these two factors could provide a highly useful tool for forecasting damaging scenarios. The approach used here could be extended to case studies of other storms to better assess this relationship.

7.3 Concluding Remarks

Extratropical storms are a regular phenomenon, but can be highly damaging and dangerous. The effects of future climate on the frequency and intensity of such storms is still uncertain. This thesis provides insights to the dynamical processes and diabatic influences on the high wind regions of the SJ and CCB, both of which can be major damaging features in extratropical cyclones. Improved knowledge and forecasting of these features can ultimately help to mitigate the economic and social costs when such events occur.

References

Alexander, L. V., Tett, S. F. B. and Jonsson, T. (2005), "Recent observed changes in severe storms over the united kingdom and iceland", *Geophysical Research Letters* , Vol. 32, pp. n/a–n/a.

Allen, J. T., Pezza, A. B. and Black, M. T. (2010), "Explosive cyclogenesis: A global climatology comparing multiple reanalyses", *J. Climate* , Vol. 23, American Meteorological Society, pp. 6468–6484.

Anthes, R. A., Kuo, Y.-H. and Gyakum, J. R. (1983), "Numerical simulations of a case of explosive marine cyclogenesis", *Mon. Wea. Rev.* , Vol. 111, American Meteorological Society, pp. 1174–1188.

Ashley, W. S. and Black, A. W. (2008), "Fatalities associated with nonconvective high-wind events in the united states", *J. Appl. Meteor. Climatol.* , Vol. 47, American Meteorological Society, pp. 717–725.

Bader, MJ, F. G. G. J. L. R. W. A. (1995), *Images in weather forecasting; A practical guide for interpreting satellite imagery.*, Cambridge University Press.

Baker, L. (2009), "Sting jets in severe northern european wind storms", *Weather* , Vol. 64, John Wiley & Sons, Ltd., pp. 143–148.

Baker, L. H., Gray, S. L. and Clark, P. A. (2013), "Idealised simulations of sting-jet cyclones", *Quarterly Journal of the Royal Meteorological Society* , John Wiley & Sons, Ltd., pp. n/a–n/a.

Barredo, J. I. (2010), "No upward trend in normalised windstorm losses in europe: 1970-2008", *Natural Hazards and Earth System Science* , Vol. 10, pp. 97–104.

Beljaars, A. C. M. (1995), "The parametrization of surface fluxes in large-scale models under free convection", *Quarterly Journal of the Royal Meteorological Society* , Vol. 121, John Wiley & Sons, Ltd, pp. 255–270.

Bennetts, D. A. and Hoskins, B. J. (1979), “Conditional symmetric instability - a possible explanation for frontal rainbands”, *Quarterly Journal of the Royal Meteorological Society* , Vol. 105, John Wiley & Sons, Ltd, pp. 945–962.

Bjerknes, J. (1919), “On the structure of moving cyclones”, *Mon. Wea. Rev.* , Vol. 47, American Meteorological Society, pp. 95–99.

Bjerknes, J. and Soldberg, H. (1922), “Life cycle of the cyclones and the polar front theory of atmospheric circulation”, *Geophysical Publications* , Vol. 3, pp. 3–17.

Bosart, L. F., Hakim, G. J., Tyle, K. R., Bedrick, M. A., Bracken, W. E., Dickinson, M. J. and Schultz, D. M. (1996), “Large-scale antecedent conditions associated with the 12-14 march 1993 cyclone ("superstorm ’93") over eastern north america”, *Mon. Wea. Rev.* , Vol. 124, American Meteorological Society, pp. 1865–1891.

Böttger, H., Eckardt, M. and Katergiannakis, U. (1975), “Forecasting extratropical storms with hurricane intensity using satellite information”, *J. Appl. Meteor.* , Vol. 14, American Meteorological Society, pp. 1259–1265.

Brill, K. F. (2013), “Revisiting an old concept: The gradient wind”, *Mon. Wea. Rev.* , American Meteorological Society, pp. –.

Browning, K. A. (1986), “Conceptual models of precipitation systems”, *Wea. Forecasting* , Vol. 1, American Meteorological Society, pp. 23–41.

Browning, K. A. (1990), Organization of clouds and precipitatation in extratropical cyclones, *in* C. Newton and E. Holopainen, eds, ‘Extratropical Cyclones: The Erik Palmen Memorial Volume’, American Met. Soc., pp. 129–153.

Browning, K. A. (1999), “Mesoscale aspects of extratropical cyclones: An observational perspective”, *The life cycles of extratropical cyclones* , Amer. Meteor. Soc, pp. 265–283.

Browning, K. A. (2004), “The sting at the end of the tail: Damaging winds associated with extratropical cyclones”, *Quarterly Journal of the Royal Meteorological Society* , Vol. 130, John Wiley & Sons, Ltd., pp. 375–399.

Browning, K. A., Ballard, S. P. and Davitt, C. S. A. (1997), “High-resolution analysis of frontal fracture”, *Monthly Weather Review* , Vol. 125, pp. 1212–1230.

Browning, K. A., Chapman, D. and Dixon, R. S. (2001), "Stacked slantwise convective circulations", *Quarterly Journal of the Royal Meteorological Society* , Vol. 127, John Wiley & Sons, Ltd, pp. 2513–2536.

Browning, K. A., Clough, S. A., Davitt, C. S. A., Roberts, N. M., Hewson, T. D. and Healey, P. G. W. (1995), "Observations of the mesoscale sub-structure in the cold air of a developing frontal cyclone", *Quarterly Journal of the Royal Meteorological Society* , Vol. 121, John Wiley & Sons, Ltd, pp. 1229–1254.

Browning, K. A. and Roberts, N. M. (1994), "Structure of a frontal cyclone", *Quarterly Journal of the Royal Meteorological Society* , Vol. 120, John Wiley & Sons, Ltd, pp. 1535–1557.

Browning, K. A. and Roberts, N. M. (1996), "Variation of frontal and precipitation structure along a cold front", *Quarterly Journal of the Royal Meteorological Society* , Vol. 122, John Wiley & Sons, Ltd, pp. 1845–1872.

Campa, J. and Wernli, H. (2011), "A pv perspective on the vertical structure of mature mid-latitude cyclones in the northern hemisphere", *J. Atmos. Sci.* , American Meteorological Society, pp. –.

Cao, Z. (2009), "The sting jet in a simulated extratropical cyclone.", *Open Atmospheric Science Journal* , Vol. 3, pp. 212–218.

Carlson, T. N. (1980), "Airflow through midlatitude cyclones and the comma cloud pattern", *Mon. Wea. Rev.* , Vol. 108, American Meteorological Society, pp. 1498–1509.

Charney, J. G. (1947), "The dynamics of long waves in a baroclinic westerly current", *J. Meteor.* , Vol. 4, American Meteorological Society, pp. 136–162.

Chen, F. and Dudhia, J. (2001), "Coupling an advanced land surface-hydrology model with the penn state-ncar mm5 modeling system. part i: Model implementation and sensitivity", *Mon. Wea. Rev.* , Vol. 129, American Meteorological Society, pp. 569–585.

Christensen, J., Kumar, K. K., Aldrian, E., An, S.-I., Cavalcanti, I., de Castro, M., Dong, W., Goswami, P., Hall, A., Kanyanga, J., Kitoh, A., Kossin, J., Lau, N.-C., Renwick, J., Stephenson, D., Xie, S.-P. and Zhous, T. (2013), *Climate Change 2013: The Physical Science Basis. Contribution of Working Group I to the Fifth Assessment Report of the Intergovernmental Panel on Climate Changes*, Cambridge University Press, Cambridge, United Kingdom and New York, NY, USA, chapter Climate Phenomena and their Relevance for Future Regional Climate Change., pp. 1217–1308.

Clark, P. A., Browning, K. A. and Wang, C. (2005), "The sting at the end of the tail: Model diagnostics of fine-scale three-dimensional structure of the cloud head", *Quarterly Journal of the Royal Meteorological Society* , Vol. 131, pp. 2263–2292.

Clough, S. A., Lean, H. W., Roberts, N. M. and Forbes, R. M. (2000), "Dynamical effects of ice sublimation in a frontal wave", *Quarterly Journal of the Royal Meteorological Society* , Vol. 126, John Wiley & Sons, Ltd, pp. 2405–2434.

CRED (2013), 'Em-dat: The ofda/cred international disaster database'.
URL: *www.emdat.be*

Davies, H. C., SchÃČÂd'r, C. and Wernli, H. (1991), "The palette of fronts and cyclones within a baroclinic wave development", *J. Atmos. Sci.* , Vol. 48, American Meteorological Society, pp. 1666–1689.

Davis, C. A. (1992), "A potential-vorticity diagnosis of the importance of initial structure and condensational heating in observed extratropical cyclogenesis", *Mon. Wea. Rev.* , Vol. 120, American Meteorological Society, pp. 2409–2428.

Davis, C. A. and Emanuel, K. A. (1991), "Potential vorticity diagnostics of cyclogenesis", *Mon. Wea. Rev.* , Vol. 119, American Meteorological Society, pp. 1929–1953.

Davis, C. A., Grell, E. D. and Shapiro, M. A. (1996), "The balanced dynamical nature of a rapidly intensifying oceanic cyclone", *Mon. Wea. Rev.* , Vol. 124, American Meteorological Society, pp. 3–26.

Della-Marta, P. M., Mathis, H., Frei, C., Liniger, M. A., Kleinn, J. and Appenzeller, C. (2009), "The return period of wind storms over europe", *International Journal of Climatology* , Vol. 29, John Wiley & Sons, Ltd., pp. 437–459.

Deser, C., Tomas, R., Alexander, M. and Lawrence, D. (2010), "The seasonal atmospheric response to projected arctic sea ice loss in the late twenty-first century", *J. Climate* , Vol. 23, American Meteorological Society, pp. 333–351.

DiMego, G. J. and Bosart, L. F. (1982), "The transformation of tropical storm agnes into an extratropical cyclone. part ii: Moisture, vorticity and kinetic energy budgets", *Monthly Weather Review* , Vol. 110, pp. 412–433.

Dixon, R. S., Browning, K. A. and Shutts, G. J. (2002), "The relation of moist symmetric instability and upper-level potential-vorticity anomalies to the observed evolution of cloud heads", *Quarterly Journal of the Royal Meteorological Society* , Vol. 128, John Wiley & Sons, Ltd., pp. 839–859.

Donat, M. G., Leckebusch, G. C., Wild, S. and Ulbrich, U. (2011), "Future changes in european winter storm losses and extreme wind speeds inferred from gcm and rcm multi-model simulations", *Natural Hazards and Earth System Science* , Vol. 11, pp. 1351–1370.

Dudhia, J. (1989), "Numerical study of convection observed during the winter monsoon experiment using a mesoscale two-dimensional model", *Journal of the Atmospheric Sciences* , Vol. 46, pp. 3077–3107.

Dyer, A. J. and Hicks, B. B. (1970), "Flux-gradient relationships in the constant flux layer", *Quarterly Journal of the Royal Meteorological Society* , Vol. 96, John Wiley & Sons, Ltd, pp. 715–721.

Eady, E. T. (1949), "Long waves and cyclone waves", *Tellus* , Vol. 1, Blackwell Publishing Ltd, pp. 33–52.

Eckhardt, S., Stohl, A., Wernli, H., James, P., Forster, C. and Spichtinger, N. (2004), "A 15-year climatology of warm conveyor belts", *J. Climate* , Vol. 17, American Meteorological Society, pp. 218–237.

Emanuel, K. A. (1983*a*), "The lagrangian parcel dynamics of moist symmetric instability", *J. Atmos. Sci.* , Vol. 40, American Meteorological Society, pp. 2368–2376.

Emanuel, K. A. (1983*b*), "On assessing local conditional symmetric instability from atmospheric soundings", *Mon. Wea. Rev.* , Vol. 111, American Meteorological Society, pp. 2016–2033.

Emanuel, K. A. (1994), *Atmospheric Convection*, Oxford University Press.

Evans, M. S., Keyser, D., Bosart, L. F. and Lackmann, G. M. (1994), "A satellite-derived classification scheme for rapid maritime cyclogenesis", *Mon. Wea. Rev.* , Vol. 122, American Meteorological Society, pp. 1381–1416.

Figa-Saldaã, J., Wilson, J. J., Attema, E., Gelsthorpe, R., Drinkwater, M. R. and Stoffelen, A. (2002), "The advanced scatterometer (ascat) on the meteorological operational (metop) platform: A follow on for european wind scatterometers", *Canadian Journal of Remote Sensing* , Vol. 28, pp. 404–412.

Forbes, R. M. and Clark, P. A. (2003), "Sensitivity of extratropical cyclone mesoscale structure to the parametrization of ice microphysical processes", *Quarterly Journal of the Royal Meteorological Society* , Vol. 129, John Wiley & Sons, Ltd., pp. 1123–1148.

Francis, J. A. and Vavrus, S. J. (2012), "Evidence linking arctic amplification to extreme weather in mid-latitudes", *Geophysical Research Letters* , Vol. 39, pp. n/a–n/a.

Froude, L. S. R. (2009), "Regional differences in the prediction of extratropical cyclones by the ecmwf ensemble prediction system", *Mon. Wea. Rev.* , Vol. 137, American Meteorological Society, pp. 893–911.

Gill, A. E. (1982), *Atmosphere-Ocean Dynamics*, Academic Press.

Gray, S. L., Martínez-Alvarado, O., Baker, L. H. and Clark, P. A. (2011), "Conditional symmetric instability in sting-jet storms", *Quarterly Journal of the Royal Meteorological Society* , Vol. 137, John Wiley & Sons, Ltd., pp. 1482–1500.

Grønås, S. (1995), "The seclusion intensification of the new year's day storm 1992", *Tellus A* , Vol. 47, Munksgaard International Publishers, pp. 733–746.

Haarsma, R. J., Hazeleger, W., Severijns, C., de Vries, H., Sterl, A., Bintanja, R., van Oldenborgh, G. J. and van den Brink, H. W. (2013), "More hurricanes to hit western europe due to global warming", *Geophysical Research Letters* , Vol. 40, pp. 1783–1788.

Harrold, T. W. (1973), "Mechanisms influencing the distribution of precipitation within baroclinic disturbances", *Quarterly Journal of the Royal Meteorological Society* , Vol. 99, John Wiley & Sons, Ltd, pp. 232–251.

Hobbs, P. V., Locatelli, J. D. and Martin, J. E. (1990), "Cold fronts aloft and the forecasting of precipitation and severe weather east of the rocky mountains", *Wea. Forecasting* , Vol. 5, American Meteorological Society, pp. 613–626.

Hobbs, P. V., Locatelli, J. D. and Martin, J. E. (1996), "A new conceptual model for cyclones generated in the lee of the rocky mountains", *Bull. Amer. Meteor. Soc.* , Vol. 77, American Meteorological Society, pp. 1169–1178.

Holton, J. R. (1992), *An Introduction to Dynamic Meteorology*, 3 edn, Academic Press.

Hong, S.-Y. and Lim, J.-O. J. (2006), "The wrf single-moment 6-class microphysics scheme (wsm6)", *Asia-Pacific Journal of Atmospheric Sciences* , Vol. 42, Korean Meteorological Society, pp. 129–151.

Hoskins, B. and Berrisford, P. (1988), "A potential vorticity perspective of the storm of 15-16 october 1987", *Weather* , Vol. 43, Blackwell Publishing Ltd, pp. 122–129.

Hoskins, B. J., McIntyre, M. E. and Robertson, A. W. (1985), "On the use and significance of isentropic potential vorticity maps", *Quarterly Journal of the Royal Meteorological Society* , Vol. 111, John Wiley & Sons, Ltd, pp. 877–946.

IPCC (2013), *Climate Change 2013: The Physical Science Basis. Contribution of Working Group I to the Fifth Assessment Report of the Intergovernmental Panel on Climate Change*, Cambridge University Press, Cambridge, United Kingdom and New York, NY, USA., chapter Summary for Policymakers., pp. 3–30.

Joos, H. and Wernli, H. (2012), "Influence of microphysical processes on the potential vorticity development in a warm conveyor belt: a case-study with the limited-area model cosmo", *Quarterly Journal of the Royal Meteorological Society* , Vol. 138, John Wiley & Sons, Ltd., pp. 407–418.

Kain, J. S. (1993), "Convective parameterization for mesoscale models: The kain–fritsch scheme", *The representation of cumulus convection in numerical models, Meteor. Monogr* , Vol. 46, pp. 165–170.

Kain, J. S. (2004), "The kain-fritsch convective parameterization: An update", *J. Appl. Meteor.* , Vol. 43, American Meteorological Society, pp. 170–181.

Kain, J. S. and Fritsch, J. M. (1990), "A one-dimensional entraining/detraining plume model and its application in convective parameterization", *J. Atmos. Sci.* , Vol. 47, American Meteorological Society, pp. 2784–2802.

Keyser, D. and Pecnick, M. J. (1985), "A two-dimensional primitive equation model of frontogenesis forced by confluence and horizontal shear", *J. Atmos. Sci.* , Vol. 42, American Meteorological Society, pp. 1259–1282.

Keyser, D., Reeder, M. J. and Reed, R. J. (1988), "A generalization of petterssen's frontogenesis function and its relation to the forcing of vertical motion", *Mon. Wea. Rev.* , Vol. 116, American Meteorological Society, pp. 762–781.

Knox, J. A., Frye, J. D., Durkee, J. D. and Fuhrmann, C. M. (2011), "Non-convective high winds associated with extratropical cyclones", *Geography Compass* , Vol. 5, Blackwell Publishing Ltd, pp. 63–89.

Kuo, Y.-H. and Reed, R. J. (1988), "Numerical simulation of an explosively deepening cyclone in the eastern pacific", *Mon. Wea. Rev.* , Vol. 116, American Meteorological Society, pp. 2081–2105.

Kuo, Y.-H., Reed, R. J. and Low-Nam, S. (1992), "Thermal structure and airflow in a model simulation of an occluded marine cyclone", *Mon. Wea. Rev.* , Vol. 120, American Meteorological Society, pp. 2280–2297.

Kuo, Y.-H., Shapiro, M. A. and Donall, E. G. (1991), "The interaction between baroclinic and diabatic processes in a numerical simulation of a rapidly intensifying extratropical marine cyclone", *Mon. Wea. Rev.* , Vol. 119, American Meteorological Society, pp. 368–384.

Lackmann, G. M., Keyser, D. and Bosart, L. F. (1999), "Energetics of an intensifying jet streak during the experiment on rapidly intensifying cyclones over the atlantic (erica)", *Mon. Wea. Rev.* , Vol. 127, American Meteorological Society, pp. 2777–2795.

Lambert, S. and Fyfe, J. (2006), "Changes in winter cyclone frequencies and strengths simulated in enhanced greenhouse warming experiments: results from the models participating in the ipcc diagnostic exercise", *Climate Dynamics* , Vol. 26, Springer-Verlag, pp. 713–728.

Laprise, R. (1992), "The euler equations of motion with hydrostatic pressure as an independent variable", *Mon. Wea. Rev.* , Vol. 120, American Meteorological Society, pp. 197–207.

Leckebusch, G. C., Ulbrich, U., Fr˝ ohlich, L. and Pinto, J. G. (2007), "Property loss potentials for european midlatitude storms in a changing climate", *Geophysical Research Letters* , Vol. 34, pp. n/a–n/a.

Malmquist, D. L. (1999), European windstorms and the north atlantic oscillation: Impacts, characteristics and predictability., Technical Report Vol, 1., Bermuda Biological Station for Research.

Martin, J. E. (2006), *Mid-Latitude Atmospheric Dynamics - A First Course*, John Wiley and Sons Ltd.

Martínez-Alvarado, O., Baker, L. H., Gray, S. L., Methven, J. and Plant, R. S. (2014), "Distinguishing the cold conveyor belt and sting jet airstreams in an intense extratropical cyclone", *Mon. Wea. Rev.* , Vol. 142, American Meteorological Society, pp. 2571–2595.

Martínez-Alvarado, O., Gray, S. L., Catto, J. L. and Clark, P. A. (2012), "Sting jets in intense winter north-atlantic windstorms", *Environmental Research Letters* , Vol. 7, p. 024014.

Martínez-Alvarado, O., Gray, S. L., Clark, P. A. and Baker, L. H. (2011), "Objective detection of sting jets in low-resolution datasets", *Meteorological Applications* , John Wiley & Sons, Ltd., pp. n/a–n/a.

Martínez-Alvarado, O., Weidle, F. and Gray, S. L. (2010), "Sting jets in simulations of a real cyclone by two mesoscale models", *Monthly Weather Review* , Vol. 138, pp. 4054–4075.

Mass, C. F. (1991), "Synoptic frontal analysis: Time for a reassessment?", *Bull. Amer. Meteor. Soc.* , Vol. 72, American Meteorological Society, pp. 348–363.

Mass, C. F. and Schultz, D. M. (1993), "The structure and evolution of a simulated midlatitude cyclone over land", *Mon. Wea. Rev.* , Vol. 121, American Meteorological Society, pp. 889–917.

Mlawer, E. J., Taubman, S. J., Brown, P. D., Iacono, M. J. and Clough, S. A. (1997), "Radiative transfer for inhomogeneous atmospheres: Rrtm, a validated correlated-k model for the longwave", *Journal of Geophysical Research: Atmospheres* , Vol. 102, pp. 16663–16682.

Morrison, H., Thompson, G. and Tatarskii, V. (2009), "Impact of cloud microphysics on the development of trailing stratiform precipitation in a simulated squall line: Comparison of one- and two-moment schemes", *Monthly Weather Review* , Vol. 137, pp. 991–1007.

Mullen, S. L. and Baumhefner, D. P. (1988), "Sensitivity of numerical simulations of explosive oceanic cyclogenesis to changes in physical parameterizations", *Mon. Wea. Rev.* , Vol. 116, American Meteorological Society, pp. 2289–2329.

Nilsson, C., Stjernquist, I., Barring, L., Schlyter, P., Jonsson, A. M. and Samuelsson, H. (2004), "Recorded storm damage in swedish forests 1901ÃćÂĂÂŞ2000", *Forest Ecology and Management* , Vol. 199, pp. 165 – 173.

Nuss, W. A. and Anthes, R. A. (1987), "A numerical investigation of low-level processes in rapid cyclogenesis", *Mon. Wea. Rev.* , Vol. 115, American Meteorological Society, pp. 2728–2743.

Ooyama, K. V. (1990), "A thermodynamic foundation for modeling the moist atmosphere", *J. Atmos. Sci.* , Vol. 47, American Meteorological Society, pp. 2580–2593.

Orlanski, I. and Katzfey, J. (1991), "The life cycle of a cyclone wave in the southern hemisphere. part i: Eddy energy budget", *J. Atmos. Sci.* , Vol. 48, American Meteorological Society, pp. 1972–1998.

Orlanski, I. and Sheldon, J. (1993), "A case of downstream baroclinic development over western north america", *Mon. Wea. Rev.* , Vol. 121, American Meteorological Society, pp. 2929–2950.

Orlanski, I. and Sheldon, J. P. (1995), "Stages in the energetics of baroclinic systems", *Tellus A* , Vol. 47, Munksgaard International Publishers, pp. 605–628.

Palmen, E. (1958), "Vertical circulation and release of kinetic energy during the development of hurricane hazel into an extratropical storm", *Tellus* , Vol. 10, Blackwell Publishing Ltd, pp. 1–23.

Papritz, L. and Schemm, S. (2013), "Development of an idealised downstream cyclone: Eulerian and lagrangian perspective on the kinetic energy", *Tellus A* , Vol. 65.

Parker, D. J. and Thorpe, A. J. (1995), "The role of snow sublimation in frontogenesis", *Quarterly Journal of the Royal Meteorological Society* , Vol. 121, John Wiley & Sons, Ltd, pp. 763–782.

Parton, G., Dore, A. and Vaughan, G. (2010), "A climatology of mid-tropospheric mesoscale strong wind events as observed by the mst radar, aberystwyth", *Meteorological Applications* , pp. n/a–n/a.

Paulson, C. A. (1970), "The mathematical representation of wind speed and temperature profiles in the unstable atmospheric surface layer", *J. Appl. Meteor.* , Vol. 9, American Meteorological Society, pp. 857–861.

Persson, P. O. G. and Warner, T. T. (1993), “Nonlinear hydrostatic conditional symmetric instability: Implications for numerical weather prediction”, *Mon. Wea. Rev.* , Vol. 121, American Meteorological Society, pp. 1821–1833.

Petterssen, S. (1936), “Contribution to the theory of frontogenesis”, *Geofysical Publications* , Vol. 11, pp. 1–27.

Pinto, J., Ulbrich, U., Leckebusch, G., Spangehl, T., Reyers, M. and Zacharias, S. (2007), “Changes in storm track and cyclone activity in three sres ensemble experiments with the echam5/mpi-om1 gcm”, *Climate Dynamics* , Vol. 29, Springer-Verlag, pp. 195–210.

Pinto, J., Zacharias, S., Fink, A., Leckebusch, G. and Ulbrich, U. (2009), “Factors contributing to the development of extreme north atlantic cyclones and their relationship with the nao”, *Climate Dynamics* , Vol. 32, Springer-Verlag, pp. 711–737.

Pomroy, H. R. and Thorpe, A. J. (2000), “The evolution and dynamical role of reduced upper-tropospheric potential vorticity in intensive observing period one of fastex”, *Mon. Wea. Rev.* , Vol. 128, American Meteorological Society, pp. 1817–1834.

Quine, C. P. (1988), “Damage to trees and woodlands in the storm of 15-16 october 1987”, *Weather* , Vol. 43, Blackwell Publishing Ltd, pp. 114–118.

Reed, R. J., Kuo, Y.-H. and Low-Nam, S. (1994), “An adiabatic simulation of the erica iop 4 storm: An example of quasi-ideal frontal cyclone development”, *Mon. Wea. Rev.* , Vol. 122, American Meteorological Society, pp. 2688–2708.

Riviére, G., Arbogast, P. and Joly, A. (2014*a*), “Eddy kinetic energy redistribution within idealized extratropical cyclones using a two-layer quasi-geostrophic model”, *Quarterly Journal of the Royal Meteorological Society* , John Wiley & Sons, Ltd, pp. n/a–n/a.

Riviére, G., Arbogast, P. and Joly, A. (2014*b*), “Eddy kinetic energy redistribution within windstorms klaus and friedhelm”, *Quarterly Journal of the Royal Meteorological Society* , John Wiley & Sons, Ltd, pp. n/a–n/a.

Roebber, P. J. (1984), “Statistical analysis and updated climatology of explosive cyclones”, *Mon. Wea. Rev.* , Vol. 112, American Meteorological Society, pp. 1577–1589.

Rossa, A. M., Wernli, H. and Davies, H. C. (2000), “Growth and decay of an extra-tropical cyclone’s pv-tower”, *Meteorology and Atmospheric Physics* , Vol. 73, Springer-Verlag, pp. 139–156.

Rossby, C. G. and Willett, H. C. (1948), “The circulation of the upper troposphere and lower stratosphere”, *Science* , Vol. 108, pp. 643–652.

Sanders, F. and Gyakum, J. R. (1980), “Synoptic-dynamic climatology of the b̈omb̈’’, *Monthly Weather Review* , Vol. 108, pp. 1589–1606.

Sawyer, J. (1950), “Formation of secondary depressions in relation to the thickness pattern”, *Meteor. Mag* , Vol. 79, pp. 1–5.

Schär, C. (1993), “A generalization of bernoulli’s theorem”, *J. Atmos. Sci.* , Vol. 50, American Meteorological Society, pp. 1437–1443.

Schemm, S. and Wernli, H. (2013), “The linkage between the warm and the cold conveyor belts in an idealized extratropical cyclone*”, *J. Atmos. Sci.* , Vol. 71, American Meteorological Society, pp. 1443–1459.

Schüepp, M., Schiesser, H., Huntrieser, H., Scherrer, H. and Schmidtke, H. (1994), “The winterstorm v̈ivianöf 27 february 1990: About the meteorological development, wind forces and damage situation in the forests of switzerland”, *Theoretical and Applied Climatology* , Vol. 49, Springer-Verlag, pp. 183–200.

Schultz, D. M. (2001), “Reexamining the cold conveyor belt”, *Monthly Weather Review* , Vol. 129, pp. 2205–2225.

Schultz, D. M. and Doswell, C. A. (1999), “Conceptual models of upper-level frontogenesis in south-westerly and north-westerly flow”, *Quarterly Journal of the Royal Meteorological Society* , Vol. 125, John Wiley & Sons, Ltd, pp. 2535–2562.

Schultz, D. M., Keyser, D. and Bosart, L. F. (1998), “The effect of large-scale flow on low-level frontal structure and evolution in midlatitude cyclones”, *Mon. Wea. Rev.* , Vol. 126, American Meteorological Society, pp. 1767–1791.

Schultz, D. M. and Schumacher, P. N. (1999), “The use and misuse of conditional symmetric instability”, *Mon. Wea. Rev.* , Vol. 127, American Meteorological Society, pp. 2709–2732.

Schultz, D. M. and Sienkiewicz, J. M. (2013), "Using frontogenesis to identify sting jets in extra-tropical cyclones", *Wea. Forecasting* , Vol. 28, American Meteorological Society, pp. 603–613.

Schultz, D. M. and Zhang, F. (2007), "Baroclinic development within zonally-varying flows", *Quarterly Journal of the Royal Meteorological Society* , Vol. 133, John Wiley & Sons, Ltd., pp. 1101–1112.

Shapiro, M. and Keyser, D. (1990), Fronts, jet streams and the tropopause, *in* C. Newton and E. Holopainen, eds, 'Extratropical Cyclones: The Erik Palmen Memorial Volume', American Met. Soc., pp. 167–189.

Shutts, G. J. (1990*a*), "Dynamical aspects of the october storm, 1987: A study of a successful fine-mesh simulation", *Quarterly Journal of the Royal Meteorological Society* , Vol. 116, John Wiley & Sons, Ltd, pp. 1315–1347.

Shutts, G. J. (1990*b*), "Scape charts from numerical weather prediction model fields", *Mon. Wea. Rev.* , Vol. 118, American Meteorological Society, pp. 2745–2751.

Skamarock, W. C., Klemp, J. B., Dudhia, J., Gill, D. O., Barker, D. M., Wang, W. and Powers, J. G. (2008), A description of the advanced research wrf version 3, Technical report, NCAR.

Slater, T. P., Schultz, D. M. and Vaughan, G. (2014), "Acceleration of near-surface strong winds in a dry, idealised extratropical cyclone", *Quarterly Journal of the Royal Meteorological Society* , John Wiley & Sons, Ltd, pp. n/a–n/a.

Slingo, J., Belcher, S., Scaife, A., McCarthy, M., Saulter, A., McBeath, K., Jenkins, A., Huntingford, C., Marsh, T., Hannaford, J. and Parry, S. (2014), The recent storms and floods in the uk, Technical report, Met Office and Centre for Ecology and Hydrology.

Smart, D. J. and Browning, K. A. (2014), "Attribution of strong winds to a cold conveyor belt and sting jet", *Quarterly Journal of the Royal Meteorological Society* , Vol. 140, John Wiley & Sons, Ltd., pp. 595–610.

Smigielski, F. J. and Mogil, H. M. (1995), "A systematic satellite approach for estimating central surface pressures of mid-latitude cold season oceanic cyclones", *Tellus A* , Vol. 47, Munksgaard International Publishers, pp. 876–891.

Sterl, A., van den Brink, H., de Vries, H., Haarsma, R. and van Meijgaard, E. (2009), "An ensemble study of extreme storm surge related water levels in the north sea in a changing climate", *Ocean Science* , Vol. 5, pp. 369–378.

Stoelinga, M. T. (1996), "A potential vorticity-based study of the role of diabatic heating and friction in a numerically simulated baroclinic cyclone", *Mon. Wea. Rev.* , Vol. 124, American Meteorological Society, pp. 849–874.

Stoelinga, M. T. (2009), 'A users guide to rip version 4: A program for visualising mesoscale model output'.
URL: *http://www.mmm.ucar.edu/wrf/users/docs/ripug.htm*

Thorncroft, C. D., Hoskins, B. J. and McIntyre, M. E. (1993), "Two paradigms of baroclinic-wave life-cycle behaviour", *Quarterly Journal of the Royal Meteorological Society* , Vol. 119, John Wiley & Sons, Ltd, pp. 17–55.

Uccellini, L. W. (1990), Processes contributing to the rapid development of extratropical cyclones, *in* C. Newton and E. Holopainen, eds, 'Extratropical Cyclones: The Erik Palmen Memorial Volume', American Met. Soc., pp. 81–105.

Uccellini, L. W., Petersen, R. A., Kocin, P. J., Brill, K. F. and Tuccillo, J. J. (1987), "Synergistic interactions between an upper-level jet streak and diabatic processes that influence the development of a low-level jet and a secondary coastal cyclone", *Mon. Wea. Rev.* , Vol. 115, American Meteorological Society, pp. 2227–2261.

Ulbrich, U., Fink, A. H., Klawa, M. and Pinto, J. G. (2001), "Three extreme storms over europe in december 1999", *Weather* , Vol. 56, Blackwell Publishing Ltd, pp. 70–80.

Ulbrich, U., Leckebusch, G. and Pinto, J. (2009), "Extra-tropical cyclones in the present and future climate: a review", *Theoretical and Applied Climatology* , Vol. 96, Springer Vienna, pp. 117–131.

Vaughan, G., Methven, J., Anderson, D., Antonescu, B., Baker, L., Baker, T. P., Ballard, S. P., Bower, K. N., Brown, P. R. A., Chagnon, J., Choularton, T. W., Chylik, J., Connolly, P. J., Cook, P. A., Cotton, R. J., Crosier, J., Dearden, C., Dorsey, J. R., Frame, T. H. A., Gallagher, M. W., Goodliff, M., Gray, S. L., Harvey, B. J., Knippertz, P., Lean, H. W., Li, D., Lloyd, G., Martínez-Alvarado, O., Nicol, J., Norris, J., Öström, E., Owen, J., Parker, D. J., Plant, R. S., Renfrew, I. A., Roberts, N. M., Rosenberg, P., Rudd, A. C., Schultz, D. M., Taylor, J. P.,

Trzeciak, T., Tubbs, R., Vance, A. K., van Leeuwen, P. J., Wellpott, A. and Woolley, A. (2014), "Cloud banding and winds in intense european cyclones: Results from the diamet project", *Bull. Amer. Meteor. Soc.* , American Meteorological Society, pp. –.

Wang, C.-C. and Rogers, J. C. (2001), "A composite study of explosive cyclogenesis in different sectors of the north atlantic. part i: Cyclone structure and evolution", *Mon. Wea. Rev.* , Vol. 129, American Meteorological Society, pp. 1481–1499.

Webb, E. K. (1970), "Profile relationships: The log-linear range, and extension to strong stability", *Quarterly Journal of the Royal Meteorological Society* , Vol. 96, John Wiley & Sons, Ltd, pp. 67–90.

Wernli, B. H. and Davies, H. C. (1997), "A lagrangian-based analysis of extratropical cyclones. i: The method and some applications", *Quarterly Journal of the Royal Meteorological Society* , Vol. 123, John Wiley & Sons, Ltd, pp. 467–489.

Wernli, H. (1997), "A lagrangian-based analysis of extratropical cyclones. ii: A detailed case-study", *Quarterly Journal of the Royal Meteorological Society* , Vol. 123, John Wiley & Sons, Ltd, pp. 1677–1706.

Wernli, H., Dirren, S., Liniger, M. A. and Zillig, M. (2002), "Dynamical aspects of the life cycle of the winter storm "lothar" (24-26 december 1999)", *Quarterly Journal of the Royal Meteorological Society* , Vol. 128, John Wiley & Sons, Ltd., pp. 405–429.

Whitaker, J. S., Uccellini, L. W. and Brill, K. F. (1988), "A model-based diagnostic study of the rapid development phase of the presidents's day cyclone", *Mon. Wea. Rev.* , Vol. 116, American Meteorological Society, pp. 2337–2365.

Wicker, L. J. and Skamarock, W. C. (2002), "Time-splitting methods for elastic models using forward time schemes", *Mon. Wea. Rev.* , Vol. 130, American Meteorological Society, pp. 2088–2097.

Young, M. V., Monk, G. A. and Browning, K. A. (1987), "Interpretation of satellite imagery of a rapidly deepening cyclone", *Quarterly Journal of the Royal Meteorological Society* , Vol. 113, John Wiley & Sons, Ltd, pp. 1089–1115.

Zappa, G., Shaffrey, L. C., Hodges, K. I., Sansom, P. G. and Stephenson, D. B. (2013), "A multi-model assessment of future projections of north atlantic and european extratropical cyclones in

the CMIP5 climate models*”, *J. Climate* , Vol. 26, American Meteorological Society, pp. 5846–5862.